

MODULPRODUKTION FÜR DEN
CMS-PHASE-I-PIXELDETEKTOR UND UNTERSUCHUNG
DER ERWARTETEN LEISTUNGSFÄHIGKEIT
ÜBER DESSEN BETRIEBSDAUER

Benedikt Freund

Zur Erlangung des akademischen Grades eines
DOKTORS DER NATURWISSENSCHAFTEN
von der Fakultät für Physik des
Karlsruher Instituts für Technologie (KIT)

genehmigte

DISSERTATION

von

Dipl.-Phys. Benedikt Freund
aus Bruchsal

Tag der mündlichen Prüfung: 28.07.2017

Referent: Prof. Dr. Ulrich Husemann Institut für Experimentelle Teilchenphysik
Korreferent: Prof. Dr. Thomas Müller Institut für Experimentelle Teilchenphysik

Benedikt Freund:
*Modulproduktion für den
CMS-Phase-I-Pixeldetektor und Untersuchung
der erwarteten Leistungsfähigkeit
über dessen Betriebsdauer*
Juli 2017

ZUSAMMENFASSUNG

Der Gedanke, dass Materie aus elementaren Bestandteilen zusammengesetzt ist, beschäftigt die Menschheit bereits seit dem Jahr 600 v. Chr. Der experimentelle Nachweis konnte jedoch erst zu Beginn des letzten Jahrhunderts erbracht werden, was den ersten Schritt hin zur modernen Teilchenphysik darstellt. Heute werden in der Teilchenphysik Beschleuniger-Experimente genutzt, um die Eigenschaften und das Verhalten der fundamentalen Bestandteile der Materie zu untersuchen. Dabei werden Teilchen wie Elektronen oder Protonen miteinander zur Kollision gebracht, um neue unbekannte Teilchen zu erzeugen und zu untersuchen. Mithilfe dieser Ergebnisse lassen sich Vorhersagen überprüfen, die auf theoretischen Modellen basieren und ein tiefergehendes Verständnis der grundlegenden physikalischen Prozesse schaffen. Die am besten geeignete Theorie, die den aktuellen Wissensstand zusammenfasst und die beobachteten Prozesse mit hoher Präzision beschreibt, ist das Standardmodell der Elementarteilchenphysik. Jedoch gibt es auch Beobachtungen wie z.B. Dunkle Materie oder Dunkle Energie, die sich nicht anhand des Standardmodells erklären lassen und die auf eine noch umfassendere Theorie, in der das Standardmodell lediglich einen Teil darstellt hinweisen.

Der derzeit leistungsstärkste Teilchenbeschleuniger ist der **Large Hadron Collider (LHC)**, der von der Europäischen Organisation für Kernforschung (CERN) in der Nähe von Genf betrieben wird. Der LHC hat einen Umfang von 27 km und beschleunigt zwei gegenläufige Teilchenstrahlen bestehend aus bis zu ca. 2800 Protonenpaketen, die bei einer Schwerpunktsenergie von 13 TeV alle 25 ns zur Kollision gebracht werden. Diese Kollisionspunkte befinden sich an vier Stellen des Beschleunigerrings, welche wiederum von Detektoren umgeben sind, um die in den Kollisionen entstehenden Teilchen zu untersuchen. Zwei dieser Detektoren sind Mehrzweckdetektoren mit einem breiten wissenschaftlichen Programm. Dies ist zum einen das **A Toroidal LHC ApparatuS (ATLAS)** Experiment und zum anderen das **Compact Muon Solenoid (CMS)** Experiment, mit welchem sich die vorliegende Arbeit befasst. Aufgrund der enormen Größe und Komplexität sowohl des Beschleunigers als auch der Detektoren können solche Vorhaben nur von Kollaborationen, die tausende von Wissenschaftlern aus unterschiedlichen Fachrichtungen umfassen, gemeistert werden.

Der Detektor des CMS-Experiments besteht aus unterschiedlichen Detektorlagen und ist zylinderförmig um einen der Kollisionspunkte herum angeordnet. Er hat einen Durchmesser von 15 m, ist 28,7 m lang und wiegt etwa 14.000 t. Im Jahr 2012 haben die ATLAS- und CMS-Kollaborationen gemeinsam die Entdeckung des Higgs-Bosons verkündet. Dieses wurde bereits im Jahr 1964 von Peter Higgs und François Englert postuliert, wofür sie 2013 mit dem Nobelpreis für Physik ausgezeichnet wurden. Mit der Entdeckung des Higgs-Bosons gelang der Nachweis des letzten noch unentdeckten und vom Standardmodell beschriebenen Teilchen. Die Suche nach dem Higgs-Boson stellt jedoch nur ein Teil des Messprogramms der beiden Experimente CMS und ATLAS dar. Zusätzlich suchen diese nach Physik jenseits des Standardmodells, um Erklärungen für Beobachtungen zu finden, die sich nicht mithilfe des Standardmodells beschreiben lassen. Um die Chancen einer möglichen Entdeckung zu steigern, werden sowohl der Beschleuniger als auch die Detektoren in mehreren Stufen Verbesserungen unterzogen. Die vorliegende Arbeit befasst sich mit den Verbesserungen des CMS-Pixeldetektors.

Der CMS-Pixeldetektor bildet die innerste Komponente des CMS-Detektors und befindet sich in unmittelbarer Nähe zum Kollisionspunkt. Seine Aufgabe ist es, die Flugbahnen aller

geladenen Teilchen, die aus den Proton-Proton-Kollisionen entstehen, zu detektieren. Außerdem spielt der Pixeldetektor die entscheidende Rolle bei der Rekonstruktion von Sekundärvertices, die von Zerfallsprodukten herrühren, die noch wenige Millimeter zurücklegen, bevor sie selbst zerfallen. Dies ist vor allem für die Identifikation von b-Quark Zerfällen relevant, welche für zahlreiche Analysen von Bedeutung sind. Der ursprüngliche Pixeldetektor wurde im Frühjahr 2017 durch den neuen Phase-I-Pixeldetektor ersetzt. Der vollständige Austausch war notwendig, da der erste Pixeldetektor für eine ursprünglich vorgesehene instantane Luminosität von $\mathcal{L} = 1 \cdot 10^{34} \text{ cm}^{-2} \text{ s}^{-1}$ ausgelegt war, diese jedoch aufgrund der hervorragenden Leistungsfähigkeit des LHCs auf bis zu $\mathcal{L} = 2 \cdot 10^{34} \text{ cm}^{-2} \text{ s}^{-1}$ gesteigert wird. Dies führt zu einer deutlichen Zunahme an simultanen Proton-Proton-Kollisionen (von im Mittel 25 auf ca. 60 pro 25 ns) und entsprechend zu mehr zu detektierenden Teilchen, was wiederum die Kapazität des ursprünglichen Pixeldetektors überstiegen hätte. Daher hat sich die CMS-Kollaboration für einen vollständigen Austausch entschieden.

Der erste Teil dieser Arbeit widmet sich der Modulproduktion für den Phase-I-Pixeldetektor am KIT. Die Produktion begann im Mai 2015 und wurde im Juni 2016 beendet, wobei insgesamt 409 Module gefertigt wurden. Zusätzlich zur Beschreibung der vollständigen Produktionskette, die auch die finale Qualifikation an der RWTH Aachen berücksichtigt, wird auf zwei Aspekte im Detail eingegangen. Dabei handelt es sich zum einen um die Qualifikation der Bare-Module, ein Zwischenprodukt bestehend aus einem Silizium Sensor und 16 Auslesechips (ROCs). Die Qualifikation bestätigte mit lediglich 17 aussortierten Bare-Modulen (von 437 produzierten) die hervorragende Qualität der Bare-Modul-Produktion. Zum anderen werden die Ergebnisse von Messungen der finalen Module, die mithilfe von Röntgenstrahlung durchgeführt wurden, vorgestellt. Diese Messungen ermöglichen die Bestimmung der Anzahl der defekten Kanäle (Pixel). Von insgesamt 409 am KIT gefertigten Modulen wurden 368 mit Röntgenstrahlung untersucht, was in etwa 24,5 Millionen untersuchten Pixeln entspricht, wovon nur 3191 defekt sind (0,013%). Unter Berücksichtigung aller relevanten Messungen ergibt sich für die gesamte KIT-Produktion ein Ergebnis von 343 Modulen (83,9%), die für den Betrieb in CMS geeignet sind und von denen wiederum 323 tatsächlich im Detektor verbaut wurden. Das vor der Produktion ausgegebene Ziel waren 310 gute Module von denen 256 für den Einbau vorgesehen waren. Die überproportionale Verwendung von KIT-Modulen (323 anstatt 256) ist ein Indikator für deren gute Qualität.

Neben der Produktion der Module für den Phase-I-Pixeldetektor ist auch die Untersuchung der Leistungsfähigkeit des Detektors von großem Interesse. Dies wird im zweiten Teil dieser Arbeit behandelt mit besonderem Fokus auf der erwarteten Entwicklung der Leistungsfähigkeit über die gesamte Betriebsdauer des Detektors. Nur durch detailliertes Wissen über die Leistungsfähigkeit ist es möglich, den neuen Pixeldetektor optimal zu betreiben. Daher untersucht diese Studie alle relevanten Größen, angefangen bei den grundlegenden Eigenschaften wie der Strom-Spannungskennlinie des Sensors bis hin zu Auflösungsvermögen und Treffereffizienz. In diesem Zusammenhang wurden zunächst Labormessungen durchgeführt, die bestätigten, dass der neue Pixeldetektor auch am Ende seiner Betriebsdauer noch verlässlich betrieben werden kann. Lediglich bei den höchsten erwarteten Strahldosen war eine Anpassung der elektrischen Kalibration notwendig, um die optimale Leistungsfähigkeit wiederherzustellen. Zusätzlich wurden Messungen mit Hilfe eines Elektronenstrahls am Deutschen Elektronen-Synchrotron (DESY) in Hamburg durchgeführt um Auflösungsvermögen und Treffereffizienz zu untersuchen. Dabei wurde gezeigt, dass die besten Ergebnisse für Betriebsspannungen 100 V oberhalb der Verarmungsspannung und bei einer Detektionsschwelle von 1750 Elektronen erzielt werden. Zusätzlich wurde die besondere Bedeutung regelmäßiger Pulshöhenkalibrationen verdeutlicht, um Verschlechterungen der Auflösung zu vermeiden. Insgesamt hat sich gezeigt, dass der Phase-I-Pixeldetektor hervorragend für die geplante Betriebsdauer geeignet ist und ein ausgezeichnetes Fundament für kommende Physikanalysen bieten wird.

MODULE PRODUCTION
FOR THE CMS PHASE I PIXEL DETECTOR
AND STUDY OF THE EXPECTED DETECTOR PERFORMANCE
FOR THE TIME OF OPERATION

Benedikt Freund

Zur Erlangung des akademischen Grades eines
DOKTORS DER NATURWISSENSCHAFTEN
von der Fakultät für Physik des
Karlsruher Instituts für Technologie (KIT)

genehmigte

DISSERTATION

von

Dipl.-Phys. Benedikt Freund
aus Bruchsal

Tag der mündlichen Prüfung: 28.07.2017

Referent: Prof. Dr. Ulrich Husemann Institute of Experimental Particle Physics
Korreferent: Prof. Dr. Thomas Müller Institute of Experimental Particle Physics

Benedikt Freund:
Module Production
for the CMS Phase I Pixel Detector
and Study of the expected Detector Performance
for the Time of Operation
July 2017

CONTENTS

I INTRODUCTION AND BASICS	1
1 INTRODUCTION AND MOTIVATION	3
2 THE LARGE HADRON COLLIDER AND THE CMS EXPERIMENT	5
2.1 The Large Hadron Collider	5
2.2 The Compact Muon Solenoid Experiment	7
2.2.1 Detector Layout	8
2.3 Upgrades of the CMS Detector	11
2.3.1 The Phase I Upgrade	11
2.3.2 The Phase II Upgrade	13
3 SILICON PARTICLE DETECTORS	15
3.1 Introduction to Semiconductor Physics	15
3.1.1 Energy Band Model	15
3.1.2 Indirect Semiconductors	18
3.1.3 Doping	18
3.1.4 p-n Junction	20
3.1.5 Depletion Voltage	21
3.2 Interaction of Particles with Matter	23
3.2.1 Charged Particles	23
3.2.2 Thin Layers	24
3.2.3 Photons	25
3.3 Radiation Damage in Silicon	26
3.4 Working Principle of Semiconductor Detectors	29
II MODULE PRODUCTION FOR THE PHASE I UPGRADE OF THE CMS PIXEL DETECTOR	31
4 THE CMS PIXEL DETECTOR FOR THE PHASE I UPGRADE	33
4.1 Detector Geometry	33
4.1.1 Mechanics and Cooling System	34
4.1.2 Material Budget	36
4.2 The CMS Barrel Pixel Detector Module	37
4.2.1 The Silicon Sensor	38
4.2.2 The Readout Chip	40
5 MODULE PRODUCTION	45
5.1 Sensor Testing	46
5.2 ROC Preparation	48
5.2.1 The Tin-Lead Bumping Process	48
5.2.2 ROC Cleaning and Inspection	49
5.3 Bare Module Production	50
5.3.1 Flip-chip Bonding	51
5.3.2 Bare Module Test	54
5.3.3 Reflow Process	59
5.4 Module Assembly	59
6 RESULTS FROM THE BARE MODULE QUALIFICATION	67
6.1 Pretest Modules	67
6.2 Bare Modules	69

6.2.1	Leakage Current	69
6.2.2	Defective Pixels	70
6.2.3	Reworked Bare Modules	71
6.2.4	Bare Module Yield	73
7	MODULE X-RAY TESTING AND QUALIFICATION	77
7.1	Leakage Current Results	77
7.1.1	Leakage currents measured during the X-ray tests	77
7.1.2	Comparison with bare module leakage currents	78
7.2	Defective Pixels	79
7.2.1	Defective pixels obtained from X-ray tests	79
7.2.2	Comparison with defective pixels on the bare module	83
7.3	Module Yield	85
	III PERFORMANCE STUDY FOR THE PHASE I UPGRADE OF THE CMS PIXEL DETECTOR	89
8	LABORATORY MEASUREMENTS	91
8.1	Samples	91
8.2	Irradiation	92
8.3	Energy Spectrum	93
8.4	Uncertainties	94
8.4.1	Fitting Functions	94
8.4.2	Measurement Repeatability	95
8.5	Phase I Barrel Pixel Module	96
8.5.1	IV Characteristics of the Module	97
8.5.2	Hit Maps of the Module	98
8.5.3	X-ray Calibration Curves of the Module	98
8.5.4	Charge Collection of the Module	101
8.6	Single Chip Assemblies	105
8.6.1	IV Characteristics of the Single Chip Assemblies	105
8.6.2	Hit Maps of the Single Chip Assemblies	106
8.6.3	Charge Collection of the Single Chip Assemblies	107
9	TEST BEAM MEASUREMENTS	111
9.1	Test Beams at the DESY-II Synchrotron	111
9.1.1	DESY-II Beamlines	112
9.1.2	The DATURA Beam Telescope	112
9.1.3	The EU Telescope Framework	115
9.1.4	EU Telescope Analysis Processor for CMS Pixel Samples	117
9.2	Measurement Program	118
9.3	Test Beam Results	118
9.3.1	Asynchronous Data	118
9.3.2	Cluster Investigation	120
9.3.3	Hit Efficiency	127
9.3.4	Spatial Resolution	136
9.4	Conclusions	145
	IV SUMMARY AND OUTLOOK	149
10	SUMMARY	151
	V APPENDIX	153
A	POSITION DISTRIBUTION OF REPLACED ROCS	155
B	ADDITIONAL RESULTS ON DEFECTIVE PIXELS OF THE KIT MODULES	157
C	SINGLE CHIP ASSEMBLIES FOR THE PHASE I PERFORMANCE STUDY	159
D	ELECTRICAL TEST SETUP	161

E	X-RAY SOURCE BASED ON AMERICIUM	163
F	ADDITIONAL LABORATORY RESULTS	165
	F.1 Threshold Maps	165
	F.2 X-ray Calibration of the Single Chip Assemblies	166
G	ADDITIONAL TEST BEAM RESULTS	169
	G.1 Asynchronous Data	169
	G.2 Cluster Size	170
	G.2.1 Intrapixel Cluster Size Distribution	172
	G.2.2 Intrapixel Cluster Signal Height	174
	G.2.3 Intrapixel Signal Height of the Seed Pixel	175
	G.2.4 Mean Cluster Size depending on the Bias Voltage and the Tilt Angle	176
	G.3 Hit Efficiency Profile	177
	G.4 Intrapixel Resolution	178
H	LOW TEMPERATURE BUMP BONDING FOR PIXEL SENSOR STUDIES	181
	H.1 Sensor Studies for the Phase II Upgrade	182
	H.2 Low Temperature Bump Bonding	184
	H.2.1 Gold Stud to Tin Lead Bump Bonding	184
	H.2.2 Ultraviolet curing Glue	187
	H.2.3 Underfill Adhesive	189
	H.3 Conclusions	190
	BIBLIOGRAPHY	193
	List of Figures	205
	List of Tables	208

Part I

INTRODUCTION AND BASICS

Science is a way of thinking much more than it is a body of knowledge.

Carl Sagan

1

INTRODUCTION AND MOTIVATION

Already in the 6th century before Christ the idea arose that all matter is composed of elementary particles. John Dalton concluded in the 19th century that each element of nature is composed of a single, unique particle type. Since then the word atom has been used to denote the smallest particle of a chemical element. Only in the early 20th century it was discovered that atoms are not the fundamental particles and instead consist of even smaller particles. This was the birth of particle physics.

Particle physics is one of many disciplines among physics. While the word "particle" can refer to various small objects like protons or gas molecules, particle physics typically studies the smallest indivisible (detectable) particles and the fundamental forces explaining their behavior. The most important tools used in the field of particle physics are particle colliders. They accelerate either elementary particles like electrons or composite particles like protons, bringing them to collision in order to create and investigate undiscovered particles. The currently most promising theory which describes elementary particles as well as their fundamental interactions is the Standard Model of particle physics (SM). The SM has its origin in the 1960s describing many observations of nature with astonishing precision.

A key parameter of particle colliders used in particle physics is the collision energy of the accelerated particles. Only a steady increase allows to extend the search for new physics into unexplored energy domains. To account for the demand of high collision energies, present-day colliders are large and complex machines. Hence, collider projects can only be covered by large collaborations of thousands of people from different disciplines. This is particularly true for the Large Hadron Collider (LHC), the most powerful particle collider in our time. It is located close to Geneva, Switzerland and operated by the European Organization for Nuclear Research (CERN). The LHC has a circumference of 27 km and collides protons at a center of mass energy of 13 TeV. Apart from the accelerator, the detectors at the four interaction points measuring the particles emerging from the collisions are of high importance. This thesis is dedicated to the Compact Muon Solenoid (CMS) experiment, which is one of two multi purpose experiments at the LHC. The second multi purpose experiment is the A Toroidal LHC ApparatuS (ATLAS) experiment. Both announced the discovery of the Higgs boson in 2012 [CMS12], [ATL12] which was postulated in 1964 [Hig64], [EB64] and for which Peter Higgs and François Englert have been awarded the Nobel Prize in Physics in 2013. The discovery of the Higgs boson was an expected SM supplement but it is only one aspect of the comprehensive research programs of CMS and ATLAS which also address physics beyond the SM (observations which cannot be explained by the SM). To improve the chances for a potential discovery of new physics the LHC and its detectors are upgraded in stages. This thesis focuses on the upgrades of the CMS silicon pixel detector, which is the innermost component of the CMS detector located closest to the interaction point.

In the first part of this thesis an introduction of the LHC and the CMS experiment is given (chapter 2) followed by a description of important properties of silicon particle detectors (chapter 3). Afterwards the main part of this thesis is addressed which is divided into two topics.

The first one focuses on the production of the Phase I upgrade of the silicon pixel detector (chapters 4 to 7), which replaced the original pixel detector in early 2017.

In chapter 4 the CMS pixel detector is described. It is the innermost component of the CMS detector located closest to the proton-proton interaction point. Its task is to precisely measure the trajectories of all charged particles emerging from the collisions and to identify secondary decay vertices which requires good spatial resolution. The original pixel detector, which performed well, had to be replaced as it would have suffered from intolerable inefficiencies due to the increasing LHC luminosity. When the LHC was designed the proposed instantaneous luminosity was $\mathcal{L} = 1 \times 10^{34} \text{ cm}^{-2}\text{s}^{-1}$, however the excellent LHC performance allows to increase it up to $\mathcal{L} = 2 \times 10^{34} \text{ cm}^{-2}\text{s}^{-1}$. Therefore, the CMS collaboration decided to replace the pixel detector completely at the beginning of 2017.

Chapter 5 addresses the workflow of the module production at KIT for the Phase I pixel detector. The production chain is introduced starting with the single components up to the complete module. This includes the actual production steps as well as the numerous quality assurance checks. The latter are of great importance to guarantee good quality of the produced modules and to assure efficient use of components. The quality checks comprise optical inspections, electrical tests and measurements with X-rays. All these tests allow to identify potential failures as early as possible and to adapt the production process, if required. Of particular interest – within this thesis – are two aspects of the production. These aspects are the qualification of bare modules, an intermediate product consisting of one sensor and 16 ReadOut Chips (ROCs), as well as the X-ray measurements of complete modules.

Chapter 6 focuses on the results of the bare module qualification. On the one hand, this includes a measurement of the current-voltage characteristic to verify the sensor quality. On the other hand, a functionality check of each ROCs is performed and the number of defective channels (pixels) is determined. Afterwards each tested bare module is graded according to predefined criteria.

In chapter 7 the results of the X-ray measurements are presented. Aside from again determining the number of defective channels a simplified check of the current-voltage behavior is carried out. In addition, these results are used to cross-check the bare module qualification. Finally, the overall yield of the KIT module production is given.

The present thesis not only covers the production of the new Phase I pixel detector but also investigates its expected performance over the entire operating period. This is the second main topic of this thesis and presented in chapters 8 and 9.

The first part of the performance study is introduced in chapter 8 showing the results of laboratory measurements performed at KIT. The samples used for these measurements are a module from the production and simplified smaller detectors consisting of a single ROC and a smaller version of the silicon sensor matching one ROC instead of 16. The laboratory measurements allow to investigate the impact of radiation damage on the electrical detector calibration and the charge collection efficiency. The second part of the performance study is addressed in chapter 9 examining the key properties of the detector in detail. This particularly refers to the hit efficiency which needs to be sufficiently high to detect all (charged) particles emerging from the proton-proton collisions. Further, the spatial resolution is studied, required for precise track reconstruction and identification of secondary vertices (relevant for various physics analyses relying on the identification of jets with b-hadrons). These measurements were performed with the help of a particle test beam at the DESY Test Beam Facility in Hamburg, Germany.

Finally, chapter 10 summarizes the results of both discussed topics.

Theory is just a human construction in order to understand the data: Nature is the boss.

Jonathan R. Ellis

2

THE LARGE HADRON COLLIDER AND THE CMS EXPERIMENT

In physics, theory helps to understand how we observe nature. Experiments in turn are the tools to study nature and among the most powerful of these tools is the **Large Hadron Collider** (LHC). Particle accelerators like the LHC are complemented by experiments detecting and analyzing the particles emerging from the particle collisions. The detector referred to in this thesis is the **Compact Muon Solenoid** experiment (CMS) which is described following the LHC introduction.

2.1 THE LARGE HADRON COLLIDER

On 16 December 1994, the European Organization for Nuclear Research (CERN) in Geneva approved the construction of the Large Hadron Collider. It was decided to build the LHC in the tunnel of the already existing **Large Electron Positron Collider** (LEP) that was operated at CERN from 1989 to 2000. As its predecessor LEP, the LHC is a synchrotron with a circumference of 27 km and up to 175 m below the earth's surface [BCL⁺04].

Particle accelerators like LEP and the LHC are designed to perform measurements with great precision and at high energies. Especially the LHC extends the search for new physics to an unexplored energy domain. Hence, the challenge regarding such circular accelerators are factors limiting their accessible energy range. The two main factors are the field strength of the magnets bending the particle beam and keeping them on track as well as the energy loss of the particles due to synchrotron radiation. The latter is emitted when the direction of motion of a charged particle is changed due to the Lorentz force caused by a magnetic field¹. While the LHC predecessor LEP used electrons which suffer strongly from synchrotron radiation due to their comparable low mass, the LHC uses protons which emit significantly less synchrotron radiation. The power P emitted via synchrotron radiation by a particle is given by equation 2.1 with the particle rest mass m_0 , its energy E and the accelerator radius r , see e.g. [Mes05].

$$P = \frac{e^2 c}{6\pi\epsilon_0 (m_0 c^2)^4} \cdot \frac{E^4}{r^2} \quad (2.1)$$

Despite the fact that protons are about 1800 times heavier than electrons, the LHC's center of mass energy is only 60 times higher than LEP's. In terms of synchrotron radiation protons could gain 1800^4 times the energy of electrons to have equal energy loss. However, the LHC's limiting factor is the magnetic field keeping the particle beam on track, not the energy loss by synchrotron radiation. Nevertheless, it only became possible to reach the center of mass energy of 13 TeV due to the development of powerful magnets [BCL⁺04].

As described above, the impact of both limiting factors decreases for larger radii and they are taken into account by the enormous size of LEP and the LHC, respectively.

¹ with field lines nonparallel to the direction of motion

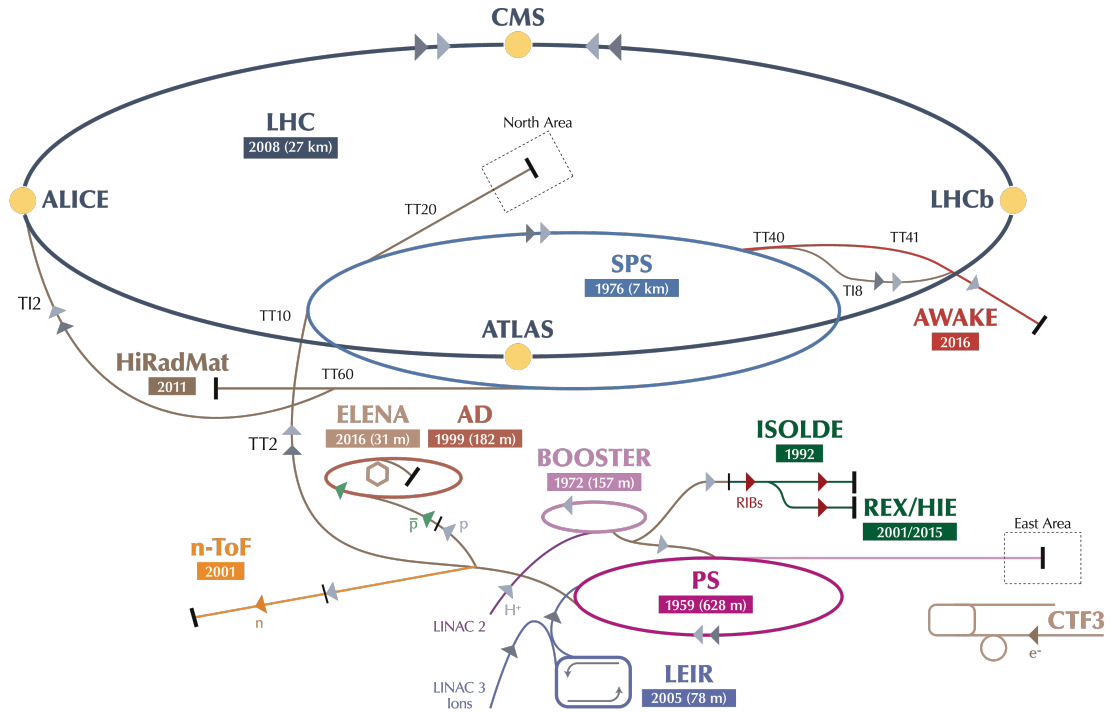


Figure 2.1: Overview of the CERN accelerator complex including the four main LHC experiments ALICE, ATLAS, CMS and LHCb. Protons (or heavy ions) pass through several preaccelerator stages before they are injected into the LHC to reach the desired collision energy. Modified from [DM16].

The particles accelerated at the LHC are typically protons (or heavy ions for about one month per year) which pass through several preaccelerator stages (see figure 2.1) before they are injected into the LHC. Within the LHC they travel in two counter-rotating beams, brought to collision at four interaction points.

These protons start their journey as bottled hydrogen gas. After removing the electrons from the hydrogen atoms the protons get into the first element of the acceleration chain, the LINAC 2, where they reach an energy of 50 MeV. Next, the protons are transferred into the Proton Synchrotron Booster (PSB) obtaining 1.4 GeV, followed by the Proton Synchrotron (PS) pushing the beam energy to 25 GeV. In the Super Proton Synchrotron (SPS) the protons are accelerated to 450 GeV before being injected into the LHC, the final element of the accelerator complex, where they reach the collision energy of 6.5 TeV [CER06].

In the LHC there is not a continuous beam of protons, instead the beam has a bunch structure with up to about 2800 bunches per beam. The distance between the bunches, containing approximately 1.2×10^{11} protons each, is about 7.5 m. The collision rate of the bunches (bunch crossing rate) at the interaction points is 40 MHz. The most relevant performance criterion – aside from the center of mass energy – for particle accelerators is the instantaneous luminosity \mathcal{L} which is given by [PRSZ04]

$$\mathcal{L} = \frac{n \cdot N_1 \cdot N_2 \cdot f}{A}, \quad (2.2)$$

where n is the number of bunches per beam, N_1 and N_2 the number of particles per bunch, f the revolution frequency and A the beam cross section at the interaction point. The design luminosity of the LHC is $\mathcal{L} = 1 \times 10^{34} \text{ cm}^{-2}\text{s}^{-1}$ providing an average of 25 proton-proton interactions per bunch crossing. For precise measurements with good statistical significance a

high luminosity is desirable, but it is important to take the performance limits of the detectors into account, since higher luminosity comes with higher track density and more data to store.

Collider physics is to some extent comparable to archeology. The more fragments of an archeological discovery are available the better the reconstruction of the original item is. This is also true for the reconstruction of particles emerging from collisions at a particle accelerator. In case of LHC, this is carried out by four main plus three smaller experiments. Aside from CMS, which is introduced in more detail in the next section, the experiments are described briefly below.

- **ALICE: A Large Ion Collider Experiment.** The ALICE experiment investigates the quark-gluon plasma, a state of very high density and temperature, where quarks and gluons are not bound. This allows to study the state of the early universe immediately after the big bang. At the LHC the quark-gluon plasma is generated by colliding lead ions instead of protons with a center of mass energy of 2.76 TeV per nucleon. For more information about ALICE see e.g. [ALI17].
- **ATLAS: A Toroidal LHC ApparatuS.** The ATLAS experiment was designed with focus on proton-proton collisions representing one of two main purpose experiments covering a broad scientific program. Aside from discovering the Higgs boson (together with CMS) the ATLAS experiment performs precision measurements of Standard Model properties and searches for physics beyond the Standard Model. For more information about ATLAS see e.g. [ATL17].
- **LHCb: Large Hadron Collider beauty.** In contrast to the other main experiments the LHCb experiment does not use a cylindrically symmetric detector, instead it relies on a single-arm design in forward direction (along the beam pipe). This special design was chosen as the LHCb experiment is specialized on interactions of b-hadrons where pairs of those are produced predominantly in the same forward cone. Its physics goal is the measurement of the CP violation which might help explaining the baryon asymmetry observed in the universe. For more information about LHCb see e.g. [LHC17a].
- **Additional experiments:** located at three of the four main experiments are the smaller ones TOTEM², LHCf³ and MoEDAL⁴. TOTEM is designed to measure the proton size with a so far unrivaled accuracy. LHCf, the smallest of the seven experiments, is investigating particles generated in the forward region, simulating cosmic rays under laboratory conditions. Results of LHCf help interpreting and calibrating large-scale cosmic ray experiments. MoEDAL is searching for potentially existing magnetic monopoles as well as highly ionizing stable massive particles. For more information about these experiments see e.g. [TOT17], [LHC17b] and [MoE17].

2.2 THE COMPACT MUON SOLENOID EXPERIMENT

The Compact Muon Solenoid experiment uses a general purpose detector and has a broad physics program. It is investigating topics like the Standard Model, the search for extra dimensions as well as dark matter, to mention just a few. CMS is operated by a worldwide collaboration of about 5250 people representing 198 institutes from 45 countries [CMS17c]. One benefit of having two general purpose experiments with similar objectives like ATLAS and CMS is an independent confirmation of measurements as they were developed independently and therefore rely on different technologies.

² TOTal Elastic and diffractive cross section Measurement

³ Large Hadron Collider forward

⁴ Monopole and Exotics Detector At the LHC

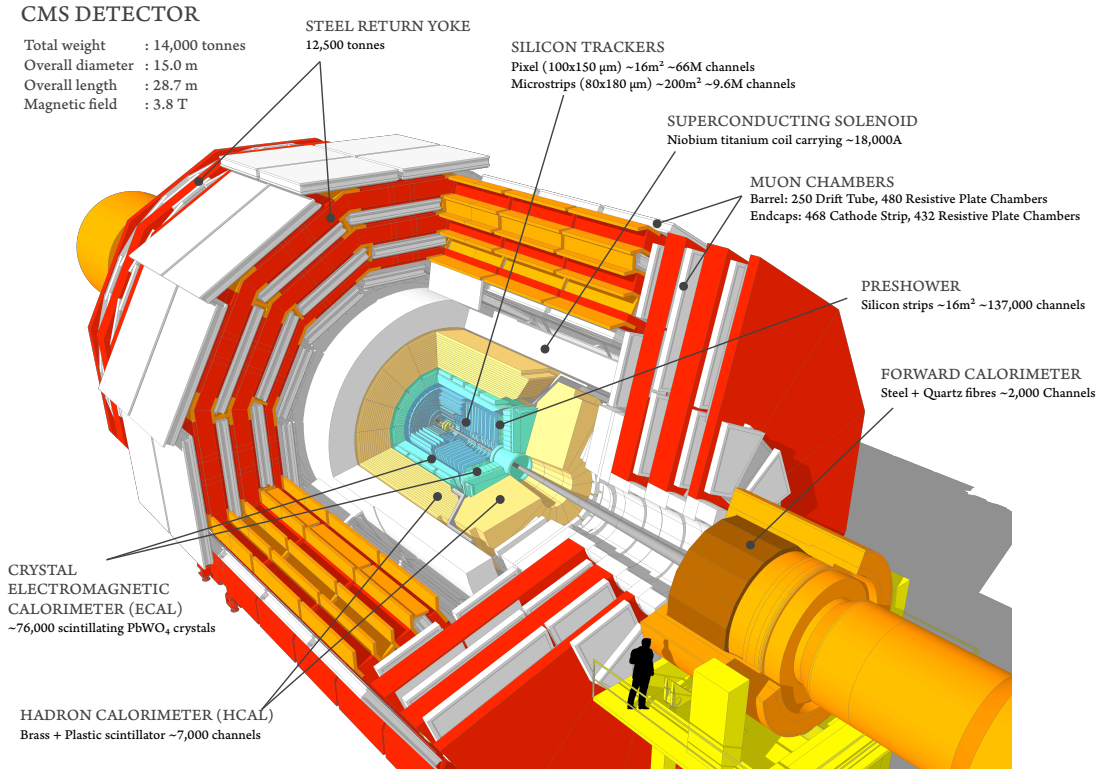


Figure 2.2: Structure of the CMS detector, from outside to inside: sandwich structure composed of muon chambers (white) and iron return yoke (red) followed by the superconducting solenoid magnet (white). Inside the solenoid are the hadronic calorimeter (pale yellow), the electromagnetic calorimeter (turquoise) and the silicon tracker consisting of strip (pale blue) and pixel detectors (yellow) [SM13].

When a detector is developed it is crucial to satisfy the constraints imposed by the physics program. For CMS, this can be summarized as follows [B⁺06]:

- Full spatial coverage around the interaction point to detect all particles emerging from the collisions.
- Excellent muon identification, momentum resolution and determination of the sign of the charge for pseudo rapidities⁵ $|\eta| < 2.5$.
- A tracker system with good momentum resolution and reconstruction efficiency of charged particles as well as reliable τ - and b -tagging by moving the innermost layer as close as possible to the interaction point.
- An electromagnetic calorimeter with good energy resolution, correct vertex localization and good photon and lepton isolation even at high luminosities.
- The hadron calorimeters need to have a wide coverage up to $|\eta| < 5$ and fine lateral segmentation to obtain a good indirect measurement of missing transverse energy.

2.2.1 DETECTOR LAYOUT

The detector – located at the LHC’s point 5 – is 28.7 m long, 15 m in diameter and weighs about 14,000 t, which is compact compared to ATLAS. Hence, the first letter of CMS stands

⁵ The pseudo rapidity η is defined as $\eta = -\ln \left[\tan \left(\frac{\theta}{2} \right) \right]$, where θ is the polar angle between the beam axis and the particle’s track.

for compact. The CMS detector relies on a design consisting of a cylindrical barrel region with perpendicular endcaps on each side which can be seen in figure 2.2. It has an onion-like structure formed by different subdetectors required to determine the particles and their properties. Starting from the outside, these subsystems are described below.

MUON CHAMBERS

The second letter in the acronym CMS highlights the importance of detecting muons efficiently, since they are expected to be produced in the decay of a number of potential new particles. The reason that the muon chambers are the outermost part takes into account that muons are the only detectable particles which are not stopped within the inner detector subsystems. There are three different types of muon chambers, which are **Drift Tubes (DT)**, **Cathode Strip Chambers (CSC)** and **Resistive Plate Chambers (RPC)**. All these types exploit the fact that traversing muons ionize gas inside the chambers. The decision to have three types of muon chambers is to account for the different requirements on resolution and response time depending on the position of the chambers [muo97].

SOLENOID MAGNET AND IRON RETURN YOKE

CMS owes its third letter to its superconducting solenoid magnet made from niobium-titanium. It delivers a magnetic field of up to 4T [CMS17b] and is the most powerful solenoid magnet ever built. The magnetic field is desired as it bends the tracks of charged particles which enables the measurement of their mass-to-charge ratio. Since the bending of charged particles gets smaller with increasing momenta, a high magnetic field is required to compensate for this effect and obtain precise measurements even at high momenta. Outside of the solenoid, the magnetic field is confined by the iron return yoke (12,500 t) which is interleaved by the muon chambers. The field strength in the yoke is still about 2T at 3.8T provided by the solenoid magnet [sol97].

HADRONIC CALORIMETER

The **Hadronic CALorimeter (HCAL)** measures the energy of hadrons like neutrons, protons, kaons or pions by absorbing these particles entirely. For this purpose the HCAL uses a sandwich-like structure composed of plastic scintillators interleaved with brass absorbers. Incoming hadrons are stopped by the brass and produce showers of secondary particles. They in turn produce light within the plastic scintillators which are read out via photodiodes. Since the volume inside the solenoid is limited, additional HCAL layers were added outside the solenoid to have an absorber thickness larger than five times the interaction length. Further outside – along the beam pipe – the forward calorimeter (see figure 2.2) is installed to cover pseudo rapidities up to $|\eta| = 5$ [CMS97b].

ELECTROMAGNETIC CALORIMETER

The **Electromagnetic CALorimeter (ECAL)** is measuring the energy of electrons, positrons and photons by stopping them completely. It is made from lead tungstate crystals (PbWO_4) which bring the benefit of a high density material and good scintillating properties. Comparable to hadrons within the HCAL, electrons, positrons and photons create showers while they are stopped inside the ECAL. In addition, the ECAL is equipped with a preshower detector (see figure 2.2) located in front of the endcaps allowing to distinguish between single high energy photons (often signs of interesting physics) and a photon pair with less energy from a neutral pion decay [CMS97a].

TRACKER

The tracker of CMS is the innermost subdetector and, as already illustrated by the name, its task is to precisely measure the trajectories of charged particles. Reconstructing trajectories enables the localization of the primary and secondary vertices while the curvature gives information about the momentum and the sign of the charge. The challenges for the tracker

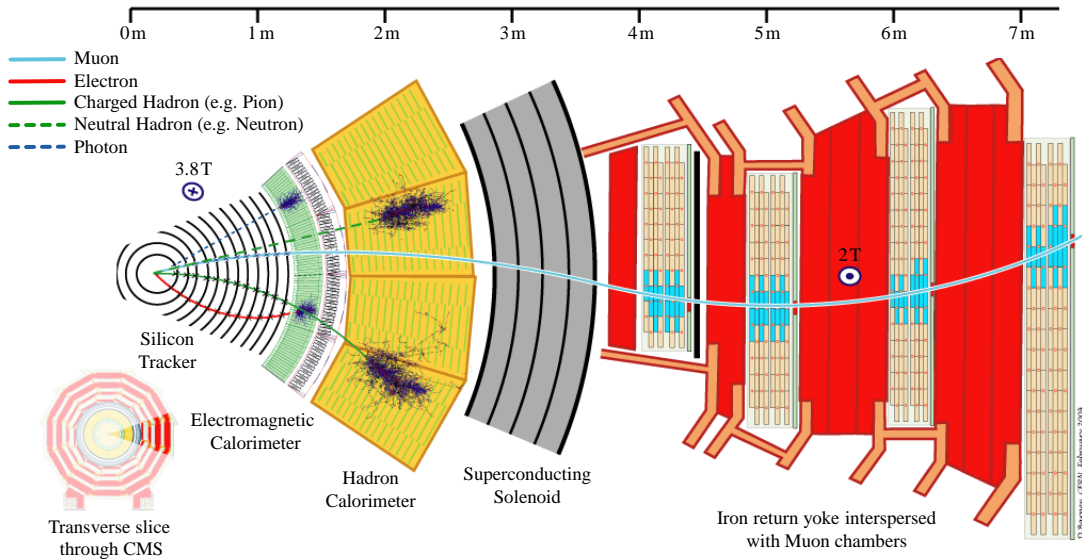


Figure 2.3: Transverse slice through the CMS detector showing the silicon tracker, the electromagnetic and hadronic calorimeters, the solenoid magnet and the sandwich-like structure consisting of iron return yoke and muon chambers. In addition several exemplary particle tracks and their interactions with the detector components are illustrated [Bar16].

are extremely high, since it needs a good spatial resolution and a high radiation tolerance as it is exposed to the highest particle rates due to the small distance to the interaction point. Further, the tracker must be able to handle the short bunch crossing time of 25 ns which corresponds to 40 million bunch crossings per second. At the same time it has to be lightweight to affect traversing particles (via multiple scattering, nuclear interactions and bremsstrahlung) as small as possible [C⁺08].

The entire tracker is based on silicon and it has a sensitive area of about 200 m² spread over multiple detector layers. As a consequence of the different distances to the interaction point, the particle rates vary strongly within the tracker. Hence it was decided to have two different detector types. A pixel detector which is able to handle the highest track density forms the center while it is surrounded by a microstrip detector.

The pixel detector uses a pixel size of 150 μm × 100 μm and has an excellent single hit resolution of 10 μm. Such fine resolution figures are necessary to correctly identify secondary vertices caused by long-living particles [Dom07].

The microstrip detector uses different geometries with sensors having lengths about 8 cm to 20 cm and pitches between 80 μm and 205 μm [Fel17]. Due to the lower particle rates, a microstrip detector is sufficient outside the pixel detector volume. In addition, it brings the benefit of lower cost compared to the pixel detector and requires fewer readout channels. The microstrip detector covers an area of roughly 200 m² equipped with about 10 million channels while the 2 m² sized pixel detector has more than 120 million channels [C⁺14].

With the combined information from all subsystems the CMS detector obtains a unique signature for each particle type. The transverse slice through CMS in figure 2.3 illustrates the particle identification in CMS for muons, electrons, charged and neutral hadrons as well as photons. Photons emerging from the collisions pass the silicon tracker without generating a signal while being completely stopped within the ECAL where they deposit their entire energy. Neutral hadrons are not detected by the silicon tracker and pass the ECAL without creating a signal. Instead, they are stopped by the HCAL losing all their energy. In contrast to neutral hadrons and photons, charged hadrons generate a signal inside the tracker, pass the ECAL with low interaction probability and are stopped – equally to neutral hadrons – within the

HCAL. Electron trajectories are also detected by the silicon tracker and they deposit all their energy in the ECAL not reaching subdetectors further outside. Since muons carry charge they also produce a signal in the tracker even though they are the only particles not being stopped by any of the subdetectors. Therefore muons are the only particles generating a signal in the muon chambers.

Nevertheless, there are also particles which CMS cannot detect at all. In the context of known, this is true for neutrinos. They have to be reconstructed indirectly, as they appear as missing transverse energy. In order to perform this reconstruction, it is indispensable to have a hermetic detector to assure that missing energy is not related to a detectable particle that left the detector unnoticed. The reconstruction algorithm CMS relies on is called particle-flow algorithm, for more information see e.g. [S⁺17].

A very important but so far unmentioned topic is related to the CMS trigger system. Since the LHC proton-proton collision rate is 40 MHz, a fast and reliable trigger system is required to reduce the available data to a storable amount. Otherwise it would be necessary to store 40 TB per second as a single event has approximately a size of 1 MB. Therefore the trigger system has the task to reject all data not containing content of physical interest, which is mostly the case for low energy events containing physics already investigated in the past [CRS02].

The CMS trigger system is divided into two parts. The first stage is carried out by the Level-1 trigger (L1) which is a hardware based system. It uses information from the muon system and the calorimeters taking a decision within 3.4 μ s. Data from other subdetectors is read out only in case of a positive trigger decision. As a result of the L1 trigger, the data rate is reduced to roughly 100 kHz. The second stage of the trigger system is the High Level Trigger (HLT) which is software-based running on a large computing cluster. In contrast to the L1 trigger stage, where the algorithms are fixed, the HLT can be adjusted according to the physics objectives. The data rate after the HLT is reduced to a few 100 Hz [B⁺05].

2.3 UPGRADES OF THE CMS DETECTOR

When the LHC was designed, it was expected to have a maximum luminosity of about $\mathcal{L} = 1 \times 10^{34} \text{ cm}^{-2}\text{s}^{-1}$, and the detectors were developed according to this value. However, it was decided to increase the luminosity to exploit the excellent LHC performance even further. The suggested luminosity increase is illustrated by the proposed timeline in figure 2.4. In a first step – which has already started in 2015 – the luminosity will be increased continuously until it reaches twice the design value. The LHC will run under these operation conditions until 2023. In a second step starting in 2024, the LHC will be upgraded to the High Luminosity LHC (HL-LHC). The scheduled start of the HL-LHC is 2026 with a luminosity of five to seven times the design value [A⁺15].

Even though the experiments were designed with a certain safety margin, this extent of luminosity increase forces the experiments to upgrade their detectors, too. Hence, there will be two upgrade phases, the first one in 2019/2020 to handle the consequences of the doubled design luminosity and the second upgrade from 2024 to 2026 to be prepared for the HL-LHC. The reason for undertaking this efforts is the desire to receive a profound understanding of nature and the physics describing it. Therefore, it is unavoidable to continuously improve the required tools.

2.3.1 THE PHASE I UPGRADE

With the luminosity increase to $\mathcal{L} = 2 \times 10^{34} \text{ cm}^{-2}\text{s}^{-1}$ the average number of simultaneous collisions (pile-up) will more than double from 25 to approximately 60. In addition, the radiation damage, the detectors suffer from, will also increase which would lead to an intolerable performance degradation. To account for this demanding new conditions, the CMS collaboration decided on several improvements during the Phase I upgrade in 2019/2020. The

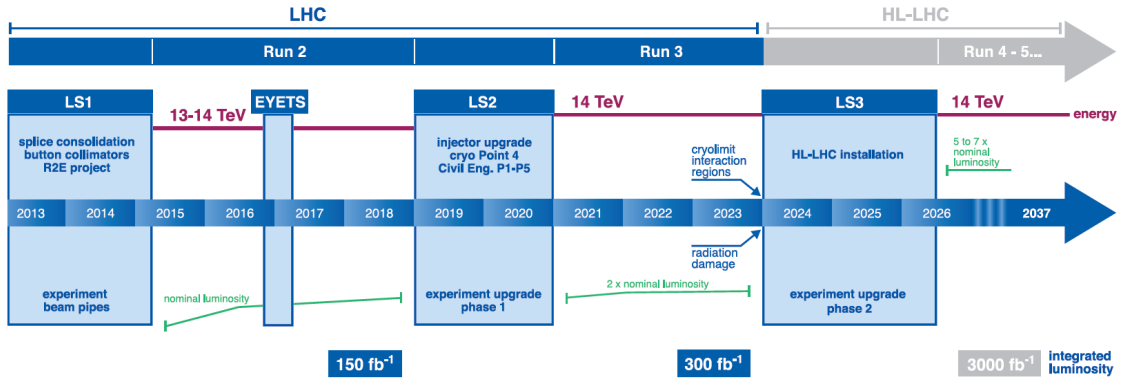


Figure 2.4: Proposed LHC schedule. The LHC luminosity is increasing over the next years until it will reach a value corresponding to five to seven times the design value presumably in 2026. Therefore, the experiments will be upgraded to cope with the consequences of the increasing luminosity. The first upgrade will take place in 2019/2020 while the second one is scheduled for 2024 till 2026 to be ready for the HL-LHC [Ros14].

subsystems addressed by the upgrade are the pixel detector (preponed installation already in early 2017), the hadronic calorimeter, the muon detectors as well as the trigger and data acquisition system. There are additional improvements concerning the beam radiation monitoring and luminosity measurement system as well as upgrades of the CMS infrastructure and facilities. The latter will not be part of the following introduction, but more information on all topics can be found in e.g. [CMS11].

PHASE I PIXEL DETECTOR

Since the CMS pixel detector is the innermost component, it is affected most by the performance increase of the LHC. In fact, the pixel detector is replaced entirely and several improvements are implemented to cope with the higher track density. Both the barrel region and the endcaps are equipped with an additional layer and a new advanced detector module version. Further, the support structure is based on lightweight carbon fibre while the new cooling system relying on CO₂ is more powerful [DA⁺12]. The pixel detector and its upgrade will be presented in detail in chapter 4.

PHASE I HADRONIC CALORIMETER

The upgrade of the hadronic calorimeter is required for several reasons. First of all, the hybrid photodiodes which show bad performance in the magnetic field, especially outside the solenoid, will be replaced by silicon photomultipliers. These photomultipliers also provide a longitudinal segmentation necessary to handle the pile up at higher luminosity. Additional timing information coming from the silicon photomultipliers will help to reduce the background while the regional calorimeter trigger will be improved by using new backend electronics [M⁺12].

PHASE I MUON DETECTOR

The muon detector upgrade addresses the installation of additional CSCs and RPCs which were already part of the original CMS plans but not realized. They are necessary, since poorly measured low momentum muons contribute to the trigger rate instead of being rejected. While this was not an issue in the past operation, it will lead to unacceptably high trigger rates with increasing luminosity. Thus, the new muon chambers will help sustaining a high trigger efficiency. Further improvements concern the readout electronics by exchanging and upgrading dedicated parts which will improve the rate capability [CMS11].

PHASE I TRIGGER AND DATA ACQUISITION SYSTEM

When CMS or more specifically its subdetectors were designed, the estimated L1 trigger rate was about 100 kHz. Due to the increase of luminosity, the trigger rate would reach values which could not be handled by the subsystems. In order to prevent this, a substantial increase of trigger thresholds is required to stay within the 100 kHz limit [TA13]. As a consequence of the higher pile up and the increasing number of channels, the bandwidth of the DAQ needs to be increased to handle the larger data volume per event. Therefore, some of the systems will be upgraded, which also brings the advantage to get independent of commercial parts which are no longer available. Further, the event builder has to be replaced completely and the HLT will be equipped with faster processors [CMS11].

2.3.2 THE PHASE II UPGRADE

When the LHC is upgraded to the HL-LHC, its new focusing and beam crossing scheme as well as the higher brightness of beams will allow an instantaneous luminosity of up to $\mathcal{L} = 2 \times 10^{35} \text{ cm}^{-2}\text{s}^{-1}$. However, it will not be possible to handle this value with the current available detector and trigger technologies. Therefore it is proposed to run with a leveled luminosity of about $\mathcal{L} = 5 \times 10^{34} \text{ cm}^{-2}\text{s}^{-1}$, which corresponds to approximately 140 proton-proton interactions per bunch crossing [C⁺15]. To be ready for the start of the HL-LHC, the detectors will be upgraded as well in the scheduled long shutdown from 2024 to 2026. In the following paragraphs a brief overview of the proposed upgrades affecting all subdetectors is given.

PHASE II TRACKER

The entire CMS tracker needs to be replaced for three main reasons. First of all, the amount of radiation damage it will accumulate, reaches a level that is no longer manageable with the current system. The Phase II tracker will rely on silicon with more radiation tolerant properties. Second, the granularity of the Phase I tracker will not be sufficient to correctly identify the tracks due to their high density caused by the increased pile up. In case of the pixel detector this is solved by pixels which will be approximately six times smaller than the Phase I pixels. Finally, it is mandatory that the Phase II tracker modules contribute to the L1 trigger decision to keep the trigger rate reasonably low while it helps to select only the most interesting events. The new outer tracker relies on two different module types, both based on a sandwich-like structure consisting of two sensors. Modules containing a pixel and a strip sensor will be installed in the inner part of the outer tracker where higher occupancies occur. In the outer part modules containing two strip sensors are used. Both module types contribute to the L1 trigger as they obtain information about the transverse particle momentum by comparing the particle penetration points in both sensors. Thus, the tracker is able to select particles with a transverse momentum greater than 2 GeV [Abb11]. Further studies even deal with the feasibility of a pixel based track trigger contributing to the L1 trigger [CMS16].

PHASE II CALORIMETERS

To be ready for the HL-LHC the calorimeter endcaps have to be replaced as the radiation damage they suffer from will reach a critical value. For instance, the PbWO₄ crystals of the ECAL will lose their transparency due to the radiation damage. The new High Granularity Calorimeter (HGC) replacing its predecessors will consist of an electromagnetic and a hadronic section. Both will use – for the first time – silicon sensors as the active material. Only the so-called backing hadron calorimeter continues using plastic scintillators. In the electromagnetic section tungsten and copper plates will be used as absorber while brass is chosen in the hadronic section. This new design has fine transverse and longitudinal segmentation providing excellent three dimensional shower images to cope with the

higher track density. The full calorimeter will provide an overall depth of approximately ten hadronic interaction lengths [C+15].

PHASE II MUON ENDCAPS

The Phase II upgrade of the muon chambers will address the lack of redundancy in the region $1.5 < |\eta| < 2.4$ where the conditions regarding background and momentum resolution are quite challenging. Since the magnetic field of the first two stations in that region is still reasonably high, the CSCs will be replaced by Gas Electron Multiplier (GEM) detectors providing a higher position resolution to improve the muon momentum resolution. In the last two stations RPCs will be installed which have a lower granularity but they deliver a good timing resolution mitigating background effects. Further, it is planned to add a GEM station behind the new endcap calorimeters to extend the muon detection coverage up to $|\eta| \approx 3$ [C+15].

PHASE II TRIGGER AND DATA ACQUISITION SYSTEM

As already true for the Phase I upgrade, the bandwidth of the trigger and DAQ system needs to be increased to manage the larger event size and the higher L1 trigger rates. In addition, the computing power needs to be upgraded to be able to handle the more complex event reconstruction caused by the high pile up. The trigger latency of the L1 trigger will be increased from a maximum of $3.4 \mu\text{s}$ to approximately $12.8 \mu\text{s}$ to be able to process the trigger information of the tracker and to use technologies like associative memory [Sab14]. Compared to Phase I conditions the Phase II luminosity of $\mathcal{L} = 5 \text{ to } 7 \times 10^{34} \text{ cm}^{-2}\text{s}^{-1}$ will increase the demands on bandwidth by a factor of 10 to 15 and on computing power by 15 to 30 corresponding to a pile up of 140 to 200. Assuming the HLT event selection rate of 1 out of 100 stays roughly the same, the subsequent data rate will increase to 5 kHz at a pile up of 140 and 7.5 kHz for a pile up of about 200 respectively.

I believe in innovation and that the way you get innovation is you fund research and you learn the basic facts.

Bill Gates

3

SILICON PARTICLE DETECTORS

In science the search for knowledge requires a persistent development of new experimental tools. Such a development were semiconductors entering the field of particle detectors. At accelerators like the LHC an enormous number of particles has to be detected simultaneously which is one of the most demanding tasks for particle detectors. During the last decades silicon semiconductor detectors have proved to be one of the best tools to fulfill this task. In this chapter basic properties of semiconductors are explained, followed by a description of the interactions of particles with matter and the effects of radiation damage in silicon. At the end the working principle of semiconductor detectors are described.

3.1 INTRODUCTION TO SEMICONDUCTOR PHYSICS

In the 1930's it was already demonstrated that certain solids can serve as solid-state ionizing detectors. However, it was only in the 1960's when it had been possible to produce silicon or germanium of sufficient size and purity to be relevant for detector physics. At that time gas-filled detectors were the standard devices measuring particle tracks. Semiconductor detectors became more common in the 1970's [Tsi09]. Although semiconductor and gas-filled detectors rely on the same detection principle, semiconductors provide a better energy resolution. In case of the most common semiconductor, silicon, only 3.6 eV are required to create an electron-hole pair while about 20 eV are necessary to ionize gas [Ros06]. Semiconductor detectors come with a sufficiently low material budget which is desired to minimize multiple scattering of traversing particles. The thickness of such a sensor is only about few hundred micrometers allowing a fast signal propagation while the signals still contain more than 20,000 electrons. They provide good radiation tolerance required for the harsh environment caused by the colliding particles and can be produced at affordable costs by using modern lithographic processes [Har08].

3.1.1 ENERGY BAND MODEL

In solid-state physics the energy band model describes the allowed states of electrons within a crystal lattice and explains physical properties like the electrical conductivity of solids. These bands are derived from the quantum mechanical wave functions of an electron in a large periodic lattice of atoms. The sharp energy levels of the single atoms split up within a solid due to quantum effects forming energy multiplets. The resulting multiplets are very dense so that they can be seen as continuous distributions of energy levels called energy bands, see e.g. [Dem16]. The highest energy band occupied by electrons is the valence band, the energy band above is the conduction band and the gap in between where no electron states exist is called band gap. Depending on the width of the band gap solid bodies are divided into insulators, semiconductors and conductors, which is illustrated in figure 3.1.

The situation in which the energy bands are either empty or fully occupied as described above is only true for $T = 0$ K. For any other temperature some electrons are thermally excited

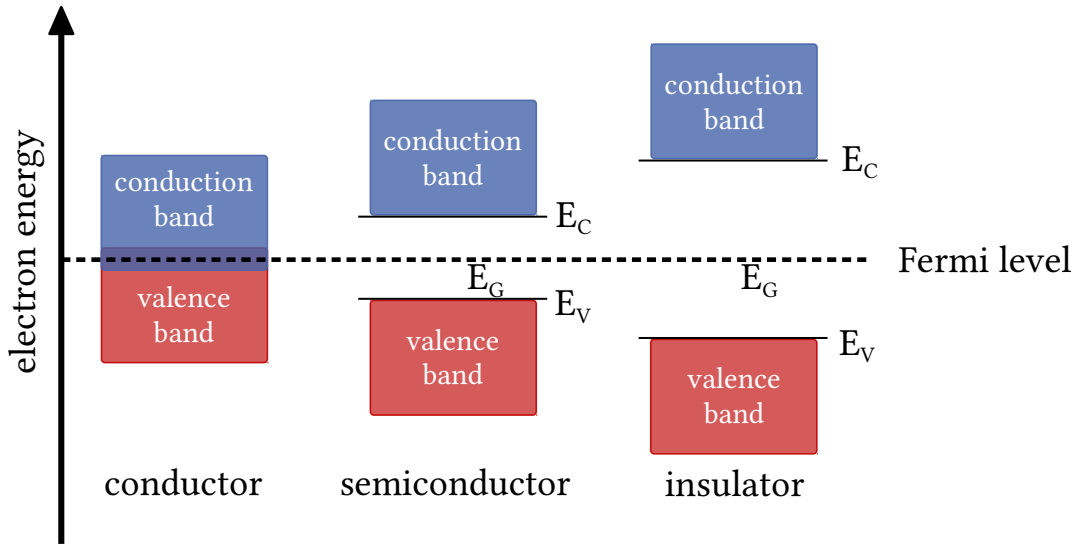


Figure 3.1: Energy band model of insulators, semiconductors and conductors (metal). Conductors (left) do not have a band gap between valence and conduction band hence electrons can simply enter the conduction band. Semiconductors (middle) have a small band gap ($E_G < 3 \text{ eV}$), electrons can be excited into the conduction band either thermally or via photon absorption. Insulators have even larger band gaps and it is not possible to bring electrons into the conduction band without destroying the solid. At absolute zero ($T = 0 \text{ K}$) all states up to the Fermi level are occupied. Modified from [Hof13].

and the energy state occupancy is described by the Fermi-Dirac distribution. The probability that an electron has the energy E is given by the equation below.

$$f(E) = \frac{1}{e^{[(E-E_F)/k_B T]} + 1} \quad (3.1)$$

E_F is the Fermi energy which corresponds to the state with an occupancy probability of 0.5, k_B is the Boltzmann constant and T the absolute temperature. The Fermi energy lies in between the valence and conduction band as shown in figure 3.1.

CONDUCTOR

In a conductor (metal or metalloid) the conduction band is either partially filled or it is overlapping with the valence band. Hence, electrons are in the conduction band providing good electrical conductivity. In general, heating up a conductor decreases its conductivity as the probability for electron scattering is increasing.

INSULATOR

Insulators have a band gap with E_G larger than 3 eV, see e.g. [GM14]. The valence band is fully occupied while the conduction band is empty. Even far above room temperature basically no electrons are in the conduction band. Nevertheless, insulators can behave like conductors if the temperature is high enough.

SEMICONDUCTOR

Semiconductors are characterized by a band gap with $0.1 \text{ eV} < E_G < 3 \text{ eV}$, see e.g. [H+95]. Due to the relatively small band gap its properties depend strongly on the temperature.

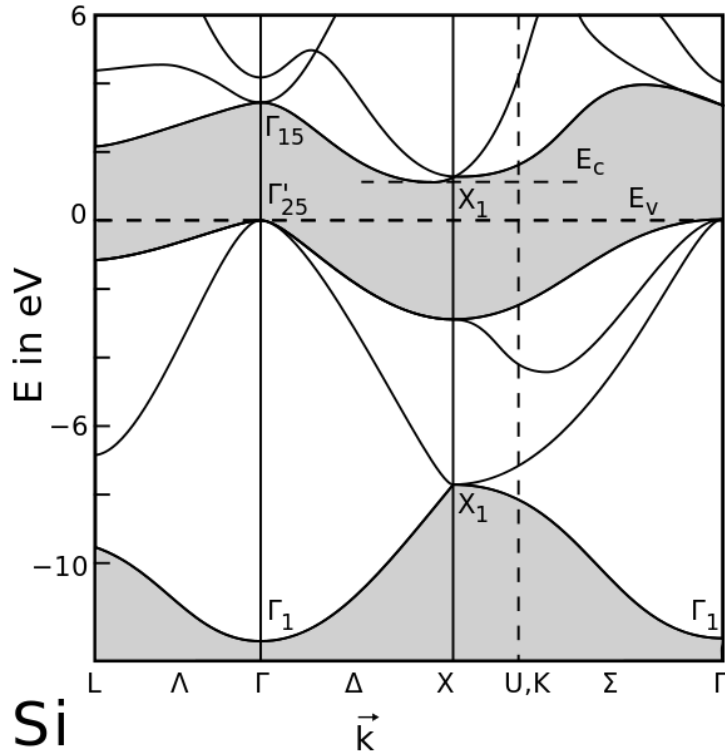


Figure 3.2: Reduced zone scheme of silicon. Silicon is an indirect semiconductor as the maximum of the valence band E_V and the minimum of the conduction band E_C are shifted in momentum (or \vec{k}) space. As a consequence, 3.6 eV are required – which is distinctively larger than the band gap of 1.12 eV – to lift an electron from the valence band into the conduction band (vertical transition). Additionally, a diagonal electron transition from the maximum of the valence band to the minimum of the conduction band is possible which requires a phonon for momentum conservation. The diagonal transition is less probable than the vertical transition. Modified from [CC74].

At low temperatures the valence band is fully occupied as the thermal energy is insufficient to lift electrons into the conduction band, so that it behaves like an insulator. As soon as the temperature is high enough, electrons get into the conduction band increasing the conductivity. Aside from these electrons (intrinsic charge carriers), the corresponding unoccupied electrons states (holes) in the valence band also contribute to the conductivity (hole conduction) as they can be occupied by electrons leading to a hole movement. Thus, semiconductors behave like conductors at sufficiently high temperatures. In addition to thermal excitation, electrons might also be lifted into the conduction band by photon absorption.

In the context of position sensitive semiconductor particle detectors, germanium seems to be a good choice as it has a small band gap ($E_G = 0.67$ eV) which is related to a good energy resolution. However, such a small band gap leads to a high number of intrinsic charge carriers which is unfavorable since this causes higher electrical noise. To counter this effect it would be necessary to cool the device to very low temperatures, for instance by liquid nitrogen, which again is unfavorable as particle detectors demand a low material budget. Silicon instead, with a band gap of 1.12 eV does not need a liquid nitrogen cooling. Therefore, and due to the good availability and costs, silicon is the favored material for position sensitive particle detectors.

3.1.2 INDIRECT SEMICONDUCTORS

As described above, the width of the material dependent band gap is an important property of a solid. However, the band gap itself is not the only determining property as in indirect semiconductors like silicon and germanium more energy than the band gap is necessary to lift an electron into the conduction band. The reason for this behavior is illustrated in figure 3.2. The silicon band structure is plotted as a function of the reciprocal momentum (or \vec{k}) vector. The band gap is indicated between the dashed lines for the maximum energy E_V of the valence band and the minimum energy E_C of the conduction band. It is clearly visible that the minimum and the maximum are not at the same position in momentum space. As a consequence 3.6 eV [P⁺16] are required – which is distinctively larger than the band gap of 1.12 eV – to excite an electron from the valence band into the conduction band (vertical transition). In addition, a diagonal transition between the two extrema is possible requiring a phonon for momentum conservation. The energy necessary for the diagonal transition is in the order of the band gap (plus respectively minus some meV due to the phonon). However the diagonal transition is significantly less probable than the vertical one [GM12].

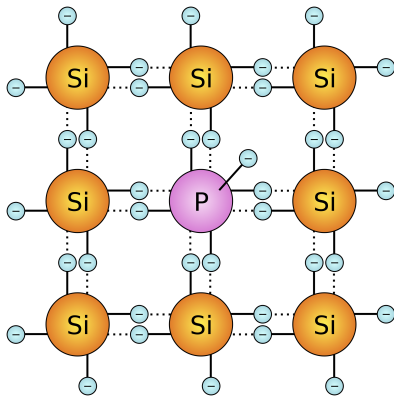
3.1.3 DOPING

Intrinsic semiconductors are not suitable for semiconductor detectors as they have too many free charge carriers. However, the properties of semiconductors can be manipulated to obtain the desired properties. The first step is the intentional implanting of impurities (dopants) into the semiconductor lattice called doping. After the doping the electrical properties are basically dominated by the impurities, hence these semiconductors are denoted as extrinsic semiconductors. Depending on the dopant semiconductors are divided into p- and n-type.

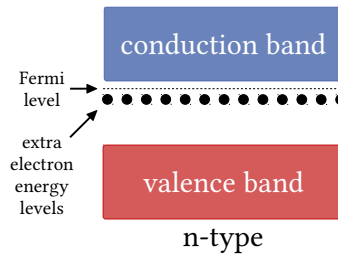
Figure 3.3 shows a doped silicon lattice and its impact on the energy levels. Silicon is an element of group IV of the periodic table carrying four valence electrons. In a silicon lattice all of these electrons enter a covalent bond with an electron of a neighboring atom. If an atom of the silicon lattice is replaced by an element of group V (e.g. by phosphorus) only four out of five valence electrons enter covalent bonds while the remaining one stays quasi-free. In this case the charge carrier is negatively charged, hence those semiconductors are called n-type. In the energy band model the dopants cause additional occupied energy states (donors) slightly below the conduction band. Electrons in such energy states can easily be excited to the conduction band which increases the conductivity. As the highest occupied energy state is now closer to the conduction band, the Fermi level is also shifted to higher values. When a silicon atom of the lattice is replaced by an element of group III (e.g. by aluminum or boron¹) no longer four valence electrons are available to enter covalent bonds. One electron state remains unoccupied and thus creates a hole. Other electrons can, in turn, easily enter this state and since holes are the charge carriers those semiconductors are called p-type. In the representation of the energy band model additional unoccupied energy states (acceptors) are generated slightly above the valence band. Accordingly, the Fermi energy is shifted closer to the valence band (see e.g. [Sch05]).

The production of doped semiconductors is either done by adding impurities during the growth of the semiconductor crystal which leads to a homogeneous doping or by processing the finished semiconductor crystal via ion implantation or diffusion. The choice of the production technique is connected to the dopant as properties like implantation depth are element dependent [Hil14]. The doping concentration is usually between one dopant per 100 million atoms (low or light) and one or even more per ten thousand atoms (heavy or high).

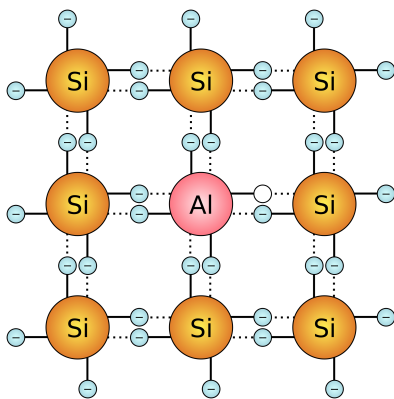
¹ For silicon the p-type dopant of choice is boron.



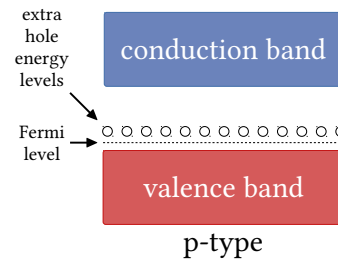
(a) n-type silicon doped with phosphorus. The additional electron is a quasi-free electron not entering a covalent bond and increasing the conductivity as it can easily travel through the lattice [Com17b].



(b) Energy band model of n-type semiconductors. The additional electrons of the dopants create energy states slightly below the conduction band. Electrons in this state can easily enter the conduction band, which increases the conductivity.



(c) p-type silicon doped with aluminum. Aluminum only has three valence electrons, the remaining hole can easily be occupied by other electrons generating a hole current [Com17a].



(d) Energy band model of p-type semiconductors. The electron holes in the silicon lattice create energy states slightly above the valence band. Electrons can easily enter these states, which enables hole conduction.

Figure 3.3: Schematics introducing doping of n- and p-type silicon lattices and the corresponding energy band levels including the shifted Fermi level.

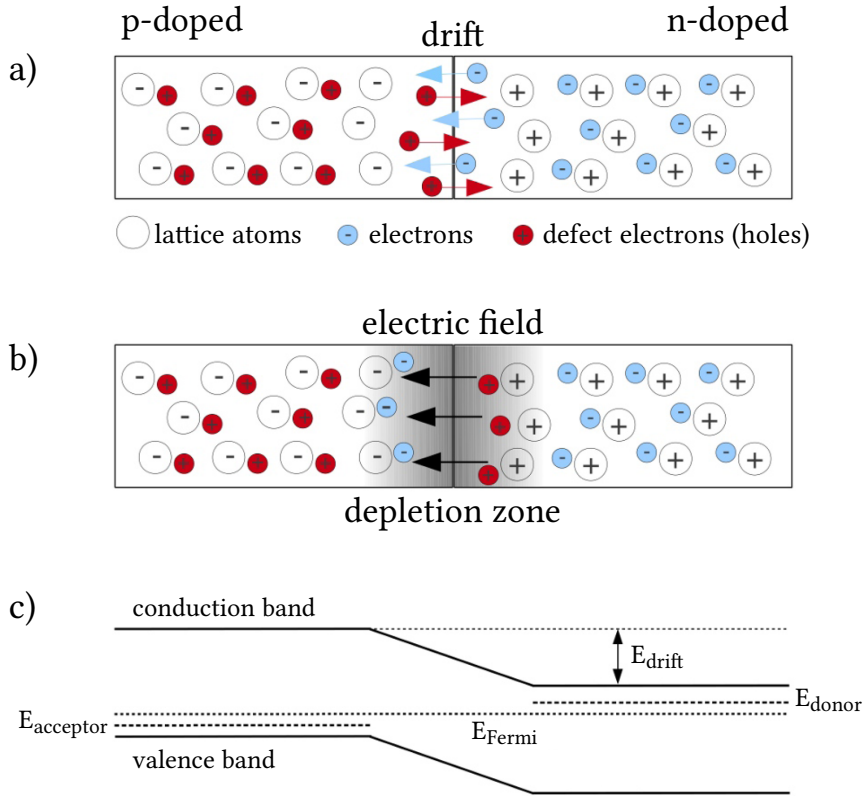


Figure 3.4: p-n junction and development of the depletion zone. a) shows a p-n junction before an equilibrium is established. Quasi-free electrons from the n-doped region diffuse into the p-doped region while holes can be considered as positive charge carriers diffusing from the p-side to the n-side. In b) an equilibrium is established forming the depletion zone (space charge region). Electrons and holes recombine near the contact surface with the result that no free charge carriers are left within this region. Due to the charge carrier diffusion positive space charge remains on the n-side where electrons are missing and vice versa. c) illustrates the energy band adjustment after an equilibrium is established. The Fermi level E_{Fermi} of the two regions equalized due to the charge carrier diffusion and the valence and conduction bands are shifted by the electric field E_{drift} . Modified from [Hos12].

3.1.4 P-N JUNCTION

As implied in the beginning of section 3.1.3, intrinsic semiconductors are not appropriate for semiconductor detectors. An intrinsic semiconductor like silicon, with a size of a position sensitive sensor as used in CMS, has about 10^9 free charge carriers. This number is too high with respect to approximately 22,000 electron-holes pairs generated by a charged particle traversing such a sensor. Therefore, it would not be possible to identify this comparable small signal within the huge number of free charge carriers [Har08]. To solve this problem the number of free charge carriers has to be reduced. This can be achieved by a p-n junction and while the doping was the first step to prepare the semiconductor properties the connection of two oppositely doped semiconductors forming a p-n junction is the second one. In fact, a p-n junction is not realized by joining p- and n-type silicon but instead it is produced by different doping of a single crystal. Nevertheless – for the sake of convenience – the following explanation of the p-n junction uses the picture of two doped semiconductors.

Extrinsic (doped) semiconductors, as introduced above, have zero net charge. There are always equal numbers of free charge carriers and fixed charges of the ionized dopants. Even though the overall charge of a p-n junction is still zero there is a local gradient of free charge carriers. When two oppositely doped (p- and n-type) semiconductors get in contact free electrons of the n-doped region diffuse into the p-doped region as illustrated in figure 3.4 a). In addition, there is an opposite diffusion of holes as they can be considered as positive charge carriers. Electrons and holes near the contact surface recombine and due to the lack of free charge carriers and the fixed ionized dopants, a net charge is formed in this region. As a consequence, an electric field is established which counteracts the charge carrier diffusion and prevents further diffusion at a certain point as shown in figure 3.4 b). The voltage related to the electric field is called built-in voltage and has usually values between 0.6V and 0.7V for silicon. The region without free charge carriers is the space charge region (or depletion zone due to the lack of free charge carriers) and its expansion depends on the doping concentrations and the intrinsic charge carrier density. The Fermi levels of the single p- and n-type materials are different, but after joining the Fermi levels adjust due to the charge carrier diffusion which is indicated in figure 3.4 c). Within the space charge region the valence and conduction bands are bent.

The space charge region is well suited to detect charged particles. First of all, there are no free charge carriers disturbing the generated electron-hole pairs. Second, the electron-hole pairs are separated by the electric field and only need to be collected. The volume outside the space charge region is not depleted and hence still not suited. However, it is possible to remove the free charge carriers from the entire volume which is the third step to turn semiconductors into excellent particle detectors.

3.1.5 DEPLETION VOLTAGE

To remove the remaining free charge carriers an external voltage (called bias voltage) with the correct polarity has to be applied. If the negative potential is applied to the n-type and the positive to the p-type material it is called forward biasing. In this case, the externally applied voltage pushes electrons and holes towards the p-n junction reducing the space charge region and hence neutralizing the electric field. Once the electric field is neutralized, a current flows through the entire semiconductor. Forward biasing does not remove the free charge carriers. If the positive potential is applied to the n-type material and vice versa, the p-n junction is operated in reverse bias mode. The positive potential collects the electrons of the n-side, while the holes in the p-side drift towards the negative potential. As a consequence, the space charge region increases as well as the electric field.

The voltage required to remove all free charge carriers (in reverse bias mode) is called depletion voltage U_{dep} . This voltage depends on the doping concentrations of the p- and n-type material as well as on the thickness² of the semiconductor. The equation below giving the depletion voltage is valid for semiconductors where one doping concentration is significantly higher than the other one, so the depletion depth of the highly doped region can be neglected [Sze85]. This is the case in semiconductor particle detectors.

$$U_{\text{dep}} = \frac{e}{2\epsilon\epsilon_0} |N_{\text{eff}}| d^2 \quad (3.2)$$

$|N_{\text{eff}}|$ is the effective doping concentration of the weaker doped region and d is the thickness of the semiconductor. The built-in voltage is neglected in this case as it is small compared to the applied reverse bias voltage. Usually, silicon sensors used in particle detectors are operated over-depleted which means that the applied voltage is typically about twice the value of the

² the size of the semiconductor perpendicular to the p-n junction

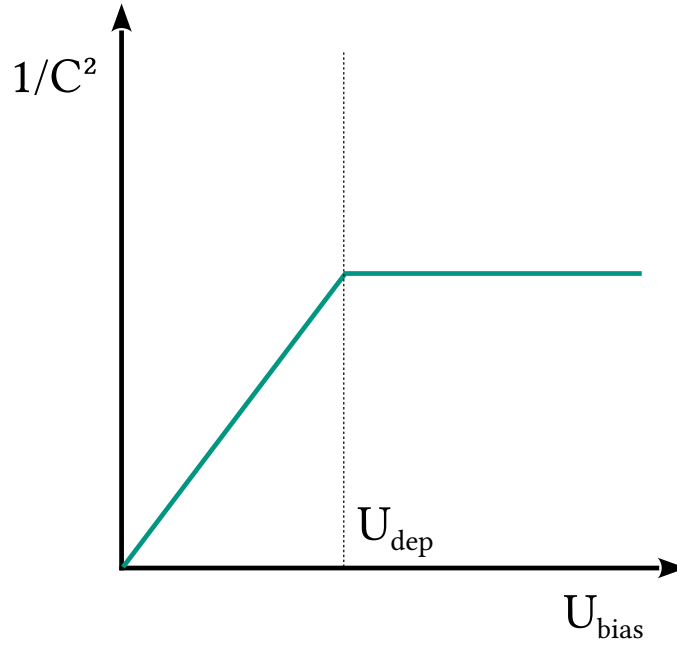


Figure 3.5: Ideal capacitance-voltage characteristic. The depletion voltage U_{dep} is determined by the kink of the curve. At this voltage the space charge region is expanded over the entire thickness of the device. Hence, a further capacitance decrease is not possible.

depletion voltage U_{dep} . On the one hand, this assures that the entire volume is depleted mitigating differences between sensors. On the other hand, the additional electric field helps to remove electrons-hole pairs generated via thermal excitation. They are separated by the electric field and drift to the electrodes of the connected bias voltage and form the leakage current.

Instead of calculating the depletion voltage, it is also possible to determine it experimentally. Since the space charge region of a p-n junction behaves like a parallel plate capacitor, its capacitance can be calculated from the width of the space charge region. Once a sensor is fully depleted, the capacitance is no longer decreasing. By measuring the capacitance for different bias voltages and plotting $1/C^2$ as a function of the bias voltage U_{bias} , the depletion voltage is determined by the kink visible in figure 3.5.

In addition, the leakage current of a semiconductor particle detector is of interest. The leakage current is formed by electrons which are thermally excited into the valence band. Hence, the leakage current increases for higher temperatures, as more electrons are excited. The leakage current is proportional to the temperature according to the equation below [Chi13].

$$I(T) \propto T^2 \exp\left(-\frac{1.21 \text{ eV}}{2k_B T}\right) \quad (3.3)$$

Where T is the absolute temperature (given in K) and k_B the Boltzmann constant. The relation between two leakage currents obtained at different temperatures is described by the following equation.

$$I(T_2) = I(T_1) \times \left(\frac{T_2}{T_1}\right)^2 \exp\left(-\frac{1.21 \text{ eV}}{2k_B} \left[\frac{1}{T_2} - \frac{1}{T_1}\right]\right) \quad (3.4)$$

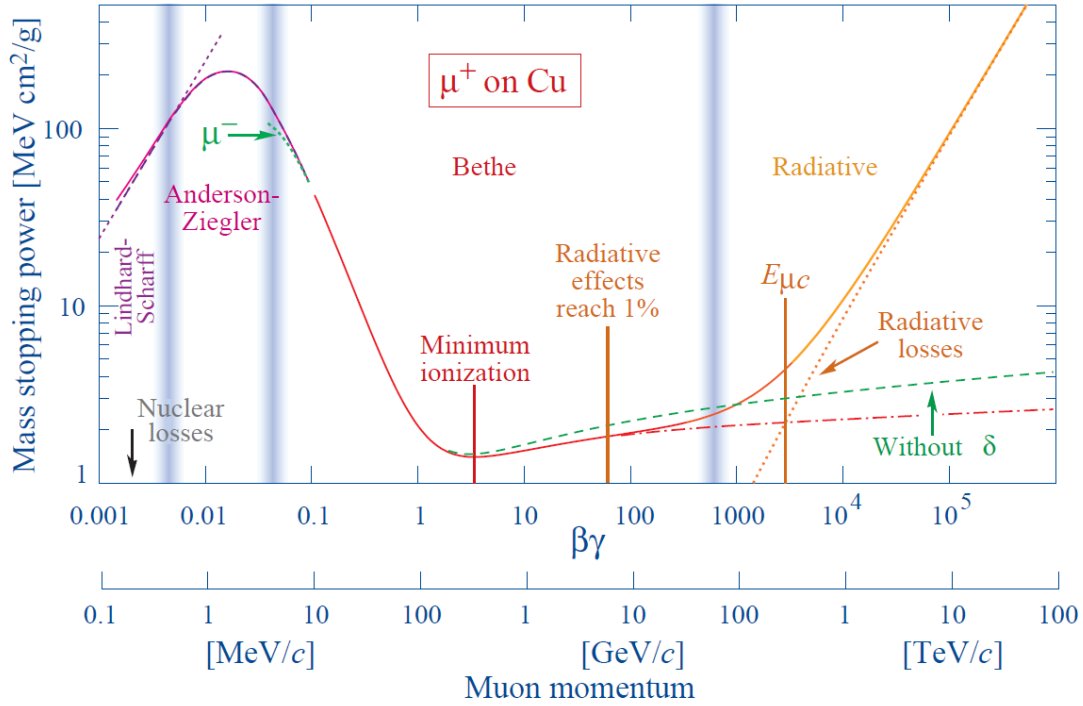


Figure 3.6: Stopping power (dE/dx) for positive muons in copper as a function of $\beta\gamma$. For $\beta\gamma \approx 2$ to 3 the stopping power has a minimum and the corresponding particles are called minimum ionizing particles. The valid range of the Bethe equation is marked by the vertical light blue bands at $\beta\gamma \approx 0.07$ and $\beta\gamma \approx 900$ [P⁺16].

3.2 INTERACTION OF PARTICLES WITH MATTER

Position sensitive silicon particle detectors as used by CMS exploit the interaction of particles with matter. In case of tracking detectors only particles interacting electromagnetically can be measured, which excludes neutral particles like neutrons. The particles interacting with a silicon sensor generate electron-hole pairs which in turn can be detected by readout electronics.

The interaction mechanisms of particles interacting with matter depend on the particle type and its energy. When charged particles traverse material they ionize or excite atoms. Photons instead interact via three mechanisms depending on the photon energy. The pixel detector of CMS for instance, measures the trajectories of charged particles while characteristic photons were used during its production for calibration purposes. Within the next subsections the different interaction mechanisms are described.

3.2.1 CHARGED PARTICLES

The energy loss of swift heavy particles³ traversing matter and scattering with shell electrons, depends on the particle energy, its charge as well as of the matter itself. The energy loss of these particles over a wide momentum range is described by the Bethe equation [Bet30].

$$-\frac{dE}{dx} = Kz^2 \frac{Z}{A} \frac{1}{\beta^2} \left[\frac{1}{2} \ln \left(\frac{2m_e c^2 \beta^2 \gamma^2 T_{\max}}{I^2} \right) - \beta^2 - \frac{\delta(\beta\gamma)}{2} \right] \quad (3.5)$$

³ Heavy particles are protons, ions or alpha particles compared to electrons.

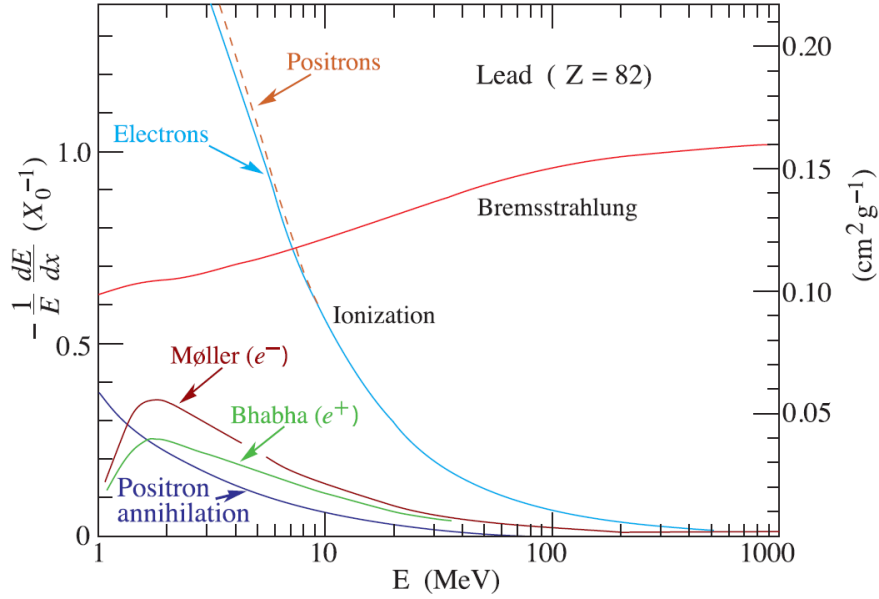


Figure 3.7: Energy loss of light particles (electrons or positrons) per radiation length in lead as a function of their energy. Bremsstrahlung is the dominant effect at energies above 10 MeV. At lower energies, ionization is the main mechanism with smaller contributions due to annihilation and scattering processes [P⁺16].

The constant $K = 4\pi N_A r_e^2 m_e c^2$ contains the Avogadro number N_A , the electron radius r_e and mass m_e as well as the speed of light c . Additional parameters are the charge z of the incident particle, the atomic number Z and the atomic mass number A of the interacting matter. $\beta = v/c$ and $\gamma = 1/\sqrt{1-\beta^2}$ are relativistic factors, T_{\max} is the maximum energy transferred to an electron in a single scattering, I is the mean excitation energy given in eV and δ is a density effect correction.

Figure 3.6 shows the Bethe equation as a function of the particle momentum for positive muons in copper. The valid range of the Bethe equation is in the center of the plot, indicated by the light blue bands at $\beta\gamma \approx 0.07$ and $\beta\gamma \approx 900$. The lower momentum range is dominated by various other effects while radiative losses are crucial at higher momenta. The stopping power shows a minimum at $\beta\gamma \approx 2$ to 3 and since the energy deposition of particles in this range is minimal they are called **Minimum Ionizing Particles (MIPs)**.

Charged particles like electrons and positrons are not described by the Bethe equation as they are significantly lighter and due to their indistinguishability with the shell electrons they scatter with. At lower energies they undergo scattering and ionization processes while they lose energy via bremsstrahlung at higher energies as illustrated in figure 3.7. In silicon, the energy of electron MIPs is about 1.5 MeV.

3.2.2 THIN LAYERS

The energy loss of charged particles in thin silicon layers is characterized by statistical fluctuations of the ionization process which is approximately described by an asymmetric Landau distribution. This distribution has a tail towards higher energies caused by secondary (knock-on or δ -) electrons [Lan44]. These electrons can be emitted from atoms when a charged particle is crossing, additionally producing electron-hole pairs while traveling in the silicon layer (secondary ionization). Figure 3.8 shows Landau distributions of 500 MeV pions in silicon layers of different thicknesses. The maximum of the distribution is usually denoted as **Most Probable**

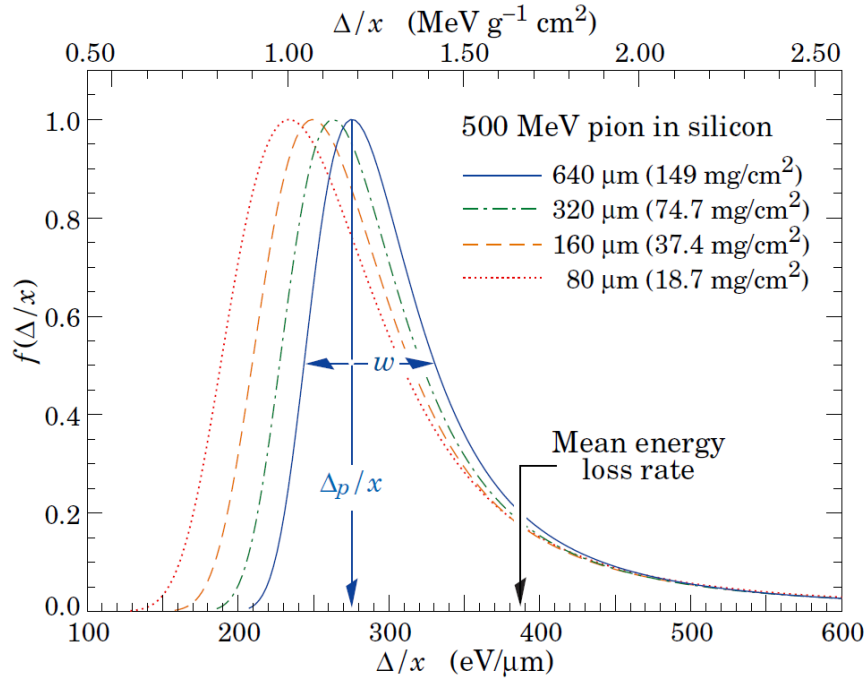


Figure 3.8: Normalized energy loss distribution of 500 MeV pions in silicon of different thicknesses. Statistical fluctuations of the ionization process lead to an asymmetric Landau distribution. The peak of the distribution (most probable value) which is also dependent on the silicon thickness is at approximately two-thirds of the mean energy loss [P⁺16].

Value (MPV) which is at about two-thirds of the mean energy loss. Combining the information that the MIP average energy loss is about 390 eV/μm and that 3.6 eV are required to generate an electron-hole pair in silicon (from section 3.1.2) reveals that on average 108 electron-hole pairs are generated per μm. Hence, the value corresponding to the MPV is roughly 73 electron-hole pairs per μm.

3.2.3 PHOTONS

Photons interact mostly via three different mechanisms depending on the photon energy and the atomic number Z of the interacting matter. The three mechanisms are the inner photoelectric effect, Compton scattering and pair production. And all three rely on photons transferring energy to charged particles. Figure 3.9 shows the cross sections for each interaction mechanism as well as the total cross section as a function of the photon energy over several orders of magnitude.

INNER PHOTOELECTRIC EFFECT

The inner photoelectric describes the absorption of a photon by a shell electron which is excited to the conduction band. The inner photoelectric effect is dominant up to photon energies of 50 keV. This effect is exploited in the calibration of silicon particle detectors which is relevant in the further course of this thesis.

COMPTON SCATTERING

Compton scattering is the main interaction mechanism for photon energies between 50 keV and 10 MeV. An incident photon scatters non elastically at an outer shell electron losing some energy and thus changing its wavelength. The amount of energy transferred to the shell electron depends on the scattering angle θ and is maximal for 180° . The Compton equation

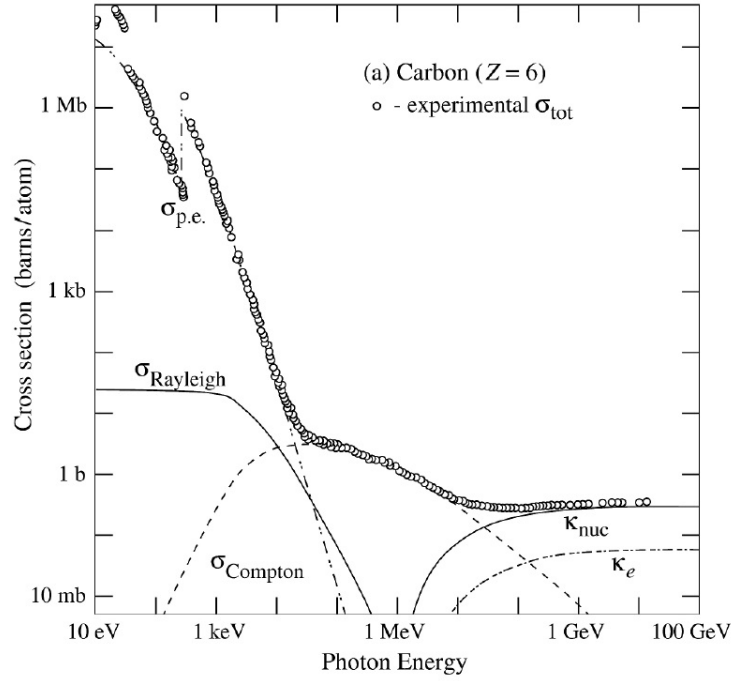


Figure 3.9: Cross sections of photon interactions with carbon as a function of the photon energy. The inner photoelectric effect is dominant for energies up to 50 keV. Compton scattering is the major interaction mechanism for energies between 50 keV and 10 MeV while pair production is dominant at energies above 10 MeV [P⁺16].

below gives the photon energy E'_γ after scattering as a function of the initial photon energy E_γ and the scattering angle θ .

$$E'_\gamma(\theta) = E_\gamma \left(1 + \frac{E_\gamma}{m_e c^2} [1 - \cos \theta] \right)^{-1} \quad (3.6)$$

The constants are the electron rest mass m_e and the speed of light c .

PAIR PRODUCTION

For energies above 10 MeV pair production becomes the dominant effect. The interaction mechanism describes a photon decaying into an electron-positron pair which is only possible in the presence of a nucleus obtaining some recoil to satisfy momentum conservation. Obviously, the photon energy has to be at least twice the value of the electron rest mass $E = 2 \cdot m_e = 1.022 \text{ MeV}$.

3.3 RADIATION DAMAGE IN SILICON

The biggest challenge during the operation of silicon particle detectors is the radiation damage they suffer from. These defects which impair the detector performance can be divided into surface damage and bulk damage. Surface damage is mostly generated by ionizing radiation such as photons or charged particles while bulk damage is dominantly created by hadrons. As surface damage is of lower relevance in the context of this thesis, it is not considered further. Information can be found e.g. in [Sze85].

Bulk defects are created when a traversing particle interacts with the silicon lattice and knocks off a silicon atom. The first atom hit is the **Primary Knock-on Atom (PKA)** which

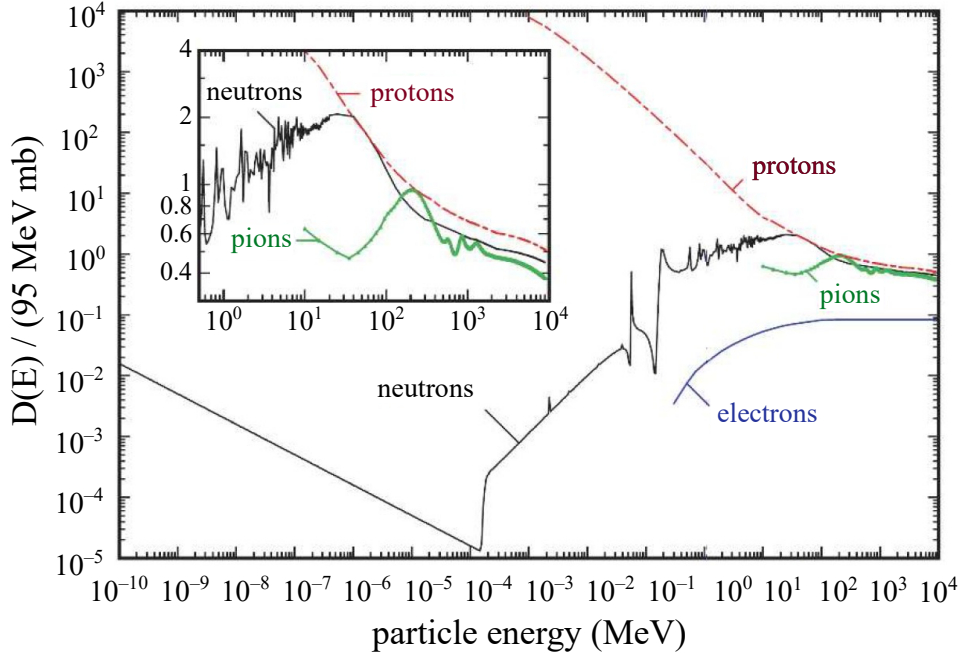


Figure 3.10: Displacement damage functions for neutrons, protons, electrons and pions in silicon normalized to 95 MeV mb (for 1 MeV neutrons) as a function of the particle energy. The functions give the damage corresponding to 1 MeV neutrons. Modified from [Lin03].

can move through the lattice as an interstitial defect leaving behind a vacancy. To knock out a silicon atom at least 25 eV are required. If this knocked out atom carries sufficient energy, it can create additional defects along its path through the lattice or lose energy via ionization. Since non-ionizing interactions dominate at low energies, clusters of displaced atoms are formed at the end of the PKA path. Charged hadrons interact mainly via Coulomb scattering generating cluster and point defects. Neutrons instead most likely create cluster defects as they can only hard scatter transferring nearly its entire energy to the PKA.

The process when a particle loses energy due to displacement of lattice atoms is called non-ionizing energy loss. According to the NIEL scaling hypothesis, the created damage scales linearly with the energy loss caused by displacement [SBD⁺87]. Depending on the recoil energy E_R , the PKA generates additional damage in the silicon lattice. The size of the damage is independent of the primary particle type and interaction process. The Lindhard partition function $P(E_R)$ calculates the energy loss due to displacement and can be used to determine the non-ionizing energy loss in silicon for different particle types. The cross section for displacement damage is given by the following equation [VG89]:

$$D(E) = \sum_{\nu} \sigma_{\nu}(E) \int_{E_D}^{E_R^{\max}} f_{\nu}(E, E_R) P(E_R) dE_R \quad (3.7)$$

with the energies E of the particle, E_R of the recoiling nucleus and E_D as the lower limit required for displacement. The sum accounts for all possible interactions. The cross section σ_{ν} describes the particle reaction ν and $f_{\nu}(E, E_R)$ is the probability to create a PKA caused by the reaction ν .

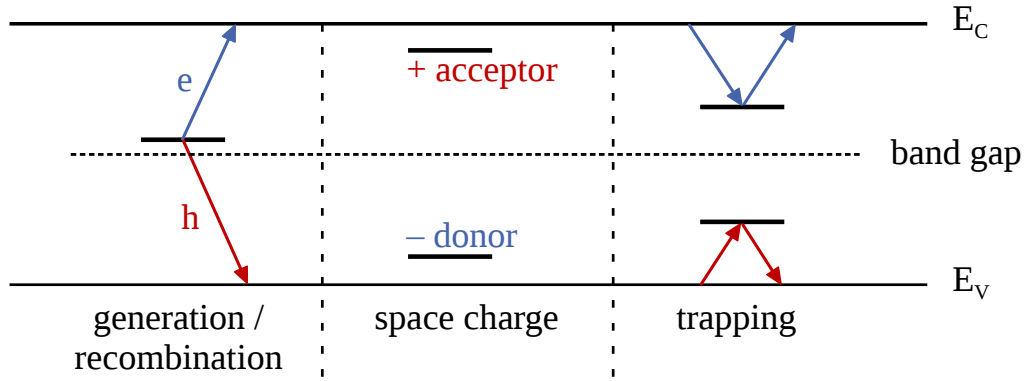


Figure 3.11: Energy band model of defects. Defect energy levels in the center of the band gap increase the leakage current as charge carriers can easily recombine or be generated (left). Charged donor and acceptor states create space charge which has an impact on the doping concentration (middle). Certain defects can trap charge carriers for some time so they do not contribute to the signal read out from readout electronics (right). Modified from [Ebe13].

To allow the comparison of damage caused by different particles at different energies the damage caused by 1 MeV neutrons is taken as reference. Accordingly, the damage is scaled to this value by applying the scaling factor, called hardness factor κ , which is described by

$$\kappa = \frac{\int D(E)F(E) dE}{D(E_n = 1 \text{ MeV}) \int F(E) dE} \quad (3.8)$$

with $D(E_n = 1 \text{ MeV}) = 95 \text{ MeV mb}$. For a given fluence $F(E)$ the damage caused by a certain particle type can now be compared to the damage done by 1 MeV neutrons of equal fluence. The corresponding fluence scaled to 1 MeV neutrons is denoted as 1 MeV neutron equivalent fluence F_{eq} .

$$F_{eq} = \kappa \times F = \kappa \times \int F(E) dE \quad (3.9)$$

For the sake of convenience, values corresponding to 1 MeV neutron equivalent fluences (per square cm) are denoted as n_{eq} within this thesis. Figure 3.10 shows the damage caused by different particles as a function of the particle energy. For high energies, all particles tend to create comparable damage. At low energies the damage caused by protons is much higher than for neutrons.

Defects in the silicon lattice can further interact with each other forming different defect types. For instance, vacancies can react with other vacancies or with impurities [Huh02]. These defect types create additional energy levels within the band gap. The resulting consequences can be divided into three groups mostly depending on the energy level introduced by the defect as illustrated in figure 3.11. The effects are either an increased leakage current, additional space charge manipulating the effective doping concentration or defects acting as temporary charge traps. Energy levels close to the band gap center primarily generate current. States close to the conduction or valence band acting as donor or acceptor create space charge as they can be ionized easily. Energy levels between an energy band and the band gap center generate space charge, lead to an increased leakage current and in addition, they are able to trap charge carriers for some time. Temporarily trapped electrons or holes do not contribute to the signal, although they are released after a certain time depending on the individual cross sections.

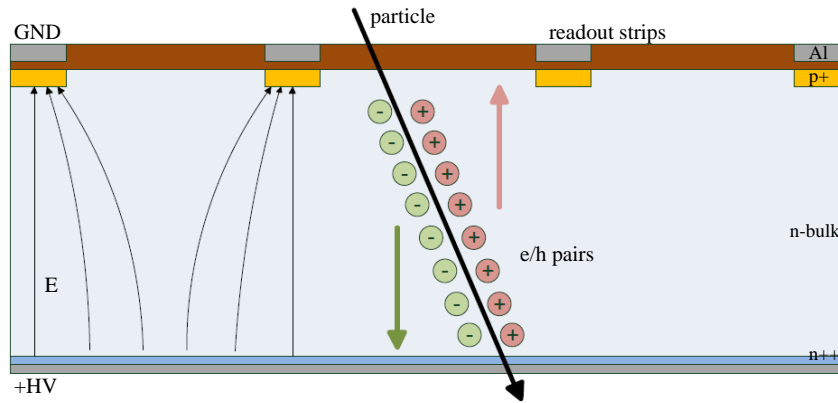


Figure 3.12: Working principle of a position sensitive silicon detector. The p-n junctions are formed by the p-type strip implants (yellow) and the large n-type bulk (light gray). The free charge carriers of the entire volume are removed by the reverse bias voltage. A particle traversing the silicon sensor creates electron-hole pairs along its path by ionizing silicon atoms. These pairs are separated due to the electric field and read out at the electrodes [Ebe13].

In fact, defects are typically point-like or cluster defects. The latter are complex conglomerates of several defects which are characterized by more than one of the effects introduced before. For more detailed information on defect formation in silicon see e.g. [Jun11].

As illustrated, radiation damage affects silicon particle detectors strongly. Hence, it is mandatory to investigate the change of the detector performance for increasing radiation damage. Therefore, small test devices of the particle detector are irradiated up to the expected life time fluence. Accelerating the accumulation of radiation damage is done by using protons of a particle accelerator or neutrons from a research reactor. In this way the target dose is reached within minutes or hours.

The defects created in the silicon lattice can move depending on the temperature of the device. As a result of their movement and recombination processes these defects can either recover the detector performance partially or form new defects impairing the performance further. This effect is called annealing. As a consequence, irradiated samples have to be stored at temperatures of -20°C or less to freeze out the annealing effects and to be able to characterize the annealing behavior under controlled conditions. For more information about annealing see e.g. [Mol99].

3.4 WORKING PRINCIPLE OF SEMICONDUCTOR DETECTORS

The working principle of a position sensitive silicon detector as illustrated in figure 3.12 is based on multiple parallel p-n junctions forming the segmentation of the sensor. The segmentation configuration can either be one dimensional forming strip sensors or two dimensional providing pixel sensors. Segmenting the sensor brings the benefit of obtaining position information corresponding to the strips or pixels which detected a signal. In the figure the p-type implants form the strips by establishing p-n junctions with the n-type bulk.

The illustrated strip sensor is operated in reverse bias mode as the positive potential is connected to the n-type backside and the negative potential (ground in this case) to the p-type implant. The applied bias voltage is larger than the depletion voltage required to remove all free charge carriers (electron-hole pairs generated due to thermal excitation) within the entire sensor volume.

The depletion voltage is not constant during the detector operation inside CMS as defects (caused by radiation damage) induce energy levels within the band gap changing the effective doping concentration (see equation 3.2). As a result, the depletion voltage will increase which is why the applied bias voltage has to be increased to keep the sensor fully depleted.

The electron-hole pairs created by a charged particle traversing the sensor are separated by the electric field established by the bias voltage. The electrons drift to the positive potential applied to the backside and the holes to the implants where they can be collected by readout electronics. The connection to the readout electronics is either AC-coupled (denoted as capacitive coupling) like the strip implants in figure 3.12 or DC-coupled as it is the case in the CMS pixel detector. The benefit of AC-coupling is that the leakage current is not entering the readout electronics which protects the electronics against too high currents. However, AC-coupling requires that each implant is individually connected to the bias voltage circuit by implementing additional bias lines and bias resistors. Therefore, DC-coupling has to be chosen if it is not possible to use AC-coupling due to size limitations as it is usually the case for pixel detectors.

For a capacitively coupled (AC) device the implant is separated from the readout by a thin layer of insulating silicon dioxide (depicted in brown in figure 3.12). The charge carriers drifting in the bulk induce a current in the readout strip which can be calculated by the Shockley-Ramo theorem [Sho38], [Ram39].

A key design parameter of position sensitive silicon detectors is the pitch. It is determined by the size of a strip or pixel in direction of the segmentation which is typically of the order of 100 μm . According to the Shockley-Ramo theorem, charge carriers generated by a traversing particle are usually spread over few strips or pixels. The magnetic field in which such a detector is placed leads to an additional charge carrier drift which is not parallel to the electric field. The angle corresponding to the drift is called Lorentz angle.

The charge sharing over several strips or pixels is to some extent desired. On the one hand, the signal collected per implant gets smaller but on the other hand, the resolution can be improved. For a detector relying simply on hit or not hit information the resolution σ is determined by

$$\sigma = \frac{\text{pitch}}{\sqrt{12}}. \quad (3.10)$$

If the resolution is calculated by the center-of-gravity method instead (requiring signal height information and charge sharing over at least two strips or pixels), the resolution follows the proportionality

$$\sigma \propto \frac{\text{pitch}}{\text{SNR}} \quad (3.11)$$

with SNR being the signal-to-noise ratio [Lut07]. In case of the CMS pixel detector, the hit resolution is improved due to the center-of-gravity method from approximately 30 μm in y- and 40 μm in x-direction to 10 μm in y- and 20 μm in x-direction [DA⁺12].

Part II

MODULE PRODUCTION FOR THE PHASE I UPGRADE OF
THE CMS PIXEL DETECTOR

If you're walking down the right path and you're willing to keep walking, eventually you'll make progress.

Barack Obama

4

THE CMS PIXEL DETECTOR FOR THE PHASE I UPGRADE

Progress in experimental particle physics strongly depends on the performance of the particle detectors. In case of the CMS pixel detector it is necessary to determine the trajectories of all charged particles as precisely as possible. Within this chapter, the CMS pixel detector will be introduced with special focus on the improvements coming with the Phase I upgrade.

During the past LHC run the CMS pixel detector proved that it is an indispensable part of the CMS experiment. Almost all physics analyses of the CMS collaboration rely on its excellent performance [Mei14]. The first CMS pixel detector was operated until 2016 and provided high resolution measurements of the first three space-points for charged particles emerging from the interaction point. Its outstanding performance is illustrated by a single hit efficiency of more than 99% for the innermost pixel layer [DA⁺12].

As the LHC instantaneous luminosity already exceeded the design value, it would not have been possible to sustain the excellent performance of the original pixel detector during the next years. Especially the short distance to the interaction point makes it the subdetector affected most by the increasing luminosity.

Table 4.1 shows the data loss (given in %) at the design and doubled design luminosity of the original and the upgraded pixel detector (hereafter denoted as Phase I pixel detector). The listed denominations are BPix for the **B**arrel **P**ixel and FPix for the **F**orward **P**ixel region (the endcaps). While the maximum data loss of the original pixel detector is 4% at the design luminosity, which is still acceptable, it would reach up to 16% at the doubled design luminosity in the innermost layer. This significant rise of data loss is caused by an increased dead time of the double column mechanism of the readout chip and due to the limited on-chip buffers [EBH⁺10]. The consequent decreasing tracking efficiency and the increasing misidentification rate would impair the physics analysis.

For that reason, the CMS collaboration refined the pixel detector concept and replaced the original detector in early 2017. The Phase I pixel detector is designed to handle higher particle and L1 trigger rates [Käs13]. Table 4.1 also shows the predicted data loss of the Phase I pixel detector. The innermost layer, which moved closer to the interaction point to improve secondary vertexing as it is used in b-tagging algorithms, has less data loss than the original detector despite the increasing luminosity. In terms of particle rates there is an expected increase from 120 MHz/cm² (original BPix layer 1 with radius $r = 4.4$ cm at design luminosity) to 580 MHz/cm² (Phase I BPix layer 1 with radius $r = 3.0$ cm at doubled design luminosity) [DA⁺12].

4.1 DETECTOR GEOMETRY

The CMS pixel detector is based on a design using a barrel region with endcaps on each side. The barrel region of the original pixel detector was equipped with three layers while the

Table 4.1: Comparison of the simulated data loss for the original CMS and the new Phase I pixel detector. The data loss of the original pixel detector at design luminosity is still sufficiently low even in the innermost layer. However, 16% data loss at twice the design luminosity is not tolerable. Instead, the Phase I detector has very little data loss even at twice the design luminosity [DA⁺12].

detector	radius (mm)	data loss in % for	
		$1 \times 10^{34} \text{ cm}^{-2}\text{s}^{-1}$	$2 \times 10^{34} \text{ cm}^{-2}\text{s}^{-1}$
original pixel detector			
BPix 1	44	4.0	16.0
BPix 2	73	1.5	5.8
BPix 3	102	0.7	3.0
FPix 1 and 2	-	0.7	3.0
Phase I pixel detector			
BPix 1	30	1.19	2.38
BPix 2	68	0.23	0.46
BPix 3	102	0.09	0.18
BPix 4	160	0.04	0.08
FPix 1 to 3	-	0.09	0.18

endcaps contained two disks each. The Phase I pixel detector is equipped with an additional layer in the barrel region and an additional disk in each endcap as illustrated in figure 4.1. Mounting the innermost barrel layer closer to the interaction point became possible as the original beam pipe was replaced by a smaller one already in 2013/2014. The outer radius of the new beam pipe is 22.5 mm compared to 30 mm of the old one.

The additional barrel layer in the formerly unoccupied space between pixel and strip tracker at a radius of 160 mm improves the tracking efficiency by reducing the extrapolation distance between the two subdetectors and by providing four instead of three 3D space points. Together with the additional disk in each endcap the CMS pixel detector provides a four space point coverage up to $|\eta| = 2.5$. Moving the innermost barrel layer closer to the interaction point is a requirement for advanced physics analysis as it improves the important reconstruction of secondary vertices. These secondary vertices originate from long-living particles like hadrons containing bottom quarks which travel distances in the order of few millimeters until they decay. Efficient b-tagging is a requirement for a variety of physics analysis [CMS13].

In the further course of this thesis only the BPix region of the Phase I pixel detector is relevant. Therefore the focus of the discussion lies mainly on the BPix detector. For further information concerning the FPix region see e.g. [DA⁺12].

4.1.1 MECHANICS AND COOLING SYSTEM

The skeleton of the Phase I barrel pixel detector is formed by its new cooling loops. These loops are made of stainless steel tubes which run parallel to the beam pipe, have an outer diameter of 2.0 mm and a wall thickness of only 0.1 mm. A prototype of the cooling loops is shown in figure 4.2 (a). The cooling loops together with the end-flanges, a sandwich-like structure made of Airex foam covered with carbon fiber, give structural stability to the barrel pixel detector. Carbon fiber facets are used to mount the detector modules with small screws. These facets have two grooves which are used to glue them onto the cooling tubes and to maximize the con-

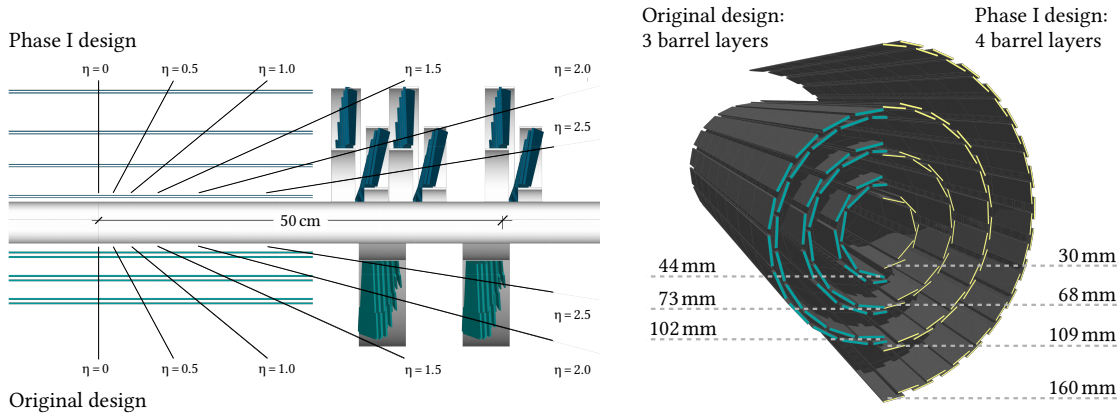


Figure 4.1: Comparison of the original and the Phase I pixel detector layout. The left picture shows a cross section of two quarters of the pixel detector along the beam pipe. The Phase I detector is presented in the top part and the original one in the bottom part. An additional layer/disk in each region of the Phase I detector provides a four space point coverage up to $|\eta| = 2.5$. The right picture compares the radii of the barrel layers. The innermost layer of the Phase I detector is moved closer to the interaction point to improve secondary vertexing and the additional fourth layer closes the gap to the adjacent strip detector. Modified from [DA⁺12].

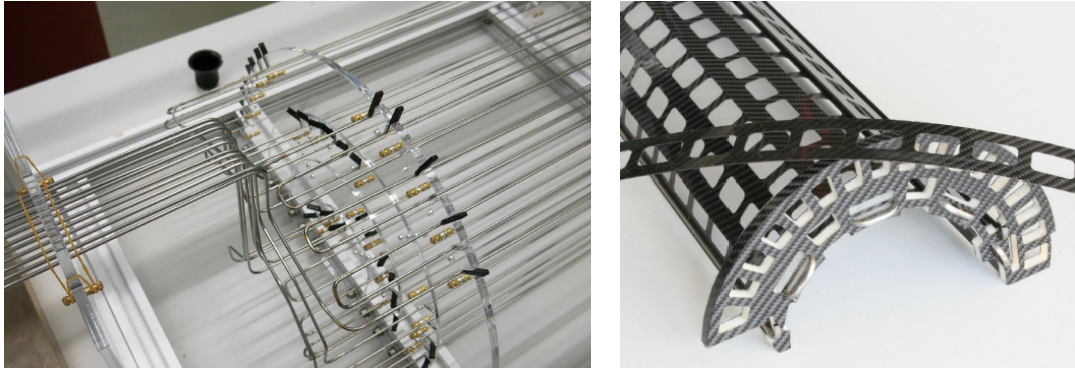
tact surface to improve the thermal conductivity. The facets have a thickness of only $200 \mu\text{m}$ and to reduce the mass as far as possible, material which is not needed to mount the modules is milled away as shown in figure 4.2 (b).

Cooling of a system like the CMS pixel detector is required for several reasons. First of all, the amount of heat which is produced by the electronic components in a more or less enclosed volume needs to be removed to protect the electronic components from overheating. Second, radiation damage leads to significantly higher leakage currents which cause an increased power consumption. In order to stay within the limitations of the power supplies, the silicon sensors have to be operated below room temperature to keep the leakage currents as low as possible (see equation 3.3). Additionally the sensors need to be cooled to avoid reverse annealing, which leads to decreasing signal heights deteriorating the detector performance. A further benefit of the cooling is related to the readout chips connected to the silicon sensors. They are calibrated electrically and since this calibration is temperature dependent (as for instance presented in [Hos12] or [Fre13]) they should be operated at stabilized temperatures.

The implementation of the new CO_2 -based two-phase cooling system is a major innovation compared to the original mono-phase fluorocarbon cooling system. The latter relies only on the heat capacity of C_6F_{14} while the new CO_2 system exploits the phase transition between liquid and gaseous. The energy required to evaporate one gram of CO_2 is 282J while the heat capacity of C_6F_{14} is only $1.1\text{J}/(\text{g} \cdot \text{K})$ [3M 17]. Due to this significant difference, the new cooling system gets along with less mass flow and smaller cooling tubes. Further advantages of CO_2 cooling are the high vapour pressure which keeps the vapour volume small as it is highly compressed. This, in turn, allows the vapour to flow more easily through small channels. In addition to these technical aspects, the new CO_2 has a much lower impact on the environment than C_6F_{14} (if released to the atmosphere) [Int14].

Although CO_2 cooling systems are already used successfully to cool silicon trackers (as it is the case for the LHCb [LHC17a] and AMS¹ [AMS17] experiments), CMS decided to install the new system, based on two identical cooling plants, beforehand to gain experience by applying

¹ Alpha Magnetic Spectrometer



(a) Cooling loops prototype. The cooling tubes are made of stainless steel, have a diameter of 2.0 mm and a wall thickness of 0.1 mm. The processing of the tubes relies on CNC bending and laser welding [Erd15b].

(b) Prototype of the carbon fiber support structure. The facets glued to the cooling tubes are used to mount the detector modules. The end-flange in the front is a sandwich-like structure made from Airex foam and carbon fiber. Additionally, a single carbon fiber facet lies on top [DA⁺12].

Figure 4.2: Prototypes of the cooling loops and the carbon fiber support structure.

dummy heat loads. Usually the two independent cooling plants are used to provide individual temperature setpoints for the BPix and FPix subdetectors. However, it is possible to cool both subdetectors with a single cooling plant if required due to a problem or maintenance. For more information on performance studies related to the cooling system see e.g. [Ren17].

4.1.2 MATERIAL BUDGET

From the point of view of physics analysis the ideal case would be a massless detector not influencing the measurements via multiple scattering. Obviously, this is not possible but the underlying demand especially affects the pixel detector since it is the innermost component of CMS. Hence, it is very important to minimize the material budget as multiple scattering in the pixel detector has an impact on measurements of all other subdetectors.

The implementation of the additional barrel layer four (and the third disk in the endcaps) is a challenging task in terms of material budget. Therefore, CMS has put special emphasis on this topic when the Phase I pixel detector was designed. In fact, CMS managed to reduce the total material amount in the sensitive tracking volume despite adding an additional barrel layer and a disk in each endcap. A big contribution to the material reduction is the new ultra-lightweight support structure described above. Further, the new CO₂ cooling system requires less mass flow and relies on smaller cooling tubes while the modified design of the modules for barrel layer 1 also come with less material.

Aside from the detector itself, the relocation of electronics boards providing the connection to the detector modules, was an important measure. New twisted-pair cables distributing power and data allowed to move these electronics boards out of the sensitive tracker volume.

Figure 4.3 shows the simulated material budget reduction in the sensitive tracker volume corresponding to $|\eta| < 2.5$. While the material budget remains basically unchanged in the barrel region $|\eta| < 1.2$ it is clearly reduced in the forward region where the endcaps are located ($1.2 < |\eta| < 2.5$). In addition, it is recognizable that the relocation of the services out of the sensitive tracker volume (indicated by the pale bands) caused an increased material budget at $|\eta| > 2.5$.

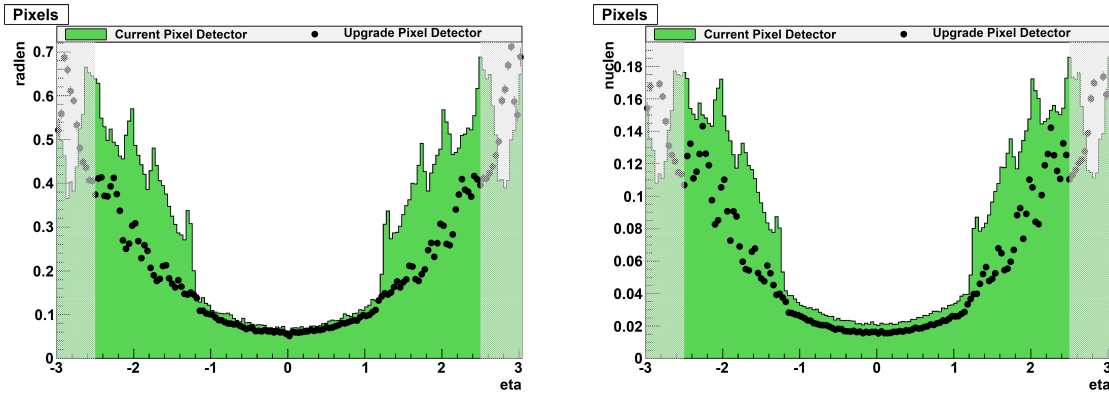


Figure 4.3: Simulated material budget of the original and Phase I pixel detector shown as a function of pseudo-rapidity $|\eta|$. The green histogram represents the original pixel detector and the black points the Phase I detector. The left plot gives the amount of material in units of radiation length (radlen) and the right plot in units of nuclear interaction length (nuclen). Both plots show that the material budget inside the sensitive tracker volume corresponding to $|\eta| < 2.5$ is reduced in the Phase I pixel detector. The relocation of electronics boards led to an increased material budget outside the sensitive tracker volume at $|\eta| > 2.5$ (pale bands) [DA⁺12].

4.2 THE CMS BARREL PIXEL DETECTOR MODULE

The implementation of the fourth barrel layer and the additional disk in each endcap led to a large increase of the sensitive area and the number of readout channels. The combined number of readout channels from the barrel region and the endcaps summed up to 66 million channels in case of the original pixel detector. The Phase I pixel detector instead provides nearly twice the number of channels, as it is equipped with 124 million pixels which is an increase by 88%.

The smallest subunit of the CMS pixel detector is the detector module which has a size of $66 \text{ mm} \times 22 \text{ mm}$ equipped with 66,650 pixels. An exploded view of a module showing all single components is presented in figure 4.4.

The core of a pixel detector module is formed by the silicon sensor where electron-hole pairs are generated when a charged particle traverses the sensor. 16 ReadOut Chips (ROCs) arranged in a 2×8 pattern are connected pixel by pixel to the sensor via small solder balls. The ROCs collect the electrons generated within the sensor and process the corresponding signal. Base strips made from silicon nitride are glued to the backside of the ROCs. They are used to mount the modules to the ultra-lightweight carbon fiber support structure. The High Density Interconnect (HDI), a flexible printed circuit board made from $50 \mu\text{m}$ thick Kapton[®] is glued to the backside of the silicon sensor². The HDI is required to distribute power, clock and trigger to the ROCs and to return the ROC data to the Token Bit Manager chip (TBM) which is glued on top of the HDI. Wire bonds, establishing the connections between HDI and ROCs, are located at the long module edges, parallel to the base strips. The TBM is wire bonded to the HDI as well and forms the control unit of the detector module. It communicates to the ROCs via the HDI, collects their data and sends it out via a twisted pair cable combining power and data. The corresponding cable connector is soldered onto the HDI.

The original detector was equipped with 768 modules in the barrel region and with 672 smaller modules (containing a maximum of 2×8 ROCs) in the endcaps. The new Phase I pixel detector is equipped with 1184 modules in the barrel region while the number of modules remains the same in the endcaps. However, the endcaps are now based on only one larger detector module type (instead of five smaller ones) which is almost identical to the barrel

² the sensor backside points upwards in figure 4.4

module design. The difference in size between the original and the Phase I barrel detector modules is rather small as they use the same sensor design. Only the ROCs are slightly larger due to additional on-chip buffers making the new modules a little bit wider.

4.2.1 THE SILICON SENSOR

The silicon sensor of the Phase I pixel detector has a size of $66.6 \text{ mm} \times 18.6 \text{ mm}$ with an active area of $64.8 \text{ mm} \times 16.2 \text{ mm}$. It is based on the same n^+ -in- n design which was already used in the original detector while its performance is still sufficient for the Phase I demands. The n -type silicon substrate is forming the bulk of the sensor and has a nominal thickness of $285 \mu\text{m}$. The highly doped n^+ -implants create the 2D-electrode segmentation on the front side. The backplane is formed by a homogeneously doped p^+ layer. Due to the choice of an n^+ -in- n design the collected charge carriers are electrons which bring the benefit of higher mobility compared to holes. This is desired as it leads to shorter collection times and a larger Lorentz drift which is of advantage regarding charge sharing.

An additional feature of the n^+ -in- n design is its behavior after radiation damage. Defects generated by radiation damage act rather like p -type energy levels instead of n -type. Hence, the effective doping concentration of the n -type bulk gets smaller with increasing radiation damage which leads to a decreasing depletion voltage according to equation 3.2. At some point the accumulating number of p -like defects will lead to a type inversion of the n -type bulk and it will behave like a p -type bulk [PCH⁺92]. Only after type inversion, the effective doping concentration starts to increase. As a consequence, the moment when the depletion voltage might be too high is delayed, as it also increases only after type inversion.

Further, the way the space charge region (depletion zone) is established changes also after type inversion. Before type inversion, the space charge region is established from the backside as the p - n junction is formed between the p -type backplane and the n -type bulk. In this state the pixel detector has to be operated fully depleted as the space charge region extends from the backside and only connects to the n^+ -implant collecting the electrons at full depletion. When operated underdepleted electrons created inside the space charge region would drift towards the n^+ -implant but would recombine inside the undepleted region between space charge region and n^+ -implant. After type inversion, the space charge region is established between the n^+ -implant and the p -type-like bulk. If it is then no longer possible to provide the full depletion voltage due to radiation damage, the pixel detector might be operated underdepleted as electrons generated inside the space charge region could still be collected by the n^+ -implants. Although the collected signals would be smaller, the pixel detector lifetime can be increased by operating underdepleted.

The isolation of the pixel cells is achieved by a uniformly applied p -spray layer. Thereby a p - n junction is formed between the p -spray and the n^+ -implant which has to be taken into account during the p -spray layer application to guarantee high breakdown voltages. The punch-through structures visible in figure 4.5 allow to apply a bias voltage to all pixel implants without providing a ground potential via a readout chip. This opens up the possibility to test the bare silicon sensor electrically. The typical quality criterion is checking if the measured current-voltage characteristic (from here on denoted as IV curve) follows a typical IV curve of a diode.

The pitch of the pixel implants is $100 \mu\text{m} \times 150 \mu\text{m}$ optimized for spatial resolution with respect to the magnetic field provided by the CMS solenoid. For the given thickness of the silicon sensors and with a Lorentz angle of about 25° the optimal pitch size to obtain mostly two pixel clusters in $r\phi$ -direction is $100 \mu\text{m}$ [Erd10]. The pitch of $150 \mu\text{m}$ in z -direction is determined by the constraints of the pixel cells (due to the size of the electrical components) of the readout chip. The silicon sensor is divided into 16 regions corresponding to the readout chips as visible in figure 4.4. Caused by the cutting, each ROC has an inactive region surrounding the pixel matrix. Accordingly, the required area to place the ROCs on the sensor is slightly larger than

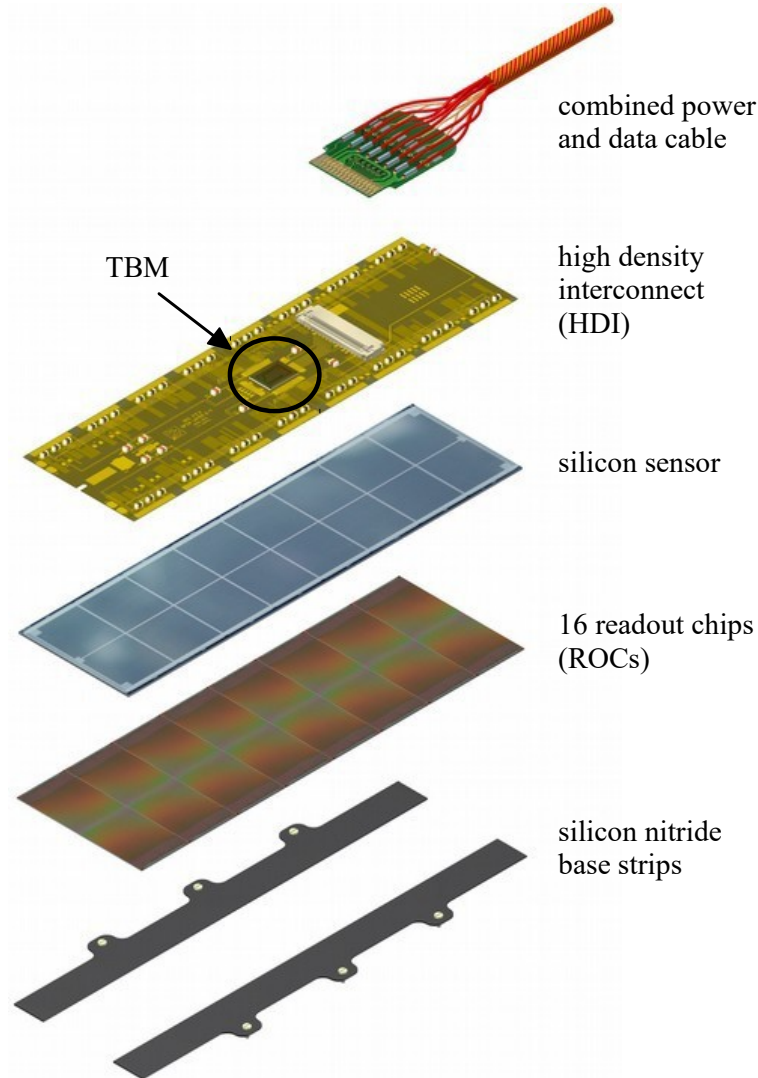


Figure 4.4: Exploded view of a Phase I pixel detector module as used in barrel layers 3 to 4. The core of the module is formed by the silicon sensor where electron-hole pairs are generated when charged particles traverse it. From below 16 (2×8) readout chips are connected to the sensor collecting and processing the charge signal. Base strips used to mount the module on the carbon fiber support structure are glued to the backside of the readout chips. A thin flexible printed circuit board (HDI) is glued on top of the sensor and wire bonds establish the connections to the readout chips. The token bit manager chip glued and wire bonded to the HDI controls all readout chips and sends the module data out via the combined power and data cable. Modified from [Erd15a].

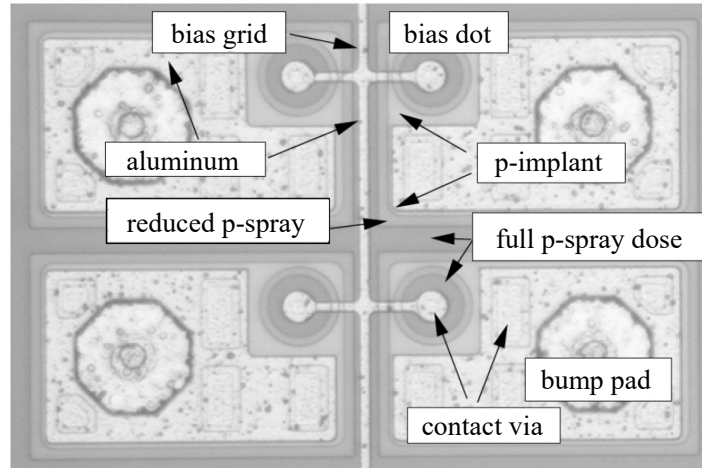


Figure 4.5: Picture of four pixel cells ($150\ \mu\text{m} \times 100\ \mu\text{m}$) from a CMS barrel pixel sensor. The displayed region is about $300\ \mu\text{m} \times 200\ \mu\text{m}$ in size. The visible features are the bump bond pads to connect the ROC, the bias grid and bias dot used for bare sensor testing and the n^+ -implants. Modified from [DA⁺12].

expected from the pixel size. Hence, the sensor pixels corresponding to three ROC edges have twice the size resulting in $100\ \mu\text{m} \times 300\ \mu\text{m}$ and $200\ \mu\text{m} \times 150\ \mu\text{m}$ pixels and $200\ \mu\text{m} \times 300\ \mu\text{m}$ sized pixels in the corners. Only the pixels at the ROC edge which is closest to the wire bond pads, have the standard pixel size of $100\ \mu\text{m} \times 150\ \mu\text{m}$.

4.2.2 THE READOUT CHIP

The readout chip of the CMS pixel detector measures, amplifies and discriminates the collected charge of each pixel of the sensor, stores the hit information and forwards the information to the TBM in case of a positive L1 trigger decision. The ROC is produced by IBM in $0.25\ \mu\text{m}$ CMOS process. It relies on storage cells which are protected against single event upsets to be suitable for the operation inside CMS [KBE⁺06]. The connection to the silicon sensor is established via bump-bonding where small solder balls with diameters of less than $30\ \mu\text{m}$ form a metal connection between the bump bond pads of the sensor and the ROCs.

The ROC version of the Phase I pixel detector is the PSI46digV2.1-respin replacing the PSI46V2 which was the version of the original pixel detector. A summary of the most relevant changes is given in table 4.2 at the end of this chapter.

The readout chip uses two independent power supplies, one for the analog and one for the digital domain. This approach minimizes the influence of the digital signal processing on the analog performance. 19 Digital-to-Analog Converters (DAC) allow to configure the ROC, while the communication relies on a custom designed Inter-Integrated Circuit interface.

The new ROC has a size of $7.9\ \text{mm} \times 10.2\ \text{mm}$ and is slightly larger than the original ROC due to an increased periphery. The ROC can be divided into three regions. The first one is the active area formed by a pixel matrix of 80 rows \times 52 columns resulting in 4160 pixels in total. The 52 columns are grouped in 26 double columns of 80×2 pixels each. Every pixel of the ROC is represented by a Pixel Unit Cell (PUC) which houses all electronic components required to process and buffer the collected signals. The pitch of these PUCs match the pixels

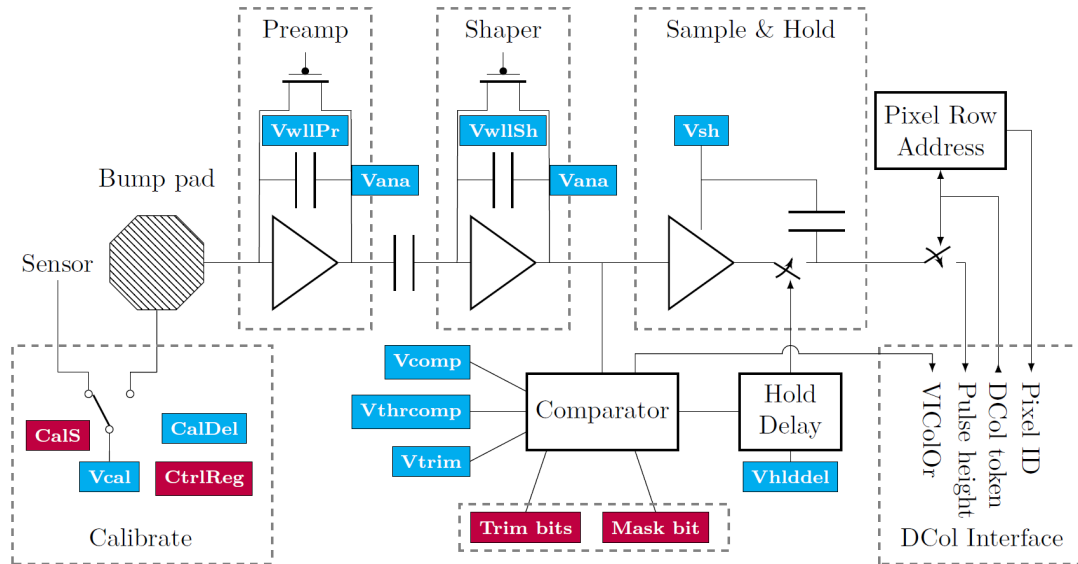


Figure 4.6: Simplified block diagram of a pixel unit cell of a Phase I pixel detector ROC. Illustrated are the bump pad required for the connection to the sensor, the preamplifier and shaper circuits, the comparator, the sample and hold circuit as well as the calibrate block used to inject calibration pulses into the preamplifier or sensor. The double column interface connects the PUC to the double column periphery. Blue labeled boxes correspond to DACs and red ones to registers [Spa16].

of the sensor to allow the connection via bump bonding. The pixel cell pitch of $150\ \mu\text{m}$ goes along the column direction and the $100\ \mu\text{m}$ pitch along row direction.

The second ROC region is the double column periphery which contains the data and time-stamp buffers. The hit information of each pixel is stored there until a L1 trigger decision is taken. The third ROC region is the control and interface block containing the logic for data transmission, the chip control infrastructure as well as the Analog-to-Digital Converters (ADC).

Pixel Unit Cell

The pixel unit cell contains all electronic components which are required to read out the charge generated in the silicon sensor and to process the corresponding signal. Therefore, the PUCs are equipped with a preamplifier, shaper, a comparator for charge discrimination and the sample and hold circuit which buffers the signal heights exceeding the comparator threshold.

A simplified block diagram of the PUC including the most relevant components and DACs is shown in figure 4.6. Charge generated in the silicon sensor drifts due to the electric field inside the sensor, is then collected by the n^+ -implants and enters the corresponding PUCs via the bump bonds. Hence, each PUC is equipped with a bump pad required to establish the bump bond connection.

Once a signal enters a PUC it is further processed by the preamplifier and shaper which are powered by the analog voltage domain (for further information about signal processing see e.g. [Spi05]). The routing scheme of the analog (controlled by the DAC V_{ana}) and digital power line (controlled by the DAC V_{dig}) is designed to minimize cross-talk between these power lines. This is important as ROC properties like noise and the lowest achievable comparator threshold are dominated by the analog performance.

The threshold of the comparator is adjusted individually for each pixel unit cell. The global DAC $V_{ThrComp}$ sets the global comparator baseline, roughly adjusting the comparator threshold for all pixels. Due to minor differences between the pixels, a fine tuning of the thresholds is necessary, which is done by 4 trim bits. By switching off trim bits the roughly adjusted threshold can be reduced while the global DAC V_{trim} defines the influence of the trim bits. The lowest achievable threshold corresponds to about 1,800 electrons instead of 3,500 electrons which was the minimum threshold of the old ROC. In addition, a mask bit can switch off single PUCs which are not working properly, especially if noisy PUCs fire continuously, creating "fake" hits.

Only signals exceeding the comparator threshold are stored in the sample and hold circuit. In this case, the PUCs notify the double column periphery via the $VIColOr$ signal. Afterwards, a token passes the pixels in the corresponding double column reading out the signal height information stored in the sample and hold circuit as well as the pixel addresses of all pixels which have registered a hit. This mechanism is called double column drain. The transmission of a pixel hit takes two clock cycles of the 40 MHz clock.

Additionally, a PUCs accommodates a calibration block. This is used to inject internally generated pulses into the PUC for calibration purposes. Alternatively, this calibration pulse can be injected capacitively into the sensor via an air capacitor established by the gap between sensor and the dedicated pad of the PUC. The signal height of this calibration pulse can be adjusted via the V_{Cal} DAC.

The number of DACs which allow to configure the ROC decreased from 26 for the original ROC to 19 for the Phase I ROC. Some DACs were simply replaced by fixed voltages or currents as they have never been adjusted during the operation of the original ROC.

Double Column Periphery and Control and Interface Block

The **Double Column** (DCol) periphery houses the data and timestamp buffers to store every pixel hit registered during the L1 trigger latency. Each DCol has 80 data and 24 timestamp buffers. In contrast to the original readout chip, the size of both buffers was increased to avoid inefficiencies caused by insufficient buffers in combination with increasing pile-up. The additional buffers are also the reason why new Phase I readout chip is slightly larger as they require more space. The DCol periphery is also responsible for the double column drain which is initialized by the $VIColOr$ signal sent by the PUCs. When the $VIColOr$ signal arrives a timestamp corresponding to the current bunch crossing is stored in a timestamp buffer cell. Additionally, the DCol periphery sends out a token which passes subsequently all PUCs of the DCol. PUCs containing a registered hit send their data to the DCol periphery before passing the token to the next PUC.

In case of a positive L1 trigger decision, all hits of the requested bunch crossing are transmitted to the control and interface block for further processing. During the request of the L1 trigger and the data transmission, the double columns are not able to detect new hits. When the transmission ends all hits within the configured trigger latency are cleared and the DCol is active again.

The control and interface block triggers the readout of the DCol buffers on arrival of the L1 trigger. When the data is transmitted to the control and interface block an ADC digitizes the analog signal heights recorded by the PUCs. Digital encoding of the signal height and the pixel address allowed to increase the readout speed from 40 MHz (for analog encoding used in the original ROC) to 160 Mbit/s. This is necessary as the rising data volume caused by increased pile-up demands a faster readout. The transmitted and digitized data is stored in a

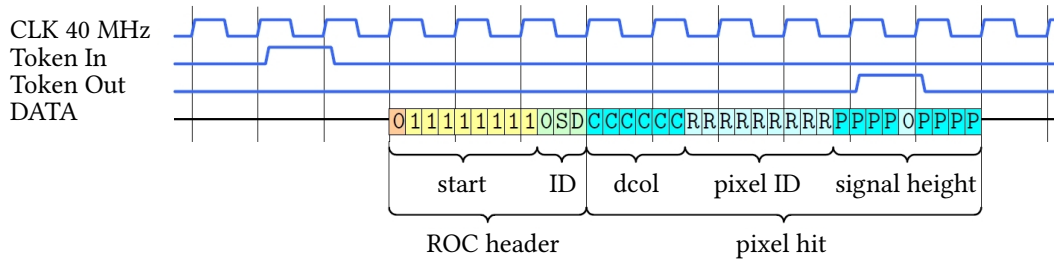


Figure 4.7: Digital encoded data format of the Phase I readout chip. The data format consists of a 12-bit ROC header followed by one or more pixel hits. The data stream starts one clock cycle after the Token In signal is transmitted from the TBM. The hit data consist of six bits for the double column (dcol) and nine bits for the row (pixel ID) forming the pixel address. Another eight bits encode the signal height with an additional zero in between the signal height stream to avoid fake headers [Spa12].

FIFO until an external token sent from the TBM arrives. This approach reduces the detector dead time significantly to less than 1% as the DCols are not blocked between the arrival of the L1 trigger decision and the external token arriving later [Käs13].

Data Encoding

The digitally encoded data is transmitted as a 160 MHz signal and starts one clock cycle after the Token In signal (sent from the TBM) arrives at the ROC. Each data stream starts with a 12-bit ROC header beginning with a leading 0, eight consecutive 1 and is completed by a further 0 plus two reserved status bits S and D. The S bit serves as start marker for the data transmitted in the D bit.

The ROC header is followed by the transmission of the pixel hits with 24 bits assigned to a single hit like illustrated in figure 4.7. The first six bits contain the double column information followed by nine bits for the row information providing the full pixel address. The 15 bits assigned to the pixel address are written in Gray Code, a binary code where consecutive numbers only differ in one bit [Gra53].

Another eight bits encode the signal height with an additional zero in between the signal height stream to avoid fake headers.

The encoded data is embedded between the TBM header and trailer. Both start with a 12 bit identifier followed by 24 bits containing trigger and status information. The Phase I TBM which coordinates the readout of all 16 ROCs of a module is capable of reading out four ROCs in parallel.

Table 4.2: Comparison of the old ROC PSI46V2 with the new one PSI46digV2.1-respin. The listed modifications are only a selection, for more information see e.g. [DA⁺12].

	PSI46V2	PSI46digV2.1-respin
ROC size	7.9 mm × 9.8 mm	7.9 mm × 10.2 mm
adjustable DACs	26	19
charge/address readout	analog	digital
readout speed	40 MHz	160 Mbit/s
timestamp buffers	12	24
data buffers	32	80
in-time threshold	3500 electrons	1800 electrons

MODULE PRODUCTION

The construction of a complex system like the CMS Phase I pixel detector is a challenging task for several reasons. First of all, there were strict time constraints imposed by the LHC schedule. This led to a short timeframe of some months at the turn of the year 2016/2017 to install the detector. Additionally, the construction of a particle detector relies on custom-designed devices which are provided by only few companies. Therefore, a close cooperation between science and the involved companies is required to meet the complex requirements and to make such projects a success.

The following chapter introduces the assembly line of the barrel pixel modules for the CMS Phase I pixel detector at Karlsruhe Institute of Technology (KIT). Along with the single assembly steps the associated qualification routines are described. This chapter puts special emphasis on the bare module, an intermediate product consisting of a sensor connected to 16 readout chips, and on the qualification routine of the final modules relying on characteristic X-rays. The results of detailed qualifications for both prioritized topics are presented in chapters 6 and 7.

To equip the entire barrel pixel detector 1184 modules plus additional spare modules (approximately 20 % of the modules required for the detector) are necessary resulting in about 1400 modules in total. The entire production is covered by multiple institutes from all over the world which provide redundancy to cope with potential downtimes of single production centers. A diversification among several countries also simplifies the funding from multiple national sources. Additionally, the parallelized production allows to complete the project in the limited period of only 18 months. Two KIT institutes are involved in the module production, which are the Institut für Experimentelle Teilchenphysik (ETP)¹ and the Institute for Data Processing and Electronics (IPE). Responsible for the final qualification of all modules produced at KIT is the Rheinisch-Westfälische Technische Hochschule Aachen (RWTH).

The KIT institutes are responsible for the production of 256 modules plus spares which corresponds to 50 % of the modules required to equip barrel layer four.

The KIT module production chain is illustrated in figure 5.1. Several external vendors and institutes are involved in the pre-processing of the single components already presented in figure 4.4. These single components are, in turn, assembled and tested at KIT before they are shipped to RWTH Aachen for the final qualification.

The distribution of responsibilities regarding the KIT production steps is as follows: the bare module production is carried out by IPE while the module assembly and the associated qualification measurements are covered by ETP.

¹ formerly known as Institut für Experimentelle Kernphysik (IEKP)

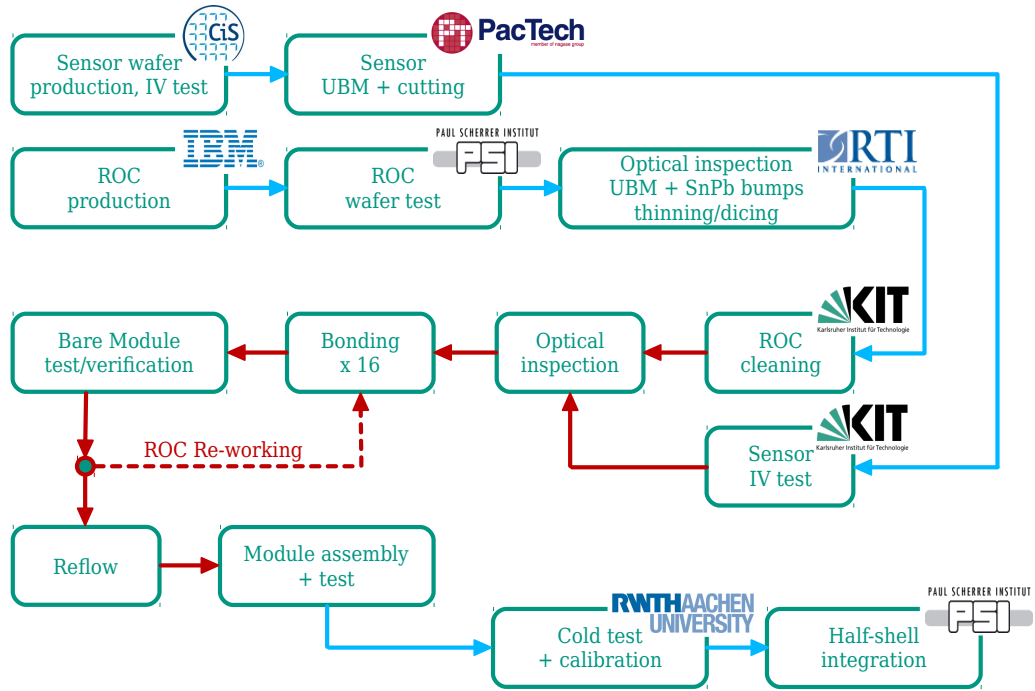


Figure 5.1: KIT workflow for the barrel pixel module production. The labels attached to the production steps are the responsible institutes and the external vendors. Steps connected via red arrows are performed at KIT.

5.1 SENSOR TESTING

All silicon sensors for the Phase I barrel pixel detector are produced on four inch wafers by CiS Forschungsinstitut für Mikrosensorik GmbH in Erfurt, Germany. Relying on the same company which already produced the sensors for the first pixel detector allows to save money as they reuse the original photolithography masks and to save time as no new vendor has to be qualified. In addition, CiS performs IV-curve measurements to determine the sensor quality according to the predefined grading criteria introduced below. Afterwards, the wafers are sent to PacTech - Packaging Technologies GmbH located in Nauen, Germany, for further processing.

PacTech applies an **Under Bump Metallization (UBM)** on the aluminum pads of each pixel relying on an electroless process (see e.g. [SLS13]). An UBM is necessary to establish a reliable contact between bumps and sensor once the ROCs get connected. The UBM is formed by several layers, a 200 nm palladium layer, a 5 μm nickel layer as well as a 50 nm gold layer. Aside from three large sensors used for production, the wafers also contain test structures, for example smaller sensors (denoted as single chip sensors), designed to be equipped with a single ROC. These structures are also equipped with the mentioned UBM. The single chip sensors are used for several test purposes, like controlling the bump bond process during the production or for detector performance studies of irradiated devices consisting of a single chip sensor and a ROC (denoted as single chip assembly). Such single chip assemblies are used in Part III and Part IV of this thesis. After deposition of the UBM the wafers are diced at PacTech and sent to KIT.

When the sensors arrive at KIT the quality determined by CiS might have changed due to UBM deposition or mechanical stress caused by wafer dicing or transport to PacTech and KIT. Therefore, a re-measurement of the IV-curve is necessary to avoid using bad sensors in the

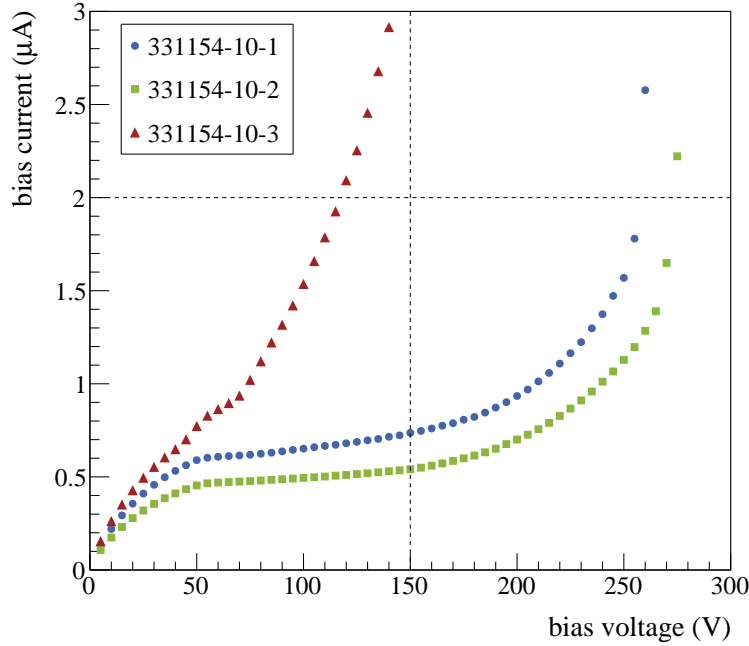


Figure 5.2: Visualization of the IV grading criteria using the example of sensor wafer 331154-10. Sensors 1 and 2 of the given wafer pass the grading criteria as they have leakage currents below $2 \mu\text{A}$ at 150 V and current ratios smaller than 2 between 150 V and 100 V . Sensor 3 instead, behaves not as desired failing the leakage current criterion at 150 V and the slow breakdown criterion (current ratio of 2.26). Failing already one criterion leads to an exclusion from the module production. The dashed lines help to identify IV-curves failing the leakage current criterion. Modified from [Hei16].

bare module production which would lead to a waste of ROCs. The IV-curve grading criteria are introduced below and visualized in figure 5.2 [DA⁺12]. As the Phase I sensor design is identical to the original sensors, the grading criteria are the same.

- Leakage current criterion: The leakage current of good sensors has to be less than $2 \mu\text{A}$ at the operation voltage (for unirradiated modules) of 150 V . This value corresponds to approximately twice the depletion voltage. For the sake of convenience, the presented bias voltages are always given as positive values, even though they are applied with negatively polarity.

$$I(150 \text{ V}) \leq 2 \mu\text{A} \quad (5.1)$$

- Slow breakdown criterion: In case of the CMS pixel sensors the slow current breakdown criterion was defined as the ratio of the leakage currents at 150 V and 100 V which has to be less or equal to 2.

$$\frac{I(150 \text{ V})}{I(100 \text{ V})} \leq 2 \quad (5.2)$$

In total, 648 sensors were delivered from CiS whereof 550 were graded good at CiS which corresponds to 84.9%. At KIT the IV-curve was measured for 533 sensors with 429 being graded good which corresponds to 80.5%. The discrepancy between delivered and tested sensors is caused by several reasons. First of all, some sensors were lost during dicing and handling

while the biggest part is attributed to sensors from the last delivery which were directly turned into bare modules due to time constraints. As the fraction of sensors which were graded good at CiS and afterwards graded bad at KIT is only about 5.6%, the skipping of the IV-curve measurement at the end of the production was tolerable. In addition, bad sensors can still be rejected in IV-curve measurements during bare module production. The little increase of bad sensors after processing at PacTech and transportation to KIT confirms the good process and sensor quality. For more detailed information on the Phase I sensor testing at KIT see [[Hei16](#)].

5.2 ROC PREPARATION

The readout chips for the pixel detector are centrally manufactured on eight inch wafers at IBM. Afterwards, all wafers – each containing 244 ROCs – are sent to Paul Scherrer Institute (PSI) in Villigen, Switzerland, where each wafer is probed. The 37 ROC wafers designated for KIT are then sent to RTI International, a company located in the US and responsible for the bumping process.

5.2.1 THE TIN-LEAD BUMPING PROCESS

At RTI the readout chips are equipped with bumps made from an eutectic mixture of tin (63%) and lead (37%). The spherical bumps are placed on aluminum pads covered with an UBM also applied by RTI which have a diameter of about 30 μm . The lithographic process applying the bumps relies on electroplating which is illustrated in figure 5.3 and can be summarized as follows. For more detailed information see [[HLBS03](#)].

1. Removal of the original wafer passivation and re-passivation with an organic spin-on polymer called BCB (**BenzoCycloButene**) to protect the surface. Further, the BCB planarizes the wafer surface providing a uniform base to form the bumps. Additionally, the BCB behaves like a stress buffer between the wafer substrate and the bumps increasing the thermo-mechanical reliability. The BCB located at the bump bond pads is removed by a lithographic process to make the pads accessible.
2. UBM deposition via electroless plating. The UBM is formed by several thin layers. Starting from the pad side: a titan tungsten layer acting as diffusion barrier, a nickel layer of few μm thickness as wettable metal and a thin gold layer to prevent oxidation. To avoid gold embedding into the solder bumps the gold layer thickness should be of the order of nanometers.
3. Application of a thick photoresist layer. Above the UBM pads the photoresist is removed by a photolithographic process.
4. Deposition of the solder bump material on the UBM via electroplating. The deposited amount of material which is relevant for the final bump size is controlled by the electroplating current.
5. Chemical removal of the remaining photoresist.
6. The spherical shape of the bumps with a diameter of approximately 30 μm is established by a reflow process. In addition, the reflow helps to create an intermetallic connection between UBM and bump material.
7. Removal of the UBM not covered by the bumps. The wire bond pads used to connect the ROCs to the HDI are re-opened via a dry etching process.

Subsequent to the bumping a thick layer of photoresist is applied to protect the ROC wafers during the remaining processing steps, transportation and handling. In the next step, the ROC wafers are thinned down to a thickness of 175 μm by removing dead material from the backside

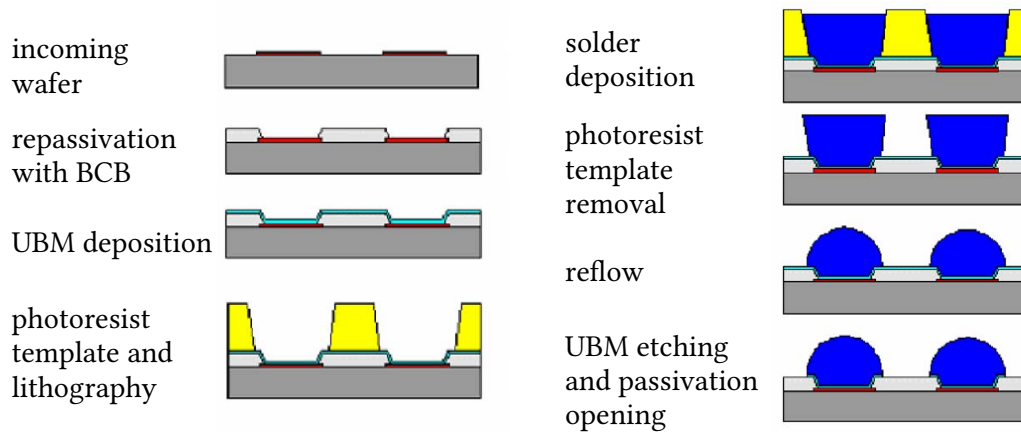


Figure 5.3: RTI SnPb bumping process. For each step of the application and forming of the spherical SnPb a cross-sectional view is given. The diameter of the final bumps is about $30\ \mu\text{m}$. Modified from [HLBS03].

to reduce the overall material budget of the detector. Afterwards, the thinned ROC wafers are diced. Both processes, the thinning as well as the dicing, are outsourced by RTI to another external company. The final step performed at RTI is an optical inspection checking for bad dicing, miss-shaped or missing bumps and marking the bad ROCs.

5.2.2 ROC CLEANING AND INSPECTION

One measure to guarantee good bump bond quality is to perform the entire bare module production inside a clean room. Therefore, all sensors and ROCs have to be cleaned before being bump bonded. Sensors do not need special treatment as the pollution caused by dicing, transport and handling can be removed easily. However, the removal of the photoresist covering the ROCs requires additional effort. Hence, a special cleaning procedure was developed at KIT [Kud14].

When the cleaning process was developed, two aspects had to be covered. First, the remaining residuals after the cleaning had to be minimized and second, the required handling steps had to stay as few as possible to keep the bumps intact especially after the removal of the photoresist. During this process, which is summarized below, 35 ROCs are cleaned in parallel.

1. 35 readout chips are placed in a custom-designed POM (PolyOxyMethylen) tray with the bumped side showing upwards. The ROCs are held in place with the help of a vacuum system and a grid made from PolyTetraFluoroEthylene (PTFE) threads.
2. The tray is then placed inside the first bath of the cleaning sequence containing ultrapure ($> 99\%$) acetone to dissipate the photoresist and possible organic contamination.
3. The second bath is filled with ultrapure isopropyl alcohol which is required to get rid of the acetone residuals. Water would not be appropriate as acetone is a non polar compound, hence they are not mixable.
4. The third as well as the fourth bath contain deionized water and complete the actual cleaning.
5. Finally the tray is placed inside a vacuum chamber heated up to 70°C to accelerate the evaporation of the remaining water.

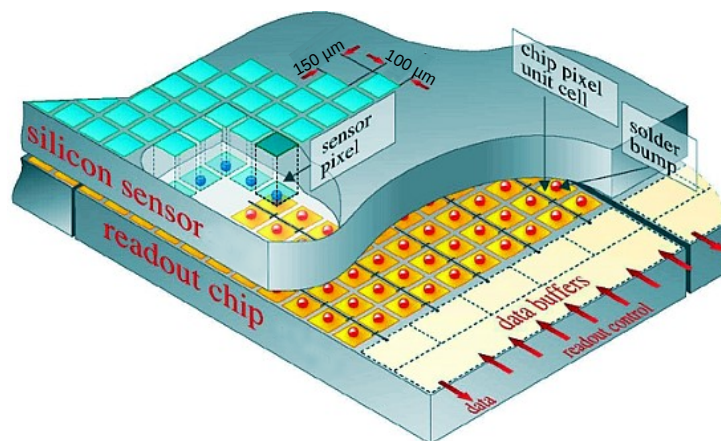


Figure 5.4: Cross-sectional sketch of a bare module. Bare modules are formed by a sensor connected to 16 ROCs where the sensor pixels (turquoise) and the PUCs (yellow) of the readout chips are connected via bumps (red). A good bump bond process is necessary to establish a reliable connection. Modified from [CMS03].

The entire cleaning process takes about 30 minutes. More detailed information on the cleaning procedure can be found in [Kud14].

The cleaning process is followed by an optical inspection to verify the cleaning results, to check for missing or deformed bumps and to screen the dicing edges which might impair the bare module production. This inspection is implemented as a semi-automated procedure relying on a microscope with camera and motorized table connected to a PC. The software controlling the setup allows to take a sequence of magnified pictures which are automatically stitched together.

In the first step of the optical inspection a tray containing cleaned ROCs is placed on the table and a high resolution picture of each ROC is stored on the PC. However, the large number of 9000 photographed ROCs in total demand a software supported defect investigation. Therefore, a custom-designed pattern recognition software was developed relying on the National Instruments Vision Development Module [Nat17c]. The pattern recognition searches picture-by-picture for the defects mentioned above and presents suspicious areas to the operator. The operator, then has to decide if the presented ROC is sufficient to be turned into a bare module, if it has to be discarded or if a re-cleaning is possible.

The cleaning and inspection efficiency is about 90 % whereof the largest defect contribution is attributed to environmental contamination, silicon splinters caused by the dicing, persistent cleaning residuals and BCB defects. The defect contribution due to missing bumps is very small with only 1 % of the ROCs having more than 5 missing bumps [Col16].

From 9000 delivered ROCs for the KIT production center about 8100 (90 %) were of production quality according to the PSI ROC wafer tests [CMS17a]. As mentioned above, the cleaning and inspection efficiency is also approximately 90 % which results in roughly 7300 good ROCs available for the KIT bare module production.

5.3 BARE MODULE PRODUCTION

The first step of the bare module production is the flip-chip bonding which is the actual process assembling the bare modules. Afterwards, the bare modules have to be tested followed by a reflow process completing the bare module production.

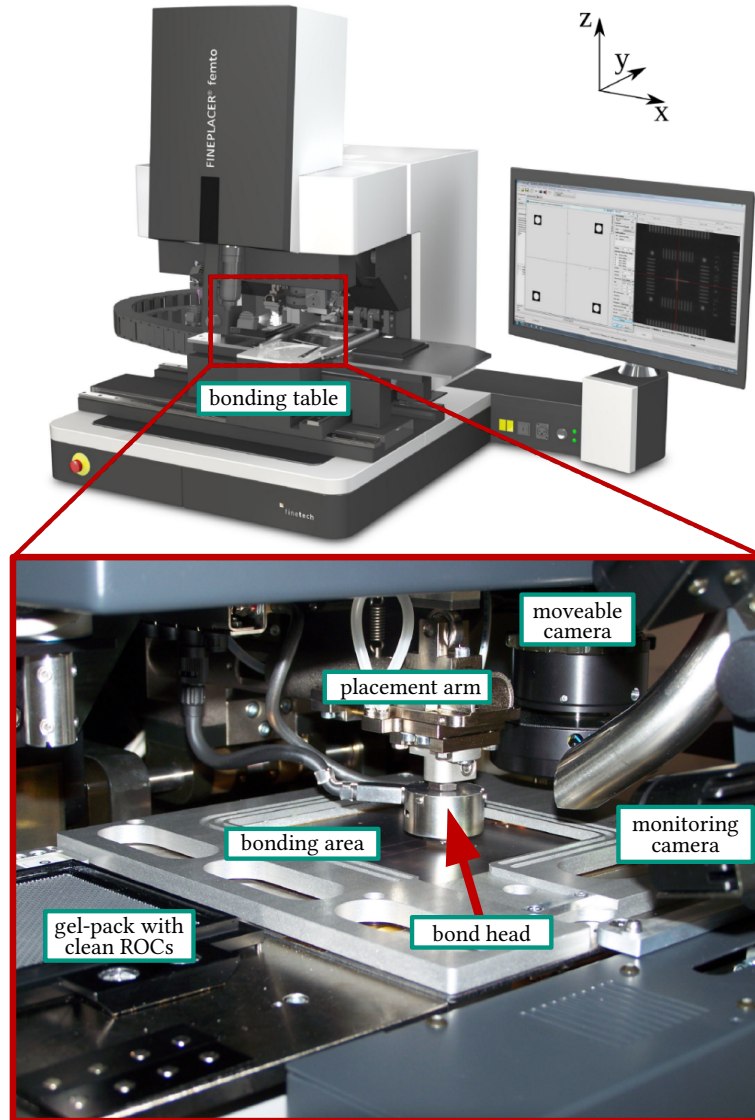


Figure 5.5: Overview of the FINEPLACER[®] femto bonding machine from Finetech. A closer view of the bonding table shows the placement arm in bonding position ($\phi = 0^\circ$). Modified from [Fin16].

5.3.1 FLIP-CHIP BONDING

The sandwich-like bare module (see figure 5.4) is produced by bonding 16 readout chips to a silicon sensor. The flip-chip bonding relies on a FINEPLACER[®] femto bonding machine from Finetech GmbH in Berlin, Germany. An overview of the bonding machine is presented in figure 5.5.

The flip-chip bonding machine is equipped with a motorized bonding table, moving in x , y , z and ϕ direction. Two presentation tables to pick up components are attached to the bonding table, one on each side. In case of the bare module production a single vacuum release tray manufactured from Gel-Pak (hence subsequently denoted as gel-packs) is placed on the left presentation table supplying up to 35 cleaned readout chips. The center part of the bonding table is equipped with a strong vacuum system provided by a Venturi tube to fix the silicon sensor during the bonding. The available bonding area has a size of about $100 \text{ mm} \times 100 \text{ mm}$ and can be heated up to 400°C . The cooling is implemented by a custom-designed system relying on compressed air. The placement arm used to pick up the readout chips from a

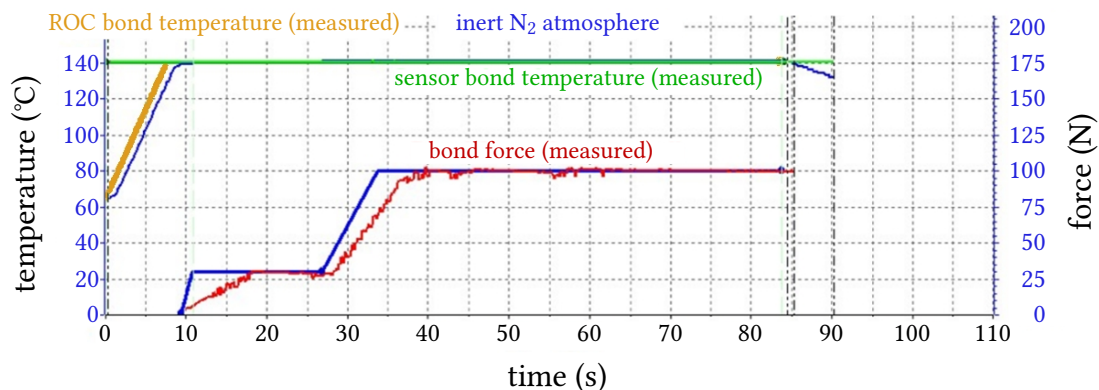


Figure 5.6: Force and temperature profiles of the KIT bump bonding process. The blue lines show the set values for the bond force and temperature. The red line gives the measured bond force while the orange line shows the measured bond head temperature. The overlapping dark and light green lines indicate the set and measured bond table temperatures. Modified from [Col16].

gel-pack is located above the bonding table. It has only one degree of freedom available to perform a rotational movement along the x-axis. At the end of the placement arm the bond head is mounted. This custom-designed heatable tool matches exactly the size of the readout chips and picks them up with the help of an integrated vacuum circuit. Due to the mechanical design of the bond head it is self-aligning as the orientation of the bond head is flexible until the vacuum is applied. This allows to keep the picked up ROCs perfectly parallel to the surface of the bonding table when the placement arm is in bonding position. In addition, the bonding machine is equipped with a movable camera running along the x-coordinate of the bonding table, while a 60 mm long light splitter allows to simultaneously view the silicon sensor (lying on the bond table) and the readout chip (picked up by the bond head). The simultaneous visualization supports a sophisticated pattern recognition used for the alignment algorithm. Further components belonging to the bonding setup are an antivibrational table housing the entire setup, a computer controlling the bonding sequence and an additional camera monitoring the bonding process. A custom-made metallic plate with a cutout matching the bond head can be used to cover the bonding area. In combination with the connected gas modules providing nitrogen and formic acid this allows to perform an in-situ reflow.

The range of the bonding force applied by the placement arm extends from 0.5 N to 500 N. The specified placement accuracy is less than 0.5 μm and the quoted planarity accuracy is below 4 μrad [Fin16].

The bonding sequence for the bare module production is summarized below.

1. Placement of the silicon sensor on the bonding table with the UBM side facing up. The vacuum circuit integrated in the bonding table fixes the sensor.
2. The bonding machine searches for the two lower corners of the sensor and stores the coordinates in an internal reference system.
3. A gel-pack containing ROCs which passed the optical inspection after the cleaning is placed on the left presentation table. The motor stage moves to allow a pattern recognition of the dicing edges of the desired ROC. Since the ROCs have to face downwards and their backside does not have any structure it is necessary to have reliable dicing edges to perform the pattern recognition successfully. Afterwards, the motor stage moves the localized ROC exactly below the placement arm which in turn goes into pick-up position ($\phi = 0$) and fixes the ROC with the help of the integrated vacuum system.

4. Due to the soft surface of the gel-pack the bond head is not necessarily flat (with respect to the bond table) when a ROC is picked up. As the bond head is fixed as soon as its vacuum is turned on an additional flattening step needs to be introduced. Hence, the picked up readout chip is placed on a very flat ceramic plate mounted onto the right presentation table. When the ROC is picked up again the flatness of the bond head is guaranteed which is mandatory to provide a parallel contact when the ROC is bonded to the sensor.
5. The bonding machine performs a pattern recognition on unique characteristic microstructures of the ROC and sensor. A recursive adjustment of the bonding table is performed until the user-defined accuracy is achieved.
6. Start of the bonding process. First the placement arm moves into bonding position ($\phi = 0^\circ$), then the bonding table moves upwards and applies a user-defined bond force. A force sensor located at the placement arm monitors the bonding profile. Simultaneously the temperature of the bond head is increased until the desired bond temperature of 140°C is reached. To avoid thermal stress on the bare module the temperature of the bonding table is fixed during the entire bonding sequence at the same value (140°C). Figure 5.6 shows the force and temperature profile as a function of the time. The bond force rises slowly and is characterized by an intermediate step at 30 N. This first step helps to establish good planarity between the ROC and the sensor before the full bond force of 100 N is applied. The actual bonding procedure of one ROC takes 85 seconds.
7. After the vacuum is switched off the placement arm returns to the upright position ($\phi = 90^\circ$) and the bonding machine waits until the bond head is cooled down to 65°C before it continues with the next ROC.

The chamber is continuously flushed with nitrogen to avoid oxidation during the bonding which would be enhanced due to the increased temperatures. The entire sequence described above takes about four minutes. This leads to a production time of roughly one hour for a complete bare module.

After the production of approximately 40 bare modules an additional step was introduced in the bare module production chain. Some sensors which were graded good in the initial KIT IV-curve measurement turned out to be bad once ROCs were bump bonded to them. This represents not only a loss of 16 ROCs per bare module but also a waste of time as those bad sensors were fully processed.

However, this indicates that the IV-curve measurement of bare sensors is not perfectly reliable even though it works fine for most sensors. This problem of unidentified bad sensors is related to the biasing scheme of bare sensors. Usually the bias voltage is connected to the backplane and the circuit is closed by providing a ground contact via the bump bonds and the ROCs. Obviously, this is not possible in the test of the bare sensors as no ROC is connected. Therefore, the ground contact is established by a probe needle connecting the bias grid which was already presented in figure 4.5. This structure is implemented on the front side of the sensors and is able to connect the implant of each sensor pixel via a structure called punch-through. The bias grid and the punch-through structures are the only option to measure the IV-curves of the bare pixel sensors, however this technique is not able to identify all bad sensors.

Nevertheless, to save material and time it was decided to first bond only a single ROC to a sensor, perform an IV-measurement and only bump bond the remaining 15 ROCs if the IV-curve measurement was okay. The corresponding in-house denotation for such devices consisting of a sensor and only a single ROC is "pretest module". This method allowed to reduce the already low number of bad bare modules even further, although it is still unclear which failure is responsible for the bad sensors.

5.3.2 BARE MODULE TEST

All produced bare modules have to be tested electrically for several reasons. First of all, it has to be guaranteed that bad bare modules are removed from the production chain to avoid wasting material (especially regarding the expensive HDIs) in subsequent production steps. In addition, the identification of problematic ROCs allows to replace them and to recover bare modules which otherwise would have been lost. The bare module test relies on common grading criteria defined by the CMS barrel pixel collaboration.

The custom-designed Bare Module Probe Station (BMPS) is located inside the clean room next to the bonding machine and the reflow oven. This allows to give fast feedback to the bonding operators in case of unexpected problems identified in the bare module test which might be related to the bonding process. Additionally, the short distance minimizes the handling between bare module production and testing as well as the handling between testing and reflow.

The bare module test addresses the following aspects.

- IV-curve measurement of the bare module to check whether the sensor is still okay.
- Electrical functionality test of all readout chips of the bare module to verify if each ROC is working correctly.
- Electrical test of each single bump bond connection to determine the number of defective (dead) channels.

Figure 5.7 shows the custom-made bare module probe station giving an overview of the most relevant components. The bare module is placed on a chuck made from PTFE which is equipped with three alignment pins. In addition, the chuck has an integrated vacuum system to keep the bare module in position. The bias voltage is provided to the bare modules via a tungsten probe needle mounted on the chuck and connected to a Keithley 2410 high voltage supply. A motor stage supports the chuck and provides movement in x , y , z and ϕ direction. In the center of the BMPS a needle card is located which allows to establish a temporary connection to the readout chips via 35 needles without harming the wire bond pads. The needle card is a passive component routing power and data signals from the Digital Test Board (DTB) to the connected ROC. The DTB is a custom-designed readout system based on an FPGA and it is used by the entire CMS pixel collaboration [SMP15]. Further, a microscope with an attached camera allows the operator to control the alignment of the needle card with respect to the wire bond pads of the ROCs. An additional fixed camera is used to perform a pattern recognition procedure to align the bare module automatically. A temperature and humidity sensor allows to monitor the testing conditions. The setup is placed inside a metal case shielding the bare module and the readout chain from electromagnetic noise and light. Especially when the needles are in contact with the ROCs a protection against vibration is required. Therefore, the entire setup is located on an antivibrational table.

Previously to the actual production a pre-production comprising 20 bare modules, based on an earlier version of the ROC, was performed to finalize the development of the flip-chip bonding process. These bare modules were used for the commissioning of the BMPS which revealed that the setup, especially the bias voltage circuit, is susceptible to noise. Hence, measures were adopted to reduce the noise and the best results are obtained for an optimized low-pass filter in the bias voltage circuit. More information on the noise reduction of the BMPS can be found in [Hit15].

The bare module probe station is controlled by a GUI-based software written with National Instruments LabWindows/CVI [Nat17b] and the National Instruments Vision Development Module [Nat17c]. The software runs automatically after the test sequence is started and only

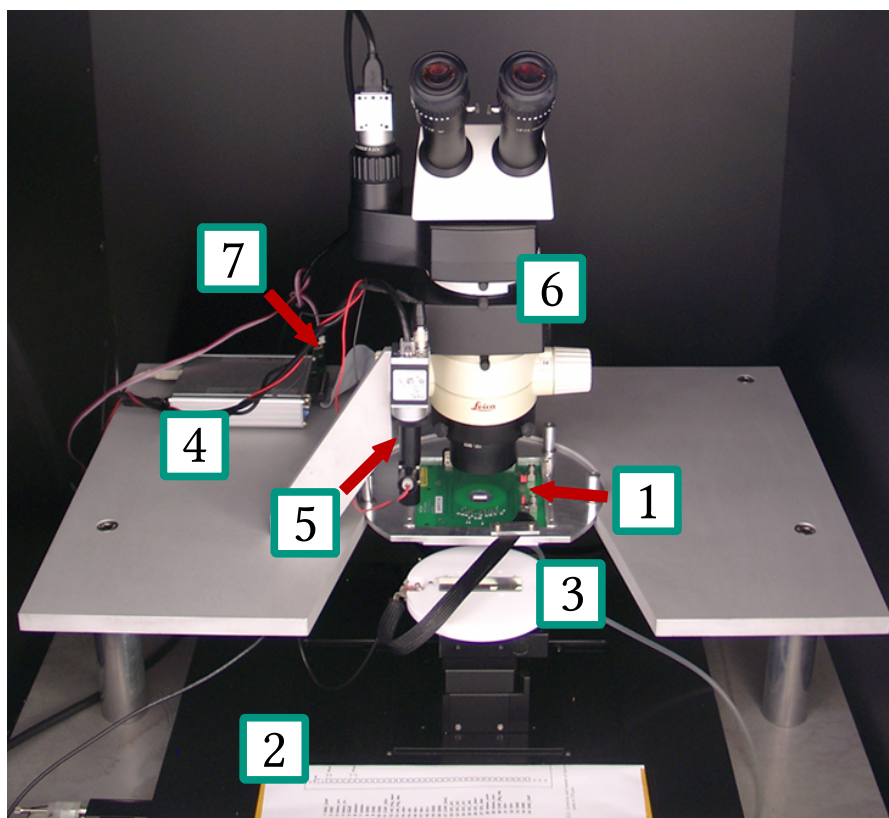


Figure 5.7: Overview of the bare module probe station. The labeled components are the needle card (1) for establishing a temporarily ROC connection, the motor stage (2), the bare module chuck (3), the digital test board (4), the pattern recognition camera (5) for automated alignment, a microscope with camera (6) and temperature and humidity sensors (7).

waits for operator confirmation at certain steps. For instance, a confirmation is required to check the bias needle contact or the needle card alignment. In case of a problem the operator interrupts the sequence and performs the desired steps manually before continuing the automated sequence. If necessary ROCs can easily be retested either at the end when the bare module is fully tested or already during the testing sequence. Once a bare module test is completed, the results are presented to the operator and files for upload to the production database are generated.

In addition to the automated test sequence, the software provides a manual operation mode which is useful for special purposes like the IV-curve measurement of pretest modules.

The electrical functionality tests of the readout chips are performed with a software written in C++ called pXar² [SMP15]. It is either controlled in command line mode or via a GUI and provides an integrated data analysis which uses ROOT libraries [BR97]. The software features a variety of routines and supports the testing of full modules as well as single readout chips as it is the case in the bare module test. Additionally, it is possible to implement user-written tests, such as various bump bond tests addressing the different bump bonding processes within the collaboration. pXar controls the DTB via a USB 2.0 connection and the DTB in turn executes the requested electrical tests. As these tests are executed on the FPGA of the DTB and only the generated data is transferred to the PC the testing duration is drastically reduced (compared to an entirely PC based execution). During the bare module test a script is passed to pXar using the command line mode and the corresponding measurements are performed autonomously.

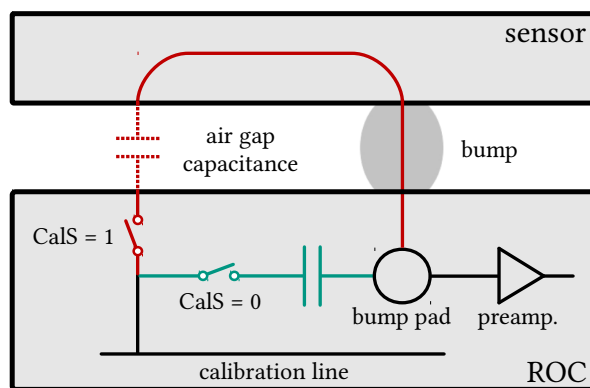
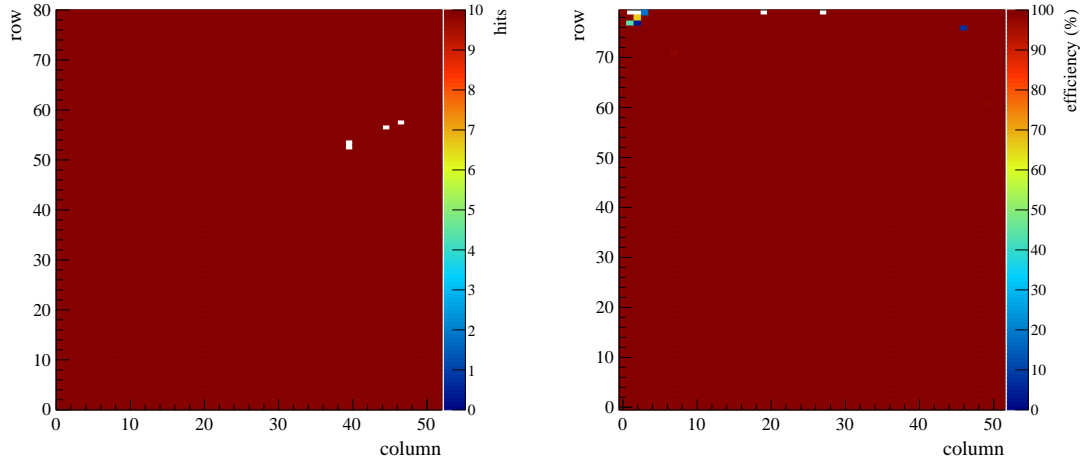


Figure 5.8: Internal calibration mechanism of the PUC. Calibration pulses generated inside the PUC can either be injected into the preamplifier (turquoise) or into the sensor via an air gap capacitance (red). The register CalS controls the associated switches with CalS = 0 corresponding to the direct preamplifier path and CalS = 1 to the air gap capacitance detour. The capacitive injection is exploited in the bump bond tests.

The bare module test sequence can be summarized as follows.

1. Lifting the bias needle mounted on the PTFE chuck with the help of tweezers.
2. Placing the bare module with a vacuum pipette and pushing it carefully against the alignment pins.
3. Switching on the chuck vacuum to fix the bare module.
4. Lowering the bias needle to establish the required bias voltage contact.
5. Start of the test sequence. The motor stage moves the bare module below the pattern recognition camera to take a picture allowing to control the contact between bias needle and sensor.
6. Automated pattern recognition of unique structures on two corner ROCs providing the alignment of the bare module. The alignment ensures that the wire bond pads of the ROCs meet the needles of the needle card.
7. The motor stage moves automatically to the first ROC and allows to validate the alignment before it brings the ROC into contact with the needle card.
8. When the needle card is in contact an IV-curve measurement is executed. This step is only performed for the first ROC.
9. Electrical test of the contacted ROC. After a delay scan providing the correct timing for the DTB-to-ROC communication a programmability and functionality check is performed.
10. Determination of the number of broken bump bonds and presentation of the results to the operator.
11. Repetition of the electrical test on the remaining 15 readout chips. After the first 8 ROCs the motor stage automatically rotates the bare module by 180°.
12. Retesting certain ROCs if necessary and generating output files for database upload.

The measurement of the IV-curve requires roughly 5 minutes, the test of a single ROC takes about 2 minutes and 30 seconds while approximately 10 minutes are required for all movements steps. Hence, a complete bare module test starting with placing the bare module on the



- (a) Result of a pixel alive test. The test validates the functionality of all PUCs in a readout chip by injecting ten calibration pulses directly into the preamplifier of each PUC. In case of a defective PUC no hits are detected like it is the case for a few pixels in the presented map.
- (b) Output of a KIT bump bond test. In this test 100 calibration pulses are injected into each preamplifier, but taking a detour via air gap, sensor and bump bond. If the bump bond is missing, the pulses cannot re-enter the PUC and no hits are detected. For broken bump bonds some pulses might still be detected but the efficiency is lower.

Figure 5.9: Results from a pixel alive and a KIT bump bond test. The results are not related as they correspond to two different readout chips.

chunk up to unloading it in the end takes less than an hour. According to the bare module test result, the bare module is either reflowed before it proceeds in the module production chain or it is reworked if one or more ROCs have to be replaced. Bare modules with problems not attributed to a ROC are completely removed from the production chain.

The electrical test performed on each ROC starts with a programmability check by modifying the DAC Vana and validating if the analog current changes. It is expected that the analog current decreases by at least 5 mA when the DAC Vana is reduced from about 80 to zero. ROCs are presumably defective and have to be replaced if they do not show the expected behavior. Afterwards, each PUC needs to be checked as too many defective pixels (subsequently also denoted as dead pixels/channels) would impair the detector performance. The associated pXar test addressing this task is called pixel alive test. During this test ten calibration pulses are injected directly into the preamplifier of each PUC and the number of detected pulses is counted. The functional principle is illustrated in figure 5.8. In case of a perfectly working ROC each PUC should register ten hits while PUCs which see no hits at all are declared dead. If the detected number of pulses is unequal to ten, as it is the case for PUCs with a high noise level, predefined cuts are applied to decide if a PUC is dead or not. A typical result is shown in figure 5.9 (a). The pixel alive test also checks if the PUC addresses are correct by verifying if the pulses were detected in the same pixel cell they were injected to. If the addresses do not match, the PUC where the pulse was injected is declared dead. In addition, each mask bit allowing to disable single PUCs is checked.

As implied above the number of dead pixels (or dead channels) is a key criterion. However, dead channels are not only caused by defective PUCs but also by broken bump bonds preventing charge from entering the PUCs. Therefore, a reliable identification of broken bump bonds is mandatory. In the context of the pixel module production this means that those defects already have to be identified within the bare module test to retain the possibility to rework the affected ROCs.

The best approach is to create charge carriers inside the silicon sensor and to test the bump bond by reading out that charge via the PUCs. However, the usage of a radioactive source like ^{90}Sr or an X-ray tube to create charge carriers in the sensor is not possible inside the clean room due to practical and legal reasons. Nevertheless, there is another option exploiting the integrated calibration unit of the PUCs, which supports capacitive pulse injections into the sensor. This is implemented via a switch controlled by the CalS register where CalS = 0 leads to a pulse injection into the preamplifier and CalS = 1 into the sensor via a metal pad on top of the PUCs as illustrated in figure 5.8.

The reliability of a bump bond test depends strongly on the separation distance between ROC and sensor which in turn depends on the flip-chip bonding process. For that reason a new bump bond test had to be developed which is custom-tailored to the demands of the KIT bonding process. To validate which attempt is suited best, the bump bond test results were compared to measurements where charge carriers are generated in the sensor by characteristic X-rays and electrons from a ^{90}Sr source. The bump bond test matching those results best was defined as the KIT bump bond test. It consists of two parts.

In the first part the global threshold determined by the DAC Vthrcomp is adjusted. The routine starts at a relatively high threshold and checks for hits caused by noise. Then the threshold is reduced successively and the lowest threshold with less than five noisy PUCs (corresponding to less than one permille) is selected. The second step is comparable to the functionality test of PUCs described above, but instead of injecting the calibration pulses directly into the preamplifier the pulses take a detour via air gap, sensor and bump bond. In case of a broken bump bond the injected pulses cannot return to the PUC. As the detour needs additional time for signal propagation it is necessary to repeat this step for several calibration pulse delays which can be adjusted via the DAC CalDel. At each delay step 100 calibration pulses are injected per pixel and the best result of each pixel is stored. The cut which discriminates best between working and broken bump bonds is at 50 % undetected pulses based on crosschecks with X-ray results [Hit15]. A exemplary result is presented in figure 5.9 (b). PUCs which were already identified dead beforehand can obviously not pass the bump bond test and must not be double counted to avoid an overestimation of dead channels.

After a bare module is completely tested it is either reflowed or reworked if it has defective ROCs. In case of rework the bare module is again placed on the bonding table of the flip-chip bonder and the table is heated up to 130 °C. At that point the problematic ROC can be removed relatively easy, but still care has to be taken to avoid damaging neighboring ROCs. Typically, some bumps remain on the sensor side which need to be sheared off before a new ROC can be bump bonded. After the replacement the new ROC has to be tested on the BMPS together with the neighboring ROCs to guarantee that none of them was damaged during the rework process.

The data generated during the bare module test is uploaded to the Phase I production database where it is automatically analyzed. According to common predefined criteria, listed below, a grade is assigned to each bare module, where A and B graded bare modules proceed within the module production chain while C graded bare modules are rejected.

- Leakage current and slow breakdown criterion. The values are obtained from the IV-curve measurement performed at room temperature.
 - Grade A: $I(150\text{ V}) \leq 2\ \mu\text{A}$ and $\frac{I(150\text{ V})}{I(100\text{ V})} \leq 2$
 - Grade B: $2\ \mu\text{A} < I(150\text{ V}) \leq 10\ \mu\text{A}$ and $\frac{I(150\text{ V})}{I(100\text{ V})} \leq 2$
 - Grade C: $I(150\text{ V}) > 10\ \mu\text{A}$ or $\frac{I(150\text{ V})}{I(100\text{ V})} > 2$
- Dead pixel criterion. The number of dead pixels is determined from the pixel alive test and the KIT bump bond test. This criterion is applied to each ROC individually.

- Grade A: < 42 defective pixels (1 %)
 - Grade B: < 167 defective pixels (4 %)
 - Grade C: \geq 167 defective pixels
- Digital current criterion. An increased digital current indicates that a ROC is defective. This criterion is applied to each ROC individually.
 - Grade A: $I_{\text{dig}} < 65 \text{ mA}$
 - Grade C: $I_{\text{dig}} \geq 65 \text{ mA}$

The final bare module grade is the worst of the single grades. Bare modules which were reworked are marked with a minus sign attached to the final grade.

5.3.3 REFLOW PROCESS

The last step of the bare module production is the reflow process. After flip-chip bonding the connection between bumps and sensor UBM is still fragile which can be exploited to rework defective ROC. However, after the bare module is completely tested and before it is turned into a final module the bump connection needs to be improved to gain long term stability. This is achieved by the reflow process.

The option to perform the reflow on the bonding machine has been discarded in production as it would be very time consuming to reflow each bare module one by one. In fact, it would cause an intolerable production bottleneck as no bonding would be possible when the machine is occupied due to reflow. Therefore, a dedicated reflow oven was acquired allowing the parallel reflow of up to twelve bare modules. The reflow oven reaches temperatures of up to 450 °C and comes with a formic acid (HCOOH) line, two nitrogen (N₂) lines which are also used for cooling and the possibility to perform reflow under vacuum.

During the reflow, which takes about 30 minutes, the chamber is heated up to 240 °C and a mixture of HCOOH/N₂ is used to create a formic acid atmosphere. This atmosphere together with the high temperature lead to a reshaping of the bump bonds which improves the bump to sensor UBM connection. For more information on the reflow and bonding process as well as the improvement of both see [Col16].

5.4 MODULE ASSEMBLY

After the reflow the bare modules are ready for the final production step at KIT which is the assembly of the final modules. Before the remaining components get joined to the bare modules they first need to be prepared. Within this section the steps related to those components are briefly described, followed by the final assembly and testing steps.

The Kapton[®] based High Density Interconnects (HDI) are flexible and thin low mass circuits with components mounted on the surface. They are produced by Hightec MC AG in Lenzburg, Switzerland, and distributed to the production centers after a short initial test.

At KIT all HDIs undergo an optical inspection which rejected 54 HDIs due to mechanical defects. The main failure modes were broken solder connections at the connector, bad cutting which damaged the internal ground plane as well as kinks, scratches and contaminated bond pads.

Each HDI which passed the optical inspection has to be equipped with a single TBM³. All TBMs are produced by IBM and distributed after a wafer test and dicing. They are glued to the HDIs with Araldite[®] 2011 two-component glue. To assure precise glue application a custom-designed station was produced supporting the simultaneous processing of 8 HDIs. Once the

³ Only the HDIs for barrel layer 1 are equipped with 2 TBMs.

glue is applied the TBMs are positioned on the HDI using a vacuum pipette and a microscope. The required accuracy is ± 0.5 mm to keep the TBM wire bond pads on the HDI accessible. After the glue is cured the electrical connection between HDI and TBM is established via wedge-to-wedge wire bonding. It is performed on a Bondjet 710 manufactured by Hesse & Knipps relying on ultrasonic welding. The wire consists of an aluminum-silicon alloy and has a diameter of 25 μm . A detailed study was performed prior to the production to optimize the bond parameters. The resulting mechanical strength is more than 10 g per wire bond. During the production all wire bonded components are optically inspected to guarantee good quality by replacing bad wire bonds.

When the connection between HDI and TBM is established an electrical test is performed to validate the functionality. This test assures that no material is lost by irreversibly gluing a bad HDI or TBM on a good bare module.

During the electrical test the HDI is fixed by a vacuum system. A custom-designed needle card is placed on top of the HDI contacting its test pads. When the electrical test is executed the digital and analog currents drawn by the TBM are verified. In addition, an oscilloscope is used to monitor multiple signal types sent by the TBM and to validate them according to predefined specifications [BM14]. Finally, the high voltage circuit routing the bias voltage to the sensor is checked. The grading of the HDI and TBM simply discriminates between passed or failed depending on whether all tests are successful.

Aside from HDI and TBM the bare module needs to be equipped with base strips. To minimize mechanical stress inside the modules the base strips are made from silicon nitride (Si_3N_4) providing a thermal expansion coefficient comparable to the silicon based sensors and readout chips. The silicon nitride wafers are produced by Kyocera Corporation in Japan and have a nominal thickness of 200 μm . The base strips are distributed to the production centers after laser-cutting at a company in Switzerland.

Before the base strips enter the production chain an optical inspection is performed at KIT. The following two aspects are important. First of all, the base strips are the only connection to the cooling system once the modules are mounted onto the carbon fiber support structure. Hence, they have to be as flat as possible to maximize the contact area between base strips and support structure as well as between base strips and readout chips. As the laser-cutting creates burrs at the base strip edges each of them has to be deburred to obtain the required flatness. Second, the base strip pairs glued to the bare modules also have to be of comparable thickness to avoid problems in the assembly process as described in [Hei16]. Therefore, the optical inspection was used to reject base strips which are not flat and to form base strip pairs of comparable thickness. Overall 25 % of the base strips delivered to KIT had to be rejected.

After the components are prepared for the last production step, the module assembly starts with gluing the base strips to the backside of the readout chips. Similar to the TBM gluing Araldite[®] 2011 is used while custom-designed gluing stations guarantee a reliable alignment. Integrated vacuum circuits keep the base strips and the bare module in position. Since the curing of the glue takes about 24 hours four identical assembly lines were set up to provide the required production throughput.

HDI's which passed the electrical test are glued to the backside of the sensors. The HDI and the silicon sensor are aligned with the help of certain markers on the HDI and the sensor. Since the same glue is used the curing takes again 24 hours.

During both gluing steps the alignment is monitored by a movable microscope with an attached high resolution camera connected to a flat screen monitor. A Zeiss coordinate measuring machine allows a validation of the alignment after the curing. For more information on the gluing steps see [Hei16].

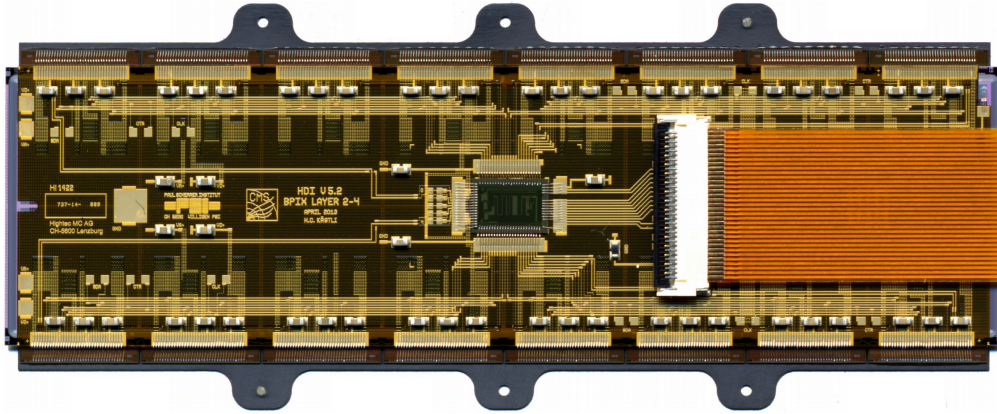


Figure 5.10: Pixel detector module for barrel layer 3 and 4 assembled at KIT. The 560 wire bonds connecting the ROCs to the HDI are visible down the long edges of the module. Additional wire bonds are located around the TBM in the center and in the top right corner establishing the bias voltage connection. The visible cable is a sacrificial one used for test purposes only.

Finally the electrical connection between the 16 readout chips and the HDI is established with the same wire bonding process already used for the TBM to HDI connection. Three additional wire bonds are placed to connect the bias voltage circuit of the HDI to the sensor. After a final optical inspection and connecting a sacrificial combined data and power cable the module is ready for testing. Figure 5.10 shows a module assembled at KIT with a sacrificial cable used for test purposes.

The final qualification at KIT is implemented in two steps. The first step is a series of electrical tests which include an IV-curve measurement and an electrical calibration, both performed at $+17^\circ\text{C}$ and -20°C . The electrical calibration is a composition of several functionality checks described below. As some of those tests are also implemented in the bare module test they were already described partially in the bare module test section 5.3.2.

PRETEST

The pretest first checks if the ROC is programmable by validating if the analog current changes as expected when the corresponding DAC Vana is tuned. Subsequently Vana is adjusted to obtain the predefined analog current target (typically to $I_{\text{ana}} = 24\text{ mA}$). A timing scan⁴ is performed to obtain the optimal DTB-to-TBM delay setting which is required to correctly deserialize the module data. In addition, the pretest performs a two dimensional scan for the DACs CalDel and Vthrcomp to obtain a reliable working point required for the following tests. The values of the tuned DACs are stored in a dedicated file.

PIXEL ALIVE TEST

The pixel alive test is divided into three subroutines. First the functionality of each PUC is tested by injecting ten calibration pulses into the preamplifier of the PUCs and verifying if all pulses were detected. The second part tests the address decoding of the PUCs. Again, calibration pulses are injected into each PUC but this time it is verified if the pulses are detected in the same PUC they were injected to. The third subroutine checks the mask bit which is implemented in each PUC and allows to deactivate single PUCs if they are not working properly.

⁴ This test is not required for single chip assemblies.

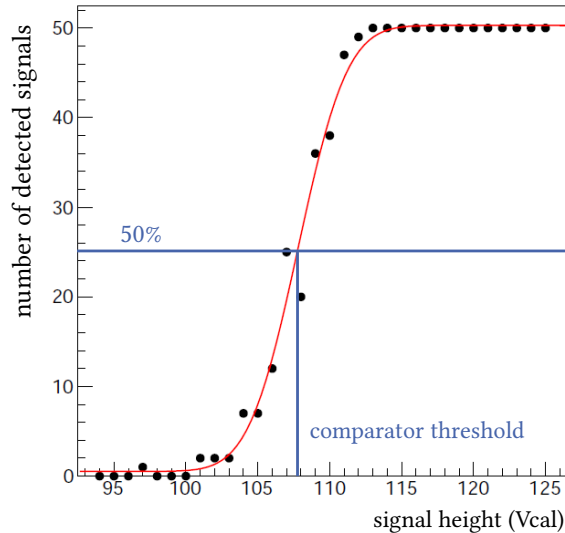


Figure 5.11: S-Curve test result of a single pixel. For every signal height (tuned by the DAC V_{cal}) 50 calibration signals are injected into a pixel at a fixed comparator threshold. The number of detected calibration pulses (black dots) is plotted as a function of the signal height. An error function describing the behavior is fitted and its width represents the noise. Additionally the comparator threshold can be derived via S-Curves by determining the signal height corresponding to 50% of the pulses detected.

KIT BUMP BOND TEST

The KIT bump bond test checks the status of each single bump bond. Each PUC injects 100 calibration pulses capacitively into the sensor. If the bump bond is intact, the corresponding signal re-enters the PUC and the pulse can be detected.

S-CURVE TEST

The S-Curve test is used to determine the noise of the pixels. At a fixed comparator threshold 50 calibration pulses are injected for different adjustable signal heights. In case of ideal components the result would be a step function. Below the comparator threshold none of the calibration pulses would be detected while above the threshold all pulses would have been registered.

However, real components behave differently due to noise. If the number of detected calibration pulses is plotted as a function of the signal height⁵, an S-shaped curve is obtained as shown in figure 5.11. The shape of the curve can be described by an error function whose width depends on the pixel noise.

In addition, the S-Curve can be used to determine the comparator threshold by identifying the signal height corresponding to 50% of the pulses detected.

TRIMMING

The Trimming routine adjusts the comparator threshold of all pixels to a predefined value. As the detector exploits charge sharing an identical or at least very similar behavior of all pixels is required which demands uniform comparator thresholds. Since each PUC behaves slightly different it is not sufficient to set the threshold globally. Therefore, each PUC needs to be tuned individually by adjusting its trim bits.

In the first step of the Trimming routine all trim bits are switched on and the global comparator baseline is adjusted via the DAC $V_{thrcomp}$. Hence, the PUC which has the lowest threshold is determined first. Then the trimming routine tunes this PUC until it reaches the

⁵ The signal height is typically given in V_{cal} as it is tuned via the DAC V_{cal} which has a range between 0 and 255.

desired threshold by adjusting $V_{thrcomp}$. In a second step the pixel with the highest threshold is determined and its threshold is tuned to the predefined threshold by switching off all trim bits and adjusting the global DAC V_{trim} which controls the impact of the trim bits on the global threshold. Different from intuitively expected V_{trim} has no influence when all trim bits are switched on as indicated by the equation below describing the absolute threshold $Q_{threshold}$.

$$Q_{threshold} = Q_{V_{thrcomp}} - (15 - \text{trim bits}) \cdot Q_{V_{trim}} \quad (5.3)$$

$Q_{V_{thrcomp}}$ is the global threshold tuned via $V_{thrcomp}$, $Q_{V_{trim}}$ the trim bit scaling factor adjusted by V_{trim} and the adjustable trim bit settings with $\text{trim bits} = 15$ corresponding to all trim bits switched on and $\text{trim bits} = 0$ to all trim bits turned off.

At this point the remaining pixels have thresholds which are slightly too high. In the third step the threshold of each pixel is adjusted by switching off trim bits to identify the correct trim bit setting for each PUC individually.

PH-OPTIMIZATION

The PH-Optimization adjusts the signal heights of each PUC. The test tunes two global DACs called PHOffset and PHScale to assure that the available range of the ADC is exploited best. As indicated by their names these two DACs shift and scale the detected signal height.

GAIN PEDESTAL

The Gain Pedestal test performs a calibration of each PUC which is required to correctly calculate the charge's center of gravity⁶ for two or more pixel clusters.

During the test calibration pulses with different signal heights are injected into each PUC, covering the entire V_{cal} DAC range. The detected signal heights (ADC) are plotted as a function of the signal height of the injected calibration pulses (V_{cal}). The obtained signal curves which are slightly different for each pixel, are individually fitted with an error function.

The inverse of each error function allows the conversion of the detected signal heights (given in ADC counts) into signal heights corresponding to the internal calibration pulse (given in V_{cal} values). Only after the conversion into V_{cal} the signal heights of different pixels are comparable which is required to determine the center of charge correctly.

READBACK TEST

This routine tests the Readback function of each ROC. The Readback function allows the investigation of chip parameters like supply voltages, reference voltages and DAC settings. A dedicated DAC called Readback is used to request the value of a specified parameter. The ROC returns the corresponding information embedded in the normal event output. In addition, the readback routine is also used to calibrate the analog ROC current.

After the modules passed the electrical tests they are irradiated with X-rays to determine the number of dead channels and to cross-check the results of the bump bond test. This is the second and last qualification step performed at KIT.

Using particles like electrons or photons to create charge carriers inside the sensor, instead of the ROCs internal calibration pulses, is more realistic and hence preferred to determine the number of dead channels. The duration of the test has to be sufficiently long to guarantee that the obtained number of hits per pixel is high enough.

In the laboratory where this measurement is performed two options are available. Either electrons emitted by a ^{90}Sr source might be used or photons generated by an X-ray tube. Although electrons precisely match the detector use case this option is unfavorable for practical reasons. As the opening angle of the ^{90}Sr source is too small to place it close to a module it would have

⁶ For the sake of convenience also called center of charge.

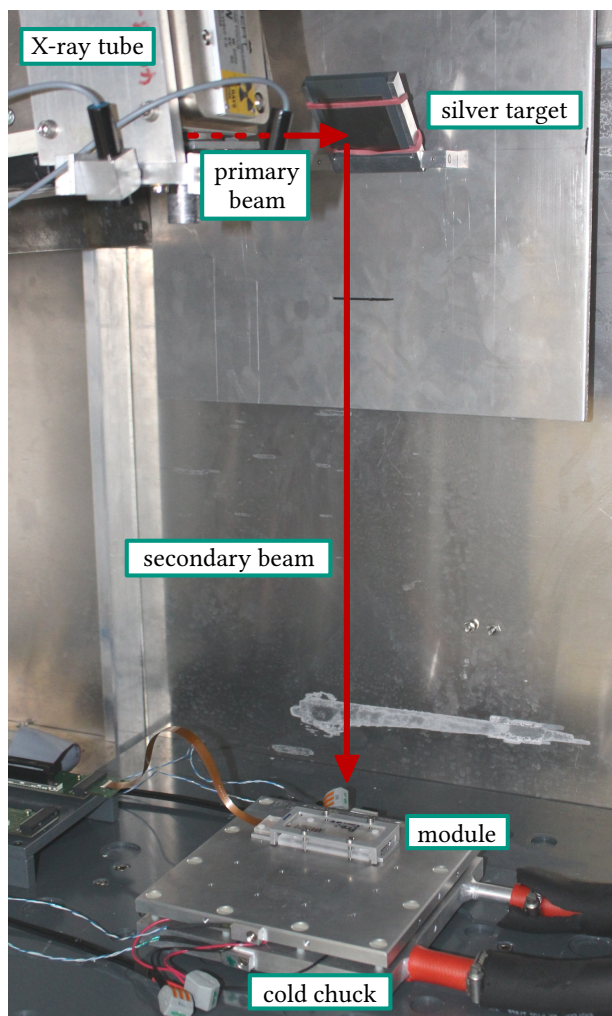


Figure 5.12: X-ray setup used at KIT to illuminate the modules with photons. A primary beam of continuous X-rays illuminates a target material (e.g. silver) and generates a secondary beam. This secondary beam is formed by characteristic X-ray photons with an energy corresponding to the K_{α} line of the target material. The module which is illuminated by the secondary beam is placed on a cold chuck on the bottom of the shielding box. The setup is used for quality checks during the production but also for additional studies on the Phase I pixel detector performance.

to be mounted at a larger distance to illuminate the entire module. This would lead to very long measurement times which are not tolerable during production. The second option are photons which can also be used to generate charge carriers inside the silicon as described in section 3.2.3. In addition, the available X-ray setup covers an area large enough to illuminate the module entirely while providing a sufficient high rate to keep the measurement time reasonable small.

The X-ray setup uses a 2000 W X-ray tube which is powered by a General Electric ISOVOLT 3003 generator. It supports acceleration voltages up to 60 kV and tube currents adjustable between 2 mA and 33 mA. Figure 5.12 gives an overview of the setup and illustrates its operating principle.

The primary beam is used to generate a wider secondary beam to obtain an illumination spot which is large enough to cover up to two modules. The continuous X-rays of the primary beam excite a target material (typically silver) which in turn emits a secondary beam of characteristic

X-ray photons. As the K_{α} line of silver corresponds to an energy of about 22.2 keV an average charge of 6156 electron-hole pairs is generated inside the silicon sensor [NIS17]. A cold chuck large enough to house two modules is located on the base plate of the shielding box. Additionally, a box can be placed on top of the chuck to encapsulate a small volume which is flushed with dry air to avoid condensation during measurements at -20°C . A thin foil serves as window to guarantee that the X-rays enter the box without being stopped.

The entire setup is operated with a Linux based PC which uses pXar for data acquisition and LabVIEW [Nat17a] to control the chuck temperature and the X-ray generator.

A detailed study regarding the X-ray setup was performed to minimize the time required to accumulate sufficient statistics [Tas16]. This resulted in a minimum measurement time of roughly 90 minutes. The hit maps obtained by pXar are analyzed using ROOT scripts and the sum of defective pixels per ROC is compared to the dead pixel criterion which was already applied in the bare module qualification.

The modules which passed the qualification tests at KIT are then shipped to RWTH Aachen for the final qualification as presented in figure 5.1. This includes electrical tests, an X-ray calibration as well as a high rate test.

Altogether three electrical tests are performed, similar to the test at KIT. The first electrical test is executed at -20°C , followed by ten thermal cycles between -25°C and 17°C to check the long term stability of the bump bonds. Then a second electrical test is performed at -20°C followed by a third one at 17°C .

Afterwards, an X-ray calibration is carried out on each module to obtain their conversion factors, which allow to translate the signal heights given in Vcal values into electrons. The X-ray setup used at RWTH is comparable to the one at KIT, but instead of using only one target, several materials are used to obtain measurements for different energies. For each material the mean generated charge is calculated according to their K_{α} energy. Then the number of generated electrons is plotted as a function of the measured signal height which is defined as the mean of a Gaussian fit describing the measured signal height distribution. The slope of a linear fit applied to the X-ray calibration data delivers the desired conversion factor. The complete X-ray calibration is described in more detail in section 8.5.3.

The final qualification step at RWTH Aachen is a high rate test which emulates the expected rates in the CMS environment and validates the high rate efficiency of each ROC.

From RWTH Aachen the modules are shipped to ETH Zürich where a thin Kapton[®] protection cap is glued to the surface-mounted capacitors of the HDI to protect the wire bonds. Afterwards, a short reception test is performed before the modules are sent to PSI to be mounted on the carbon fiber support structure.

RESULTS FROM THE BARE MODULE QUALIFICATION

The bare modules form the heart of the CMS pixel detector modules and should be of high quality to guarantee good detector performance. Otherwise, a reliable tracking of the charged particles emerging from the interaction point inside of CMS might not be possible. However, the desired high quality is not the only aspect which needs to be addressed. Using material efficiently is of similar importance in order to stay within the suggested financial scope. In addition, it would not have been possible to meet the pixel detector installation slot in early 2017 without a certain efficiency.

Therefore, thorough quality checks are carried out in parallel to the bare module production. This approach allows the early identification and correction of potential problems as well as efficient component handling. This chapter presents the results of the quality checks performed on the bare module probe station starting with the results of the pretest modules.

The KIT bare module production and qualification took about one year, starting in May 2015 and being completed in May 2016. In total, 437 bare modules have been produced and qualified.

6.1 PRETEST MODULES

The experience from the pre-production and the first 40 bare modules produced revealed an unexpected loss of bare modules caused by bad sensors neither identified in the CiS wafer test nor in the KIT sensor test. To avoid that with each of these bad bare modules 16 ROCs and the time needed for bonding and optical inspection are lost, the concept of pretest modules was introduced. The pretest modules which only consist of a single ROC bonded to a sensor, are electrically checked by performing an IV-curve measurement on the BMPS.

During the pretest module test the BMPS is operated in manual mode as the automated pattern recognition and alignment process cannot be performed due to the lack of the ROCs required for the pattern recognition. A modification of the software to test the pretest modules automatically is not necessary since the test duration only takes few minutes (typically less than five minutes) in manual mode. Because of the missing ROCs the alignment pins support the pretest modules only partially. To be able to fix the pretest modules with the chuck vacuum circuit a thin plastic foil was used to imitate the missing ROCs in order to close the vacuum openings.

Table 6.1 shows the results of the IV-curve measurements for all 422 pretest modules. The applied IV-criteria are the same as used in the bare module test introduced in section 5.3.2. This resulted in 389 grade A, 13 grade B and 20 grade C pretest modules. Although grade B material is sufficient, it was decided to reject most grade B pretest modules as they also behave differently than expected from the initial IV-curve measurement, which might be a hint for a sensor problem. Only two grade B pretest modules which had leakage currents slightly above $2\ \mu\text{A}$ were used at the end of the production to make use of the remaining ROCs. With the help of the pretest module approach 465 ROCs have been saved which allowed the production of

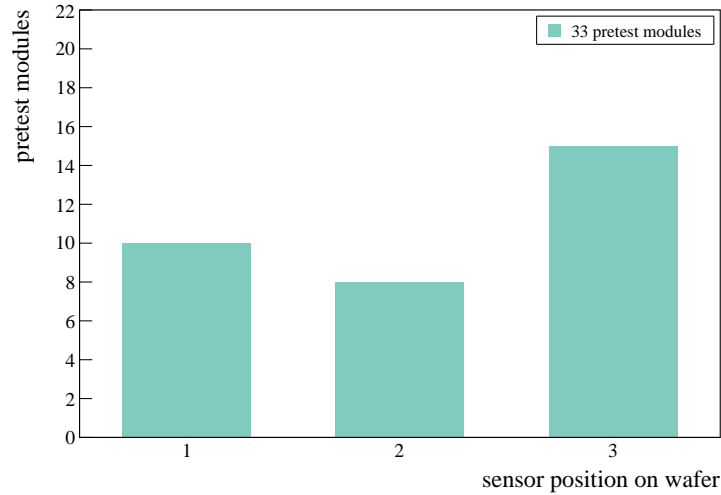


Figure 6.1: Sensor wafer position of the bad pretest modules. The number of bad pretest modules is given depending on the sensor wafer position. The distribution shows that bad pretest modules are caused by sensors from each wafer position. The result is compatible with a flat distribution regarding the uncertainty given by $\sqrt{33} = 5.7$.

29 additional bare modules. This corresponds to more than 11 % of the 256 modules required to equip half of barrel layer 4.

In addition to developing a procedure which rejects bad sensors during the bare module production investigating the problem itself is important for two major reasons. First of all, finding the reason potentially allows to identify bad sensors earlier, which would save more time and material if pretest modules would not be necessary at all. In addition, an early identification in the production might allow a process adjustment solving the actual problem instead of addressing the symptoms.

Therefore, the sensors causing bad pretest modules were analyzed further. Figure 6.1 presents the number of bad pretest modules as a function of the sensor wafer position based on all grade B and C pretest modules (as described in section 5.1 one wafer comprises three production sensors). A potential sign for processing or handling problems could be bad pretest modules related to only one or two positions on the sensor wafers. However, the distribution shows that all sensor wafer position are related to bad pretest modules. Due to the relatively low statistics, it is not possible to evaluate the ratios between the sensor positions as the result is compatible with a flat distribution regarding the uncertainty given by $\sqrt{33} = 5.7$. Additionally, a potential bias might be caused by the CiS wafer pre-selection rejecting wafers with less than 2 good tiles. The next step would have been to check if only consecutive wafers are affected, but unfortunately PacTech lost the assignment of the wafer IDs for a large fraction of wafers.

Table 6.1: IV-curve measurement results of the pretest modules. Since the pretest routine was introduced during the production the total number of grade A pretest modules (389) is smaller than the number of produced bare modules (437). Aside from two grade B pretest modules which missed the grade A criterion closely, all remaining grade B and C pretest modules were not turned into bare modules.

grade A	grade B	grade C
389	13	20

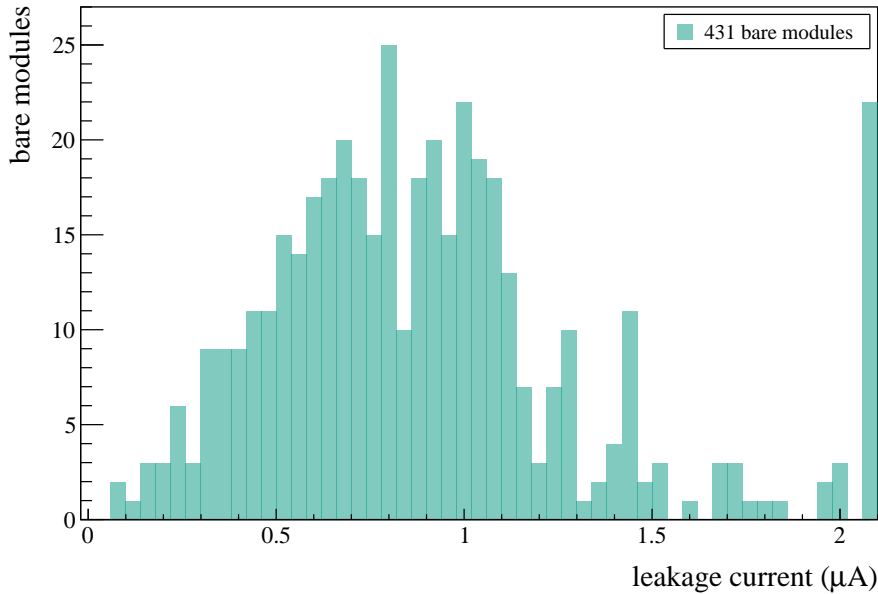


Figure 6.2: Leakage current distribution for 431 out of 437 bare modules produced at KIT. The major part of the bare modules has leakage currents distinctly smaller than $2 \mu\text{A}$ at 150 V . The last bin contains all bare modules which had larger leakage currents. Only for six bare modules no leakage current measurement could be obtained at 150 V due to early breakdowns.

Hence, this check is not possible. Since an unambiguous attribution to a production step is not possible it cannot be excluded that the problem is caused by the sensor design itself. The most sophisticated sensor part is the punch-through structure which allows to apply the bias voltage to all pixels even without a connected ROC (providing the ground contact). Detailed investigations of the punch-through structure are carried out at the time of writing this thesis and will be presented in [Sch].

6.2 BARE MODULES

After the successful testing of the pretest modules they are equipped with the remaining 15 ROCs before they are fully qualified in the bare modules test performed on the BMPS. The following sections present the results according to the grading criteria as well as detailed information about the rework efficiency and the overall yield.

6.2.1 LEAKAGE CURRENT

Figure 6.2 presents the leakage current distribution at 150 V for 431 out of 437 produced bare modules. The remaining six bare modules are not included as no leakage current measurement could be obtained due to early breakdowns leading to a measurement abort at voltages lower than 150 V . Nevertheless, 409 bare modules passed the grade A leakage current criterion as their measured values are below $2 \mu\text{A}$, which is a sign of good quality. The average leakage current of the grade A bare modules is about $(0.90 \pm 0.36) \mu\text{A}$. The last bin represents the 22 bare modules with leakage currents higher than $2 \mu\text{A}$. According to the leakage current criterion, these bare modules are graded B or C.

In addition, the shown distribution of the leakage currents confirms the excellent sensor selection at KIT which was improved even further by the pretest module approach. A total of only 28 bare modules (including the six early breakdowns) did not pass the grade A leakage current criterion. This means that the introduction of the pretest modules reduced the non-grade A

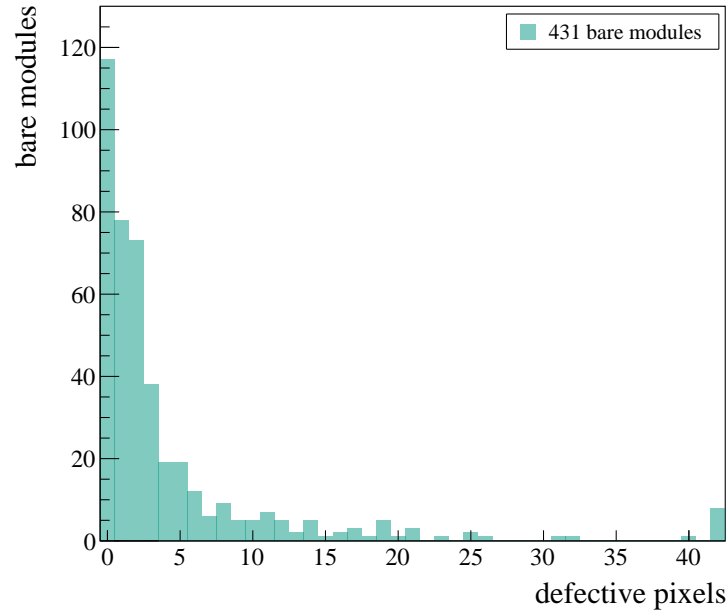


Figure 6.3: Defective pixel distribution for 431 out of 437 bare modules produced at KIT. The number of dead pixels is determined from the pixel alive test and bump bond test. The maximum of the distribution is at zero defective pixels which is the case for 117 tested bare modules (27.1%). 344 bare modules (79.8%) have only five or less dead pixels. Only 8 bare modules have more than 41 dead pixels. Four out of these eight bare modules are still grade A as the dead pixel criterion corresponds to individual ROCs and not bare modules. The four remaining bare modules are grade C.

bare modules by more than 50% as 31 grade B and C pretest modules were rejected and not turned into bare modules.

6.2.2 DEFECTIVE PIXELS

The performance of the CMS pixel detector strongly depends on the number of working channels. A high fraction of working channels guarantees a high hit and tracking efficiency of charged particles traversing the pixel detector layers and endcaps. Further, clustered defects are more problematic than single defects as the probability to miss a particle is higher. Hence, bare modules of good quality are not only characterized by the current-voltage characteristics but also by a very low number of unclustered defective (dead) pixels.

Figure 6.3 shows the number of dead pixels for all 431 tested bare modules. The number of dead pixels is determined from the pixel alive test and the KIT bump bond test. The last bin represents the small number of only eight bare modules which have more than 41 dead channels. As described in section 5.3.2 the maximum number of dead pixels is 41 for a grade A readout chip while figure 6.3 gives the number of dead pixels per bare module. Hence, four out of those eight bare modules corresponding to the last bin are still grade A and only the remaining four bare modules are grade C. Altogether 427 bare modules (97.7%) fulfill the grade A dead pixel criterion. Another prominent feature of the distribution is the maximum of 117 bare modules (27.1%) which have zero dead pixels. Overall, 344 bare modules (79.8%) have only five or less dead pixels.

These results nicely illustrate the good quality of the bare modules. A key component to achieve this excellent result was the possibility to rework bare modules with problematic or defective readout chips.

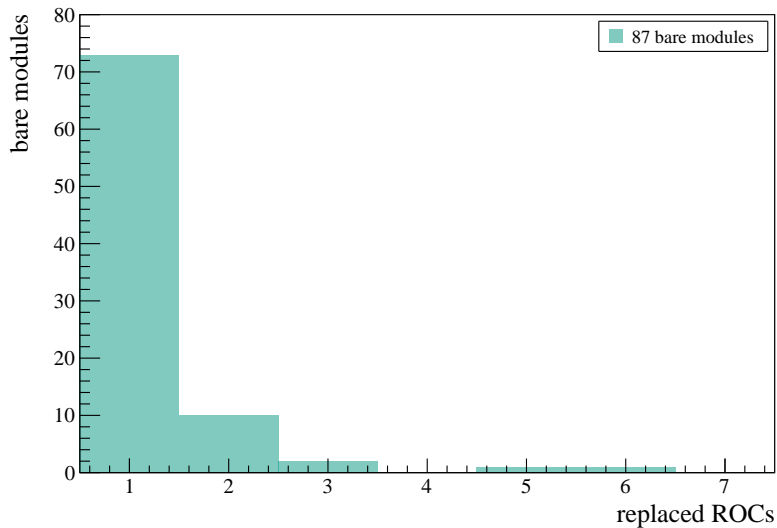


Figure 6.4: Number of replaced ROCs per reworked bare module. Altogether 87 bare modules had to be reworked whereof 73 bare modules (83.9%) required a replacement of a single readout chip. Two outliers, with five and six ROCs respectively, were mechanically damaged due to handling failures.

6.2.3 REWORKED BARE MODULES

The KIT rework process was developed to recover bare modules which would have been rejected without. In addition, it allowed to improve the overall quality since also bare modules which passed the bare module qualification but with a certain number of dead channels were reworked. The rework process was already tuned during the pre-production phase to be fully exploited during the actual production.

Figure 6.4 presents the number of replaced ROCs per bare module for all 87 reworked bare modules. This corresponds to 19.9% of all produced bare modules at KIT. In 73 cases only a single ROC had to be replaced (83.9% of all reworked bare modules). In case of the two bare modules with the highest number of defective ROCs, five and six dead ROCs had to be replaced, respectively. In both cases the readout chips were mechanically damaged due to handling failures which caused the rework.

As the rework turned out to be very successful it was decided to also rework some grade A bare modules. The cut for a rework of grade A bare modules was at about 20 dead channels of at least one ROC, but only if the dead channels were clustered to some extent (e.g. at a ROC corner).

The results of all rework procedures are presented in table 6.2. The qualification of the 87 bare modules before being reworked delivers seven grade A, nine grade B and 71 grade C bare modules.

In only one case the rework led to a downgrade of a bare module. This was an initial grade B bare module which became grade C afterwards due to a breakdown of the IV-curve at 50 V. Either the sensor was damaged during the rework or the sensor already had a defect which emerged only after the rework. In two cases the quality of grade B bare modules remained unchanged after the rework. In both cases the first bump bond test showed a pattern indicating a sensor issue. After the ROCs were removed a detailed optical inspection revealed scratches on the sensor across the UBM. As those scratches matched the patterns from the bump bond tests they very likely caused the bump bond failures. As expected from that the bump bond

test results did not improve for the replacement ROCs. Six grade C bare modules could not be recovered at all. Two of them had IV-curve breakdowns after the rework, in one case the replaced ROC had been damaged mechanically and in another case the replaced ROC was electrically dead. When this occurred it was precautionally decided to reject bare modules which would have required a double rework of a single position. The remaining two grade C bare modules which could not be recovered showed large-scale discolorations of the sensor UBM. The bump bonds corresponding to the affected UBM were broken as they could not establish a working connection. Both sensors should not have passed the optical inspection prior to the bonding as the sensor UBM was probably suspicious already beforehand. Altogether 76 out of 87 reworked bare modules had grade¹ A- after the rework which corresponds to 87.4%. However, the most remarkable feature is the successful recovery of 65 bare modules which would have been rejected without the rework. Those 65 bare modules represent more than 25% of the 256 modules required to equip half of barrel layer 4.

These results confirm that the identification of problematic ROCs and the rework process were well understood and controlled. Both were major contributions to the success of the entire production at KIT.

Table 6.2: Yield of the bare module rework process at KIT. Grade A bare modules were reworked if a ROC had more than ≈ 20 dead channels. 65 bare modules which would have been rejected were recovered due to the rework. Altogether the rework was successful in 78 (89.7%) cases.

grade before rework	grade after rework	bare modules
A	A-	7
	B-	0
	C-	0
B	A-	6
	B-	2
	C-	1
C	A-	63
	B-	2
	C-	6

Further, it is important to identify the rework reasons to reveal potential risks and to guarantee a successful production. Therefore, it is necessary to verify if the rework was caused mostly by a single failure mode related to a certain production step.

Figure 6.5 gives a detailed overview of the reasons for all 110 replaced ROCs. Most of the ROCs reworked due to mechanical damage can be attributed to the two bare modules introduced in figure 6.4 with five and six damaged ROCs, respectively. In addition, there are four main causes whereof three are related to the number of dead channels. Rework caused by defective pixels or broken bump bonds are treated equally as both affect the bare module grade via the same criterion. The third rework reason which is also related to dead pixels are one or more dead double columns. Already a single dead double column would result in a grade C bare module although one double column contains only 160 pixels, which still would be grade B. However, the CMS pixel collaboration decided to reject bare modules with such ROCs due to the local concentration of dead pixels. This had no impact on the KIT rework process since such ROCs were already replaced from the start of the bare module production. The fourth major contribution is caused by an increased digital current ($I_{\text{dig}} > 65 \text{ mA}$) of the readout chips failing the digital current criterion described in section 5.3.2. Smaller contributions causing a rework

¹ As announced in section 5.3.2 all reworked bare modules are labeled with a minus sign.

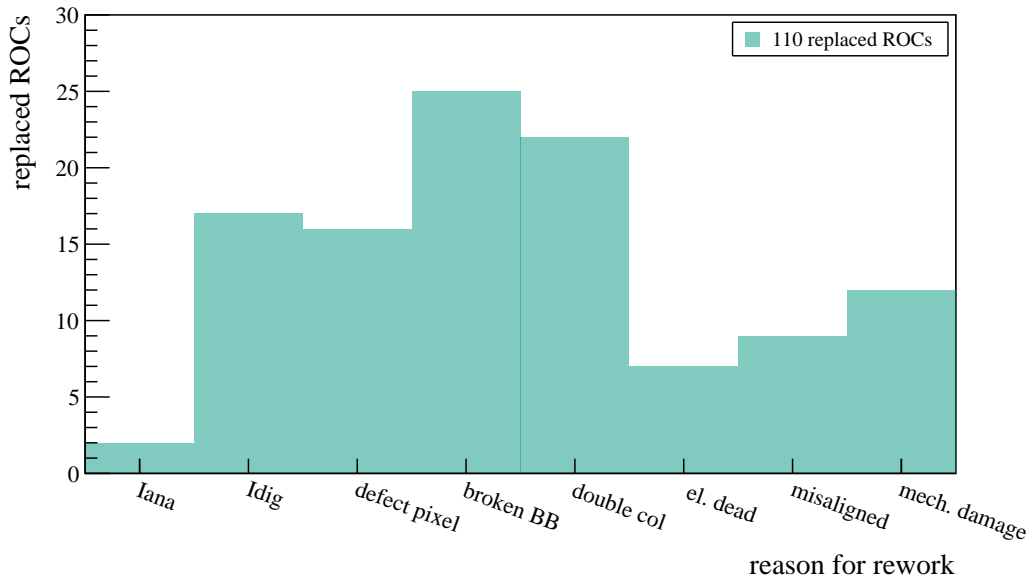


Figure 6.5: Number of replaced readout chips as a function of the rework reason. I_{dig} and I_{ana} correspond to the digital and analog currents of the ROC. The abbreviation el. dead refers to electrically dead ROCs. Mechanical damage is mostly related to two bare modules damaged during bonding. The main causes are broken bump bonds (BB), defective pixels, dead double columns and increased digital current. ROC misalignments are created by rare failures of the bonding machine.

came from electrically dead ROCs, defective analog voltage circuits and alignment problems. Alignment problems are caused by rarely occurring bonding failures such that affected ROCs are either rotated or shifted with respect to the sensor. Typically the misalignment was easily identified by eye and additionally the bump bond test on these ROCs confirmed that most bump bonds were not connected. The barely existing connection to the sensor allowed to remove these ROCs easily.

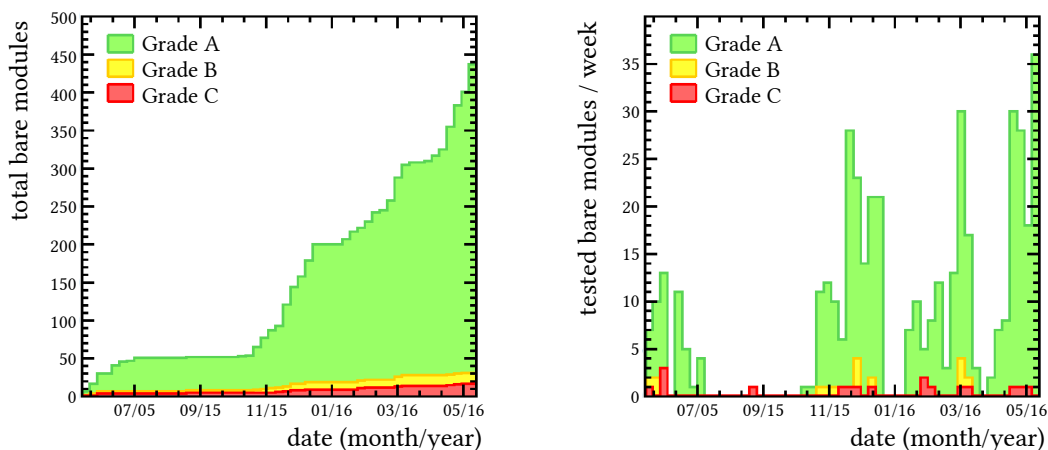
Additional information about the statistics on the replaced readout chips can be found in appendix A.

As the rework process has been triggered by multiple different reasons it is very unlikely that a single production step is responsible. This indicates that all bare module production steps were well controlled, which is further supported by the overall bare module yield presented in the last section of this chapter.

6.2.4 BARE MODULE YIELD

The most important parameter is the yield of working bare modules. Hence, this section introduces the bare module yields as a function of time and the overall yield of the entire bare module production.

In the bare module production which took roughly a year, 437 bare modules were produced and qualified. Figure 6.6 (a) shows the accumulated number of tested bare modules. The grades are illustrated with color, whereof grade A (green) and B (yellow) proceed in the module production chain while grade C (red) bare modules were rejected. The flat trend at the beginning of the production corresponds to a readout chip shortage caused by the vendor manufacturing the ROCs as well as by the company responsible for the bumping and cutting



(a) Cumulative number of tested bare modules as a function of time. The stagnation of tested bare modules in the beginning was caused by a shortage of ROCs. The strong increase of grade A bare modules together with the very low number of B or C graded bare modules confirm the excellent production quality.

(b) Bare modules qualified per week. The first gap when no bare modules were tested corresponds to the ROC shortage, the second to holidays at the turn of the year and the third to a brief sensor shortage.

Figure 6.6: Accumulated number of tested bare modules and bare module qualification rate per week [Col16].

of the ROC wafers. Two additional but smaller steps in the curve are related to the production and qualification stop during the Christmas break 2015/16 and a temporary shortage of sensors close to the end of the production. The disproportionately high increase of grade A bare modules with respect to grade B and C bare modules illustrates the constantly improving bare module production due to measures like the pretest modules. Additionally, the ratios of the colored areas illustrate the dominating fraction of grade A bare modules.

Figure 6.6 (b) gives the weekly bare module qualification rate for the same period. A throughput of up to 36 tested bare modules per week was achieved, which is nearly twice the proposed value of 20 as described in the original production schedule. This confirms that the bare module schedule was reasonably designed and that the production and qualification was well controlled. In addition, this high testing throughput allowed to follow the bare module production without creating a large stock of untested bare modules. This is desirable to be able to identify potential process-related bare module defects without creating a large backlog suffering from the same defect. Due to the high throughput the total number of tested bare modules is also a good progress indicator for the bare module production.

Figure 6.7 shows the overall bare module yield. Out of 437 produced and qualified bare modules 406 are graded A or A- which corresponds to 92.9%. Further, there are 14 grade B and B- bare modules (3.2%) and only 17 rejected grade C and C- bare modules which represent less than 3.9%. This means that in total 420 bare modules – more than 96.1% – are qualified for the next production step.

The major part of the grade B and grade C bare modules is caused by IV-curves corresponding to leakage currents higher than $2\ \mu\text{A}$ at 150 V or ratios between 150 V and 100 V higher than 2. Only in very few cases too many dead pixels are the reason for grade B or C while mechanical damage causing a grade C is an exception.

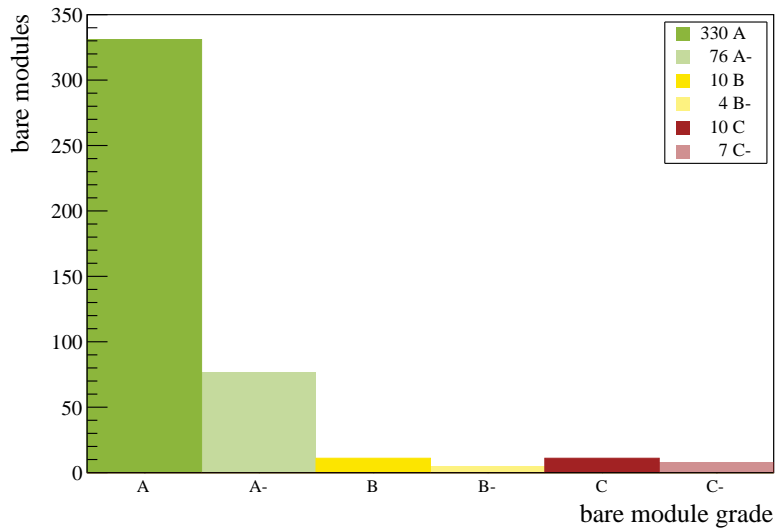


Figure 6.7: Yield of the KIT bare module production. In total, 437 bare modules were produced at KIT whereof 406 are grade A/A- corresponding to approximately 92.9%. Only a very small fraction of 17 grade C/C- bare modules which represent 3.9% of the entire bare module production had to be rejected during the bare module qualification.

About 7300 ROCs have been available for the bare module production and roughly 7000 (nearly 96%) of them were turned into bare modules. The remaining 300 ROCs can be attributed to the rework (more than 100), the bonding quality control (cross section of single assemblies) and the preproduction. At the end of the KIT bare module production only a handful of good sensors were left while there were no more good ROCs. Hence, these sensors were sent to the DESY / University of Hamburg production center as they had a small ROC surplus.

All results presented in this section confirm the excellent performance of the KIT bare module production. This includes the component selection, the quality control performed on the BMPS and the reflow process as well as the pretest module approach and the rework procedure.

Great things in business are never done by one person. They're done by a team of people.

Steve Jobs

7

MODULE X-RAY TESTING AND QUALIFICATION

In science, just like in any kind of business, big projects can only be mastered by a team of people. In case of the module production for the CMS Phase I pixel detector the team is formed by the participating institutes. The KIT module production, covered by ETP and IPE, took slightly longer than one year from May 2015 to June 2016. Out of 420 good KIT bare modules 416 were processed further and 409 were turned into modules. This represents more than 98.3 % of the available 416 bare modules. The remaining four bare modules were sent to the Swiss production center due to the lack of HDIs which passed the quality criteria.

After the modules are completed, each of them has to undergo a detailed qualification sequence to guarantee that only the best modules are mounted in the detector. At KIT the qualification is split into two parts. In the first part, an electrical calibration is performed at $+17^{\circ}\text{C}$ and -20°C verifying the functionality of the ROCs and measuring the IV-curves of the sensors for both temperatures.

In the second part, the modules are tested with the help of X-rays to determine the number of dead channels. These results are an excellent opportunity to cross-check the results of the bump bonding test on the bare modules.

This chapter introduces the results of the second qualification step at KIT including a comparison with bare modules. At the end, the final grades after the qualification at RWTH Aachen and the reception test at ETH Zürich are presented.

7.1 LEAKAGE CURRENT RESULTS

The leakage current is the most frequently tested property during the production. It allows to monitor the sensor quality over the entire production as any kind of damage would very likely lead to an increased leakage current.

7.1.1 LEAKAGE CURRENTS MEASURED DURING THE X-RAY TESTS

The X-ray setup, which was already introduced in section 5.12, is equipped with a temperature stabilized cold chuck. The selected temperature for the X-ray tests is $+17^{\circ}\text{C}$. Additionally to each X-ray measurement, the leakage current at 150 V is determined as this measurement can be done in parallel to the X-ray test.

Figure 7.1 shows the measured leakage current distribution of 368 out of 409 produced modules. Only 16 modules corresponding to slightly more than 4.3 % of the modules tested in the X-ray setup have leakage currents higher than $2\ \mu\text{A}$. 352 modules have leakage currents lower than $2\ \mu\text{A}$ and hence, pass the grade A leakage current criterion. Those 95.7 % of the modules have an average leakage current of $(0.39 \pm 0.22)\ \mu\text{A}$. Out of the 41 modules which could not be tested in the X-ray setup, 27 were shipped directly to RWTH Aachen due to time constraints.

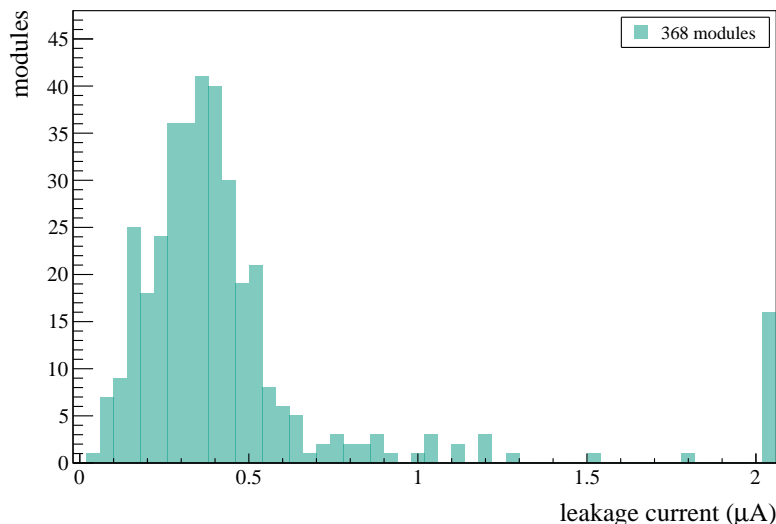


Figure 7.1: Module leakage current distribution obtained during the X-ray test. Out of 409 produced modules at KIT 368 were tested in the X-ray setup. Only 16 modules have leakage currents higher than $2\ \mu\text{A}$ which are represented by the last bin. The largest fraction of the distribution, which are 352 modules have leakage currents less than $2\ \mu\text{A}$ with an average of $0.39\ \mu\text{A}$.

The remaining 14 modules did not pass the electrical test prior to the X-ray test, hence, it was skipped to save time.

Although the shown leakage current distribution only represents a single grading criterion, it indicates the good quality of the produced modules.

7.1.2 COMPARISON WITH BARE MODULE LEAKAGE CURRENTS

A comparison of the leakage currents measured during the X-ray test with the ones obtained during the bare module test is an opportunity to validate if the sensor quality changed for instance due to potential mechanical damage caused by the assembly process.

However, it has to be taken into account that the bare module probe station is not equipped with a cooling system providing a constant temperature for all measurements. Therefore, the leakage current, which is exponentially temperature dependent has to be scaled according to equation 3.3. Only then the leakage currents of the X-ray test and the bare module test are comparable. To scale the leakage current the temperature during the test has to be known. In case of the bare module testing the temperature was monitored via a sensor inside the BMPS. The sensor was simply placed inside the BMPS volume as it could not be attached to the bare module chuck (made from polytetrafluoroethylene) for practical reasons. Hence, the measured temperature is just a rough estimation of the actual sensor temperature and the leakage current comparison only provides a qualitative description.

The average temperature during the bare module tests was $25.5\ ^\circ\text{C}$, which means that the measured leakage currents should be about twice as high as the leakage currents measured at $+17\ ^\circ\text{C}$ during the X-ray tests. Indeed the average leakage current of the grade A bare modules is about $0.90\ \mu\text{A}$ (as presented in section 6.2) while it is $0.39\ \mu\text{A}$ for the grade A modules measured during the X-rays tests as introduced above.

Figure 7.2 shows the correlation between the module leakage current obtained at $+17\ ^\circ\text{C}$ and the bare module leakage current scaled to the same temperature. It contains the values of 348 modules out of the 352 which passed the grade A leakage current criterion of the X-ray

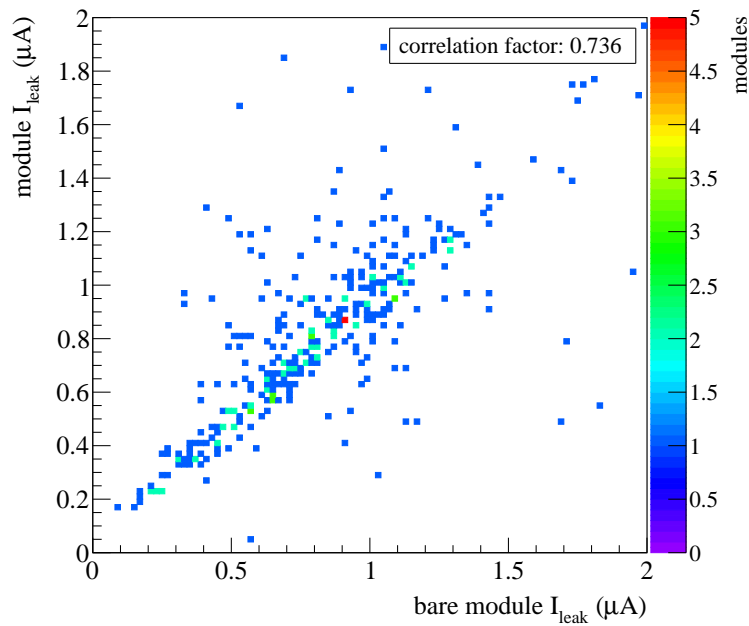


Figure 7.2: Correlation between the leakage currents obtained from the X-ray and bare modules tests. Leakage currents from the X-ray tests are measured at $+17^{\circ}C$. The bare module leakage currents were determined at room temperature and scaled to be comparable. A correlation is visible indicating that the sensor quality did not change. Most outliers are probably a consequence of the bare module temperature used for the current scaling, which is only roughly measured.

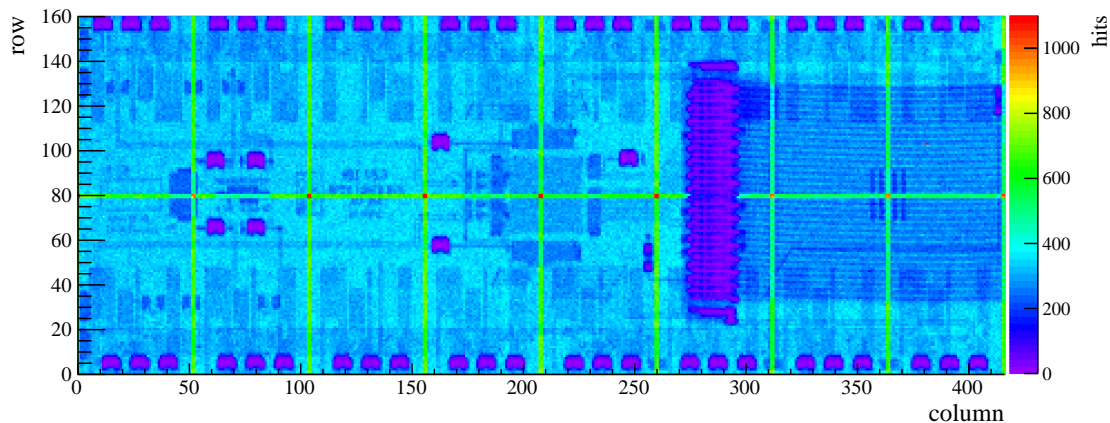
test. The remaining four modules are not included as the corresponding bare module leakage currents were higher than $2 \mu A$. The correlation confirms that the silicon sensor quality of most modules did not change during the production. Despite of some outliers, the correlation coefficient is still 0.74. However, a deviation of few values from the correlation curve is to some extent expected as the determination of the sensor temperature, which was used for the leakage current scaling, is only a rough estimation limited by the setup. Nevertheless, the results confirm the good material selection and appropriately designed production steps protecting the sensors against mechanical damage.

7.2 DEFECTIVE PIXELS

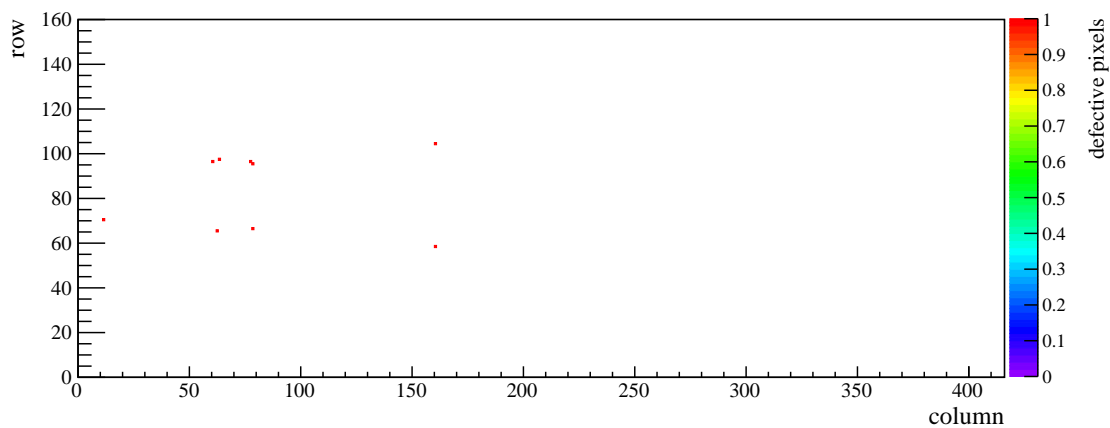
The number of working channels is one of the most important properties of the modules. Therefore, it is frequently tested during the module production starting on the bare modules and repeated during several module qualification steps. Aside from the bump bond and pixel alive tests, the measurements exploiting X-rays are an excellent option to determine the number of dead pixels.

7.2.1 DEFECTIVE PIXELS OBTAINED FROM X-RAY TESTS

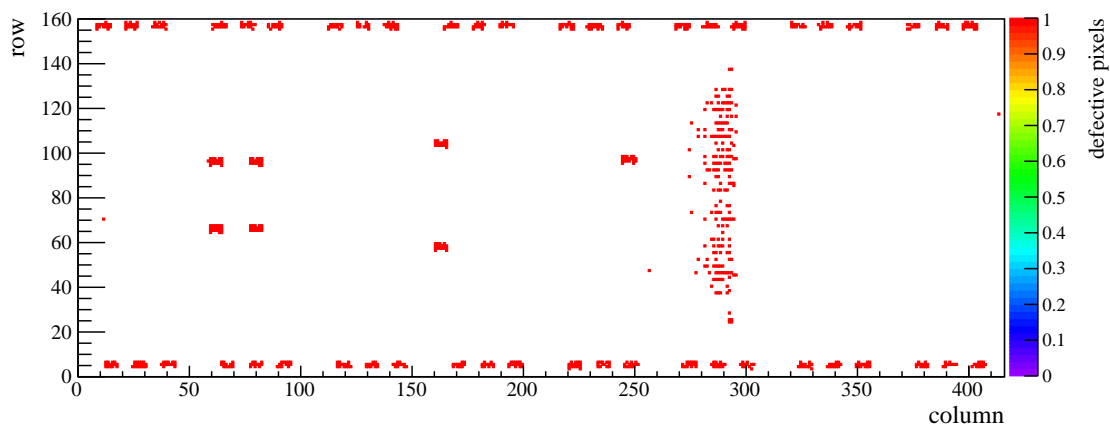
Since the measurements in the X-ray setup rely on photons depositing their energy inside the sensor, the accumulated statistics is very important to guarantee that each working pixel has sufficient entries. Especially the surface mounted capacitors and the soldered connector on top of the HDI shield the sensor from most photons and decrease the number of hits in the pixels below. Therefore, the measurement duration should be as long as required but at the same



(a) Module hit map obtained from an X-ray measurement. The segmentation of the 16 ROCs is recognizable by the increased number of hits due to larger pixels at the ROC edges (green lines). In addition, it is clearly visible that the number of hits for pixels below surface mounted HDIs components (capacitors and connector) is significantly reduced.



(b) Module map showing the dead pixel locations determined for an X-ray cut of 5. The number of wrongly identified pixels is very low, in fact only eight of 66,560 pixels have a false-positive result (0.012%). The single dead pixel at column 10 and row 70 is identified correctly (only recognizable with a zoom on figure 7.3 (a)).



(c) Module map showing the dead pixel locations determined for an X-ray cut of 20. The number of wrongly identified pixels below the capacitors and the connector is significantly increased. Already more than 1000 pixels show a false-positive result (1.5%).

Figure 7.3: Results from an X-ray measurement. Figure (a) shows a module hit map obtained from an X-ray test. Figures (b) and (c) are the corresponding dead pixel maps determined for X-ray cuts five (b) and 20 (c).

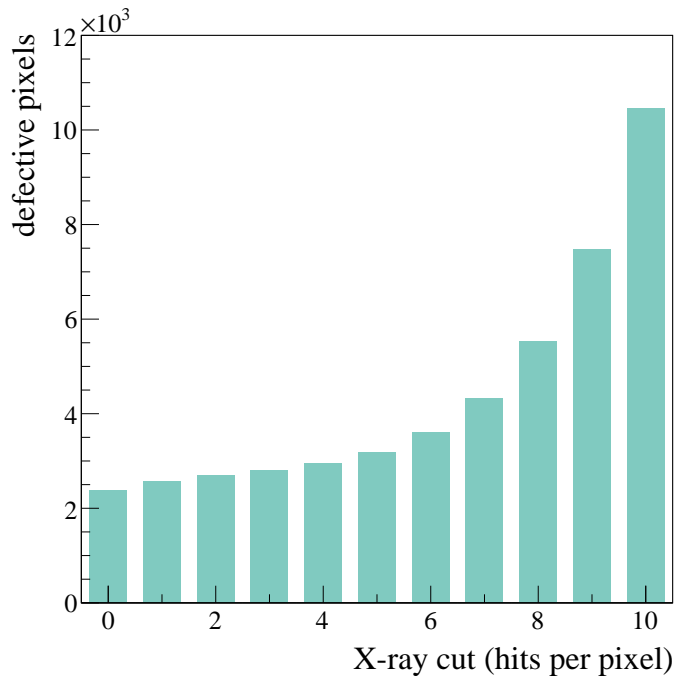


Figure 7.4: Total number of dead pixels for different X-ray cuts. For all modules tested in the X-ray setup the total number of dead pixels is presented as a function of the X-ray cut. The strong increase of dead pixels above an X-ray cut of six is caused by the relatively small number of hits in pixels below the surface mounted components. Therefore, the standard X-ray cut of five is a conservative selection barely suffering from statistical effects.

time as short as possible to stay within the time constraints of the production. This results in a measurement time of 90 minutes with two modules being illuminated simultaneously. A further increase of the duration is not possible as the X-ray setup is also occupied for module calibration measurements which are presented in [Tas16]. Actually, some modules had to be shipped to RWTH Aachen without being tested in the KIT X-ray setup for lack of time.

In the context of the production it is fine to skip some X-ray tests at KIT, as the full qualification is performed in Aachen while the number of modules tested at KIT is still sufficiently high to provide fast feedback about their quality. This feedback is necessary to monitor the bump bond quality throughout the entire production and to optimize the bump bond test which was particularly important during the early production phase.

The X-ray cut which distinguishes between working and dead pixels needs to be reliable and has to be tuned carefully. When the cut is set to zero hits per pixel some not correctly working channels might stay unidentified if they are not completely dead. If the cut is too high, pixels especially below the surface mounted HDI components could wrongly be considered as dead due to a small number of hits. Figure 7.3 shows a module hit map obtained from an X-ray measurement and two module maps showing the dead pixels determined from X-ray cuts five and 20 (where all pixels with less or equal than five and 20 entries respectively, are declared dead).

The X-ray module hit map in figure 7.3 (a) clearly shows the reduced number of hits below the capacitors and the connector mounted on top of the HDI (all these components are recognizable on the module presented in figure 5.10). Indeed only about ten hits are detected in these areas while the average number of hits per pixel is about 400 which is already more than one order of magnitude higher. Figure 7.3 (b) presents the locations of the dead pixels determined from an X-ray cut of five. Only eight of 66,560 pixels have a false-positive result which

corresponds to 0.012%. In addition, the module has a single dead pixel at column 10 and row 70 which was correctly identified but is only recognizable with a zoom on figure 7.3 (a). The third figure 7.3 (c) shows the dead pixel locations for an X-ray cut of 20. The number of wrongly identified pixels is significantly higher caused by the small number of hits below the surface mounted components. Comparing the red dots with the small statistics areas of the X-ray module hit map confirms that they match perfectly. Altogether more than 1000 pixels have a false-positive result at this cut which already represents 1.5% of all pixels on a module.

As indicated by the presented module maps the X-ray cut has to be selected carefully to make a reliable statement on the number of working channels. Hence, the total number of dead pixels for all X-ray tested modules is presented in figure 7.4 as a function of the applied X-ray cut to obtain a cut which is conservative but at the same time not overestimating. The graph shows a clear increase of dead pixels starting from an X-ray cut of six. Obviously the small number of hits obtained in certain areas of the modules (as described above) starts to dominate the defective pixel results for those cuts. For cuts between zero and five hits per pixel the number of dead channels is quite stable. The slow increase in this region is caused by some working pixels with a small number of hits but also from defective pixels which respond very rarely. Therefore, the standard X-ray cut is set to five, as it is a conservative selection which barely suffers from pixels with a small number of hits. In the further course, the presented number of defective pixels determined from the X-ray test always refers to a cut of five as long as not stated differently.

Figure 7.5 shows an overlay map of all dead channels from the modules tested in the X-ray setup. The map reveals several remarkable areas caused by various reasons. In the lower part between columns 220 and 310 the silhouettes of at least six capacitors are indicated. In the upper part there are no recognizable silhouettes probably due to slightly higher statistics related to the orientation of the modules in the X-ray setup. The corresponding pixels (at least most of them) are marked defective because of a small number of hits below the surface mounted capacitors, caused by too low particle rates and measurements times respectively. There are additional locations also related to capacitors even though they are less distinct, for example four spots around column 60 and 80 at row 65 and 95. The false-positive declaration of single pixels is to some extent expected and owes the conservative X-ray cut selection. Nevertheless, the number of wrongly identified dead channels is relatively low as confirmed by the small number of entries related to those areas.

Aside from that there are two vertical bars caused by two dead double columns around column numbers 165 and 260. These dead double columns had to be intact during the bare module qualification and the electrical module test. Otherwise the bare module would have been reworked or rejected as grade C material. This illustrates that a frequent retesting of the module properties is necessary during production and qualification as some of them become grade C and should not be installed in the detector.

A further prominent feature is located around column 310 and between rows 110 and 150. There is a straight line visible which in fact was already observed during the bare module qualification. Already after the bare module test a scratch across the sensor UBM was revealed with the help of pictures from the sensor inspection. Therefore, it was expected to identify those dead pixels also on the module where the relatively small number of 20 affected pixels is still fine. In addition, the rework of such a ROC would not have been promising as explained in section 6.2.3. The overlay map also shows that some areas are more susceptible in terms of defective pixels. At the lower edge starting from column 0 to 100 and from column 160 to 200 as well as in the top right corner an increased number of dead channels is visible. In general, edges and especially corners are more prone to dead pixels as their probability to experience mechanical stress during production, transport and handling is higher.

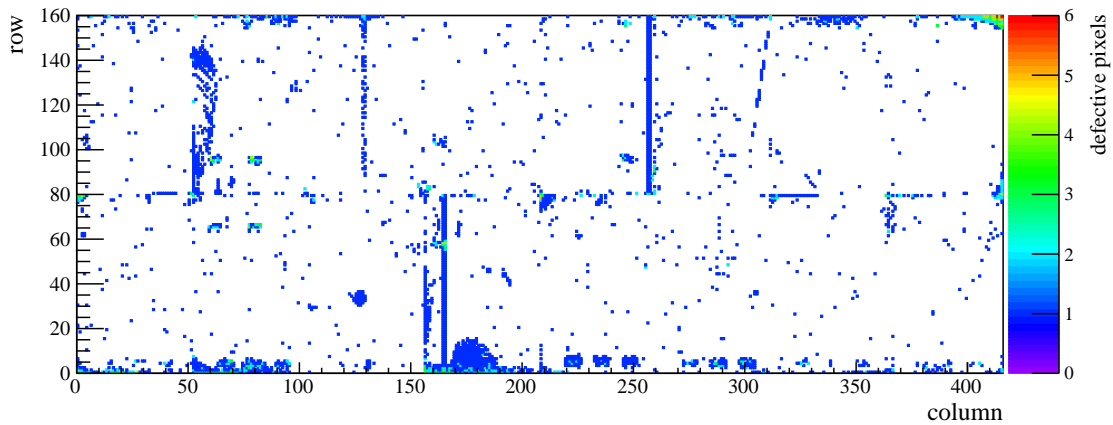


Figure 7.5: Overlay map of all defective pixels determined from the X-ray tests. In the lower part the silhouettes of some capacitors are visible formed by pixels marked dead due to a small number of hits. In the upper part no silhouettes are visible probably due to slightly higher statistics related to the orientation of the modules in the X-ray setup. Additionally, two dead double columns are easy recognizable. Around column 310 and rows 110 to 150 a scratch across the sensor UBM caused several defective channels in a straight line. Some vulnerable areas are visible at the lower edge and the top right corner.

Last to mention are two large areas, one located at columns 50 to 65 and rows 80 to 145 and the second at columns 165 to 190 and rows 0 to 20. These areas are related to only two ROCs on different modules and are probably caused by problematic sensor UBM.

Nevertheless, the overlay map is a sign of the excellent quality which is also indicated by the scaling of the z-axis. Even though one part of modules is systematically affected by dead pixels (see top right corner) its effect is very small as no pixel position was defective more than six times for all 368 tested modules.

7.2.2 COMPARISON WITH DEFECTIVE PIXELS ON THE BARE MODULE

The X-ray measurements, where photons generate signals inside the sensor, allow to cross-check the bare module test results, which rely on the internal calibration circuit. For this purpose the number of correlated dead channels, referring to pixels which were identified defective in the bare module test as well as in the module X-ray test, is discussed below.

Determining the number of correlated dead pixels between bare modules and modules is an additional opportunity to validate the X-ray cuts. Figure 7.6 gives the total number of correlated dead pixels as a function of the applied X-ray cut for all available bare module/module pairs. The number of correlated defective pixels clearly saturates for increasing X-ray cuts. This indicates that there is no benefit above a certain cut while the standard X-ray cut of five already exploits the saturation.

Altogether the bare module qualification identified 1442 defective pixels referring to the 368 bare modules of figure 7.6. The X-ray measurements of the corresponding modules revealed 2371 defective pixels at cut zero with 830 correlated dead pixels and 3191 dead pixels at cut five whereof 881 are correlated. For cut ten already 10,460 pixels are declared dead while the correlated number of 885 dead pixels stays more or less the same.

While the number of correlated pixels saturates early as presented above, the total number of dead pixels determined from the X-ray tests increases and is more than one order of magnitude

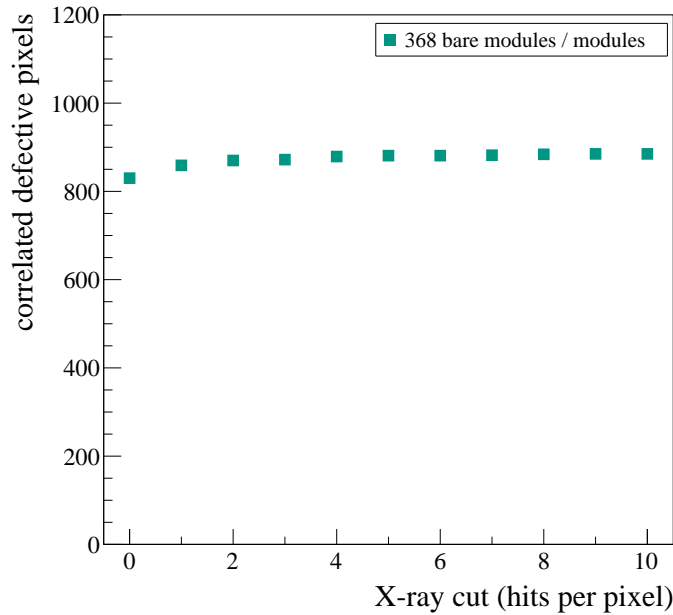


Figure 7.6: Total number of correlated defective pixels between bare modules and modules as a function of the X-ray cut. The number of correlated pixels saturates for increasing X-ray cuts. As desired, this is already the case at the standard X-ray cut of 5.

higher at an X-ray cut of ten hits (with respect to the number of correlated dead pixels). More details about correlated and uncorrelated dead pixels are available in appendix B.

The absolute number of dead channels determined from the X-ray tests at cut five is about 2.2 times larger compared to the bare module results. This might be caused either by a small number of hits (as described before), the different measurement mechanism relying on photons instead of the internal calibration circuit or by an actually increased number of defective channels. To investigate this further more information about dead pixels per module and bare module is required as introduced below.

Figure 7.7 shows a correlation plot between bare modules and modules regarding the number of dead pixels per (bare) module. Only the 351 pairs are included where the bare modules as well as the modules have 41 or fewer dead channels. As most of them only have a few or even zero dead pixels the major part clusters in the bottom left region of the graph providing a good correlation. The color scaling shows that more than 60 pairs have zero defective pixels. Only a small fraction of about 10% of the entries is not clustered in the bottom left region. Instead they are less correlated due to several outliers with a higher number of dead pixels on the modules. Nevertheless, the major part of the bare modules/module pairs is well correlated as confirmed by the correlation coefficient of 0.56. In addition, this shows that bare modules and modules typically have similar numbers of dead channels. However, this implies that the 351 (out of 368) available bare modules/module pairs in figure 7.7 cannot explain the discrepancy between 1442 dead pixels determined from the bare module test and 3191 dead pixels identified in the X-ray test.

Therefore, the remaining 17 modules which are not included in the figure have to be responsible for the difference. In fact, 1783 out of 3191 dead pixels identified in the X-ray test are related to those 17 modules only. Moreover, some of those 17 modules can be assigned to the features described in the overlay map presented in figure 7.5 like the two dead double columns or large area defects. Considering only the 351 pairs from figure 7.7 results in 1154 defective channels from the bare module test and 1408 from the X-ray measurements.

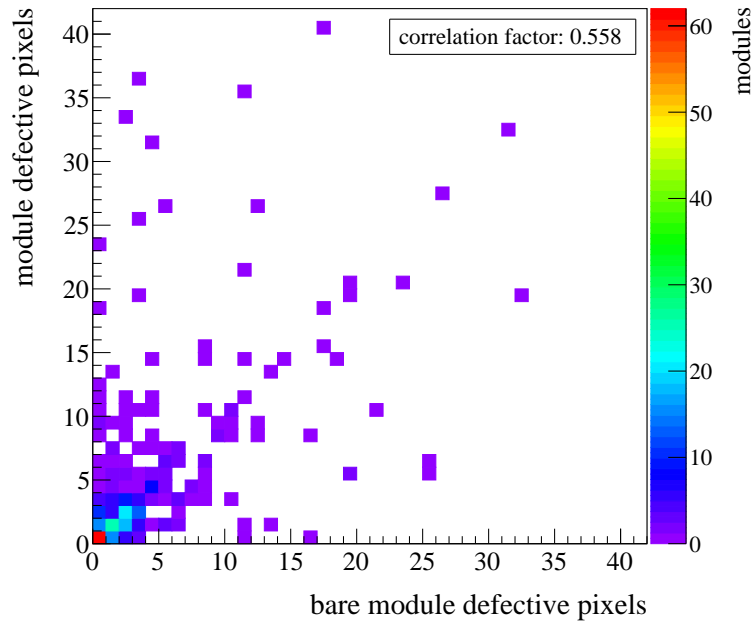


Figure 7.7: Correlation of defective pixels between bare modules and modules. The number of defective pixels per module is presented as a function of the number of defective pixels per bare module. As most bare modules and modules only have a few or no dead pixels the major part of the entries clusters in the bottom left part. The correlation coefficient is 0.56 approving a correlation with some outliers.

The given results approve that the bare module qualification and the X-ray test agree sufficiently for the purpose of quality control. This includes the determination of the defective pixels as well as the leakage current measurements at $+17^\circ\text{C}$.

7.3 MODULE YIELD

The KIT module production for the CMS Phase I pixel detector was finished in June 2016 when the last of the 409 produced modules were sent to RWTH Aachen for full qualification. Afterwards the modules were shipped to ETH Zürich where a thin Kapton[®] protection cap was applied and short reception tests were performed before they were mounted onto the ultra-lightweight support structure at PSI.

All modules had to undergo several tests during the production and qualification each providing a single independent grade. The final module grade, which decides if a module is installed in the detector or not is based on the full qualification at RWTH Aachen as well as the reception tests at ETH Zürich and is determined from the worst of the corresponding single grades.

Before the results are presented, the effect with the largest impact on the final grade is introduced. A large fraction of modules were graded B only due to the current-voltage characteristic at -20°C . According to equation 3.3 a scaling factor of approximately 40 between $+17^\circ\text{C}$ and -20°C is expected. However, most modules do not show this behavior and have leakage currents which are not as small as expected at -20°C . Since measurements at -20°C are only performed on complete modules, this could not be discovered during bare module production or in the bare sensor tests. Identifying the unexpected scaling earlier would have been without

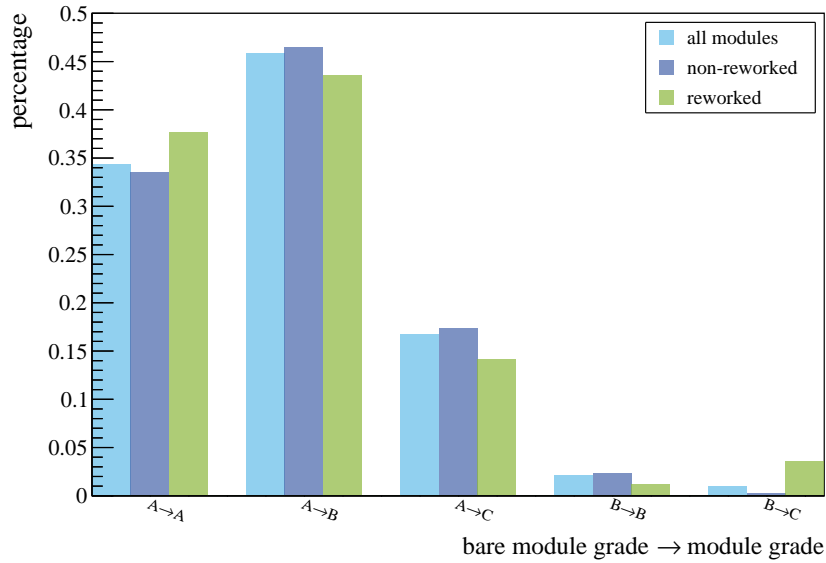


Figure 7.8: Comparison between bare module and module grades. The comparison is given for all modules (light blue), non-reworked modules (dark blue) and reworked modules (green). According to the chart, there is no considerable difference between the reworked and non-reworked modules. A very high fraction of grade A bare modules became grade B modules due to unexpected leakage current scaling factors.

consequences. Since this property is a sensor feature, which was confirmed by all production centers, it would not have been possible to tune a production step in order to adjust the scaling factor. Nevertheless, this behavior does not present a problem for the following reasons. First of all, it is not a sensor bulk defect but instead surface currents not scaling according to equation 3.3 contribute to the leakage current and lead to higher than expected currents at -20°C . Second, the leakage currents of unirradiated modules are too small to be relevant as they would never exceed the limits of the power supplies. For irradiated modules however, where the leakage currents increase significantly due to the generated defects, the currents are getting relevant. Hence, the leakage current has to be kept as low as possible by cooling the modules. Aside from that, the leakage current is described correctly by equation 3.3 as soon as the current is dominated by bulk defects. As a consequence, the estimated currents will not exceed the power supply limitations. More information on the leakage currents of irradiated modules is given in chapter 8.

Figure 7.8 illustrates how the grades have developed between bare module qualification and final module grading. The light blue bars correspond to all modules, the dark blue ones to the non-reworked and the green bars to the reworked modules. A very prominent feature of the chart is the high fraction of grade A bare modules which became grade B modules. Nearly all of them were graded B due to the unexpected leakage current scaling described above. In addition, about 15 % of the modules became grade C, which is a decent result. The figure also shows that the reworked modules behave almost exactly like the non-reworked ones. This is a good sign for the rework process and an indication that the reworked modules will perform like the non-reworked modules during the lifetime of the Phase I pixel detector.

Regarding the grade C modules, there are several causes. A large fraction is related to bad HDIs with wire bond pads not bondable at all. Additional HDIs had broken solder connections at the connector on top of the HDI due to bad soldering. Since these problems could not be identified during the HDI test, the affected modules are lost as HDIs are not removable. However, HDIs with bad wire bond pads (probably due to wrong material composition and

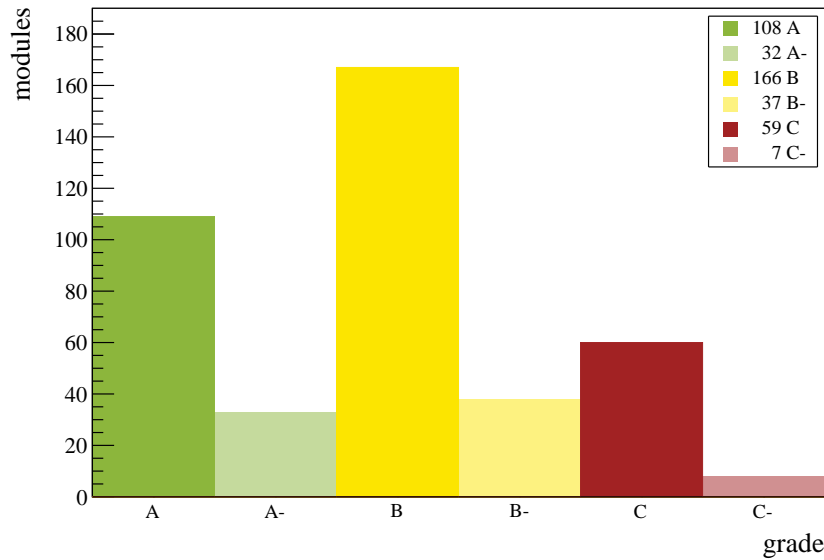


Figure 7.9: Final grades of the modules produced at KIT. Altogether 140 modules were graded A (green) and 203 were graded B (yellow) resulting in 343 modules ready to be installed inside CMS. Most grade B modules were caused by an unexpected leakage current behavior at -20°C which is still fine. Only 16.1 % are grade C (red) and had to be rejected, mostly due to problems related to the HDIs or problematic ROCs.

pollution) and weak solder connections should never have passed the quality control at High-tec MC AG. Further reasons for grade C modules are attributed to ROC problems, like dead or inefficient double columns as presented in the overlay map in figure 7.5 or electrically dead ROCs. In very rare cases modules had to be rejected because of mechanical damages.

The final grades are determined after the qualification at RWTH Aachen and the reception tests at ETH Zürich. The results for all modules produced at KIT are presented in figure 7.9. Out of 409 produced and qualified modules 140 are graded A and 203 are graded B. This results in 343 modules which are qualified to be installed in CMS and represent 83.9 % of all KIT modules. The suggested number of good modules was 310 consisting of 256 modules corresponding to half of layer 4 and 20 % spares. In the end 34 % spares were produced confirming the excellent quality of the module production at KIT.

The KIT module production for the CMS Phase I pixel detector was a great success which was shown by a variety of results presented in chapters 6 and 7. In addition, the excellent quality of the KIT modules is confirmed by the overproportionally high number of 323 mounted modules (the target quantity was 256 mounted modules). Thereof 193 modules are mounted on barrel layer 3 and the remaining 130 are mounted on barrel layer 4. Together with the modules from all production centers the new pixel detector is a good basis for the measurements and physics analysis of the next years.

Part III

PERFORMANCE STUDY FOR THE PHASE I UPGRADE OF
THE CMS PIXEL DETECTOR

There is nothing more exciting than having a life devoted to fundamental knowledge and to contributing to advance the borders of knowledge.

Fabiola Gianotti

8

LABORATORY MEASUREMENTS

While the previous chapters addressed the production of the CMS Phase I pixel detector, the following ones will focus on the expected detector performance and how it may develop during the coming years of operation. Only in-depth knowledge of the detector performance allows to exploit its full potential and to obtain the best physics results. This includes basic properties like the current-voltage characteristics but also high-level quantities such as detector resolution and hit efficiency. First measurements on the detector performance relying on precursor versions of the **ReadOut Chip (ROC)** were carried out prior to the production, as described in [EM13], [Ren15] or [Kop15].

To determine the actual detector performance it is necessary to perform studies based on the final ROC version PSI46digV2.1-respin. Basic measurements similar to the ones relying on the precursor ROC versions were already carried out prior to the module production. Nevertheless, a more detailed study regarding the performance especially with respect to accumulating radiation damage has to be carried out. Hence, it is necessary to verify if and to which extent the detector performance will deteriorate. A special focus lies on the ROC and the determination of reliable ROC settings to mitigate the impact of radiation damage.

For that reason the present thesis covers, aside from the production, studies on the pixel detector performance in the following two chapters. The material from the production allows to investigate the performance of pixel detector modules for layer 2 to 4. Therefore, the selected radiation levels are the expected accumulated radiation doses of modules on layers 2 to 4 at the end of their operating time. These estimated radiation doses are calculated with the Radiation Simulation Plotting tool from the CMS BRIL group [GT17], which relies on FLUKA a fully integrated particle physics Monte Carlo simulation package [BCC⁺14].

All measurements introduced within this chapter are performed at KIT laboratories. This includes measurements with a module from KIT production which was rejected due to a non-responding ROC. It is not possible to use one of the fully working modules for testing purposes as they are required for the detector and as spares. Nevertheless, the available module allows to study the detector performance under realistic conditions.

In addition, **Single Chip Assemblies**¹ (SCA) are used during this study, as they have a good availability and enable additional measurements which cannot be carried out on modules without major effort (like the test beam study introduced in chapter 9).

8.1 SAMPLES

Since the module design was already introduced in figure 4.4 only the SCAs are described below. The SCAs cannot be connected directly via a cable due to the lack of a connector. Hence, the SCA is placed on a **Printed Circuit Board (PCB)** as it is presented in figure 8.1.

¹ Single chip assembly: a device only consisting of a single ROC connected to a smaller version of the production sensor which exactly matches single ROCs.

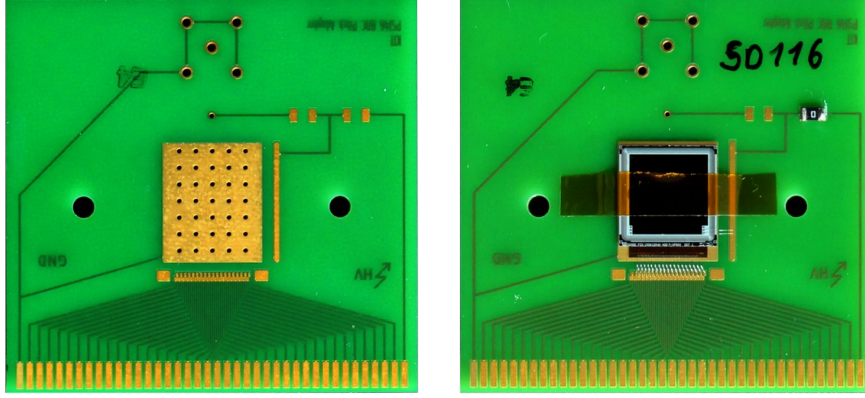


Figure 8.1: Custom designed PCB used to mount the single chip assemblies. In the left picture a bare PCB is shown with the fanned out conducting paths in the bottom region. The metal surface in the center of the PCB is connected by metal-coated holes to a metal layer on the backside providing good cooling contact. In the right picture an SCA is placed on the PCB and fixed by Kapton[®] tape. The electrical connection to the ROC and sensor is established via wire bonds. A small 0Ω resistor below the internal denotation SD116 closes the high voltage line. In the top region a Lemo connector can be mounted to connect the bias voltage directly to the PCB instead of routing it via the DTB.

The PCB serves as a pitch adapter, fanning out the conducting paths and providing a connection to another adapter (called SCA adapter) which in turn is connected to the digital test board. In the center of the PCB front side a metallic surface is visible where the SCA is placed. Metal coated holes in this surface are connected to an additional metal layer on the backside used to cool the device (by attaching a cooling system to the backside metal). The SCAs are either glued on the PCB by a two component glue (Araldite[®] Rapid) or simply fixed by Kapton[®] tape with the sensor facing upwards and the ROC wire bond pads pointing to the bottom as shown in the right picture. Wire bonds establish the electrical connection between the ROC and the PCB. The sensor is connected via a few wire bonds to the bias voltage line of the PCB. A 0Ω resistor (black square, right PCB) closes the bias voltage line and routes the voltage either via the SCA adapter or to a Lemo connector which can be placed in the top region to bypass the high voltage directly to the PCB. In the given figure the 0Ω resistor is used to route the bias voltage via the SCA adapter. The label SD116 is the KIT-internal denotation of SCAs and corresponds to Single chip assembly with Digital ROC (SD) followed by a consecutive numbering.

For all samples investigated in the test beam an additional plastic cover is glued on the PCB protecting the SCA and the wire bonds. A list of all available SCAs is given in appendix C.

8.2 IRRADIATION

As mentioned in the beginning of this chapter some samples are irradiated to investigate the pixel detector performance for the entire operating time. The selected fluences for the samples are 1, 2 and $4e14 n_{eq}$ corresponding to the end of the operation fluence of layer 4, 3 and 2.

The irradiation of the module was executed in steps, according to the three values introduced above. In between, several measurements were performed. Additionally, there are 14 single chip assemblies, whereof 4 remained unirradiated, 3 were irradiated to 1 and $2e14 n_{eq}$ respectively, and 4 were irradiated to $4e14 n_{eq}$. This allows to have at least two backup SCAs for each irradiation step and even 3 for the highest dose. Keeping 4 unirradiated SCA allows to stay flexible, if further irradiations have to be carried out while at least one serves as reference

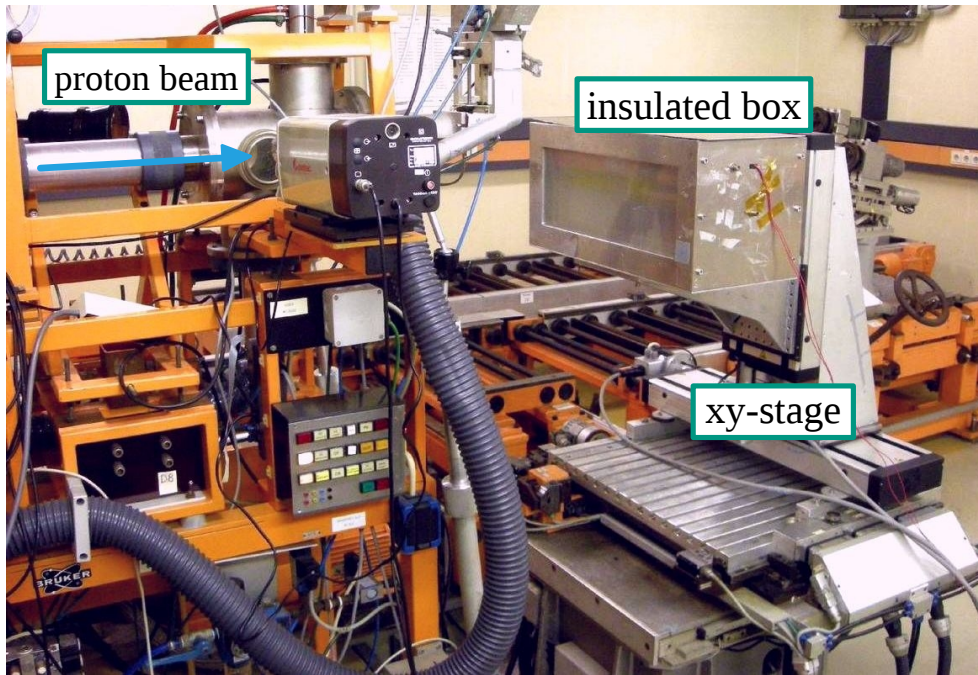


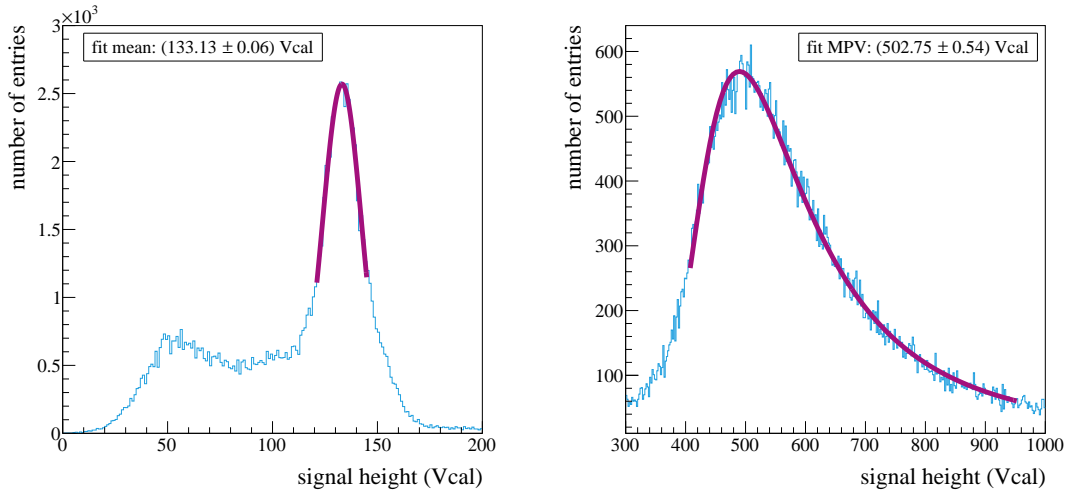
Figure 8.2: ETP irradiation setup at the Karlsruhe Kompaktzyklotron (KAZ) operated by Zyklotron AG. Protons with an energy of 23 MeV exit the beam pipe (recognizable in the top left part) and enter the cooling box (shown in the center region) via a window, made from two Kapton[®] foils. Inside the box the protons hit the samples and generate radiation damage. The box, which is cooled down to -30°C to avoid annealing, is mounted on an xy-stage to scan multiple samples [Die17].

device. A benefit of having SCAs with different irradiation doses is the possibility to repeat measurements at any time for each irradiation step. In case of the module only measurements after the last irradiation step of $4e14 n_{eq}$ can be repeated.

The irradiation is done at the Karlsruhe Kompaktzyklotron (KAZ) operated by the Zyklotron AG located at KIT Campus North. The KAZ is able to accelerate protons to energies between 15 MeV and 40 MeV at a beam current of up to $100 \mu\text{A}$. For the irradiation of silicon sensors the proton energy is limited to 23 MeV and the beam current to $2 \mu\text{A}$ to avoid annealing of sensor bulk defects (see section 3.3) due to heating by the proton beam. Figure 8.2 presents the ETP setup at the KAZ with the proton beam exiting the stainless steel beam pipe in the top left part. The samples are mounted on an aluminum frame inside a thermally insulated box (visible in the center of the picture) which is cooled down to -30°C to avoid annealing. The front side of the box consists of a large window made from two thin Kapton[®] foils to minimize the energy loss of the protons entering the box. As the beam spot only has a diameter of 4 mm to 8 mm, the entire box is attached to an xy-stage allowing to scan and irradiate multiple samples during a single run. Dosimetry measurements after the irradiation allow determination of the applied fluences with an uncertainty of 15%.

8.3 ENERGY SPECTRUM

In each laboratory measurement with characteristic X-ray photons or electrons from a ^{90}Sr source a distribution of the energy deposited by the particles is obtained. It shows the number of detected particles as a function of the measured signal height. Two typical spectra for characteristic X-ray photons and electrons from a ^{90}Sr source are shown in figure 8.3.



- (a) Measured signal height distribution obtained with characteristic X-ray photons emitted from a silver target. Aside from the Gaussian shaped part there is a large non-Gaussian region due to missing clustering. Hits corresponding to a two or more pixel cluster are treated as individual hits having smaller signals consequently. However, the Gaussian shaped region is large enough to apply a reliable fit, even without clustering as implied by the small fit uncertainty of the Gaussian mean.
- (b) Measured signal height distribution of electrons. The given Landau distribution contains only clusters of two or more pixels. One pixel clusters are excluded as they are mostly caused by photons from the ^{90}Sr decay and electrons mostly generate two or more pixel clusters. Therefore, offline clustering is mandatory to obtain reasonable results, although it is more time consuming. The Landau fit describes the distribution well providing a small uncertainty on the MPV.

Figure 8.3: Signal height distributions including Gaussian and Landau fit functions for characteristic X-ray photons from the X-ray setup and electrons emitted from a ^{90}Sr source.

The type of the applied fit depends on the particles. The photons used in the laboratory measurements mostly deposit their entire energy inside the silicon sensor via the photoelectric effect (according to the available energy range of the photons). Hence, the obtained distribution is Gaussian shaped. The mean of a Gaussian fit function, applied to the distribution, is defined as the signal height of the characteristic X-ray photons. Signals generated by traversing electrons emitted from a ^{90}Sr source form a Landau distribution as described in section 3.8. In that case the value to be determined is the Most Probable Value (MPV) of the applied Landau fit function. The energy distributions and the corresponding fit functions are discussed in more detail in section 8.4.1.

8.4 UNCERTAINTIES

In order to reliably interpret measurements a good understanding of potential uncertainties is required. Therefore, it is necessary to identify the uncertainties and to determine their relevance as well as their values. Aside from the uncertainty of the radiation dose there are two major aspects which are described below.

8.4.1 FITTING FUNCTIONS

The first uncertainty to be discussed is given by the uncertainty of the fit functions which are used to describe the measured energy distributions. The magnitude of the uncertainty strongly depends on the number of detected hits.

Figure 8.3 shows two typical distributions as obtained during the detector performance studies. In figure 8.3 (a) a signal height distribution obtained from a measurement using characteristic X-ray photons, with the K_{α} energy of silver, is shown. It is clearly visible that there is a large non-Gaussian shaped part. This is mostly caused by the missing offline clustering, which means that a photon depositing its energy in two or more pixels will not be considered as a single hit but instead as two or more hits. Thus, the measured signal heights of these hits are smaller causing the non-Gaussian part at lower values. Even without clustering, the Gaussian shaped part is clearly visible as most photons generate single pixel clusters. Hence, a reliable Gaussian fit can be applied as seen in figure 8.3 (a) which is also indicated by the small uncertainty of only 0.06 Vcal on the mean (133.13 Vcal) of the fit. This allows to skip the offline clustering and the required storage of the measurement raw data which is very time consuming.

Only if all pixels show an identical response behavior, which is ensured by the electrical calibration (see section 5.4), the obtained signal height distribution can be described by a single Gaussian function. Hence, a good fit confirms the excellent electrical calibration of the readout chip.

Figure 8.3 (b) presents the signal height distribution of two and more pixel clusters generated by electrons emitted from a ^{90}Sr source. Electrons generate typically two or more pixel clusters due to their (mostly) non-perpendicular path through the sensor and because of δ -electrons. This demands offline clustering to obtain a Landau shaped distribution. Since the raw data needs to be stored to perform the clustering these measurements are thus more time consuming.

Discarding the single pixel fraction allows to filter most photons which are also emitted by the ^{90}Sr source and mostly create single pixel clusters. Instead of the mean, which is determined for the Gaussian fit, the value of interest for the Landau fit is the MPV. The mean of the Gaussian fit represents the entire photon energy, while the MPV corresponds to the most probable energy deposition of electrons traversing the sensor. The uncertainty on the MPV (502.75 Vcal) of the given Landau fit is 0.54 Vcal.

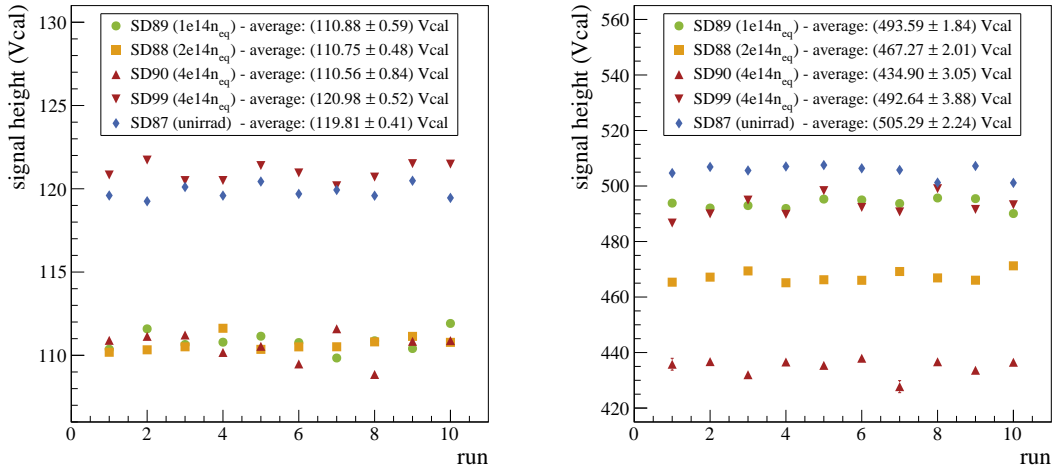
Measurements with a similar number of recorded hits, as the examples presented in figure 8.3, have comparable uncertainties. This is the case for almost all measurements performed in the context of this thesis. Hence, the results presented in the next section refer to such measurements only.

There is only one single case, where the number of recorded hits is much smaller leading to distinctly larger fit uncertainties. This is mentioned in the corresponding section and the associated uncertainties are treated differently.

8.4.2 MEASUREMENT REPEATABILITY

If single measurements of a sample are compared to each other, several effects have an impact on the absolute uncertainty. A variety of them is explained and determined individually in [Tas16] and [Fre13]. Within this section the absolute uncertainty is determined, as it is the relevant value which needs to be considered. For this purpose many measurements were performed under identical conditions over a time period of some weeks.

Figure 8.4 shows two measurement series for electrons and characteristic X-ray photons (corresponding to the K_{α} energy of silver). For each radiation dose, according to the target values introduced above, ten measurements were performed. All measurement series show certain variations, while the individual uncertainties coming from the Gaussian and Landau fit functions are too small to be recognizable, except for two electron measurements of sample SD90. Figure 8.4 (a) shows the photon measurements with similar deviations for all irradiation steps. The uncertainties, given by the standard deviation, are similar and range from 0.41 Vcal to



(a) Measurement uncertainties for characteristic X-ray photons (K_{α} energy of silver). For each irradiation step ten measurements were performed under identical conditions. All measurements show variations within a comparable range. The uncertainties of the Gaussian fit functions are too small to be recognizable. The stated values in the legend correspond to the average of the Gaussian means and the associated standard deviation which determines the uncertainty. The differences on the uncertainty are almost negligible.

(b) Measurement uncertainties for electrons emitted from a ^{90}Sr source. Again ten measurements, performed under identical conditions and for different irradiation steps, are presented. The deviations at the highest irradiation dose seem to be larger. The uncertainties of the Landau fit functions are only visible in two measurements of SD90. The values given in the legend are the average and the standard deviation of the MPVs per measurement series. As indicated by the deviations the uncertainty is larger at the highest radiation dose.

Figure 8.4: Measurement uncertainties for characteristic X-ray photons and electrons determined for different levels of radiation damage. The single points correspond to the mean of the Gaussian fit and the MPV of the Landau fit respectively.

0.84 Vcal. For each sample investigated in this study the uncertainty is individually determined and considered in the further course.

The deviations in figure 8.4 (b) of the ^{90}Sr measurements behave barely differently. The uncertainties of the averaged MPVs for the unirradiated sample and both lower irradiated samples are again very similar (1.84 Vcal to 2.24 Vcal). Only the $4e14 n_{eq}$ samples seem to have a slightly larger uncertainty. Similar to the photon measurements the uncertainty is calculated individually for each sample and considered in all electron measurements.

All uncertainties stated in both figures are below 1% with respect to the mean and MPV, respectively. Differences regarding the absolute signal heights between samples at the same radiation step (see e.g. SD90 and SD99) are related to minor variations in the individual ROC behaviors.

As illustrated by the results of figure 8.4, the uncertainties obtained from the reliability measurements are significantly larger than the bare fit uncertainties. Therefore, the uncertainties considered in this thesis are typically obtained from such reliability measurements. Only in a single case the fitting uncertainty has to be considered because of a very small number of recorded hits resulting in a significantly larger fitting uncertainty.

8.5 PHASE I BARREL PIXEL MODULE

In this section the measurements performed with the pixel detector module are presented. Although modules are the optimal option to investigate the pixel detector performance, it is not favored to spend a good module which could be installed in the detector. Therefore, a grade C module, which was rejected due to an electrically defective ROC, is chosen as

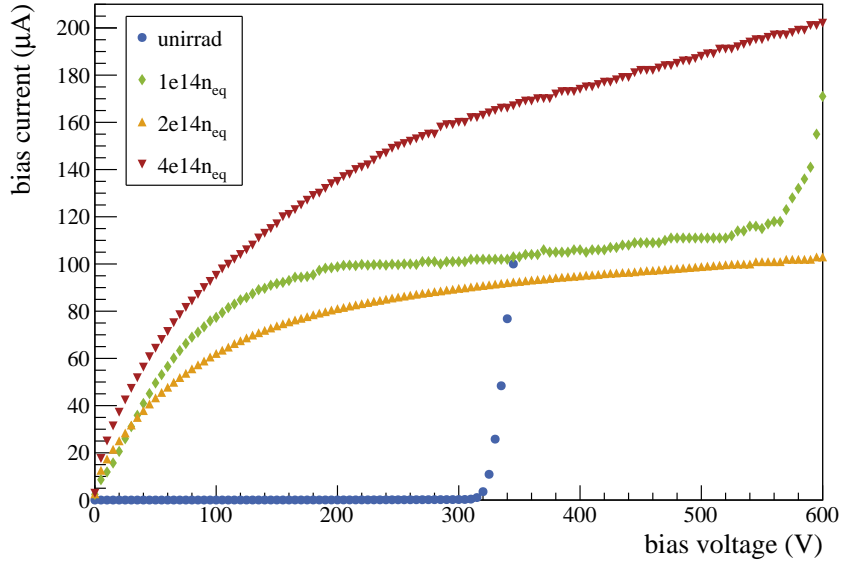


Figure 8.5: Current-voltage characteristics of the investigated module for each irradiation step and the unirradiated case. As expected, the lowest IV-curve corresponds to the unirradiated case and the highest one to the $4e14 n_{eq}$ radiation level. However, the IV-curve obtained for the $1e14 n_{eq}$ irradiation step is higher than the one corresponding to $2e14 n_{eq}$. This behavior cannot be explained by the defects introduced in section 3.11.

announced in the beginning of this chapter. This module is a perfect candidate for such a study as it behaves flawlessly except for the defective ROC.

The measurements regarding this module are performed at KIT. They provide information on basic properties like current-voltage characteristics or signal heights and how they change with increasing radiation damage. Measurements concerning the hit efficiency or resolution (as performed during test beam studies) were not possible on the time scale of this thesis, due to the lack of a test beam setup which supports cooling of an entire module.

8.5.1 IV CHARACTERISTICS OF THE MODULE

As already explained in section 5.1 the current-voltage characteristic (IV-curve) of the silicon sensor is an important basic property. Hence, it is also investigated in the performance study. Figure 8.5 shows the IV-curves of the investigated module, measured at -20°C before irradiation and after each irradiation step. As already described in section 3.3 defects caused by radiation introduce additional energy levels in the band gap, which lead to an increased leakage current. This means that the sensor leakage current should rise with increasing radiation damage.

As expected, the IV-curve of the unirradiated case shows the lowest leakage current. The sensor has a breakdown at about 300 V which is typical for these sensors before irradiation as shown during the module production [Hei16]. The IV-curve corresponding to the $4e14 n_{eq}$ irradiation step is the highest one which was equally expected. However, this is not true for the IV-curves of the $1e14 n_{eq}$ and $2e14 n_{eq}$ irradiation steps, since the IV-curve corresponding to $1e14 n_{eq}$ is higher. A simple confusion of both measurements is excluded. This is also confirmed by the leakage current breakdown which is shifted to higher voltages for increasing radiation damage. As visible in figure 8.5 only the blue (unirradiated) and the green curve ($1e14 n_{eq}$) show a breakdown, while there is none for the yellow one ($2e14 n_{eq}$).

Accordingly, the presented behavior cannot be explained with the defects introduced in section 3.3. Nevertheless, it was possible to obtain additional information regarding this issue with the results presented in the next section.

8.5.2 HIT MAPS OF THE MODULE

After each irradiation step a measurement with a ^{90}Sr source was performed. Such measurements provide information on the measured signal heights and how they will change during the detector lifetime. Further, these measurements provide hit maps which are analyzed subsequently.

Figure 8.6 shows the hit maps obtained before irradiation and after the $1e14 n_{eq}$ and the $2e14 n_{eq}$ irradiation steps. A prominent feature is the white area in the bottom left corner, corresponding to the electrically defective ROC of this module. The silhouettes of the connector and the capacitors on top of the HDI are visible in each hit map as well as the spot of the ^{90}Sr source. As indicated by the z-axis, the number of events recorded differs, especially for the measurement after the $1e14 n_{eq}$ irradiation step. Due to time constraints imposed by the measurement and irradiation schedule of this module, the measurement time had to be smaller in that particular case.

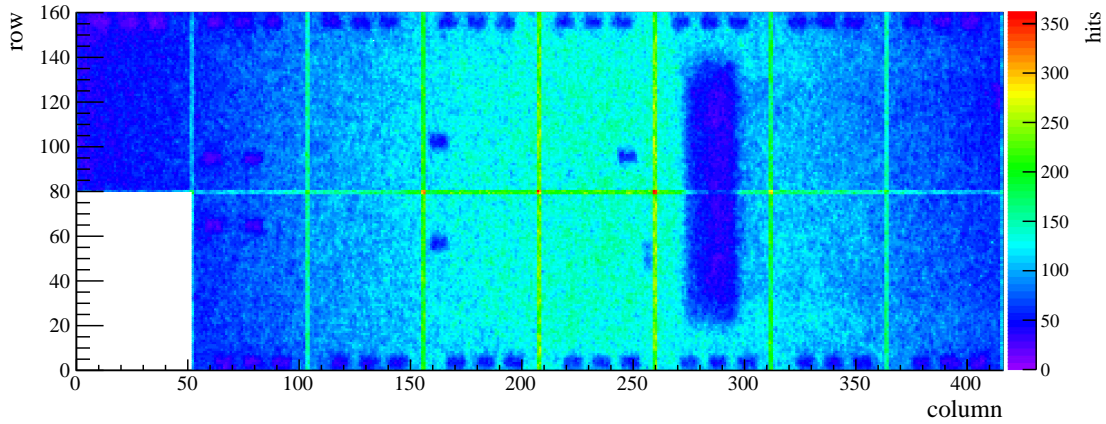
Nevertheless, there is another prominent feature in the hit maps after irradiation. Around column 190 and row 45 a problematic spot emerged during the first electrical test after irradiation. The associated channels are noisy containing distinctly more entries. This localized defect is either created by the irradiation or a potential pre-existing damage is revealed. The spot size decreased after the $2e14 n_{eq}$ irradiation step which indicates that the defect is related to a sensor problem as defective PUCs are typically not able to recover. The decreasing spot size is also a potential explanation for the unexpected current-voltage characteristic presented in figure 8.5 where the leakage current values obtained after the $2e14 n_{eq}$ irradiation step are lower than the ones at $1e14 n_{eq}$. The hit map recorded after the final irradiation step ($4e14 n_{eq}$) is similar to the one at $2e14 n_{eq}$. Aside from the described spot of noisy pixels there is no apparent change in the hit maps.

This means that the leakage currents presented in figure 8.5 are barely meaningful, since the defect probably has an impact on each leakage current measurement obtained after irradiation. More reliable results regarding the IV-curves are available in the section covering the single chip assemblies.

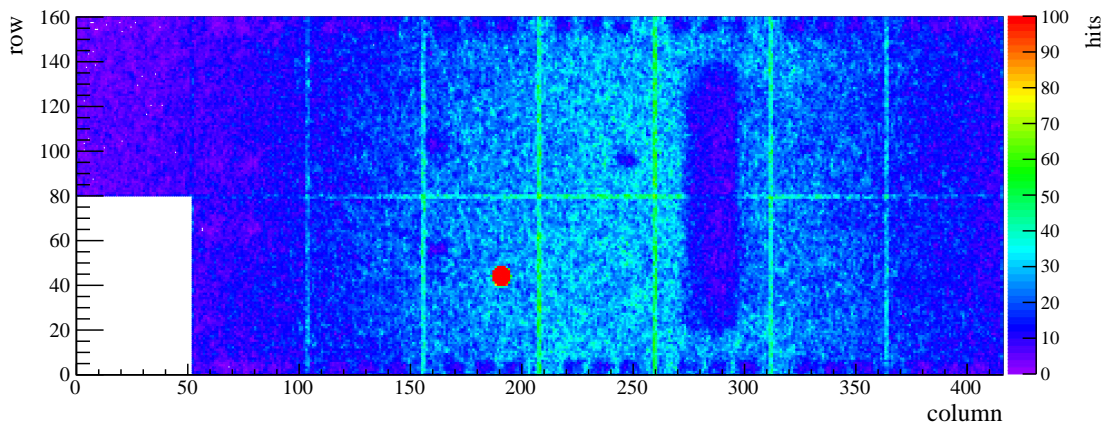
8.5.3 X-RAY CALIBRATION CURVES OF THE MODULE

All results presented so far, whether obtained with electrons or characteristic X-ray photons, refer to signal heights given in Vcal values. However, it is not intuitive to present values like signal height, noise or comparator threshold in Vcal units. Even though it is sufficient for comparison purposes a more meaningful interpretation demands a conversion of the Vcal values into a more convenient unit like the number of electrons. This can be achieved with an X-ray calibration which is performed individually for each sample and irradiation step to account for the slightly different response behaviors.

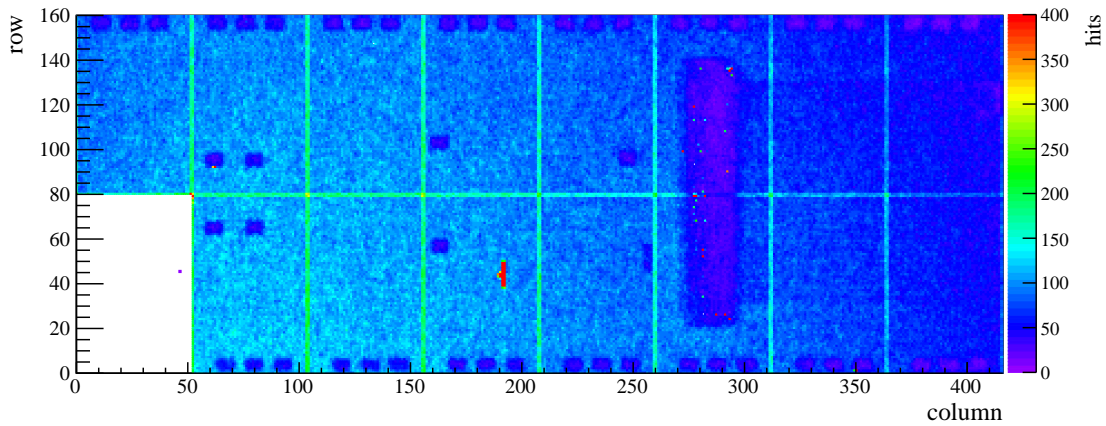
The X-ray calibration, prior to the first irradiation step of the investigated module, was performed in the X-ray setup introduced in section 5.4. It was performed at $+17^\circ\text{C}$, since at this time only a simplified cooling was available, providing stabilized temperatures above approximately $+10^\circ\text{C}$. This in turn means that it was not possible to perform the X-ray calibrations after irradiation inside the X-ray setup. Otherwise the leakage currents would be too high leading to thermal runaway which might have damaged the module.



(a) Module hit map before irradiation. There is nothing conspicuous aside from the electrically defective ROC.



(b) Module hit map after the $1e14 n_{eq}$ irradiation step. A problematic region emerged around column 190 and row 45 in the first electrical test after irradiation. The corresponding pixels are noisy and detect significantly more hits. The damage was either caused by the irradiation or a pre-existing defect became apparent.



(c) Module hit map after the $2e14 n_{eq}$ irradiation step. The size of the problematic spot clearly decreased. Hence, the defect is probably related to the sensor as defective PUCs of the ROC are typically unrecoverable. Additionally, a partially recovered sensor defect might explain why the IV-curve corresponding to the $2e14 n_{eq}$ irradiation step provides a lower leakage current than the IV-curve at $1e14 n_{eq}$.

Figure 8.6: Module hit maps obtained with a ^{90}Sr source before irradiation and after the $1e14 n_{eq}$ and $2e14 n_{eq}$ irradiation steps. The module has a single defective ROC in the bottom left corner. All hit maps show the silhouettes of the connector and the capacitors on top of the module which shield the module against electrons. In addition, the spot of the ^{90}Sr source is recognizable.

Therefore, the X-ray calibration after irradiation had to be performed in the electrical test setup (see appendix D) which was built for the KIT module production and already equipped with a cold chuck. This allowed to select a measurement temperature of -20°C . Due to the lack of an X-ray tube in this setup the measurements had to be performed with an X-ray source (see appendix E) based on ^{241}Am illuminating a selectable target material. Although this source relies on the same principle as the X-ray setup it has significantly smaller rates of characteristic X-ray photons leading to very small number of recorded hits. Actually, this is the single case mentioned in section 8.4.2 where the fit uncertainties are distinctly larger.

The available target materials of the X-ray setup and the X-ray source are presented in table 8.1, with an asterisk (*) corresponding to materials available in the X-ray setup and a dagger (†) to the X-ray source. Aside from the K_α energies the average number of generated electrons is stated, determined by dividing the K_α energy by 3.6 eV which is the required energy to generate an electron-hole pair in silicon (as described in section 3.1.2).

Table 8.1: K_α transition energies of the available target materials. The table lists the available target materials and the associated K_α energies together with the number of electrons generated in silicon. The target materials available in the X-ray setup are labelled with an asterisk (*) and the ones of the X-ray source with a dagger (†) [NIS17].

target	K_α energy (eV)	$n_{\text{electrons}}$
Fe*	6403.13 (43)	1778.64 (12)
Cu*†	8048.11 (45)	2235.59 (13)
Zn*	8639.10 (45)	2399.75 (13)
Rb†	13,395.05 (51)	3720.85 (14)
Mo*†	17,479.10 (55)	4855.31 (15)
Ag*†	22,162.99 (66)	6156.39 (18)
In*	24,209.78 (69)	6724.94 (19)
Sn*	25,271.34 (72)	7019.82 (20)
Ba†	32,192.87 (88)	8942.46 (24)
Nd*	37,361.40 (100)	10,378.17 (28)
Tb†	44,482.90 (120)	12,356.36 (33)

Typically, measurements with four or more targets are performed for an X-ray calibration. Afterwards the number of generated electrons is plotted as a function of the measured signal height (given in Vcal) as presented in figure 8.7. Both figures rely on the same X-ray calibration data showing the same eight ROCs of the investigated module. For the sake of clarity only eight ROCs (out of 15 working ROCs of the module) are considered. The calibration curves (obtained by linear regression) presented in figure 8.7 (a) are not suitable to convert the signal heights into an electron value as the parameters of the calibration curves (slope, y-intercept and the corresponding uncertainties) are correlated. This is unfavorable with respect to the corresponding error propagation used for the signal height conversion. To decorrelate the parameters a coordinate transformation of the x-axis is performed where each curve is shifted by its mean as it is the case in figure 8.7 (b). In addition, the uncertainty σ_b of the y-intercept b decreases according to equation 8.1. When the x-values (the measured signal heights) are shifted by the mean, the numerator decreases while the denominator remains unchanged.

$$\sigma_b = \sigma_y \cdot \sqrt{\frac{1}{N} \frac{\sum_{i=1}^N x_i^2}{\sum_{i=1}^N (x_i - \bar{x})^2}} \quad (8.1)$$

The given properties are the signal heights x_i , their mean \bar{x} , the total number of measured target materials N and the uncertainty σ_y on the number of electrons. After the coordinate transformation of the x -axis the signal heights given in Vcal (x_{Vcal}) can be converted into electron values ($x_{electron}$) with the following equation.

$$x_{electron} = x_{Vcal} \cdot a + b \quad (8.2)$$

The parameters are the slope a of the X-ray calibration curve (given in electrons/Vcal) and the corresponding y -intercept b (given in electrons). The uncertainty $\sigma_{electron}$ of the electron signal height is determined via

$$\sigma_{electron} = \sqrt{(x_{Vcal} \cdot \sigma_a)^2 + \sigma_b^2} \quad (8.3)$$

where σ_a and σ_b represent the uncertainties of the slope and the y -intercept, respectively.

Aside from translating signal heights into electrons the calibration curves can be exploited to convert the noise (obtained via S-Curve tests introduced in section 5.4) into electrons. The noise is typically slightly larger than 3 Vcal. This results in about 150 electrons² when multiplied with the slopes of the X-ray calibrations [Tas16].

While the X-ray calibration works for unirradiated devices, it is less reliable for irradiated modules or single chip assemblies. The number of electrons forming a signal is derived from the K_α energy of the selected target. However, this is no longer true for irradiated devices, as the absolute number of electrons contributing to the signal is reduced due to trapping. As a consequence, the slopes of the calibration curves are overestimated and the conversion of Vcal signals into electrons is no longer correct. The impact of X-ray calibrations performed after irradiation becomes apparent in the next section where charge collection is discussed.

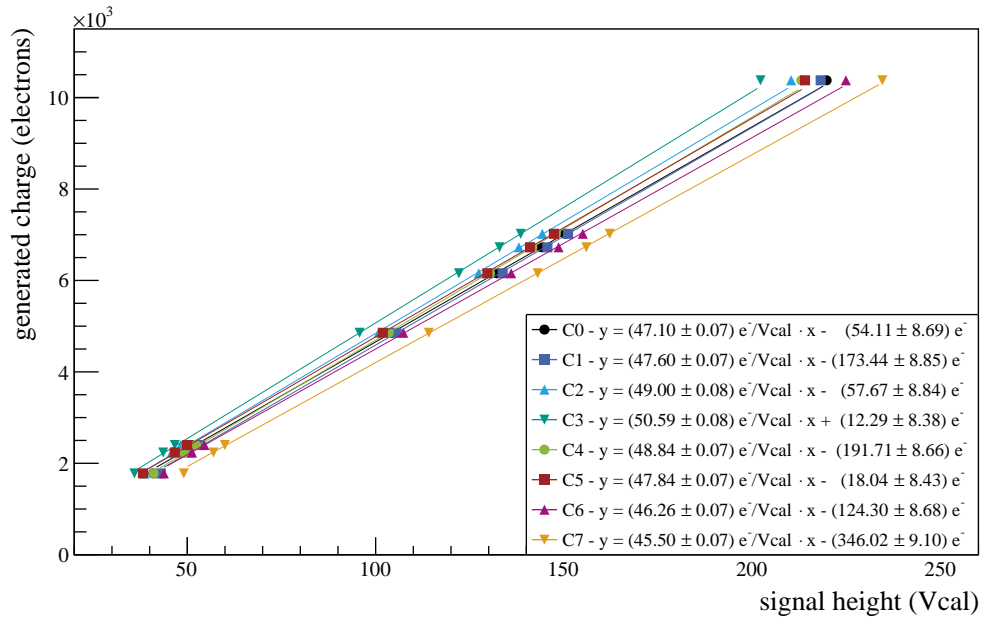
8.5.4 CHARGE COLLECTION OF THE MODULE

The charge collection efficiency is an important parameter of the detector performance. To guarantee a good hit efficiency the generated signals need to be sufficiently high to exceed the comparator threshold of the PUCs.

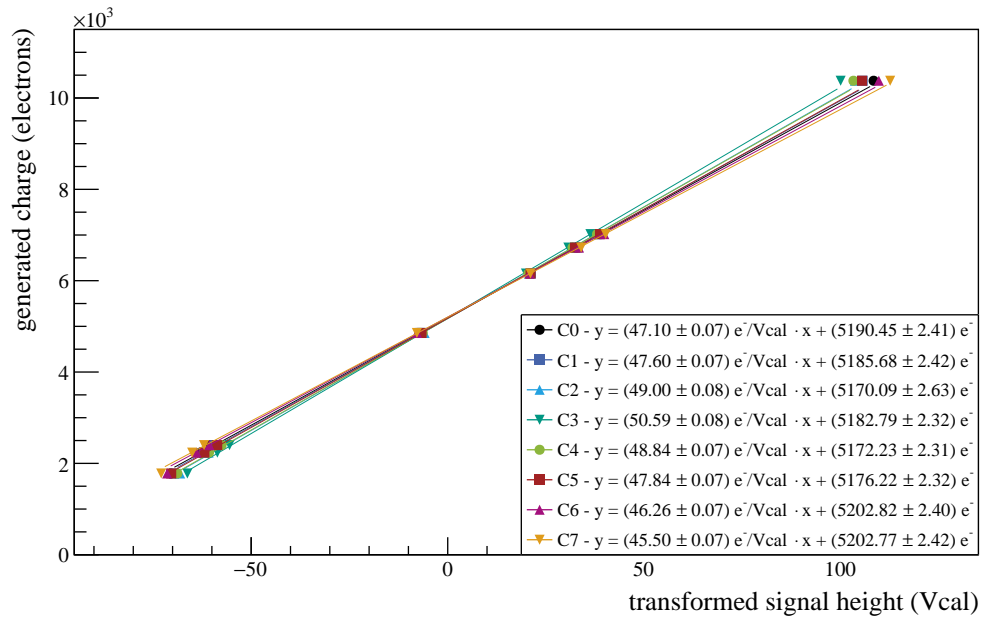
Defects inside the silicon sensor, generated by irradiation, lead to charge carrier trapping which prevents some electrons from contributing to the signal. In order to reduce the trapping probability, a higher bias voltage can be applied to generate a higher electric field, which increases the electron drift velocity and decreases the drift time. For that reason several measurements with a ⁹⁰Sr source at different voltages are performed and introduced in this section.

Figure 8.8 shows the measured signal heights as a function of the bias voltage before and after irradiation of the module. For the sake of clarity it was decided not to show the single measurement points for each of the 15 ROCs. Instead, each marker visible in the figure represents the mean of the 15 ROC measurements at a given voltage. The indicated uncertainty is determined by the standard deviation of the mean value, which is larger than the uncertainty obtained from reliability measurements (see section 8.4.2). This is caused by the different response behavior of the ROCs as indicated by the shifts of the calibration curves in figure 8.7 (a). At $4e14$ n_{eq}, the highest irradiation step, it was not possible to obtain reasonable measurements for all 15 ROCs without fine tuning the ROC settings. Hence, the corresponding data is based on only ten ROCs. A more detailed ROC tuning in order to obtain the optimal performance after irradiation is performed for the single chip assemblies presented in the next section.

² which is a reasonable value compared to the threshold of 1750 electrons



(a) X-ray calibration without coordinate transformation. The presented calibration curves have similar slopes between $45.50 \text{ e}^-/\text{Vcal}$ and $50.59 \text{ e}^-/\text{Vcal}$. Due to minor differences of the ROC behaviors the curves are slightly shifted in x-direction. The uncertainties on the slope and on the y-intercept are correlated.



(b) X-ray calibration after coordinate transformation of the x-axis. The slopes of the calibration curves remain unchanged after the transformation while the slope and the y-intercept (and the corresponding uncertainties) are no longer correlated. According to equation 8.1 the y-uncertainty decreases.

Figure 8.7: Module X-ray calibration of eight ROCs before irradiation. Both figures show the same measurement data, but for figure (b) a coordinate transformation is performed to decorrelate the fit parameters. The uncertainties on the measured signal heights are determined from reliability measurements as introduced in section 8.4.2. Uncertainties on the K_α energy and the number of electrons, correspond to theoretical calculations from [NIS17].

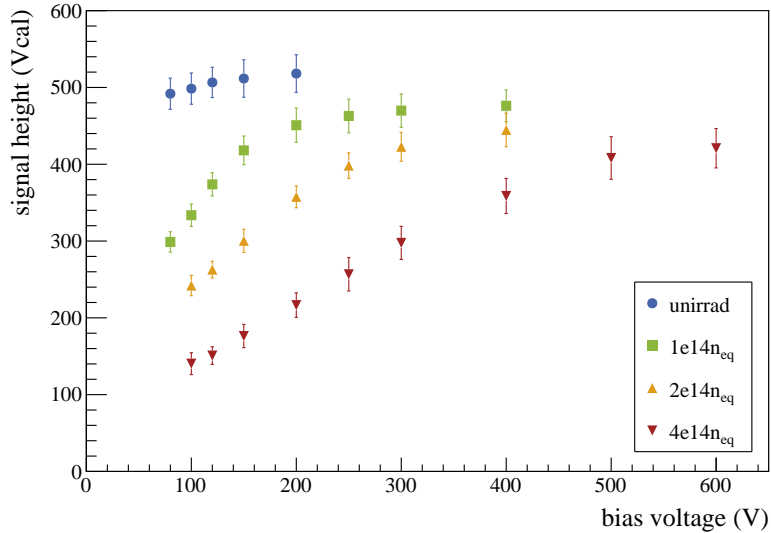


Figure 8.8: Signal heights in Vcal as a function of the bias voltage obtained from ^{90}Sr measurements with a module. The signal heights clearly decrease with radiation damage while they recover for increasing bias voltages. Even at $4e14 n_{eq}$ the measured signal heights are sufficiently high with respect to the comparator threshold of 35 Vcal.

Figure 8.8 shows that the measured signal heights decrease for increasing radiation damage while they recover at higher bias voltage as expected from the increasing electric field both before and after irradiation. The signal heights are well above the comparator threshold, which is set to 35 Vcal by default (before and after irradiation). Even at the highest irradiation step signal heights ten times higher than the comparator threshold can be achieved.

While the shown figure allows to make a qualitative statement on the signal height differences, it is more difficult to evaluate the absolute differences, which is especially true for the $4e14 n_{eq}$ sample. For the first two irradiation steps $1e14 n_{eq}$ and $2e14 n_{eq}$ only minor adjustments of the ROC parameters were performed to operate them reliably (the analog and digital currents are basically unchanged). However, there is an additional effect influencing the ROC performance which is described in [HK⁺16]. According to this publication, the band gap reference of the ROC, which serves as internal reference voltage, changes due to radiation damage. This in turn affects many parameters of the electrical calibration such as gain and offset of the detector response behavior. Therefore, the obtained signal heights are only partially comparable.

The following comparison of the absolute signal heights needs to be treated with caution for the reasons mentioned above. The maximum signal height at $2e14 n_{eq}$ is 450 Vcal which still corresponds to approximately 85% of the maximum signal height of the unirradiated state. This shows that the signal height degradation at the end of the lifetime of layer 3 is reasonably low. Accordingly, the signal height degradation for layer 4 of the barrel pixel detector is even less and the signal height reaches about 92% of the unirradiated signal height.

Comparing the signal heights obtained for the highest irradiation step ($4e14 n_{eq}$) to the signal heights of the unirradiated case is not meaningful for several reasons. In order to operate the ROCs reliably a more extensive manual adjustment of the pulse height calibration³ was required leading to a distinctly different gain and offset of the detector response behavior. Further, the band gap reference is affected even stronger due to the increased radiation damage at the highest irradiation step making a comparison even less reliable. Hence, it was decided to skip the comparison with the absolute signal heights of the highest irradiation step $4e14 n_{eq}$.

³ The pulse height calibration consists of the electrical tests PH-Optimization and Gain Pedestal as explained in section 5.4.

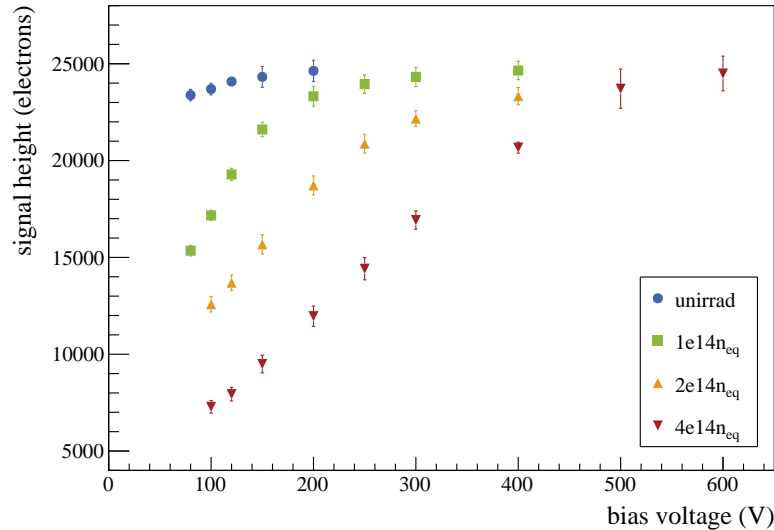


Figure 8.9: Signal heights given in electrons as a function of the bias voltage obtained from ^{90}Sr measurements with a module. The signal heights at each irradiation step seem to recover entirely with increasing bias voltage reaching pre-irradiation values. This is caused by wrong X-ray calibrations as trapping is neglected and thus the number of electrons is overestimated as described in section 8.5.3.

Figure 8.9 shows the measured signal heights given in units of charge in electrons. For each irradiation step an X-ray calibration was carried out and the V_{cal} values were converted into charge with the help of equations 8.2 and 8.3.

The measured signal heights increase with higher bias voltages as expected. However, as pointed out above, the absolute values of the signal heights are only correct for the unirradiated case as the X-ray calibrations after irradiation neglect trapping (see section 8.5.3). This becomes apparent by having a closer look at the figure. The signal heights of the module before irradiation are in good agreement with the predicted number of electron-hole pairs. According to section 3.2.2 about 73 electron-hole pairs are generated per μm for MIPs which results in about 21,000 electrons for the nominal sensor thickness of 285 μm . The measured signal heights are between 23,000 and 24,000 electrons, which is slightly higher than expected. The actual measured sensor thickness is about 290 μm which cannot explain the difference between measured and expected signal height.

The problem regarding the signal heights measured for irradiated sensors is related to the X-ray calibrations. As mentioned in the section before, the X-ray calibration does not take into account that the number of electrons contributing to the signals is reduced due to trapping. Therefore, the signal heights presented in figure 8.9 overestimate the number of generated electron-hole pairs. For instance, the measurement at 600 V for the highest radiation level reaches the same value (24,000 electrons) as obtained for the unirradiated case. This value is too high as confirmed by other publications investigating irradiated sensors like [Pri16], [Nür14] or [Ebe13].

Further, it is not possible to apply a calibration curve obtained before irradiation to convert the signal heights measured after irradiation is not meaningful for two reasons. First of all, since the performance of the ROC is also affected by the radiation damage and second, as the adjusted ROC settings for irradiated samples influence the response behavior (which is especially the case after the highest irradiation step) as mentioned above.

The results presented in this section demonstrate that the signal heights are sufficiently high even at the highest radiation dose (see figure 8.8). However, it is not possible to precisely deter-

mine the charge collection efficiency from the absolute signal heights given in electrons after irradiation, especially after the irradiation to $4e14 n_{eq}$.

As the design of the silicon sensor is identical to the one of the original CMS barrel pixel detector, there are already publications concerning the evolution of the charge collection efficiency (see e.g. [RBC⁺05] or [RBE⁺10]). However, there are no results exactly corresponding to the radiation damage at the end of the lifetime of barrel layers 2 to 4.

A possibility to investigate the charge collection efficiency would be to irradiate the bare sensors and to connect the ROCs afterwards. It would still not be possible to perform an X-ray calibration to convert the signal heights into charge values, but it would be acceptable to apply a calibration curve obtained with another unirradiated sample. This would allow to convert the signal heights within an uncertainty of about 10% according to the spread of calibration curves for unirradiated samples (see figure 8.7).

In such a study an additional topic needs to be addressed. During the flip-chip bonding, where the ROCs are connected to the sensor, heat is required to establish a good connection. To avoid annealing of an irradiated sensor it would be necessary to perform the bonding at lower temperatures of about 50°C instead of 150°C. This is a complex process, but as it is relevant in the context of many studies it is addressed in appendix H.

8.6 SINGLE CHIP ASSEMBLIES

Single chip assemblies are an excellent choice to perform a variety of measurements (for instance regarding detector resolution and hit efficiency). Compared to modules they require fewer components while they still allow to investigate the most interesting parts, the sensor and the ROC. Using multiple SCAs compared to a single module also gives more redundancy. Hence, SCA studies are less prone to corrupted measurements like the IV-curves of the module that developed a hot spot after irradiation. In case of an entirely defective sensor only a single ROC is lost instead of 16 on a module. Further, the experimental setups available at test beam facilities, as introduced in chapter 9, mostly support single chips assemblies as they are much more compact than modules.

8.6.1 IV CHARACTERISTICS OF THE SINGLE CHIP ASSEMBLIES

The IV measurements of the SCAs are interesting for two reasons. First of all, they are used to verify that the SCAs behave as expected before and after irradiation. Second, it allows to compare the leakage current behavior at different irradiation steps, which was not possible for the module due to the localized sensor defect.

For all available single chip assemblies the IV-curves were measured before and after irradiation (see appendix C). Figure 8.10 presents the IV-curves at -20°C of the SCAs which were later investigated during the test beam study discussed in chapter 9. In contrast to the module the IV-curves behave as expected.

Before irradiation all samples show comparable leakage currents which are significantly smaller than the ones after irradiation. The breakdown, visible in three unirradiated measurements above 250 V, is fully acceptable and consistent with the results of good sensors from the pixel module production [Hei16]. Further, the results of figure 8.10 allow to compare the measured leakage currents of the irradiated samples with the expected leakage currents I_{fluence} calculated according to the equation below.

$$I_{\text{fluence}} \approx \alpha \times \text{fluence} \times V_{\text{depletion}} \quad (8.4)$$

The value of the current related damage rate α (calculated with the help of [Mol99]) is $5.7e^{-17}\text{A/cm}$ which refers to an annealing of 12 hours at room temperature. The fluence

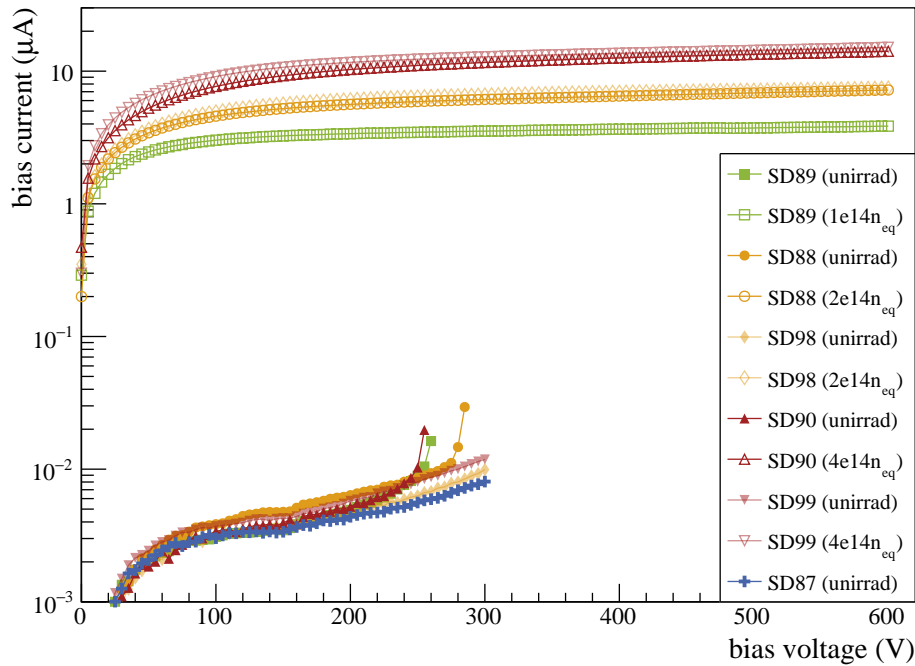


Figure 8.10: Current-voltage characteristics of the single chip assemblies investigated during the test beam. For each single chip assembly an IV-curve before and after irradiation is presented. The IV-curves obtained before irradiation are very comparable, providing a good starting point for the study. The five IV-curves after irradiation confirm the expected behavior with the $1e14 n_{eq}$ SCA (green) having the lowest leakage current. It is followed by both $2e14 n_{eq}$ samples (yellow) and the two curves with the highest currents corresponding to the $4e14 n_{eq}$ SCAs.

corresponds to the three irradiation steps $1e14 n_{eq}$, $2e14 n_{eq}$ and $4e14 n_{eq}$ while $V_{depletion}$ is the depleted volume of the silicon sensor (about 0.021 cm^3).

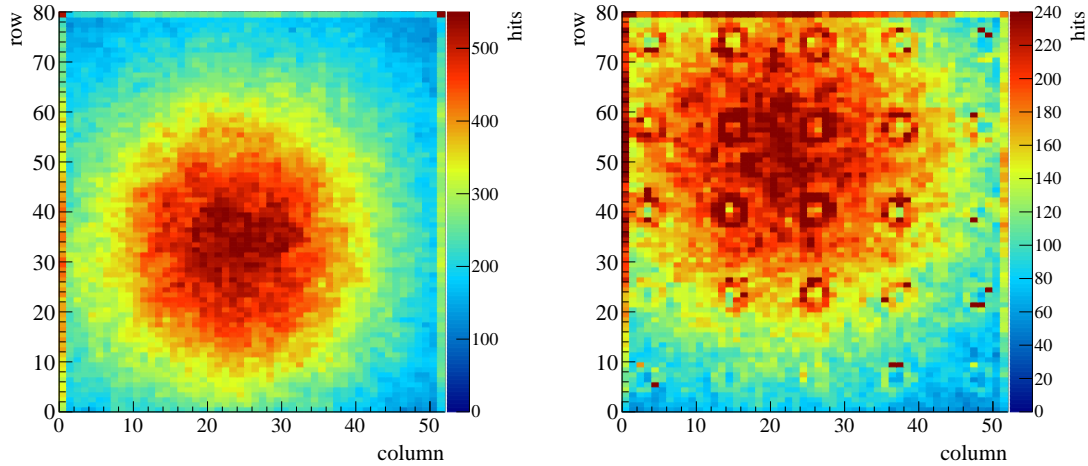
The calculated leakage currents are $I_{1e14 n_{eq}} = 2.5 \mu\text{A}$ ($3 \mu\text{A}$), $I_{2e14 n_{eq}} = 5.1 \mu\text{A}$ ($6 \mu\text{A}$ to $7 \mu\text{A}$) and $I_{4e14 n_{eq}} = 10.1 \mu\text{A}$ ($10.1 \mu\text{A}$ to $10.5 \mu\text{A}$) with the values in the brackets referring to the measured leakage currents above 300 V. This confirms that the measured and calculated leakage currents are in good agreement with respect to the 20% uncertainty of the calculated leakage current.

In terms of leakage currents the SCAs are perfect candidates for the test beam study. Further, these results confirm that the leakage currents at the proposed end of the lifetime of layer 2 to 4 modules are below 1 mA ($16 \times (10\text{-}20 \mu\text{A}) = 160\text{-}320 \mu\text{A}$) which is sufficiently small. However, there is an abnormality for irradiated samples which is neither caused by the ROC nor by the sensor as described in the next section.

8.6.2 HIT MAPS OF THE SINGLE CHIP ASSEMBLIES

For each SCA at least one measurement with a ^{90}Sr source was performed to obtain information regarding the signal height and to identify potential dead channels. The hit maps obtained during these measurements revealed an additional unexpected feature.

Figure 8.11 presents two hit maps of the same SCA, one before and one after irradiation to $4e14 n_{eq}$. In both of them the spot of the ^{90}Sr source is clearly visible. However, the irradi-



(a) The hit map before irradiation shows the expected behavior with the highest number of detected hits being located in the center of the source spot. There are no dead channels recognizable. (b) Hit map after irradiation. Due to holes in the PCB holding the single chip assembly, the irradiation of the sample is not homogeneous. Pixels at these holes behave differently and detect more hits.

Figure 8.11: Hit maps obtained from measurements with a ^{90}Sr source before and after irradiation. The spot of the source is clearly visible in both figures.

ated sample (figure 8.11 (b)) shows an additional feature in form of a regular pattern of circles caused by pixels with a higher number of detected hits. These circles correspond to the holes in the printed circuit boards (see figure 8.1) on which the SCAs are mounted.

For practical reasons the SCAs have to be mounted with the PCB facing the proton beam during irradiation at the cyclotron. As a result, the protons cause different radiation damage depending on the location which is probably related to the following two effects. First, the protons remain unaffected until they reach the SCA for paths through holes while they are already affected before reaching the SCA when they traverse the PCB material. The protons going through the PCB are slowed down and the corresponding damage factor increases 3.3. Secondly, there is an additional effect at the edges of the holes which is not fully understood. In a former irradiation (at KAZ) for an LHCb project, a comparable effect was observed which was caused by an edge [Die16].

In any case the holes of the PCB and (or) the edges of the holes lead to pixels behaving differently. The higher number of hits for the affected pixels might be related to a few noise induced hits or to smaller thresholds increasing the cluster size which leads to more entries. Threshold maps of such samples can be found in appendix F.

The described effect is visible for all irradiated samples and is most distinct at $4e14 n_{eq}$. It will be taken into account during the test beam analysis in chapter 9 by either excluding these pixels from the analysis or showing their impact on the results.

For all investigated single chip assemblies two X-ray calibrations (before and after irradiation) were performed. As the results are not relevant for the remaining measurements they are not presented here, but they can be found in appendix F for the sake of completeness.

8.6.3 CHARGE COLLECTION OF THE SINGLE CHIP ASSEMBLIES

The charge collection of the SCAs is investigated to validate them prior to the test beam study presented in chapter 9 and to guarantee that only working samples are used.

Compared to the investigated module there is an important difference regarding the charge collection measurements of the irradiated SCAs. The fine tuning of the SCAs after irradiation

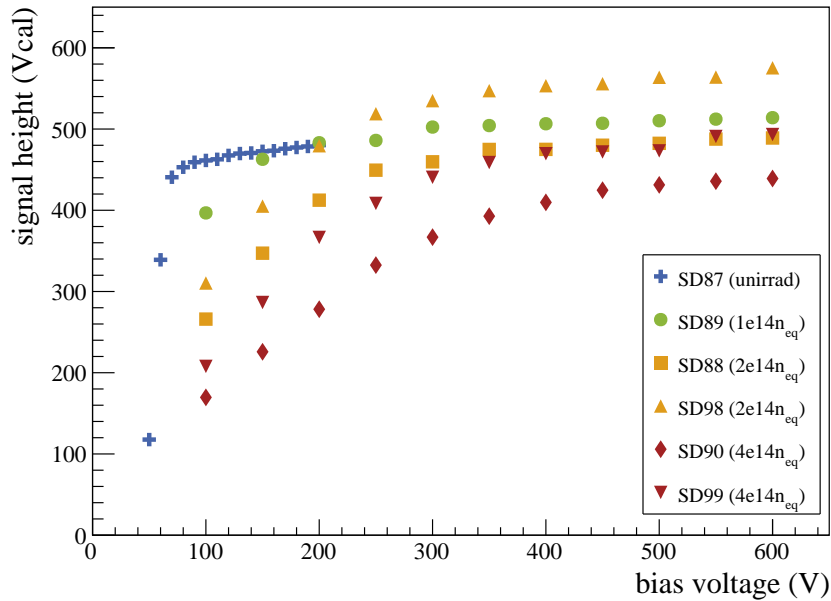


Figure 8.12: Signal heights in Vcal as a function of the bias voltage obtained from ^{90}Sr measurements for different SCAs. All signal heights increase for higher bias voltages as expected. The measured signal heights are not sorted according to the radiation damage due to different signal gains caused by a detailed fine tuning of the ROC settings. Nevertheless, the depletion voltages can be determined roughly by the start of the signal height plateau. The unirradiated samples fully deplete above 70 V, the $1e14 n_{eq}$ SCAs at about 150 V, the $2e14 n_{eq}$ samples at approximately 250 V and the $4e14 n_{eq}$ SCAs above about 400 V. These results are in good agreement with the corresponding module measurements.

is performed in more detail to obtain the optimal ROC operation settings. The analog and digital currents are increased from 24 mA up to 28 mA and from 25 mA to more than 30 mA, respectively. This in turn has an influence on the measured signal heights. In addition, the feedback of the preamplifier and the shaper are adjusted which both affect the amplifier gain. Last, the pulse height calibration has to be adjusted manually to recover the desired shape of the measured spectra and to obtain results comparable to the ones in figure 8.3. Therefore it is necessary to increase the lower limit of the available ADC range (the accessible range for the measured the signal heights). In the pulse height calibration of unirradiated samples, the DACs PHScale and PHOffset are adjusted in order to optimally exploit the available ADC range between 20 and 255 ADC counts. For irradiated samples the lower margin is increased from 20 to 40 to obtain reasonable signal height spectra. Especially for the highest irradiation step of $4e14 n_{eq}$ it is barely possible to operate them reliably without manual adjustment. Additionally, as a result of the changing band gap reference a comparator threshold of 35 Vcal corresponds to different electron values depending on the irradiation step. For higher radiation damage it corresponds to fewer electrons. This effect can be reduced by increasing the analog current.

Figure 8.12 shows the measured signal heights as a function of the bias voltage. As expected, the measured signal heights of all SCAs increase for higher bias voltages, but the results differ from those obtained for the module, where only little tuning of the ROC settings was performed. The measured signal heights are no longer sorted by radiation damage. Actually, four out of five irradiated samples provide higher signal heights than obtained with the unirradiated SCA. However, the comparison between different irradiation steps is not reasonable for the stated reasons.

Nevertheless, the key point is that all irradiated SCAs deliver sufficiently high signals. In case of the highly irradiated samples the signal heights are clearly above 400 Vcal while the threshold is set to 35 Vcal without suffering from noise hits.

The results presented in this chapter demonstrate that optimal settings can be obtained for both pixel detector modules and SCAs allowing a reliable operation under laboratory conditions also after irradiation. Hence, the next important task is to investigate the detector performance under realistic conditions. This is done in test beam studies, which are introduced in the following chapter.

*An experiment is a question which science poses
to nature and a measurement is the recording of
nature's answer.*

Max Planck

9

TEST BEAM MEASUREMENTS

The performance of the CMS pixel detector can be characterized by two figures. These are the hit efficiency as well as the hit and track resolution. On the one hand, a high hit efficiency is necessary to guarantee that no charged particle leaves the detector unnoticed. On the other hand, an excellent resolution allows to detect secondary vertices caused by particles traveling a few hundred micrometers up to some millimeters before they decay. This is mandatory for b-tagging, which in turn is indispensable in many physics analyses. Only when both aspects are well satisfied, it is possible to perform analyses with the potential of providing new insights into particle physics.

Therefore, previous studies (see e.g. [Spa16]) examined the hit efficiency and the resolution of the CMS Phase I pixel detector with the help of non-irradiated samples. These results provide information on the detector performance during its early phase. However, there is no study which investigated the hit efficiency and the spatial resolution as a function of the radiation damage the detector will suffer from during the proposed operation time. This is covered by the test beam study presented in this chapter.

In addition, the influence of different thresholds as well as the effect of the pulse height calibration on the hit efficiency and resolution are evaluated. To test these properties it is not sufficient to perform only laboratory measurements, as introduced in the previous chapter. Instead, measurements are necessary where particle tracks are reconstructed with the help of tools called beam telescopes. To be able to perform these measurements, particles having sufficient energy to traverse several detector layers are required. This is the case for test beam facilities which are available for instance at CERN or at DESY in Hamburg.

The study performed in the context of this thesis was carried out at the DESY Test Beam Facility. The corresponding results were obtained with SCAs only, as the test beam setup did not support the cooling of modules at the time of this thesis.

This chapter starts with the introduction of the test beam infrastructure and the EUTelescope analysis framework. Afterwards the measurement program is described. This is followed by the test beam results beginning with unexpected problems and basic properties related to hit efficiency and spatial resolution. Finally, a conclusion is given including a summary of the most important results.

9.1 TEST BEAMS AT THE DESY-II SYNCHROTRON

Test beams are a popular tool to study the performance of particle detectors. They provide reference tracks, which are required to investigate hit efficiency and spatial resolution. To reconstruct the tracks custom designed beam telescopes consisting of several detector layers are used.

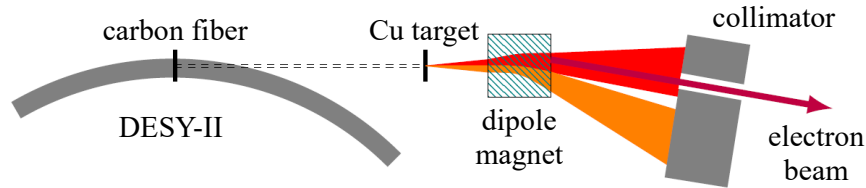


Figure 9.1: Test beam generation at the DESY II synchrotron. A carbon fiber is moved into the DESY II primary beam generating bremsstrahlung. The emerging photons are then converted back into electron-positron pairs with the help of a copper target. A dipole magnet allows to choose between electrons or positrons and to select the desired particle momentum. Finally the test beam is collimated and enters the beam area. Modified from [Spa16].

9.1.1 DESY-II BEAMLINES

The results presented in this thesis are obtained from test beam measurements at the DESY Test Beam Facility¹. The main function of the DESY II synchrotron is to serve as the injector for the PETRA III synchrotron light source. DESY II has a circumference of almost 300 m and delivers a maximum particle energy of 6.3 GeV [Deu17a]. The DESY II synchrotron accelerates a single bunch of electrons or positrons (containing 1 to 3×10^{10} particles) with a revolution frequency of 1.024 MHz and a circulation period of 80 ms [BGG07]. Further it offers three test beam lines providing electrons or positrons at a maximum rate of a few kHz [Deu17a].

Figure 9.1 illustrates the test beam generation at DESY II. The test beams have to be created via a twofold conversion due to the high number of particles in the DESY II bunch. This is achieved by moving a carbon fiber into the primary beam which generates bremsstrahlung. The emerging photons exit the DESY II synchrotron tangentially and are converted back into electron-positron pairs with the help of a copper or aluminum target. A dipole magnet behind the target allows to choose between electrons or positrons and to select the desired particle momentum. Finally, the beam is collimated before it enters the test beam area. This approach allows to reduce the number of particles to a value which can be handled by the beam telescope. Each of the three test beam lines is equipped with its own beam extraction setup and can select the particle type and momentum individually.

One specific property of DESY II is related to the particle energy, which varies over time in a sinusoidal mode with a frequency of 12.5 Hz between the injection energy of 450 MeV and the maximum energy. Hence, electrons or positrons are only able to enter the test beam area when they have at least the energy chosen by the test beam operators. Accordingly, the particle rates of the test beams decrease if higher energies are selected. At the same time, higher energies are desired to reduce multiple scattering of the electrons or positrons in the telescope planes and the investigated sample.

In this study, electrons with an energy of 5.6 GeV are chosen. This is a compromise as the value is close to the maximum energy of about 6 GeV (to minimize multiple scattering), while it still provides a sufficient electron rate of about 800 Hz [Deu17a].

9.1.2 THE DATURA BEAM TELESCOPE

Performing test beam measurements requires precise reconstruction of the particle tracks. This task is covered by beam telescopes, which consist of several layers of position sensitive detectors. The resolution of the telescope should be better than the one of the investigated sample, also called **Device Under Test (DUT)**, to avoid being limited by the telescope resolution. In

¹ The Test Beam Facility at DESY Hamburg (Germany), a member of the Helmholtz Association (HGF).

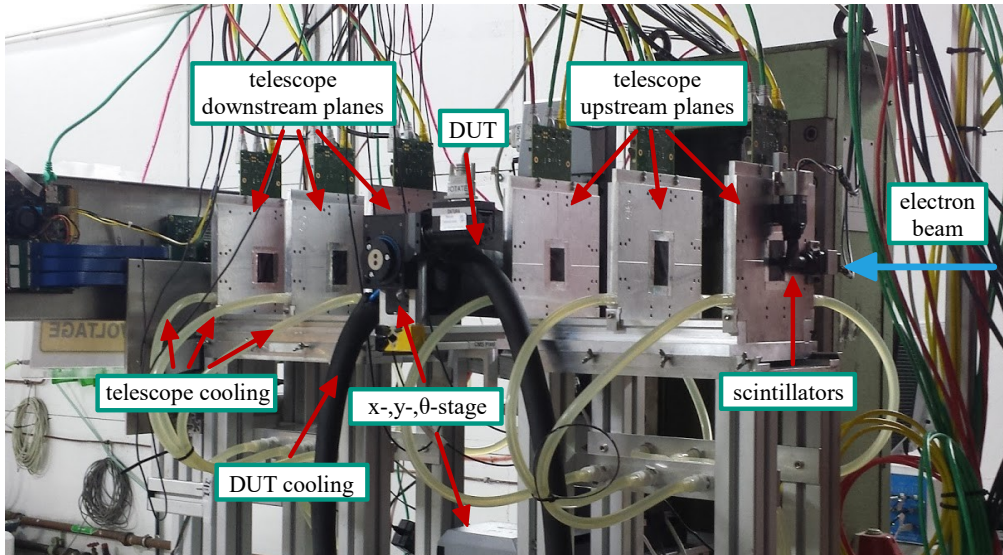


Figure 9.2: The DATURA beam telescope setup. The telescope consists of six planes: the three planes in front of the DUT are the upstream planes and the three planes behind the DUT are the downstream planes. A water cooling system keeps the telescopes planes at $+18^\circ\text{C}$. The DUT is placed in the center of the telescope. It is attached to a x -/ y -/ θ -stage, which allows to obtain the desired DUT alignment and orientation. An ethanol chiller cools the DUT down to -22°C . Scintillators in front of and behind the telescope are used to trigger the readout.

order to guarantee good track finding and to simplify track interpolation, the DUT is placed in the center of the beam telescope.

The beam telescope used for this study is called DATURA, which is a EUDET telescope. EUDET was an R&D project for the International Linear Collider (ILC) that ended in 2010. It was supported by the European Union in the 6th framework program of the European Research Area [A⁺12]. The EUDET beam telescope was developed as part of this project, together with the data acquisition EUDAQ and the analysis framework EU Telescope. So far, seven EUDET telescopes have been built and they are operated at CERN, DESY and SLAC [Deu17b].

The DATURA telescope relies on six detector planes which are based on the MIMOSA26, a high resolution Monolithic Active Pixel Sensor (MAPS). The heart of the MIMOSA26 is formed by a matrix of 576×1152 quadratic pixels, which have a pitch of only $18.4\ \mu\text{m}$. In total it covers a sensitive area of $21.1\ \text{mm} \times 10.6\ \text{mm}$. To minimize the material budget and thus multiple scattering, the sensitive area is thinned down to $50\ \mu\text{m}$. The EUDET-type telescopes achieve pointing resolutions of up to $(3.24 \pm 0.09)\ \mu\text{m}$ [JSB⁺16]. A drawback of the MIMOSA26 is the rolling-shutter readout, which operates at 80 MHz with an integration time of $115.2\ \mu\text{s}$. Rolling-shutter means that each pixel row has to be read out consecutively [BBB⁺09].

Due to the long integration time, EUDET-type telescopes are not suited to be operated at high rates². In case of the 800 Hz used in the present test beam study, already up to five telescopes tracks are detected per readout cycle. At the same time, the DUT, which relies on parallel readout with 25 ns time resolution, detects mostly one hit per readout cycle. This means that the DUT only provides hit information for the first particle which triggered the readout. For all remaining particles detected by the beam telescope, no DUT information is available as only hits can be considered which are within the requested DUT readout cycle. Therefore, an additional external timing reference is required. This is implemented by a second unirradiated SCA, also denoted as REFERENCE device REF, mounted behind the last telescope plane. The DUT and REF are operated synchronized to guarantee that their 25 ns clock phases, which correspond to a DUT and REF event, are synchronous. In the offline analysis, the telescope

² Optimal hit efficiency and spatial resolution results are obtained for particle rates below 1 kHz.

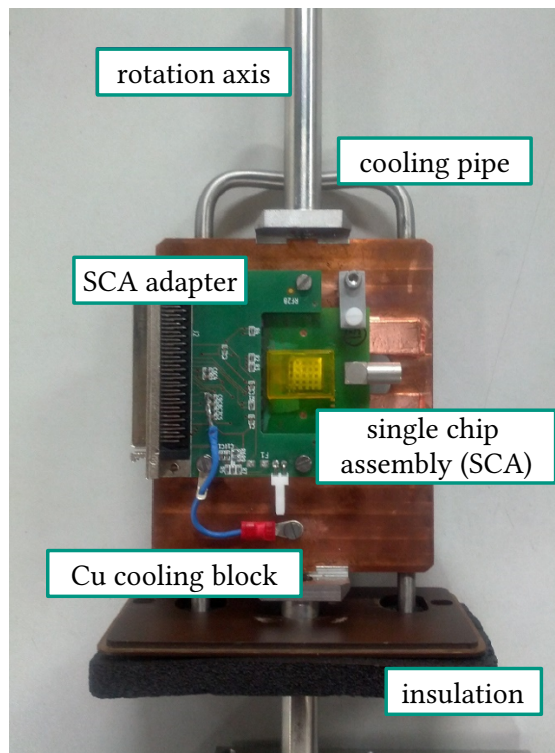


Figure 9.3: DUT cooling chuck used for the test beam. The DUT, connected to an SCA adapter, is placed on a copper block which is cooled down to -22°C with the help of an ethanol chiller. A small part of the box and its insulation are visible in the lower part, while the main part is removed in this picture. The rotation axis, connected to the θ -stage, allows to perform DUT measurements under different tilt angles with respect to the particle beam.

tracks are matched with the REF hits. Hence, all tracks having a REF link correspond to the correct time frame and are thus suited for the analysis of the DUT.

The setup used in the test beam study including the DATURA beam telescope and the DUT is shown in figure 9.2. In contrast to the telescope planes and the REF, the DUT is mounted upside-down for practical reasons. This means that row 1 of the DUT is at the top and row 80 is at the bottom. Similarly, the columns are oriented in reverse order compared to the telescope planes and the REF. A water cooling system allows to operate the telescope planes at a stable temperature of $+18^{\circ}\text{C}$.

The DUT is placed on a copper cooling block inside a thermally insulated box, as shown in figure 9.3. To avoid condensation inside the box it is flushed with dry air. In the center of the copper cooling block a window is milled out to avoid absorption and multiple scattering of the particle beam. The cooling system required to operate irradiated samples and to obtain stable temperatures relies on an ethanol chiller providing a temperature of -22°C . The entire setup is mounted on a motorized x -, y - and θ -stage allowing to align the DUT precisely in the particle beam. Additionally the θ -stage is used to investigate the SCA performance for different tilt angles. This emulates the possible entrance angles of particles in the CMS pixel detector.

The readout of the telescope, the DUT and the REF is triggered by four scintillators equipped with Silicon PhotoMultipliers (SiPM). Two of them are mounted directly in front of the first telescope plane and the other two are located behind the last plane but in front of the REF. Three out of the four SiPMs are directly connected to the Trigger Logic Unit (TLU), which controls the readout of all devices. The fourth SiPM is used to implement a simplified trigger logic to guarantee that the trigger signal arrives within the 25 ns clock cycle of DUT and REF.

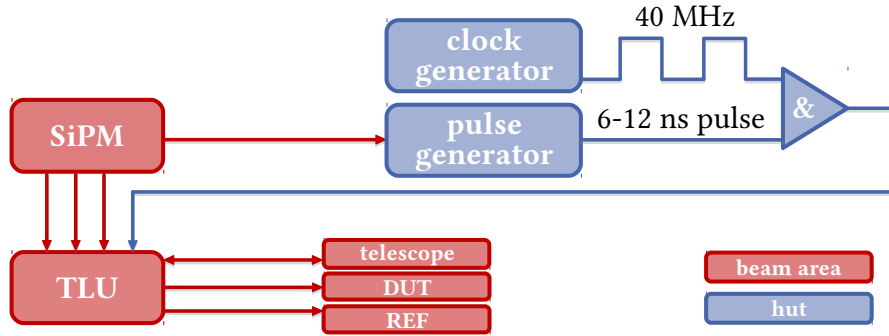


Figure 9.4: Triggering scheme of the DESY test beam setup. Three out of four SiPMs are directly connected to the TLU. The fourth SiPM signal triggers a short pulse, which is used to build the trigger logic. A coincidence unit guarantees that only trigger signals, which arrive within the 25 ns clock cycle of the DUT and REF clock are considered.

Therefore, the fourth SiPM serves as external trigger of a pulse generator which in turn creates a pulse with an adjustable length between 6 ns and 12 ns. Only in case of a coincidence between this pulse and the external DUT and REF clock, the trigger signal is passed to the TLU. The readout is triggered only when a signal of each of the three SiPMs and the coincidence signal arrive at the TLU. An additional feature of the TLU is the busy veto to account for the long readout time of the DATURA telescope, which is about 4500 times longer compared to the DUT and the REF. The busy veto remains active as long as the readout of the telescope is ongoing. This means that incoming trigger signals from the SiPMs are discarded until the readout is finished and the busy veto is inactive again [Cus09]. The complete trigger scheme is illustrated in figure 9.4.

9.1.3 THE EUTELESCOPE FRAMEWORK

The test beam analysis is part of the EUTElescope framework which was developed within the EUDET project. The EUTElescope framework, in turn, is embedded in the ILCSOFT framework used for detector development for the ILC [GE07]. The ILCSOFT framework relies on the Linear Collider I/O (LCIO) data format, the Modular analysis & reconstruction for the linear collider (Marlin) event processor, the GEOMETRY API for Reconstruction (GEAR) markup language and the Abstract Interface for Data Analysis (AIDA). Marlin controls the successive execution of several subroutines called processors. All processors have their own set of individual parameters stored in customizable eXtensible Markup Language (XML) files. Each processor stores its results in an LCIO file, together with the results obtained by the previous processors. Due to the modular approach of the analysis chain, it is very flexible and can be used in a variety of applications. The EUTElescope framework contains several event processors and XML files which are well adapted to the needs of test beam analyses.

LCIO is an event-based data format. For each positive trigger decision an event is generated containing all data of the corresponding trigger. The events are numbered consecutively and consist of an event header and the event data. The event header, which comprises information about the detector, the timestamp and the measurement (run) number, remains unchanged during the analysis. In the event data part several data collections are stored. For each executed processor one or more collections are added to the associated LCIO file. The individual collections can be addressed by their unique hexadecimal ID.

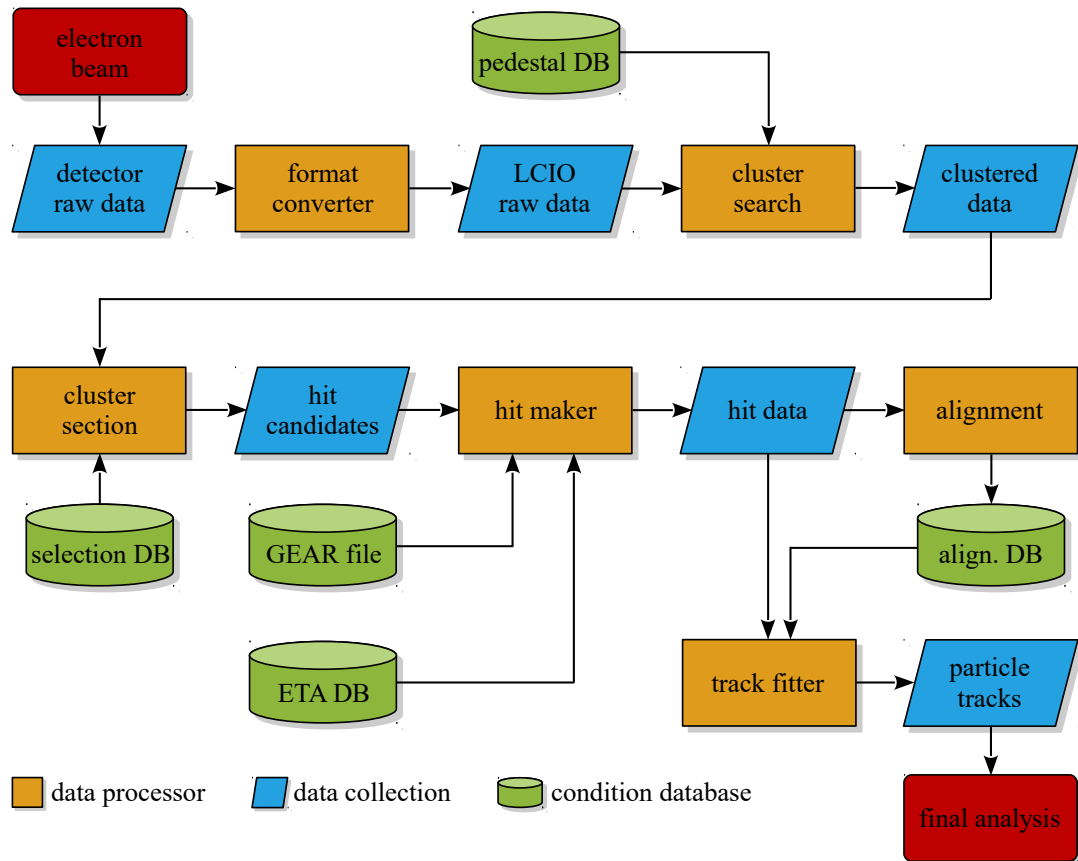


Figure 9.5: Workflow of the EUTelescope analysis framework. The particle tracks are reconstructed from the raw data by consecutively executing several Marlin processors. In each processor a new LCIO data collection is created. Additionally, databases are either loaded to obtain information about the telescope geometry or generated to store alignment parameters. Finally, the obtained particle tracks are used to perform the DUT analysis. Modified from [EUT17].

The DATURA telescope geometry is stored in GEAR files, containing information about each telescope plane, its material properties and pixel size. When a processor is executed, it accesses the GEAR files – if required – to obtain the geometry data.

An overview of the analysis workflow is illustrated in figure 9.5. Each analysis starts with the tracker raw data, containing zero-suppressed data of the telescope, DUT and REF. Zero-suppressed data means that pixels without hit information are excluded in order to keep the file size as small as possible. In the first processor, the raw data is converted into the LCIO format, which brings the benefit that the data of all detectors is available in the same format. Afterwards the clustering processor searches for adjacent pixels containing hit information to combine them into clusters. The pixel with the highest signal height in a cluster is called the seed pixel. The search for the seed pixel is only implemented for DUT and REF, as the MIMOSA26 does not provide information about the signal height. The clustering processor also determines noisy pixels of the telescope and excludes them from the analysis. From here on, only the DATURA telescope data is processed further, while the DUT and REF data remain unprocessed until the final analysis step. The next processor is the hitmaker, which uses the telescope geometry stored in the GEAR files to transform the cluster coordinates into the global telescope reference frame. All clusters in the reference frame are called hit candidates. They are used by the alignment processor to precisely align the telescope planes to each other. This

step is necessary, as the geometrical description which is stored in the GEAR files is only approximately determined by the test beam user. Then, the hit candidates are used by the track fitter processor to determine the particle tracks. In the final analysis step, the particle tracks are applied to perform the analysis of the DUT data.

9.1.4 EUTELESCOPE ANALYSIS PROCESSOR FOR CMS PIXEL SAMPLES

This section is dedicated to the EUTelAnalysisCMSPixel processor, which is the last step of the analysis chain. This processor is custom-tailored according to the needs of SCAs equipped with PSI46dig ROCs. It combines the particle track data with the DUT and REF data to determine the DUT performance.

First, the processor performs a rough pre-alignment of DUT and REF by using tracks of the upstream and downstream planes, respectively. This pre-alignment is already sufficient for the REF. For the DUT, a more precise alignment has to be performed with the help of the Millepede-II [BKM11]. Millepede-II relies on a global minimization approach of all track and alignment parameters, which is applied for the alignment of the CMS silicon tracker, as well. It determines the alignment parameters and stores them in a dedicated file. When the processor is executed the next time, the parameters are read and applied to the data. This means that the final alignment is obtained by an iterative execution of the EUTelAnalysisCMSPixel processor, which converges typically after few times.

As explained previously in this chapter, the REF serves as time reference to perform a pre-selection of the telescope tracks. To investigate certain DUT properties, only tracks with a REF hit can be used. This is especially true for the detector efficiency, which is defined by the following equation.

$$\text{efficiency}_{\text{DUT}} = \frac{\text{tracks with REF and DUT hit}}{\text{tracks with REF hit}}$$

In the DUT analysis a distinction between several hit types is made to account for the different investigated properties. The first type are all DUT hits without any restrictions, called DUT hits. The second type are DUT hits having a corresponding REF hit which are denoted as linked hits. The third type are called fiducial hits and refer to all hits in pixels with a size of $100 \mu\text{m} \times 150 \mu\text{m}$. As described in section 4.2.1, the pixel sensor has larger pixels at three of its four edges. These larger pixels are excluded for several results as they behave differently. The strictest hit type are thus linked fiducial hits. The following list contains the investigated properties and the associated hit type.

- Cluster Size: As explained in section 3.4 charge sharing leads to clusters of pixel hits in the silicon sensor. The average number of pixels hit by a particle traversing the sensor increases with tilt angle. To study this property no track information is required, hence fiducial hits are sufficient.
- Hit efficiency: With the help of reconstructed tracks it is possible to determine the DUT hit efficiency. The reconstructed tracks also allow to measure the efficiency as a function of the track impact position inside the pixels (intrapixel efficiency). In this case linked fiducial hits are necessary.
- Spatial resolution: Due to the excellent resolution of the telescope track it is possible to investigate the DUT resolution. Similar to the hit efficiency study, the absolute and the intrapixel resolution can be determined. However, there is one special requirement related to the investigation of the absolute resolution. To measure the resolution precisely, it is necessary to take the pointing resolution of the telescope tracks (at the DUT position) into account. Regarding the intrapixel resolution this is of less relevance. Again linked fiducial hits are required.

9.2 MEASUREMENT PROGRAM

Several potential measurement programs were elaborated prior to the test beam measurement. They address identical topics, but differ in the number of measurement points to stay flexible regarding the test beam uptime. Technical problems interrupting the test beam operation are not typical, but still occur every now and then, requiring an adjustment of the measurement program. Extending the measurement time is not possible due to the schedule of the test beam facility.

The program introduced in table 9.1 refers to the measurements as they were finally performed during the test beam study. The given parameters are selected with respect to the investigation of the hit efficiency and the spatial resolution.

First of all, the test beam measurements cover a wide range of tilt angles (up to 75° exclusively in y-direction) to account for all possible entrance angles of charged particles traversing the pixel detector inside CMS. The second parameter of interest is motivated by the observed effect of the bias voltage on the measured signal heights (see chapter 8). Hence, a potential impact of the bias voltage on the hit efficiency and the spatial resolution is investigated. Thirdly, two different comparator thresholds are studied, the standard threshold of 35 Vcal and a lower one of 30 Vcal. This allows to test if the detection of even smaller signals is beneficial for the detector performance.

Table 9.1: Measurement schedule of the test beam study. The impact of different comparator thresholds, bias voltages and tilt angles is investigated for all irradiation steps. A detailed measurement program was performed for the first four SCAs shown in the table. The remaining SCAs (SD98 and SD90) were used in a finer tilt angle scan at a fixed threshold and bias voltage. Tilt angles marked with a (*) were investigated for additional bias voltages, comparable to the first four SCAs.

Sample	irradiation (n_{eq})	threshold (Vcal)	bias voltage (V)	tilt angle ($^\circ$)
SD87	unirrad	30/35	100/150/200	0/15/35/55/75
SD89	1e14	30/35	100/200/300/400/500	0/15/35/55/75
SD88	2e14	30/35	100/200/300/400/500	0/15/35/55/75
SD99	4e14	30/35	200/300/400/500/600	0/15/35/55/75
SD98	2e14	35	500	0*/5/10/15/20/35/55/75
SD90	4e14	35	500	0*/5/10/15/20/35/55/75

9.3 TEST BEAM RESULTS

In the following section the results of the test beam study are discussed. Prior to the measurements the samples were electrically calibrated in the test beam setup. All samples were fully operational and the desired measurements have been performed for each irradiation step. The irradiated samples were operated at a temperature of -22°C , while the unirradiated sample was tested at 0°C . For each measurement – also called run in the context of the test beam – a minimum of 500,000 events was recorded.

9.3.1 ASYNCHRONOUS DATA

The EUDAQ software responsible for data taking comes with an online monitoring tool providing rough data quality control already during data taking. It allows to monitor the hit maps

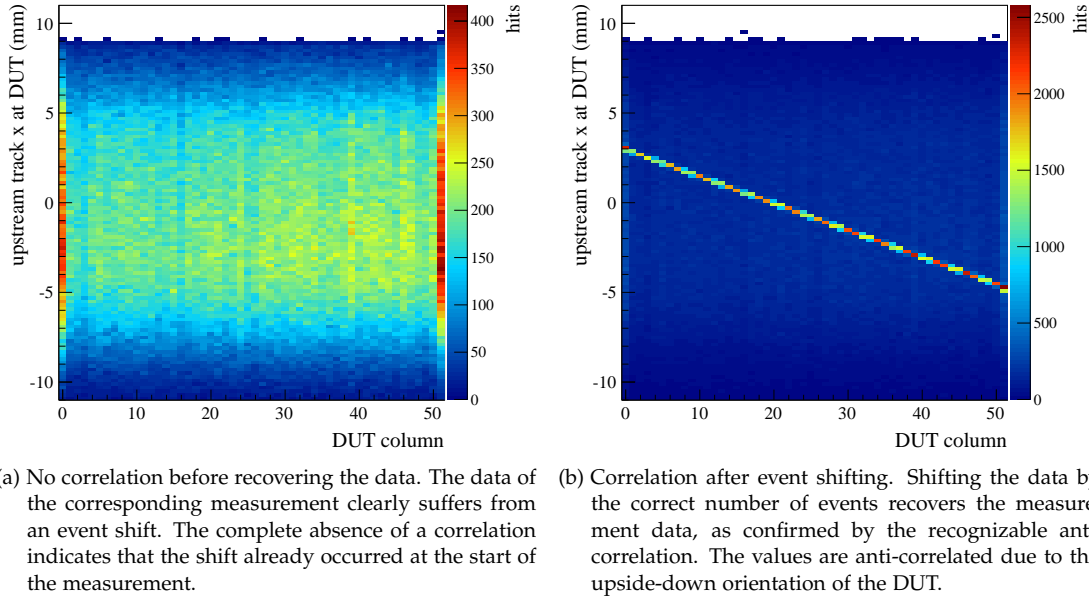


Figure 9.6: Correlation plots before and after event shifting. The two plots contain the same data. They allow to investigate the correlation between the column information of the DUT hits and the x-coordinates of the upstream tracks extrapolated to the DUT position.

of the telescope planes, the DUT and the REF as well as the associated correlation plots. To guarantee that the **Online Monitor (OM)** is able to keep up with the data acquisition, only every tenth event is processed. Since the OM crashed sometimes, a complete live control of the data quality could not be carried out during the test beam campaign.

A single problem occurred during data taking, which remained unidentified in the OM and thus was only revealed in the data analysis. It became apparent that the DUT and REF data of some measurements was not synchronous to the telescope data. This is caused by one or more missing events in the DUT and REF data. As soon as the data is asynchronous, it is no longer possible to find DUT and REF hits matching the telescope tracks. With such data, an investigation of properties like hit efficiency and spatial resolution would be impossible. Nevertheless, the data of all affected runs was successfully recovered by performing a comprehensive investigation, where events were shifted over a wide range (by skipping telescope events). Altogether, shifts of up to 100 events were performed. However, this implies that the last processor of the analysis chain had to be executed 100 times for each run, which is very time-consuming. While the processing time of a single run typically is of the order of a few minutes, it takes several hours for this investigation. To make use of the entire data, it has to be taken care of that only asynchronous events are shifted in the final analysis. Therefore, the analysis was divided into blocks of 10,000 events to determine at which event number the shift occurred. Since a manual evaluation of the corresponding results would be too time-consuming, an automatic approach was implemented. It relies on the correlation between the column information of the DUT hits and the x-coordinate of the upstream tracks. Only if the DUT data is shifted by the correct number of events, a correlation is visible (see e.g. figure 9.6 (b)). The occurrence of a correlation is recognized by a simple routine, which stores in turn the correct shift value in a text file. Once all shifts are identified, the final analysis is executed once more, but this time reading in the shift values and applying them to the corresponding events.

Figure 9.6 (a) gives an example of a run in which a shift occurred already at the start of the measurement, so that no correlation is visible at all. The same run is shown in figure 9.6 (b), but after reestablishing the data synchronicity via event shifting. The correlation, or more

precisely the anti-correlation (due to the upside-down orientation of the DUT), is clearly visible. Because of the smaller DUT size compared to the telescope planes the correlation line does not extend over the entire y-axis range.

As mentioned before, this problem was not identified in the OM tool for multiple reasons. First of all, the event shifts cannot be recognized in the hit maps of the DUT, the REF and the telescope planes. Second, the correlation plots between DUT and REF remain intact, as both suffer equally from the event shifts. The same is true for the correlation plots between the six telescope layers. Only the correlation plots between the telescope planes and the DUT respectively the REF are affected. However, also these plots might contain a correlation as the shifts do not necessarily occur at the start of the measurement. In such cases, the correlation remains visible even after the event shift. Only a deliberate investigation concerning the entries per pixel of such a plot might reveal a too small ratio between the calibration line and the background (blue area in figure 9.6 (b)). Therefore, it is barely possible to identify this problem in the OM without knowing of its existence. Additionally, the identification of the problem is complicated further due to occasional crashes of the OM.

After the problem was identified in the analysis, the persons responsible for the DESY test beam were contacted who could confirm that they had observed the same behavior. They assume that the problem is linked to the trigger logic [Sch17], which matches the results (on the asynchronous data) presented in appendix G.1. Nevertheless, the most important result is that all runs were recovered successfully.

9.3.2 CLUSTER INVESTIGATION

As described previously in this thesis, the CMS pixel detector exploits charge sharing to improve its spatial resolution. To be able to benefit from charge sharing, clusters containing at least two pixels are required which makes the cluster size an important property. Inside CMS the magnetic field guarantees that practically all charged particles traverse the pixel detector layers under an angle, which is an excellent condition to avoid single pixel clusters. In fact, depending on the position inside the CMS pixel detector, large angles of at least 75° are possible. Aside from the tilt angle, there are additional interesting properties which might affect the cluster size, like bias voltage, comparator threshold or radiation damage. Hence, this section is dedicated to studies of the cluster size.

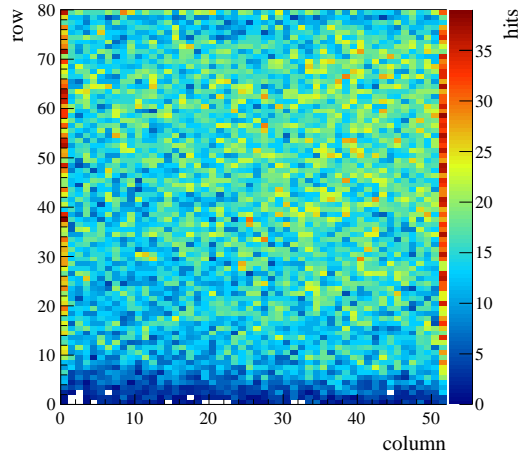
There are several methods to perform the clustering. The method employed by the CMS experiment is called Template Matching (see e.g. [CSF⁺08]) which requires a detailed simulation of the detector response depending on properties such as the particle incident angle and the radiation damage. However, this method is too complex to be applied in a test beam study. The method used instead is the **C**enter of **G**ravity (CoG) algorithm, which is probably one of the most popular clustering algorithms. It relies on the first raw moment of the cluster charge distribution where the cluster center is determined by the following equation.

$$x_{\text{CoG}} = \frac{\sum Q_i x_i}{\sum Q_i} \quad (9.1)$$

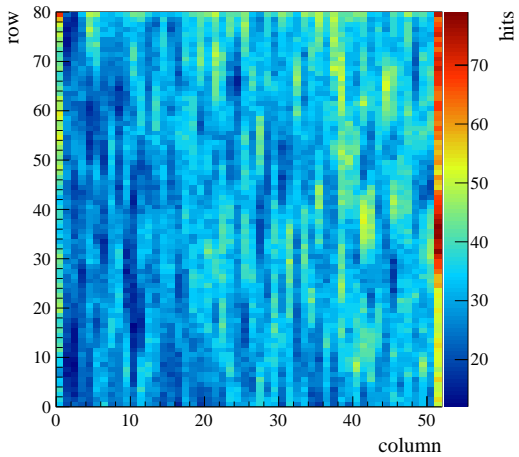
Q_i is the charge collected by a pixel i at the pixel coordinate x_i . For clusters formed by more than two pixels there is no further gain in resolution. Additional clustering algorithms are described for instance in [Tur93].

9.3.2.1 Test Beam Hit Maps

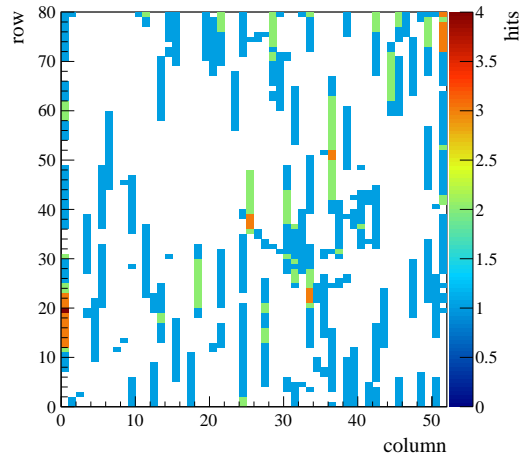
The hit maps obtained during the test beam show the impact of different tilt angles on the cluster size. Figure 9.7 (a) shows the hit map for an unirradiated SCA at a tilt angle of 0° . Since



(a) Hit map obtained at 0° . Electrons penetrate the DUT perpendicularly creating mostly single pixel clusters. There is no recognizable pattern.



(b) Hit map obtained at 75° . Electrons traversing the DUT generate large clusters due to the large tilt angle. A pattern along the columns is clearly visible.



(c) Hit map obtained at 75° for a small data fraction. The pattern, caused by clusters containing ten or more pixels, is clearly visible.

Figure 9.7: Hit maps of an unirradiated SCA obtained from the test beam study. The hit maps correspond to measurements at 0° and 75° . All other other parameters like bias voltage or comparator threshold are identical.

the electrons traverse the sample perpendicularly they mostly generate one pixel clusters. In figure 9.7 (b) a measurement of the same SCA at 75° is presented. Due to the large tilt angle, the clusters are significantly larger along the columns as particles traversing the SCA deposit charge in multiple pixels. The corresponding pattern is clearly visible in the hit map. This is even more distinct in figure 9.7 (c) which shows only a small fraction of the 75° data presented in figure 9.7 (b).

9.3.2.2 Cluster Size Distribution

The hit maps presented above clearly show the influence of the tilt angle on the cluster size. In the following, the cluster size distribution depending on the tilt angle is discussed in more detail.

Figure 9.8 presents the normalized cluster size distribution for each irradiation step including the unirradiated case. For the sake of convenience the irradiated samples are called $1e4 n_{eq}$, $2e14 n_{eq}$ or $4e14 n_{eq}$ sample. The measurements cover a wide range of tilt angles from 0° to 75° and the values given in the legends refer to the set tilt angles. The actual tilt angles are determined in the analysis and can deviate by up to $\pm 3^\circ$ from the set values. However, in this special case where four different graphs are compared, the set values are considered for convenience.

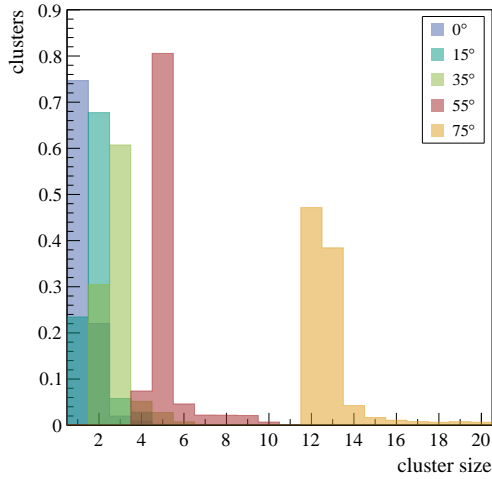
In all four graphs a significant increase of the cluster size is visible for higher tilt angles. As expected, the fraction of single pixel clusters is dominant in all measurements at 0° . Already at 15° the distributions are clearly shifted towards two pixel clusters, which is desired to improve the spatial resolution via charge sharing. At 75° , the highest investigated tilt angle, the clusters are formed by ten and more pixels. Comparing the four distributions reveals that there are some differences especially at the 75° measurements. But in fact, these differences are explained by purely geometrical considerations. As stated above, the uncertainty on the set tilt angles is about $\pm 3^\circ$, which has the strongest impact on the cluster size at high angles. Using the tangent of the actual tilt angles together with the sensor thickness of $285 \mu\text{m}$, provides estimated cluster sizes, which match the results of figure 9.8. The actual tilt angles (determined from the analysis) are $\theta_{unirrad} = 76.5^\circ$, $\theta_{1e14 n_{eq}} = 77.5^\circ$, $\theta_{2e14 n_{eq}} = 74^\circ$ and $\theta_{4e14 n_{eq}} = 75^\circ$. The corresponding calculated cluster sizes are $C_{unirrad} = 12.9$ (12.8), $C_{1e14 n_{eq}} = 13.8$ (13.9), $C_{2e14 n_{eq}} = 11.0$ (10.8) and $C_{4e14 n_{eq}} = 11.6$ (11.4) with the values in brackets referring to the 75° results of the distributions.

In any case, the results presented in figure 9.8 are fine, as the cluster size distributions are very comparable within the given uncertainty. This proves that the clusters sizes at the end of the operating period for layers 2 to 4 of the CMS pixel detector are barely affected by radiation damage.

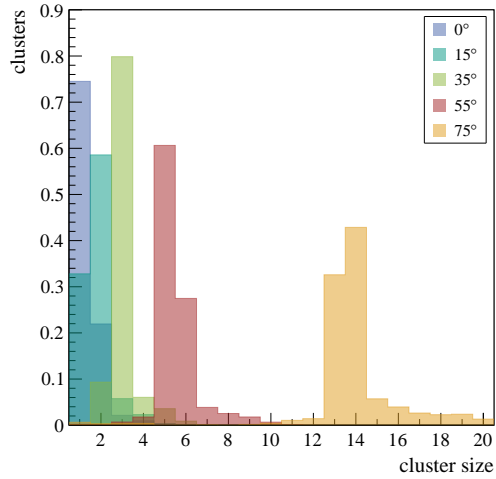
9.3.2.3 Tilt Angle Dependency of the Mean Cluster Size

In this section, the cluster size dependency on the actual tilt angle is discussed. The actual tilt angle is determined during analysis and has an uncertainty of 0.2° which is rather small compared to the set values (see the previous section 9.3.2.2). Additionally, the investigation of the tilt angle includes a comparison of two different comparator thresholds.

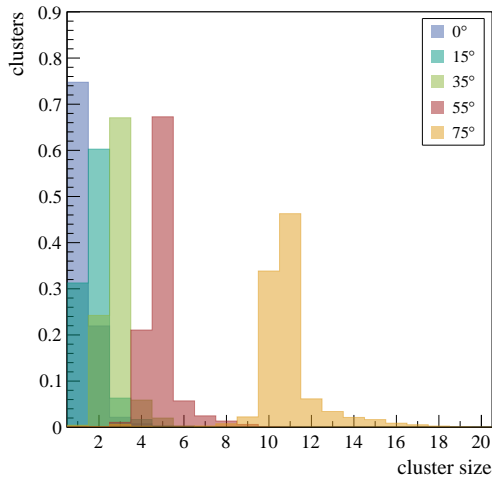
Figure 9.9 shows the cluster size as a function of the actual tilt angle. The uncertainty of the cluster size is given by the standard deviation, while the uncertainty on the tilt angle is too small to be recognized (hidden by the markers). At large tilt angles the cluster size uncertainty increases, as the recorded number of tracks penetrating the DUT decreases due to the shallow angle. For each irradiation step and tilt angle there is one measurement with the standard comparator threshold of 35 Vcal and another one obtained with a lower threshold of 30 Vcal . In case of the unirradiated SCA these thresholds correspond to 1750 and 1500 electrons, respectively.



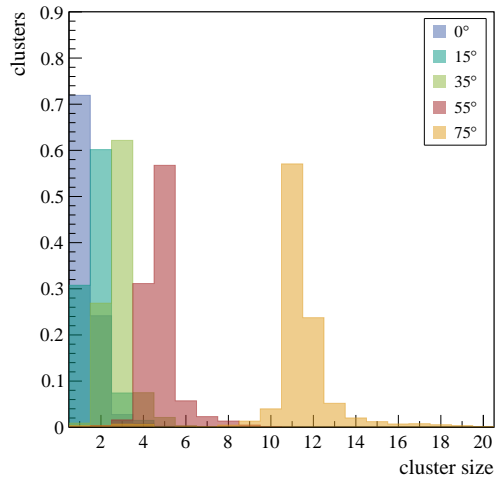
(a) Cluster size distributions for different tilt angles for an unirradiated SCA.



(b) Cluster size distributions for different tilt angles for a $1e14 n_{eq}$ SCA.



(c) Cluster size distributions for different tilt angles for a $2e14 n_{eq}$ SCA.



(d) Cluster size distributions for different tilt angles for a $4e14 n_{eq}$ SCA.

Figure 9.8: Normalized cluster size distributions for different tilt angles and levels of radiation damage. The tilt angles stated in the legends correspond to the set values which are more suitable for comparing the distributions. The actual tilt angles are determined in the analysis and differ by up to $\pm 3^\circ$. All graphs show a significant cluster size increase for larger angles. Differences between the distributions are caused by small deviations of the actual tilt angle.

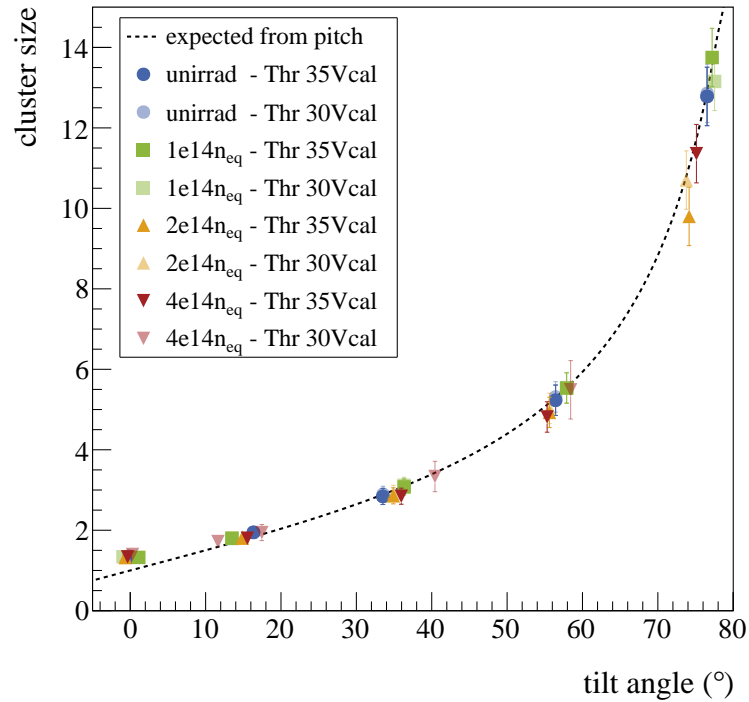


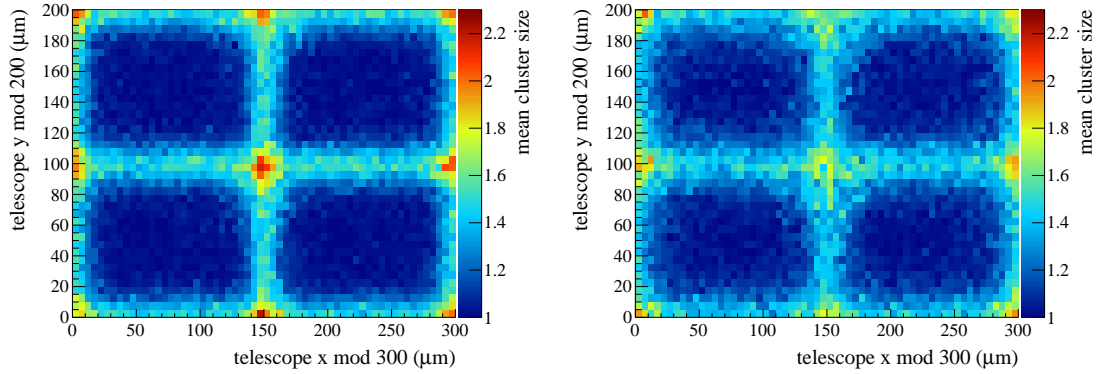
Figure 9.9: Cluster size as a function of the actual tilt angle. The graph shows the cluster size over a wide range of tilt angles for all irradiation steps including the unirradiated case. The uncertainty on the cluster size is calculated by the standard deviation, while the uncertainty of the tilt angle is 0.2° (from the analysis), which is too small to be recognizable. The cluster size clearly increases for higher values and matches the expected values for the entire range (there is only a small deviation at 0°). Irradiation as well as different comparator thresholds do not seem to affect the cluster size.

The graph confirms, as already indicated in section 9.3.2.2, that the actual tilt angles of the investigated DUTs are different. However, considering the actual values reveals a good correlation between the measured cluster size and the calculated cluster size expected from pure geometry. In addition, there are no deviations caused by the different irradiation steps. Further, there is also no impact of the two different comparator thresholds. Probably the threshold difference has to be larger to affect the cluster size. Investigating even smaller thresholds is almost impossible, as the comparator working point is no longer optimal below thresholds of 30 Vcal as observed in [Zim16].

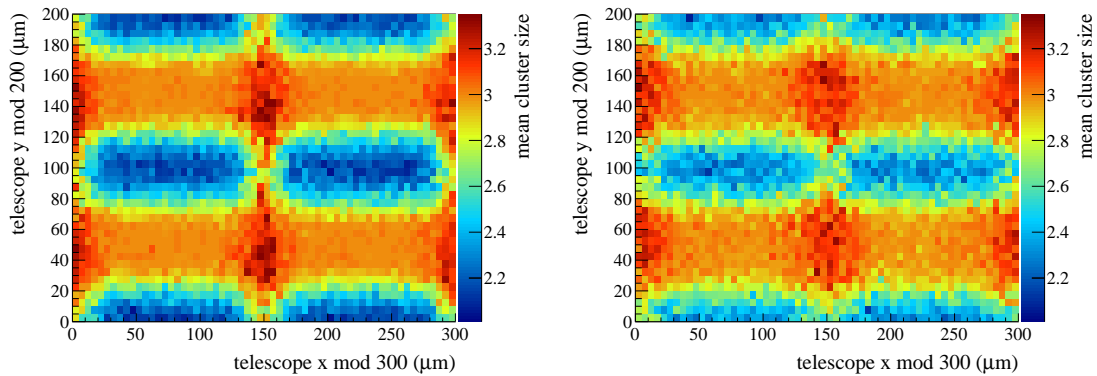
9.3.2.4 Intrapixel Cluster Size Distribution

The analysis also provides the option to investigate detector properties, like cluster size, spatial resolution and hit efficiency as a function of the position inside the pixels. This allows to verify if there are positions inside the pixel cells which behave differently than expected. All measurements referring to this intrapixel behavior are shown as 2×2 pixel arrays. Instead of relying only on the hits recorded with four pixels all fiducial hits are folded into the mentioned 2×2 array while the corresponding axis titles are marked with the suffix mod³. The results presented in this section refer to the tilt angles (0° and 35°) that provide the most interesting effects. Results for additional tilt angles are given in appendix G.2.1.

³ Derived from the modulo function applied to create such 2×2 pixel arrays.



(a) Mean cluster size for an unirradiated sample at 0° . The large clusters correspond to electron impact positions between pixels. The mean cluster size inside the pixels is close to one.
 (b) Mean cluster size for a $2e14 n_{eq}$ sample at 0° . Due to radiation damage the contours are less sharp compared to the unirradiated SCA. Apart from that the samples behave identically.



(c) Mean cluster size for the unirradiated sample at 35° . Due to the tilt the electrons travel $200 \mu\text{m}$ in y-direction. As a result, large cluster sizes correspond particularly to impact positions in the pixel center. If, in addition, electrons enter the DUT between two pixels in x-direction, the mean cluster size becomes even larger.
 (d) Mean cluster size for a $2e14 n_{eq}$ sample at 35° . Again the contours are less sharp for the irradiated sample due to radiation damage. Besides that the overall behavior is similar.

Figure 9.10: Mean cluster size depending on the electron impact position inside the pixels. The results correspond to an unirradiated and a $2e14 n_{eq}$ SCA measured at tilt angles (in y-direction) of 0° and 35° . The unirradiated sample was tested at a bias voltage of 200 V and the $2e14 n_{eq}$ sample at 500 V . All fiducial hits are folded into 2×2 pixel arrays to increase the statistics.

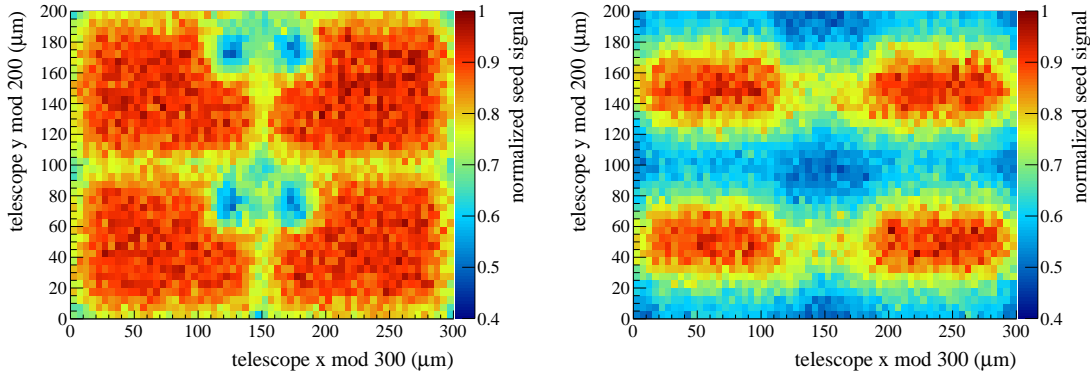
The plots in figure 9.10 show the mean cluster size as a function of the electron impact point inside the pixels. It compares the results obtained for an unirradiated SCA and an SCA irradiated to $2e14 n_{eq}$. Additionally, it shows the influence of the tilt angle on the intrapixel cluster size. As mentioned in the introduction of the measurement program the tilt always refers to the y-direction.

The results were obtained with bias voltages of 200 V for the unirradiated SCA and 500 V for the irradiated SCA. Figure 9.10 (a) shows the result of the unirradiated SCA for a tilt angle of 0° . The mean cluster size in the center of the pixels is close to one. This is expected as electrons hitting the DUT perpendicular in the pixel center deposit energy almost exclusively in the corresponding pixel. For electron impact positions between two pixels, the mean cluster size clearly increases as charge is typically collected by two pixels. Accordingly the largest cluster size is located at the corners where four pixels meet. All these results match the expectation. The result of the $2e14 n_{eq}$ sample at 0° is shown in figure 9.10 (b). The basic structure, which has been seen in the result of the unirradiated SCA, is still visible. However, the contours are less sharp (for comparable statistics) indicating the influence of radiation damage on the detector performance. Nevertheless, the mean cluster sizes of the unirradiated and the $2e14 n_{eq}$ SCA are basically identical as recognizable by the color scaling. Figure 9.10 (c) and (d) allow to compare the mean cluster sizes for a tilt angle of 35° . The distribution inside the pixels clearly changed in contrast to the 0° results. On the one hand, the mean cluster size increased as indicated by the z-axis. This is expected according to the results presented in section 9.3.2.2. On the other hand, both plots show that the large clusters no longer correspond to electron impact positions between pixels (referring to the y-direction). Instead, large clusters are generated when electrons hit the DUT in the center of the pixels. This is related to the distance of $200 \mu\text{m}$ which electrons travel – in y-direction – inside the DUT at 35° . It means that electrons traverse almost exactly two pixels if they enter the DUT in between two pixels. However, if the electron impact position is in the center of a pixel, they traverse the first pixel partially, a second one completely and a third one again partially. Hence, they deposit energy in three pixels. This is also indicated by the color scaling showing a mean cluster size of three in the pixel center. If, in addition, electrons enter the DUT between two pixels in x-direction, the cluster sizes became even larger. Further, a comparison of the plots shows that the contours are less sharp for the irradiated sample. Aside from that they behave identically.

9.3.2.5 Intrapixel Signal Height of the Seed Pixel

In order to obtain additional information about the behavior of the pixel detector, the seed pixel can be investigated. The seed pixel is the pixel of a cluster which has the highest signal. Investigating the measured signal height of the seed pixel, depending on the position inside the pixel, provides information about the charge collection efficiency. Again the tilt angles (0° and 15°) providing the most interesting effects are selected. For results at additional tilt angles see appendix G.2.3.

Figure 9.11 shows two normalized seed pixel maps of the unirradiated SCA obtained at tilt angles of 0° and 15° . The signal heights are normalized to the highest measured signal height of the corresponding map. As expected, especially at 0° , the highest measured signal heights correspond to the pixel centers as shown in figure 9.11 (a). For electron impact positions in between pixels the generated charge is spread over two or more pixels, which leads to smaller signals per pixel. Further, there is another interesting observation. Each pixel contains a circular spot where the measured signals are smaller. These spots exactly correspond to the bias dot locations on the sensor which were shown in figure 4.5. The reason for the reduced signal heights is that not all charge carriers created below a bias dot are collected by the pixel implant. Instead some charge carriers are collected by the bias dot and hence do not contribute to the signal. Nevertheless, the measured signal height is still about 50% to 60% of the maximum signal height corresponding to approximately 11,000 electrons. This value is still well above the comparator threshold of 1750 electrons. A comparison with the cluster size maps shown



(a) Normalized seed pixel map at 0° . The highest measured signal heights correspond to the pixel centers. Between pixels the signal height of the seed pixel is getting smaller due to charge sharing. Each pixel has a circular spot with reduced signal heights (about 50 % to 60 % of the maximum signal). These spots correspond to the bias dots which cause a decreased charge collection as they collect some charge carriers, as well.

(b) Normalized seed pixel map at 15° . The highest measured signal heights are still in the center of the pixels. The area of reduced signal heights between the pixels is larger (compared to 0°) due to better charge sharing. The effect of the reduced charge collection efficiency caused by the bias dot is still recognizable but less distinct and smeared due to the tilt.

Figure 9.11: Normalized seed pixel map for the unirradiated SCA. The signal heights of the seed pixels are normalized to the highest measured signal. Both measurements were obtained at a bias voltage of 200 V.

in figure 9.10 reveals that the bias dot has almost no effect on the mean cluster size. In case of a negative impact a reduced mean cluster size should be visible at the bias dot location. In figure 9.11 (b) the normalized seed pixel map of a measurement at 15° is given. The area between pixels with reduced signal heights is clearly enlarged. This is caused by better charge sharing as a result of the tilt angle. Further, the influence of the bias dot is still recognizable but less distinct as it is blurred in y-direction. This reflects the expectations as the charge is no longer generated below a single position due to the tilt. Hence, the charge fraction collected by the bias dot is reduced but it has an effect on more impact positions.

The reduced signal height of the seed pixels is mostly tolerable, as the missing charge is collected by the remaining pixels of the clusters. Only charge lost due to the bias dot does not contribute to the cluster signal (see appendix G.2.2).

The results above show that there is a charge collection inefficiency caused by the bias dot. Although this inefficiency has no effect on the cluster size, it needs to be investigated if it has an impact on properties like hit efficiency or spatial resolution.

A detailed and comprehensive investigation revealed no abnormalities regarding the cluster size. This is an excellent foundation for measurements on the spatial resolution and the hit efficiency, which is discussed next. For further results on the cluster size see appendix G.2.

9.3.3 HIT EFFICIENCY

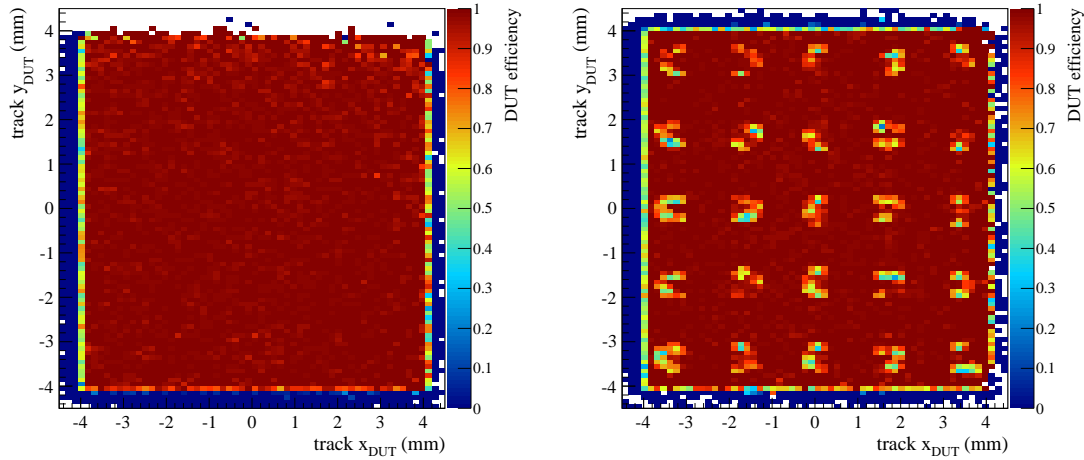
As introduced in the beginning of this chapter, the hit efficiency is an important property of the pixel detector and a requirement for reliable physics analyses. Among others, a good tracking detector is characterized by a high hit and tracking efficiency over its entire lifetime despite suffering from radiation damage. Therefore, the next sections present a detailed study of the hit efficiency.

9.3.3.1 Efficiency Maps

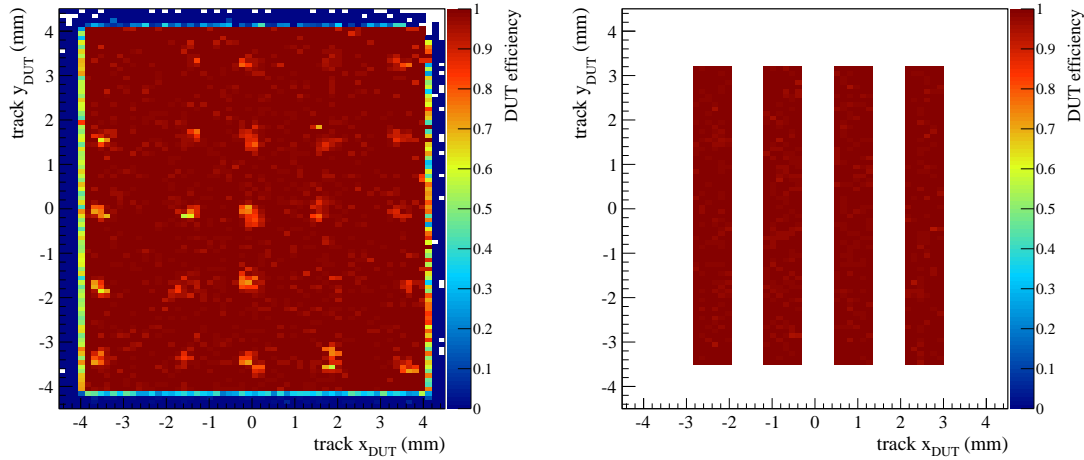
The starting point of each hit efficiency result are the efficiency maps. In the context of this thesis they are of even greater interest as they are affected by the inhomogeneous irradiation caused by the holes in the carrier PCBs of the SCAs (see section 8.1). To obtain efficiency maps, as shown in figure 9.12, all tracks having a REF link are interpolated to the DUT position. Afterwards it is examined if the DUT has a hit corresponding to the interpolated impact point (the search window is discussed in section 9.3.3.2) and the results are used to create the efficiency maps. The coordinates given in the efficiency maps are the track impact positions on the DUT in the global reference frame.

Figure 9.12 (a) shows the efficiency map of the unirradiated sample obtained at 0° . Three out of the four DUT edges are clearly recognizable. Only the upper edge of the DUT is not visible as there are no entries in the very top part. However, this is not related to a DUT inefficiency, but to the absence of tracks with a REF link. The missing linked tracks in this region are caused by a small downward shift of the REF, hence there are no REF hits in the top region. Apart from that, the efficiency map reveals no conspicuous behavior showing a homogeneous efficiency of almost 100% over the entire DUT area. In figure 9.12 (b) an efficiency map of a $4e14 n_{eq}$ sample at a tilt angle of 0° is given. Since the position of the REF was corrected meanwhile, all four edges of the DUT are recognizable. Compared to the unirradiated sample, the efficiency map contains a regular pattern of spots where the efficiency decreased to about 50% to 60%. This pattern corresponds exactly to the holes in the carrier PCBs of the single chip assemblies and is consistent with the hit maps already shown in figure 8.11, where the pattern is characterized by an increased number of hits. Figure 9.12 (c) shows a measurement of the same $4e14 n_{eq}$ SCA, but at a tilt angle of 35° . The effect of the inhomogeneous irradiation is less distinct, as recognizable by the barely visible regular pattern. This behavior is expected as the electrons traverse through more pixels compared to measurements with a tilt of 0° . Thus, the probability decreases that a particle traverses the DUT without generating a hit in one of the pixels. Nevertheless, even at 55° the pattern does not vanish completely. The results introduced above lead to the fact that the impact of the inhomogeneous irradiation must not be neglected. Therefore a cut on the efficiency map is applied as shown in figure 9.12 (d) excluding the affected pixels. The results shown in the further course are always obtained with the help of such cuts. Only at the end of the section a comparison between results obtained with and without cut is given, where the results without cut include the entire fiducial DUT area.

In addition, the effect of the inhomogeneous irradiation is clearly visible if the DUT efficiency is given as a function of the x-coordinate of the track impact position. In principle, this is equivalent to showing the efficiency as a function of the column. Figure 9.13 shows the results for an unirradiated and a $4e14 n_{eq}$ SCA. Both results are obtained at a tilt angle of 35° . The unirradiated SCA shows a constant efficiency, while the irradiated one contains distinct efficiency drops. This indicates that even at a tilt angle of 35° the efficiency is reduced by more than 5% in the affected regions (or columns). The efficiency uncertainty at the corresponding columns is slightly larger. This is due to the fact that these columns comprise both entirely intact pixels as well as less efficient ones. A comparison between the two samples in unaffected regions shows no remarkable deviation while the absolute efficiency for both is at least 99%. The efficiency results shown in the next sections focus primarily on relative values as they are less susceptible to (small) global – setup related – efficiency losses.



(a) Efficiency map of the unirradiated sample obtained at 0° . Three out of four DUT edges are visible. The upper edge is not visible as the REF was shifted downwards which led to missing tracks with REF link in this region. Apart from that the efficiency is constant (close to 1) over the entire DUT area. (b) Efficiency map of a $4e14 n_{eq}$ sample obtained at 0° . All four DUT edges are recognizable. The efficiency map shows a regular pattern of less efficient regions (50% to 60%). They are caused by inhomogeneous irradiation due to holes in the PCB holding the DUT (see section 8.1).



(c) Efficiency map of a $4e14 n_{eq}$ sample obtained at 35° . The regular pattern is less distinct, as the electrons traverse several pixels. This decreases the probability that an electron passes the DUT undetected. (d) Efficiency map of a $4e14 n_{eq}$ sample including a region cut. As the inhomogeneous irradiation clearly affects the hit efficiency a cut was applied to exclude the corresponding pixels from the analysis.

Figure 9.12: Efficiency maps for an unirradiated and a $4e14 n_{eq}$ sample. Tracks with REF link are interpolated to the DUT position. If the DUT contains a hit corresponding to the interpolated impact point a 1 is inserted, otherwise a 0 which determines the DUT efficiency per impact point. The given coordinates are the track impact positions on the DUT referring to the global reference frame.

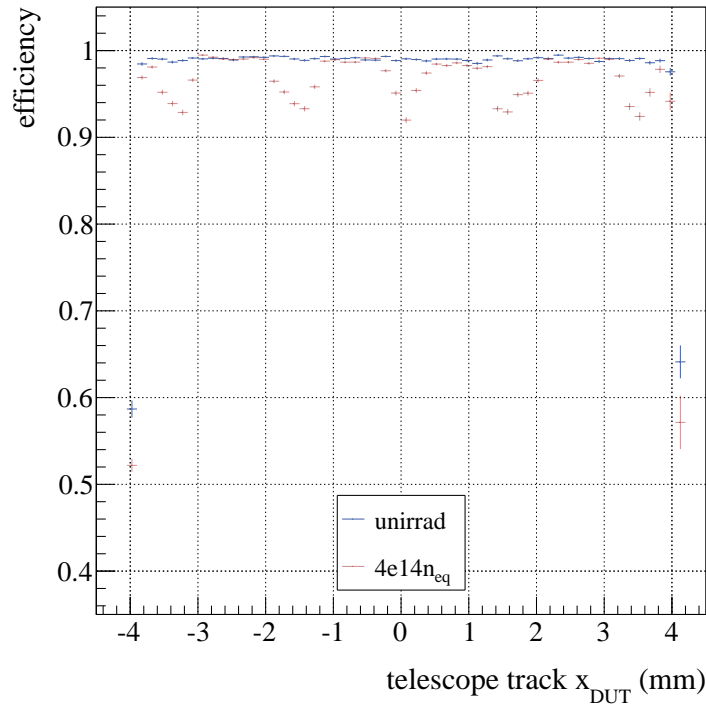


Figure 9.13: Mean DUT efficiency as a function of the x-coordinate of the track impact position. The error bars refer to the standard deviation of the mean efficiency in y. The results correspond to an unirradiated and a $4e14 n_{eq}$ SCA for a tilt angle of 35° . The unirradiated sample has a constant efficiency over the entire range, while the irradiated sample has efficiency drops of more than 5% due to the less efficient spots shown in figure 9.12.

9.3.3.2 Acceptance Window for DUT Hits

As described previously, telescope tracks with a corresponding REF hit are necessary to determine the hit efficiency. These tracks are interpolated to the DUT position and it is checked whether the DUT contains a hit at the calculated impact position or not. To identify a potential DUT hit the size of the search window around the calculated point needs to be selected reasonably. If it is too small actually existing DUT hits are not considered when they are not inside the search window. This leads to an artificial decrease of the hit efficiency. In case of a too large search window a track might be assigned to a wrong DUT hit. The optimal size of the search window is determined by investigating the hit efficiency depending on the window size. The size of the search window is described by the maximum allowed distance to the impact point (called residual cut) which is quoted in multiples of the pixel pitch. For instance, a residual cut of two times the pixel pitch considers DUT hits within $\pm 300 \mu\text{m}$ in x-direction and $\pm 200 \mu\text{m}$ in y-direction around the calculated impact point.

Figure 9.14 shows the hit efficiency as a function of the residual cut, given in multiples of the pixel pitch. This scan was performed for all irradiation steps including the unirradiated case. At large residual cuts a saturation of the hit efficiency is visible for all samples. This is expected as almost all searched hits should be considered above a certain cut. Additionally a further efficiency increase would only be possible if DUT hits not corresponding to the actual track, are wrongly considered as an actually missing hit. Since the particle rates at the test beam are relatively small, the probability to have more than one DUT hit in an event, which would be required for such an error, is negligible. Hence, the effect of too high residual cuts is almost negligible. At small residual cuts (below one pixel pitch) a distinct drop of the hit

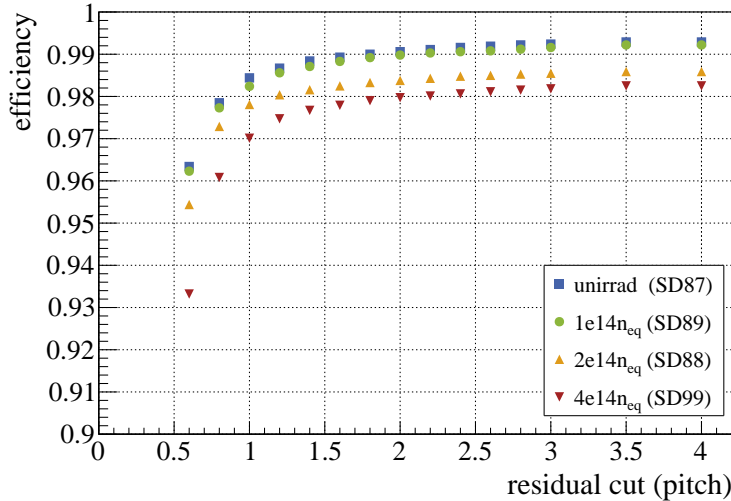


Figure 9.14: Hit efficiency as a function of the residual cut. The residual cut scan is performed for all irradiation steps. At high residual cuts the hit efficiency saturates, as all searched hits are found. A further efficiency increase due to fake hits is almost negligible because of the very low DUT occupancy. For small residual cuts a significant efficiency drop is visible, as some existing hits are no longer within the search window. The residual cut applied in the analysis corresponds to twice the pixel pitch.

efficiency is visible as existing hits are no longer within the search window. Remarkable is the fact that all samples show the efficiency drop at the same residual cut. The differences regarding the absolute efficiencies of the given samples are rather small as indicated by the range of the y-axis. In addition, a slight decrease of the hit efficiency for increasing radiation damage is visible (investigated in the next sections). The residual cut applied in the analysis corresponds to twice the pixel pitch. This value does not suffer from the effect of too small cuts, while it is still quite conservative as only DUT hits within two pixels around the impact point are considered.

9.3.3.3 Intrapixel Hit Efficiency

After determining the optimal residual cut and defining a reasonable cut on the efficiency maps (to exclude the less efficient pixels, see 9.12) a more precise investigation of the hit efficiency is possible. On this basis the intrapixel hit efficiency is investigated, similar to the cluster size and seed pixel maps.

The four intrapixel efficiency maps in figure 9.15 present the hit efficiency as a function of the track impact position. For the sake of comparison, the z-axis giving the hit efficiency is set to a fixed range between 0.7 and 1. Figure 9.15 (a) shows an intrapixel efficiency map of an unirradiated sample obtained at a bias voltage of 200 V and a tilt angle of 0° . The hit efficiency is very homogeneous over the entire area and well above 95 % as indicated by the color scaling. The result of a $2e14 n_{eq}$ SCA for a bias voltage of 500 V and a tilt of 0° is presented in figure 9.15 (b). The overall hit efficiency is still high, but four less efficient spots (less than 90 %) emerge. These spots exactly match the bias dot positions similar to the seed pixel results shown in figure 9.11. This indicates that the interplay of radiation damage and bias dots leads to a modification of the electric field inside the sensor causing an efficiency loss. As a consequence, the number of electrons collected by the bias dot increases, so that the remaining charge entering the ROC might be too small to be detected. Figure 9.15 (c) shows an intrapixel efficiency map for the same $2e14 n_{eq}$ sample at 0° , but with a bias voltage of only 100 V. At this bias voltage the sensor is not fully depleted, which is the reason for the hit efficiency decreasing further at the bias

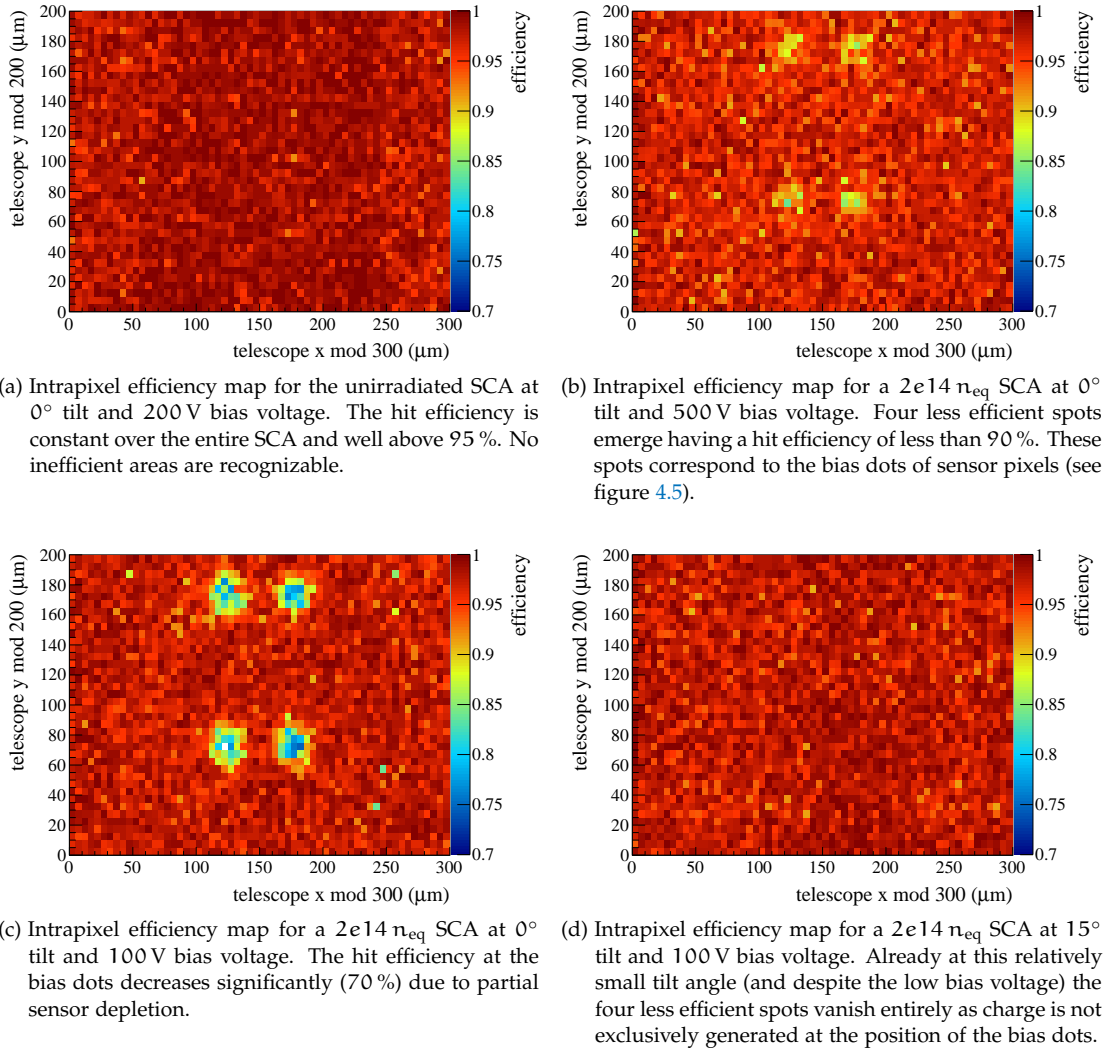


Figure 9.15: Hit efficiency as a function of the electron impact position inside the pixels. The results correspond to an unirradiated and a $2e14 n_{eq}$ sample.

dots. In fact it decreases to about 70 %. In figure 9.15 (d) again a result of the $2e14 n_{eq}$ SCA is given, but this time at a tilt angle of 15° and a bias voltage of 100 V. Already at this tilt angle the inefficiency caused by the bias dot vanishes entirely. This is due to the fact that it is not possible to generate charge exclusively at the bias dots for particles traversing the DUT not perpendicularly. Apart from that, the hit efficiency is very homogeneous and comparable to the result of the unirradiated SCA.

The effect shown in figures 9.15 (b) and (c) respectively, should be rather small for the operation of the CMS pixel detector as perpendicular particle traversals are unlikely due to the magnetic field and the non perpendicular orientation of most pixel modules with respect to the interaction point. Nevertheless, the results show that the efficiency might drop, especially if the bias voltage is too small. Hence the impact of different bias voltages on the hit efficiency is investigated next.

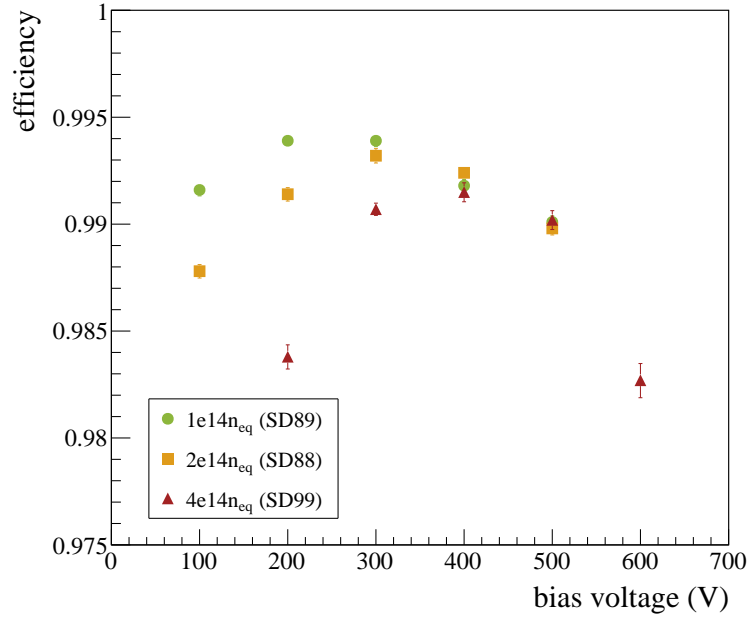


Figure 9.16: Hit efficiency as a function of the bias voltage for each irradiation step at 0° . The error bars refer to a Clopper-Pearson confidence interval of 68.3% (some error bars are too small to be visible). The SCAs show a reduced hit efficiency at lower bias voltages due to underdepleted operation resulting in smaller signal heights, which might be too small to be detected. At higher voltages the efficiency first increases before it decreases at even higher voltages. This decrease is not expected and cannot be explained by the measured signal heights.

9.3.3.4 Hit Efficiency depending on the Bias Voltage

In chapter 8 the importance of the bias voltage and its impact on the signal height especially for irradiated samples was described. Therefore this section addresses the hit efficiency depending on the bias voltage. Unirradiated samples are not relevant in this investigation, since the bias voltage has almost no effect on them and they cannot be operated underdepleted.

Figure 9.16 shows the hit efficiency for all available irradiation steps as a function of the bias voltage. All measurements were performed at a tilt angle of 0° . The efficiencies are a result of the hit efficiency maps presented in figure 9.12 and correspond to the average efficiency of the pixels inside the region cuts. The uncertainties refer to a Clopper-Pearson confidence interval of 68.3%.

First of all, it is recognizable that the maximum hit efficiency is slightly lower for higher irradiation fluences. All samples show a reduced efficiency at low voltages. Since the irradiated SCAs are not fully depleted at these low bias voltages, fewer detectable electron-hole pairs are available. This can result in some hits not being detected due to too small signal heights (especially for impact positions at the bias dot). At higher bias voltages the hit efficiency increases first, before it decreases again which is observed for all irradiation steps. This efficiency drop is not expected as the measured signal heights are continuously increasing (see figure 8.8). In fact a further increase of the hit efficiency would have been more likely according to the measured signal heights. It was not possible to identify the cause for the unexpected efficiency decrease. The results presented in this section recommend to operate the CMS pixel detectors at moderate bias voltages. In case of radiation damage caused by a fluence of $1e14 n_{eq}$ this refers to a bias voltage of 200 V to 300 V, for $2e14 n_{eq}$ it is about 300 V and 300 V to 500 V at $4e14 n_{eq}$. This guarantees to operate the sensors fully depleted without suffering from decreasing hit efficiency.

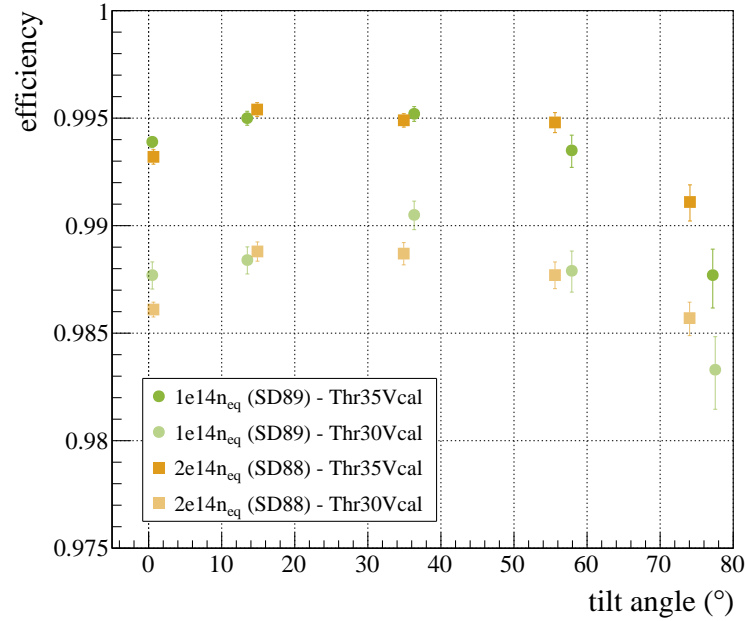


Figure 9.17: Hit efficiency depending on tilt angle and threshold. The results refer to a $1e14 n_{eq}$ and a $2e14 n_{eq}$ sample at a bias voltage of 300 V and comparator thresholds of 30 Vcal and 35 Vcal. The uncertainties refer to a Clopper-Pearson confidence interval of 68.3%. All four measurements series show a comparable trend starting with a lower efficiency at tilt angles of about 0° . At higher angles the efficiency increases before it decreases again at tilt angles larger than 55° . The hit efficiency corresponding to the lower threshold is at least 0.5% smaller.

9.3.3.5 Hit Efficiency depending on the Tilt Angle

The final investigation regarding the hit efficiency addresses the dependency on the tilt angle. Additionally, the results include a comparison between the comparator thresholds of 30 Vcal and 35 Vcal.

Figure 9.17 shows the hit efficiency depending on the tilt angle for a $1e14 n_{eq}$ and a $2e14 n_{eq}$ sample. Based on the results presented in figure 9.16 the given values correspond to measurements with a bias voltage of 300 V. Again, the uncertainties refer to a Clopper-Pearson confidence interval of 68.3%.

The four measurement series show a comparable dependency on the tilt angle starting with slightly lower hit efficiencies at a tilt angle of about 0° . This is expected as the mean cluster size is one at 0° . As a consequence, a pixel not detecting a traversing electron causes an inefficiency in most cases. At larger tilt angles the hit efficiency increases, as the cluster size rises and the probability decreases that a particle traverses several pixels without causing a hit. For the largest investigated tilt angles, the efficiency seems to decrease, but uncertainties are significantly larger. This is caused by the small number of tracks traversing the DUT at shallow tilt angles. An explanation for a potential hit efficiency drop might be related to increased multiple scattering of the traversing electrons, either because of the longer electron path inside the DUT or due to a higher scattering probability with the tilted DUT setup. Therefore, the hit efficiency values obtained for large tilt angles have to be treated with caution. Comparing the efficiency values of the two samples shows that they behave almost identically, especially with respect to the uncertainties. This is an indication that the performance remains stable for increasing radiation damage.

A comparison of the different thresholds shows that the hit efficiency obtained for the lower threshold is at least 0.5% lower. This behavior is observed for all irradiation steps including

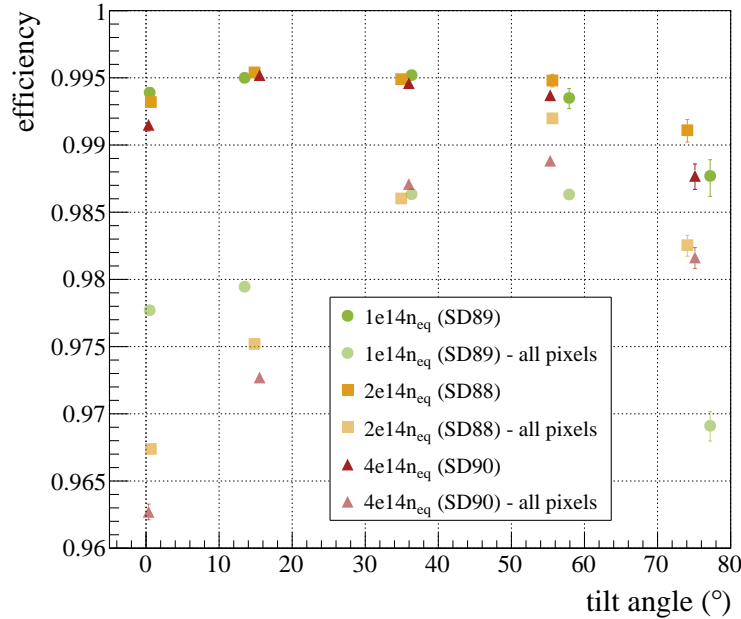


Figure 9.18: Hit efficiency depending on the tilt angle and the uniformity of the irradiation. The uncertainties refer to a Clopper-Pearson confidence interval of 68.3%. The pale markers refer to the hit efficiency determined from all pixels (including the less efficient ones) of the efficiency maps introduced in figure 9.12. The solid markers refer to the standard approach where only pixels inside the cut areas are used. All results show similar trends but the absolute efficiency values differ by up to 3%.

the unirradiated sample. Particularly at a tilt of 0° the opposite is expected, as the probability of not detecting a hit due to too small signals should be reduced. A possible explanation for the reduced efficiency might be related to the operating point of the comparator circuit which might already be slightly outside of the optimal range at 30 Vcal. A definite cause cannot be given with the available measurements. Nevertheless, the recommendation to operate the CMS pixel detector at a threshold of 35 Vcal can be made, based on the hit efficiency results.

In figure 9.18 the hit efficiency is given as a function of the tilt angle for all available irradiation steps and at the optimal bias voltage with uncertainties referring to a Clopper-Pearson confidence interval of 68.3%. The graph allows to compare the hit efficiency obtained with cuts on the efficiency maps presented in figure 9.12 to the efficiency obtained without these cuts, which considers all pixels including the less efficient ones (caused by inhomogeneous irradiation). The consideration of all pixels leads to an increased uncertainty of the hit efficiency due to the larger deviation of the efficiency per pixel.

The comparison shows that the basic behavior is similar, while there are distinct differences regarding the absolute values. In fact, the hit efficiency obtained from all pixels is up to 3% lower. This difference is smaller at higher tilt angles and gets minimal for 55° due to larger clusters (see figure 9.7). Large clusters minimize the probability that a particle traverses the DUT without generating a hit in a pixel. However, it is necessary to increase the residual cut in y -direction (from two to five times the pixel pitch) for the results including all pixels because of the following reason. The increased residual cut accounts for clusters which are split up by a less efficient pixel and thus have shifted centers of charge. These shifted centers of charge might be outside of the search windows surrounding the impact point and would not be considered if the residual cut is not increased. Still, figure 9.18 confirms the negative impact of the inhomogeneous irradiation.

The investigation of the hit efficiency shows, that the estimated amount of radiation damage only has a minimal impact. This is a positive indication for the expected performance of the CMS pixel detector. An inhomogeneous irradiation as observed in this study is not expected for the pixel detector, so that the corresponding negative impact should not be relevant for its operation. For additional results on the hit efficiency see appendix G.3.

9.3.4 SPATIAL RESOLUTION

Apart from the hit efficiency, the spatial resolution is the second property determining the performance of the CMS pixel detector. A high spatial resolution is necessary to provide good momentum resolution and efficient τ - and b-tagging. Therefore, the final sections of this chapter are dedicated to the investigation of the spatial resolution of the CMS pixel detector.

9.3.4.1 Intrapixel Resolution

First of all, the spatial resolution depending on the track impact position is studied. The resolutions given in the next two sections are simply determined by the **Mean Absolute Difference (MAD)** which is the average of the absolute distances between DUT hit and track impact position. Although these resolutions are already a good indication they are not to be confused with the actual resolution (or intrinsic resolution) which will be stated in sections 9.3.4.5 to 9.3.4.7. The intrinsic resolution is not considered here as it would cause too much analysis overhead without providing a benefit for the intrapixel resolution results.

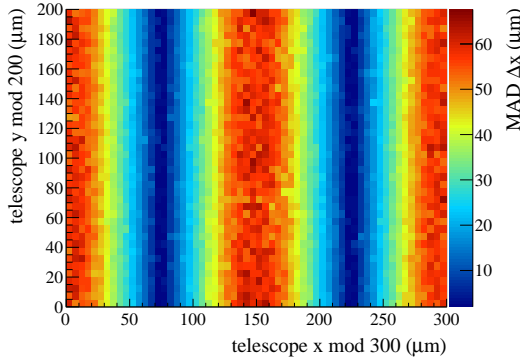
The MAD is calculated via equation 9.2 and it includes an uncertainty of the track. Nevertheless, the results obtained with the MAD method provide excellent information on the intrapixel resolution.

$$\text{MAD}_x = \frac{1}{N} \sum_{i=1}^N |x_{i,\text{DUT}} - x_{i,\text{track}}| \quad (9.2)$$

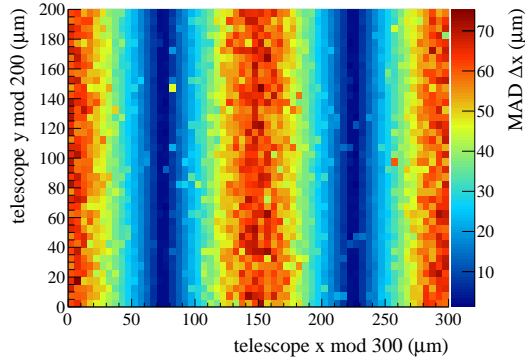
N gives the number of tracks and DUT hits, $x_{i,\text{DUT}}$ the x-coordinate of the DUT hit and $x_{i,\text{track}}$ the x-coordinate of the interpolated track impact point on the DUT. MAD_y is calculated in the same way.

Figure 9.19 shows results of the intrapixel resolution in x- and y-direction at different tilt angles of a $2e14 n_{\text{eq}}$ sample. In the first figure 9.19 (a) the DUT resolution in x at a tilt angle of 0° is given as a function of the track impact position. A clear dependency of the resolution on the impact position is visible. For track impact positions with x-coordinates close to the pixel centers (at $75 \mu\text{m}$ and $225 \mu\text{m}$) the best resolution of approximately $5 \mu\text{m}$ is achieved while the resolution is worst between the pixels (at $0 \mu\text{m}$, $150 \mu\text{m}$ and $300 \mu\text{m}$) with values above $60 \mu\text{m}$. This is caused by two reasons. First, at a tilt of 0° mostly single pixel clusters are created, which means it is not possible to exploit charge sharing to improve the resolution. Even at the pixel edges the mean cluster size is only about 1.4 (see figure 9.10) which shows that the resolution does not benefit from charge sharing in most cases. Second, the resolution is best for tracks traversing the pixel center since the coordinates of single pixel clusters always correspond to the pixel center. The resolution in x remains unchanged for measurements at a tilt angle of 55° as visible in figure 9.19 (b). A change of the resolution in x is not expected since the tilt is in y-direction. Only the reduced statistics caused by the tilt leads to less sharp contours.

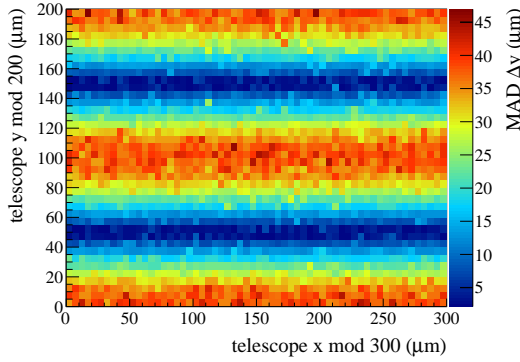
Figure 9.19 (c) shows the resolution in y at 0° . Again the best resolution is about $5 \mu\text{m}$, achieved for tracks with y-coordinates corresponding the pixel centers (at $50 \mu\text{m}$ and $150 \mu\text{m}$). Due to the smaller dimension in y-direction the worst resolution between pixels (at $0 \mu\text{m}$, $100 \mu\text{m}$ and $200 \mu\text{m}$) is only $45 \mu\text{m}$ compared to $60 \mu\text{m}$ in x. However, the situation changes entirely for the y resolution at 55° which is presented in figure 9.19 (d). At 55° there is no longer a dependency on the impact position recognizable since the resolution improves by exploiting charge sharing



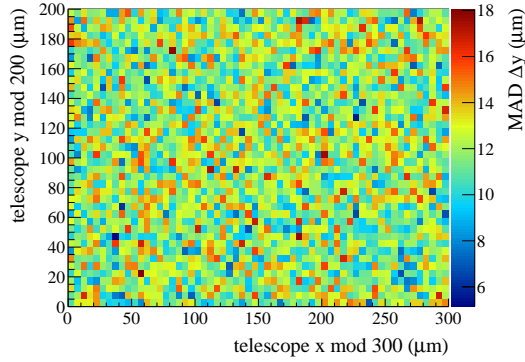
(a) Resolution in x at a tilt of 0° . The resolution in x depends clearly on the track impact position. The best resolution (about $5\ \mu\text{m}$) is achieved for track impact positions with x-coordinates close to the pixel centers. In between pixels the resolution is only about $60\ \mu\text{m}$.



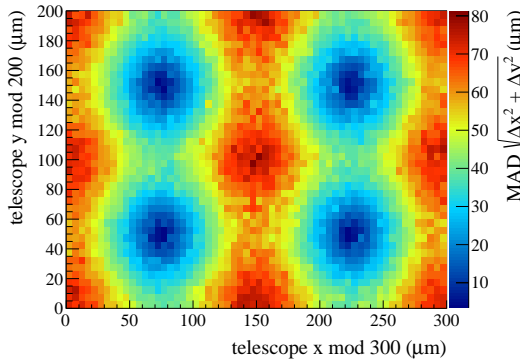
(b) Resolution in x at a tilt of 55° . The results are basically identical to 0° since the tilt in y-direction has no effect on the resolution in x. Only the recorded statistics is reduced due to the tilt resulting in less sharp contours.



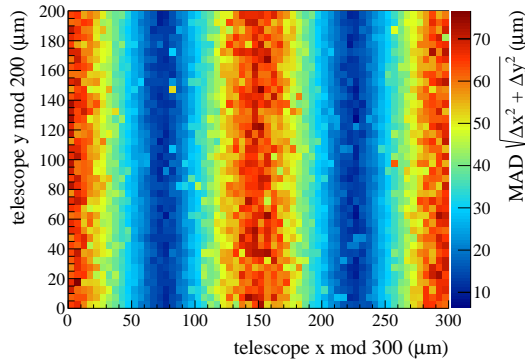
(c) Resolution in y at a tilt of 0° . The best resolution (about $5\ \mu\text{m}$) is measured for impact positions with y-coordinates corresponding to the pixel centers. Due to a smaller pixel size in y-direction (compared to the x-direction) the worst resolution is only about $45\ \mu\text{m}$.



(d) Resolution in y at a tilt of 55° . There is no longer a resolution dependency on the impact position since the resolution improves by exploiting charge sharing in y-direction. The worst resolution improves from $45\ \mu\text{m}$ to $20\ \mu\text{m}$.



(e) Resolution in xy at a tilt of 0° . Combining the results of the individual dimensions provides the xy resolution. The best resolution (about $5\ \mu\text{m}$) is achieved in the pixel center as expected and the worst (about $80\ \mu\text{m}$) at the pixel corners.



(f) Resolution in xy at a tilt of 55° . The resolution in y does not depend on the impact position at this angle and is (on average) smaller compared to the x resolution. Hence, the xy behavior is mostly determined by the resolution in x.

Figure 9.19: Intrapixel resolution of a $2e14\ n_{\text{eq}}$ SCA at tilt angles of 0° and 55° . The resolutions refer to the mean of the absolute distances (MAD) between DUT hit and track impact position, which is not the actual resolution but a convenient approach to investigate the intrapixel behavior.

in y-direction. As indicated by the z-axis, the upper limit corresponding to the worst resolution is reduced from about $45\ \mu\text{m}$ to $20\ \mu\text{m}$.

Figure 9.19 (e) shows the xy resolution by combining the results of figures 9.19 (a) and 9.19 (c). For this purpose the root of the square sum is determined which is also illustrated by the title of the z-axis. As expected from the results above, the resolution in xy is best (approximately $5\ \mu\text{m}$) in the center of the pixel and is worst at the pixel corners (up to $80\ \mu\text{m}$). The xy resolution at 55° is given in figure 9.19 (f) based on the results of figures 9.19 (b) and 9.19 (d). It is clearly different from the one obtained at 0° , while it is comparable to the resolution in x at 55° (see figure 9.19 (b)). This behavior is expected, since the resolution in y does not depend on the track impact position and is (on average) smaller compared to the resolution in x at 55° . Hence, the xy behavior is dominated by the resolution in x.

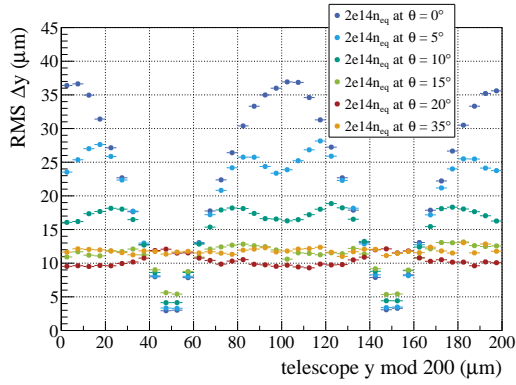
The results presented above show that the intrapixel resolution depends significantly on the track impact position. As the results of the tilt in y-direction are transferable to a tilt in x-direction no dependency on the impact position is expected for large incident angles in xy direction. No statement is being made on the actual spatial resolution, since the application of the MAD method and the included track uncertainty do not allow it. The results of the unirradiated sample and the remaining irradiation steps are very similar. Further measurements on the intrapixel resolution for additional tilt angles are shown in appendix G.4.

9.3.4.2 Intrapixel Resolution Profiles

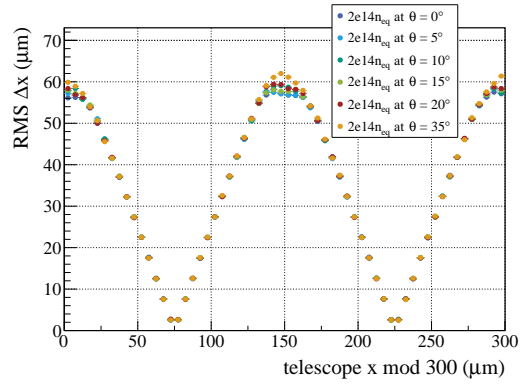
The results on the intrapixel resolution introduced in the previous section are supplemented by profile plots. They provide additional information on the intrapixel resolution by showing the resolution as a function of the x- or y-coordinate of the track impact position. These results also rely on the MAD method.

In figure 9.20 five profile plots for different tilt angles, irradiation steps and comparator thresholds are given. Figure 9.20 (a) shows the y-resolution as a function of the y-coordinate of the track impact point for a $2e14\ n_{\text{eq}}$ SCA and different tilt angles. It is clearly recognizable that the track impact position dependency of the resolution decreases for larger tilt angles. At 0° the resolution varies between $2\ \mu\text{m}$ and $37\ \mu\text{m}$ while it is almost constant (about $10\ \mu\text{m}$) for tilt angles larger than 20° . A tilt angle of 20° corresponds almost exactly to the optimal angle (19.3°) to obtain two pixel clusters. Hence, for most DUT hits charge sharing is exploited to improve the resolution which is responsible for the constant resolution above 20° . Further, it is visible that the resolution for most track impact positions improves with increasing tilt angle, only at the pixel centers (at $50\ \mu\text{m}$ and $150\ \mu\text{m}$) the resolution is slightly worse. In figure 9.20 (b) the resolution in x of the same measurements is presented. The identical resolution profiles clearly confirm that the tilt angle has no effect in x-direction. The resolution varies between $2\ \mu\text{m}$ and $60\ \mu\text{m}$.

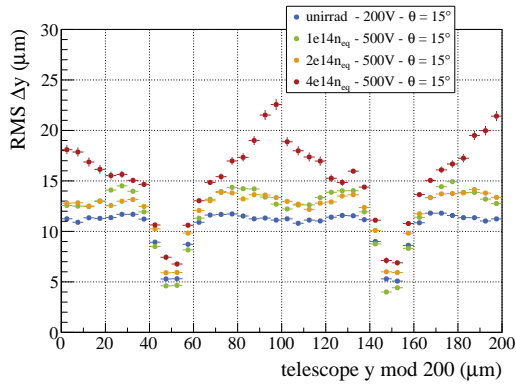
A comparison of the resolution in y as a function of the y-coordinate of the track impact position is given in figure 9.20 (c). It shows the resolution profiles at a tilt of 15° for all irradiation steps including the unirradiated case. The graph confirms the results of the previous section that the best intrapixel resolution corresponds to the pixel centers (at $50\ \mu\text{m}$ and $150\ \mu\text{m}$) of small tilt angles ($\theta \leq 15^\circ$). In addition, the resolution between pixels deteriorates from about $11\ \mu\text{m}$ to more than $20\ \mu\text{m}$ with increasing radiation damage. This is addressed in more detail within the next sections, when the intrinsic detector resolution is discussed. Figure 9.20 (d) refers to the same measurements presenting the resolution in x as a function of the x-coordinate of the track impact position. The tilt angle of 15° in y-direction is not relevant as it has no effect on the resolution in x. All four profiles are characterized by an almost identical shape with resolutions between approximately $2\ \mu\text{m}$ and $60\ \mu\text{m}$. There is only a minor deviation between the pixels (at $0\ \mu\text{m}$, $150\ \mu\text{m}$ and $300\ \mu\text{m}$) where the $4e14\ n_{\text{eq}}$ sample seems to behave slightly better. As the difference of the resolution is very small this might be an artifact of the MAD method and the track uncertainty.



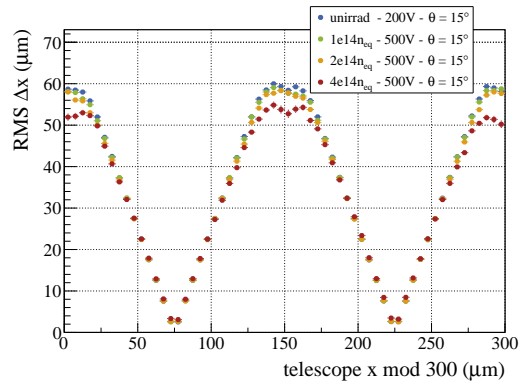
(a) Resolution in y for a $2e14 n_{eq}$ sample at several tilt angles. The dependency on the impact position decreases for larger tilt angles and is almost constant ($10 \mu\text{m}$) above 20° . Except for the pixel centers the resolution improves with increasing tilt angles.



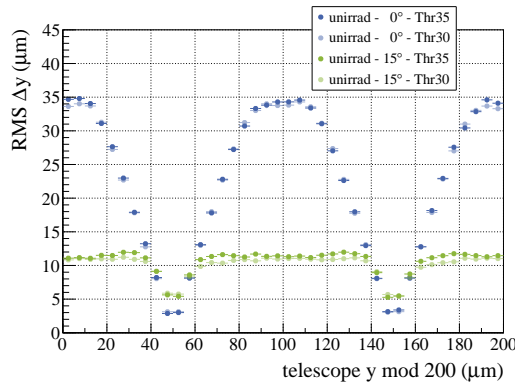
(b) Resolution in x for a $2e14 n_{eq}$ sample at several tilt angles. The identical resolution profiles confirm that the tilt in y-direction has no influence on the resolution in x. The resolution varies between about $2 \mu\text{m}$ and $60 \mu\text{m}$.



(c) Resolution in y depending on the y-coordinate of the impact position at a tilt of 15° . For all irradiation steps the best resolution corresponds to the pixel center (at $50 \mu\text{m}$ and $150 \mu\text{m}$). The resolution deteriorates with increasing radiation damage from about $11 \mu\text{m}$ to more than $20 \mu\text{m}$.



(d) Resolution in x depending on the x-coordinate of the impact position at a tilt of 15° . The profiles of all irradiation steps are basically identical. Only the $4e14 n_{eq}$ sample shows a slightly better resolution between pixels (at $75 \mu\text{m}$ and $225 \mu\text{m}$). This might be an artifact of the MAD method.



(e) Resolution in y for the unirradiator SCA and different thresholds. The profiles match the results of figure 9.20 (a). The differences between the two comparator thresholds are rather small (less than $2 \mu\text{m}$) with a slightly better resolution for the lower threshold.

Figure 9.20: Profile plots showing the intrapixel resolution for different tilt angles, irradiation steps and thresholds.

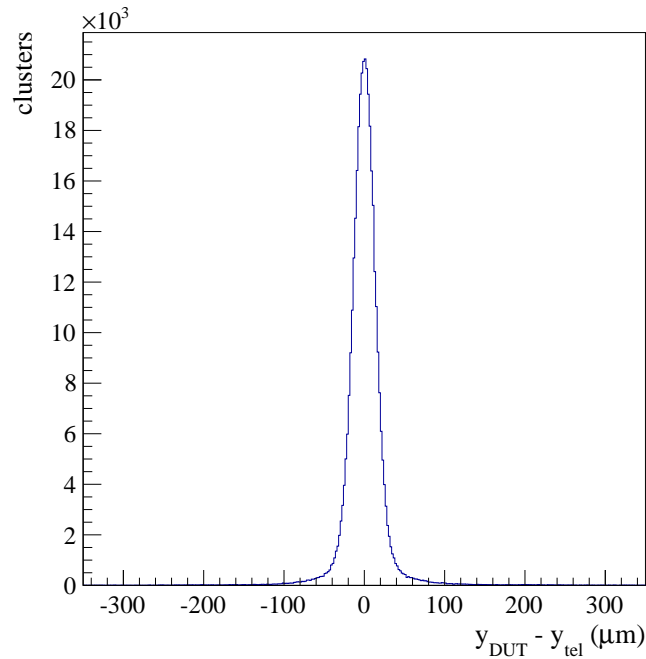


Figure 9.21: Residual distribution of the y-coordinates for a tilt of 15° . The number of clusters is given as a function of the distance in y between DUT hit and track impact position. The residual distribution is well modeled by a Gaussian and the corresponding width determines the DUT resolution.

Figure 9.20 (e) gives a comparison of the intrapixel resolution between the standard comparator threshold of 35 Vcal and the additional one of 30 Vcal. The profiles correspond to measurements of the unirradiated sample performed at 0° and 15° . The results are quite comparable to the profiles of $2e14 n_{\text{eq}}$ sample presented in figure 9.20 (a) at the same tilt angles. Comparing the resolutions obtained with the two thresholds reveals only a minor difference of less than $2 \mu\text{m}$, independent from the track impact position. Although the resolution improvement is relatively small, it matches the expectations, as a lower threshold should be beneficial for the determination of the center of charge by considering even smaller signals. Nevertheless, such small effects should be investigated with the help of the intrinsic resolution instead of the MAD as already mentioned above. This is addressed in the following section.

9.3.4.3 Residual Distributions

In the next two sections a discussion of the intrinsic resolution is given. The starting point are the residual distributions provided by the analysis.

The residual distribution in figure 9.21 shows the number of clusters as a function of the distance between the DUT hit and the impact point of the extrapolated upstream track. For tilt angles larger than 10° such distributions can be described by a Gaussian fit function, where the width determines the measured resolution. At smaller tilt angles the residual distributions contain a non-Gaussian part due to the large fraction of one pixel clusters causing a box distribution. The measured resolutions σ_{meas} contain the intrinsic resolution σ_{int} and the pointing resolution of the upstream track σ_{track} . The determination of the pointing resolution is introduced in the following section 9.3.4.4. Assuming they are uncorrelated (the intrinsic resolution

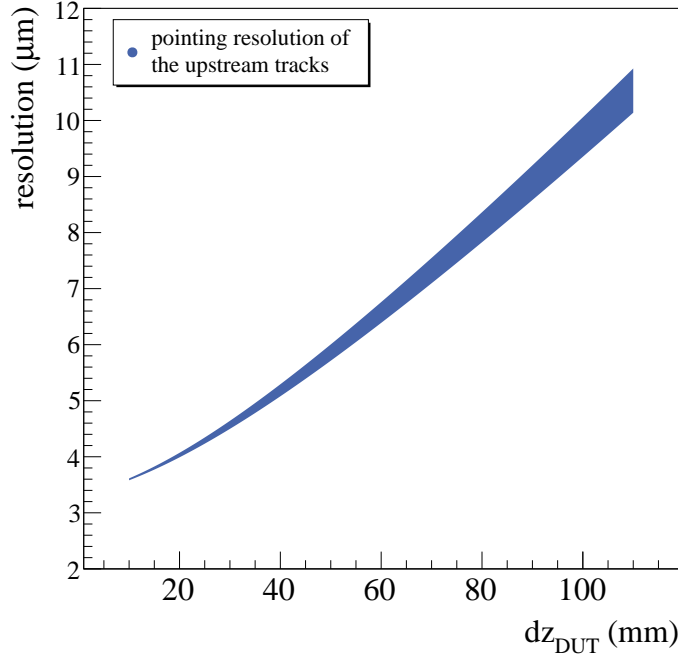


Figure 9.22: Pointing resolution for upstream tracks. The pointing resolution at the DUT is given as a function of the distance dz_{DUT} between the DUT and the closest upstream plane. The pointing resolution and its uncertainty increase for higher distances z_{DUT} [S16].

depends on the DUT and the pointing resolution on the telescope), σ_{int} can be determined as in equation 9.3.

$$\sigma_{\text{int}} = \sqrt{\sigma_{\text{meas}}^2 - \sigma_{\text{track}}^2} \quad (9.3)$$

The uncertainty on the intrinsic resolution is described by

$$\Delta_{\text{int}} = \sqrt{\frac{1}{\sigma_{\text{meas}}^2 - \sigma_{\text{track}}^2} \cdot (\sigma_{\text{meas}}^2 \cdot \Delta_{\text{meas}}^2 + \sigma_{\text{track}}^2 \cdot \Delta_{\text{track}}^2)} \quad (9.4)$$

with Δ_{meas} and Δ_{track} representing the uncertainties of the measured resolution and the track pointing resolution, respectively.

9.3.4.4 Track Pointing Resolution

One of the most important properties of test beam telescopes is the pointing resolution. First of all it depends on the number of detector planes or more precisely on the number of measurement points of the reconstructed tracks. Additionally, as the tracks need to be extrapolated or interpolated⁴ to the DUT position, the telescope geometry affects the pointing resolution as well. In order to keep the track uncertainty small the DUT should be located as close as possible to the telescope planes. Further, depending on the particle energy, Coulomb scattering in the detector planes and the surrounding air causes a non-negligible contribution to the overall track resolution.

Figure 9.22 shows the pointing resolution of the upstream tracks at the DUT. The resolution is given as a function of the distance z_{DUT} between the DUT and the closest upstream plane.

⁴ Depending on whether the DUT is located behind or between the telescopes planes.

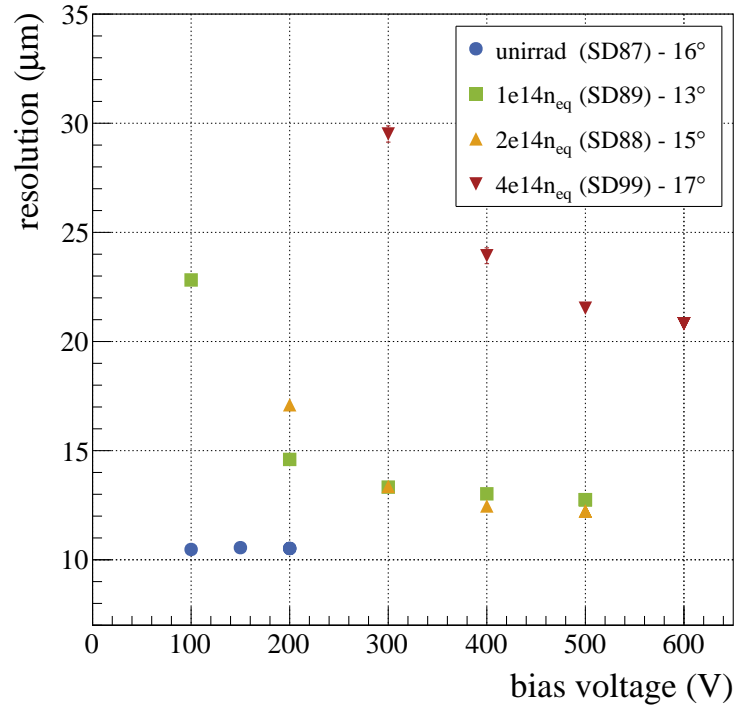


Figure 9.23: Intrinsic resolution depending on the bias voltage. The irradiated samples show an improved resolution for higher bias voltages saturating above the depletion voltage. The best achieved resolution is about $10 \mu\text{m}$ for the unirradiated sample degrading to more than $20 \mu\text{m}$ for the $4e14 n_{\text{eq}}$ sample. The given tilt angles represent the actual angles calculated in the analysis.

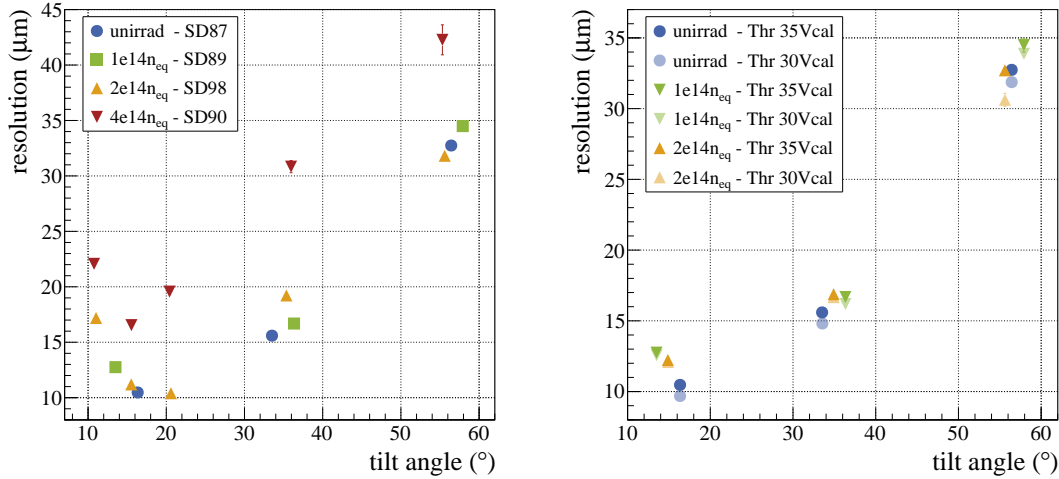
The benefit of considering only the upstream planes – which is the case for all following resolution results – is that additional effects due to scattering downstream of the DUT are excluded. The width of the given curve represents the uncertainty of the track pointing resolution at the DUT position assuming an uncertainty of the particle energy of $\pm 5\%$ [Deu17c].

Since the distance z_{DUT} differs between most measurements, the pointing resolution is determined and applied individually for each run to determine the intrinsic resolution correctly.

9.3.4.5 Intrinsic Resolution depending on the Bias Voltage

The results shown in the following sections address the intrinsic resolution of the pixel detector. Since the tilt is always in y -direction (in the context of this thesis), the intrinsic resolution in x is of less interest. Hence, all results refer to the resolution in y . The first investigated property is a potential bias voltage dependency of the intrinsic resolution calculated with equation 9.3 and figure 9.22.

Figure 9.23 shows the intrinsic resolution as a function of the bias voltage for both the unirradiated case and the three irradiation steps at a tilt of 15° . It is visible that the resolution of the irradiated samples increases for higher bias voltages and saturates above the depletion voltage. This is expected, as the sensors have to be fully depleted to exploit charge sharing correctly. In a not entirely depleted sensor charge carriers recombine inside non-depleted regions. As a consequence, the measured signals of some pixels of a cluster might be smaller than expected. This leads to a shift as the center of charge is calculated wrongly which impairs the resolution. Additionally, the graph shows a deterioration of the resolution with increasing radiation damage. This is probably related to increased trapping, which also affects the measured signal heights resulting in a less efficient determination of the center of charge. The best intrinsic



- (a) Tilt angle dependency of the intrinsic resolution for the unirradiated case and the three irradiation steps. All samples show comparable trends. The best achieved results correspond to tilt angles between 15° to 20° with resolutions of $10 \mu\text{m}$ to $13 \mu\text{m}$ except for the $4e14 n_{\text{eq}}$ sample. The resolution of the $4e14 n_{\text{eq}}$ sample is about $5 \mu\text{m}$ to $15 \mu\text{m}$ worse compared to the other three SCAs.
- (b) Tilt angle dependency of the intrinsic resolution for two different comparator thresholds (30 Vcal and 35 Vcal). All three given samples have a slightly improved intrinsic resolution at the lower threshold of 30 Vcal. However, the differences are rather small and barely recognizable at the 15° results of the irradiated samples. On average the resolution improved only by about $1 \mu\text{m}$.

Figure 9.24: Intrinsic resolution as a function of the tilt angle. Both figures show results for the same unirradiated and $1e14 n_{\text{eq}}$ sample while they refer to different $2e14 n_{\text{eq}}$ samples. In figure (a) SD98 is considered as it provides more tilt angles while (b) shows the results of SD88 as it was tested at two different thresholds.

resolutions are about $10 \mu\text{m}$ for the unirradiated SCA, $12 \mu\text{m}$ to $13 \mu\text{m}$ for the $1e14 n_{\text{eq}}$ and $2e14 n_{\text{eq}}$ samples and more than $20 \mu\text{m}$ at the highest irradiation of $4e14 n_{\text{eq}}$.

The results of the bias voltage investigation recommend to operate the sensors sufficiently overdepleted to avoid a potential deterioration of the intrinsic resolution. Thus the results introduced in the next sections always refer to measurements with optimal bias voltage settings.

9.3.4.6 Intrinsic Resolution depending on the Tilt Angle

In this section the tilt angle dependency of the intrinsic detector resolution is investigated for different irradiation steps and comparator thresholds. In addition, the impact of the pulse height calibration is discussed.

Figure 9.24 shows the intrinsic resolution as a function of the tilt angle for all available irradiation steps and for comparator thresholds of 30 Vcal and 35 Vcal. In figure 9.24 (a) the extended tilt angle scans of SD98 and SD90 (see table 9.1) are considered providing additional measurement points at $2e14 n_{\text{eq}}$ and $4e14 n_{\text{eq}}$. All samples show a similar dependency on the tilt angle. Especially the results of the $2e14 n_{\text{eq}}$ and $4e14 n_{\text{eq}}$ SCAs show that the resolution improves at first for higher tilt angles. This is caused by a decreasing number of single pixel clusters associated with an increased exploitation of charge sharing. The best resolutions correspond to tilt angles of about 15° to 20° , where the unirradiated, the $1e14 n_{\text{eq}}$ and the $2e14 n_{\text{eq}}$ sample have resolutions between $10 \mu\text{m}$ and $13 \mu\text{m}$. The $4e14 n_{\text{eq}}$ SCA has an intrinsic resolution of about $16 \mu\text{m}$ in the corresponding region. For higher tilt angles a deterioration of the resolution is visible. At about 35° the resolution of the unirradiated SCA and the two lower irradiated ones still is in the range of $15 \mu\text{m}$ to $20 \mu\text{m}$, while it is above $30 \mu\text{m}$ for a tilt of approximately 55° .

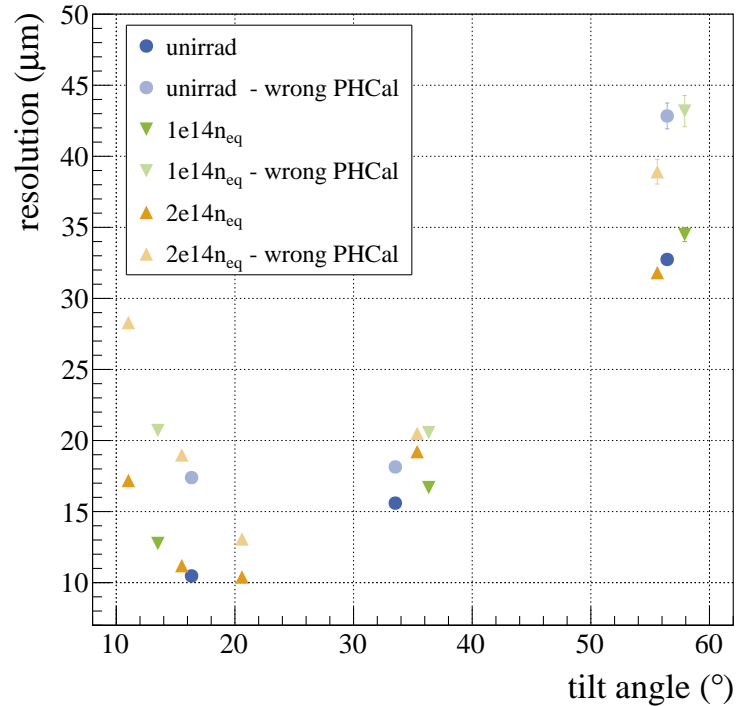


Figure 9.25: Impact of the pulse height calibration on the intrinsic resolution. The resolution is about $5 \mu\text{m}$ worse for results obtained with a wrong pulse height calibration due to incorrectly calculated centers of charge.

The reason for the worse resolutions is probably related to the larger cluster sizes causing a less efficient determination of the center of charge. Apparently, the $4e14 n_{\text{eq}}$ SCA has a worse resolution over the entire tilt angle range, which was already indicated in figure 9.23.

Figure 9.24 (b) gives a comparison of the intrinsic resolution for two different comparator thresholds. For all three samples a slightly improved resolution is visible for the lower threshold, which is expected as charge sharing should benefit from detecting smaller signals. However, the difference is rather small and barely recognizable in some cases, for instance at the 15° measurements of the $1e14 n_{\text{eq}}$ and $2e14 n_{\text{eq}}$ samples. Altogether, the intrinsic resolution improves only by about $1 \mu\text{m}$. Based on these results a lower threshold does not provide a significant advantage.

Figure 9.25 shows the impact of the pulse height calibration on the tilt angle dependency of the intrinsic resolution. The graph presents results of the unirradiated, the $1e14 n_{\text{eq}}$ and one of the $2e14 n_{\text{eq}}$ samples for their correct pulse height calibrations and for a wrong one. The latter was created with another SCA, which was operated with different analog and digital currents comparable to the $4e14 n_{\text{eq}}$ samples.

The wrong pulse height calibration clearly has a negative impact on the intrinsic resolution for all investigated samples and tilt angles. Due to the wrong calibration the center of charge is calculated incorrectly which impairs the resolution by about $5 \mu\text{m}$ on average. This illustrates the importance of a correct pulse height calibration and recommends to repeat the pulse height calibration of the pixel modules in CMS regularly. Actually, this was already the case in the original CMS pixel detector. While a full calibration was performed only once a year due to time constraints, the pulse height calibration was carried out three to four times a year [Kot16]. The results presented in this section confirm that this approach should be kept for the Phase I pixel detector.

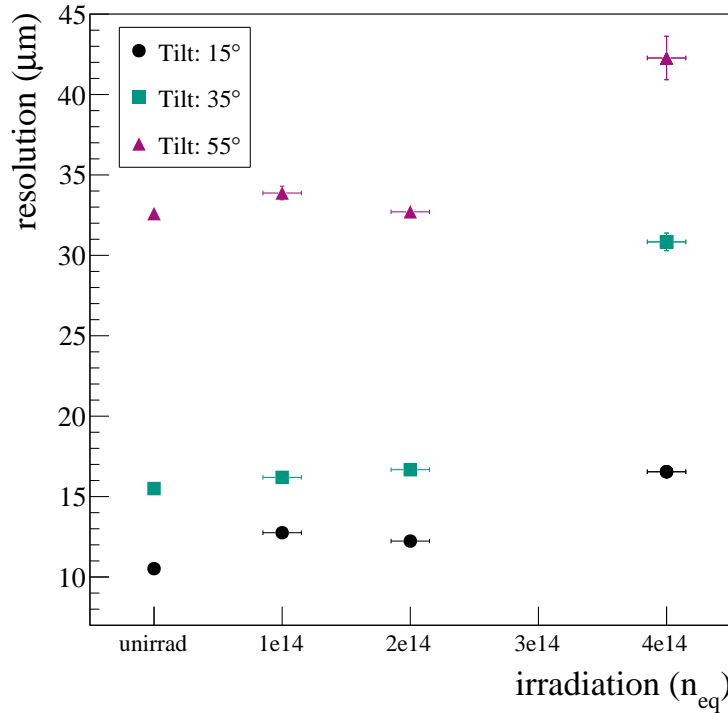


Figure 9.26: Intrinsic resolution depending on the irradiation fluence. The resolution for the unirradiated case, the $1e14 n_{eq}$ and $2e14 n_{eq}$ samples are very similar at the three given tilt angles. The resolution of the $4e14 n_{eq}$ sample is about $5 \mu\text{m}$ to $15 \mu\text{m}$ worse.

9.3.4.7 Intrinsic Resolution depending on the Irradiation Fluence

The final test beam result investigates the intrinsic resolution as a function of the irradiation fluence.

Figure 9.26 confirms that the resolutions at $1e14 n_{eq}$ and $2e14 n_{eq}$ are almost as good as the resolution of the unirradiated sample. These samples achieve resolutions of $10 \mu\text{m}$ to $13 \mu\text{m}$ at 15° , slightly more than $15 \mu\text{m}$ at 35° and $32 \mu\text{m}$ to $34 \mu\text{m}$ at 55° . At the highest irradiation of $4e14 n_{eq}$ the resolution is $5 \mu\text{m}$ to $15 \mu\text{m}$ worse. Nevertheless, even the result for the $4e14 n_{eq}$ sample is sufficient for operation as it corresponds to resolutions for layer 2 only at the estimated end of operation of the CMS Phase I pixel detector. The results of the $1e14 n_{eq}$ and $2e14 n_{eq}$ samples indicate that the performance of layers 3 and 4 will barely deteriorate over the entire pixel detector lifetime. This confirms that the CMS Phase I pixel detector is well suited for the upcoming tasks.

9.4 CONCLUSIONS

In the course of the test beam study presented in this chapter it has been shown that the new CMS pixel detector is perfectly suited for the operation during the next years. Both important properties, the hit efficiency and the spatial resolution, which determine the detector performance, behave as desired even at the expected fluences. Further, the detailed investigation allows to make some recommendations for the operation of the Phase I pixel detector.

The investigation of the bias voltage showed that a compromise between a very high and a moderate bias voltage settings needs to be found. Higher voltages are desired as they guarantee the best achievable resolutions while moderate bias voltages, but still above the depletion

Table 9.2: Optimal bias voltage settings regarding hit efficiency and spatial resolution. A common optimal bias voltage exists only for the unirradiated case. For all three irradiation steps a compromise is required.

sample	optimal bias voltage (V)	
	efficiency	resolution
unirrad	100	100
1e14 n _{eq}	300	500
2e14 n _{eq}	300	500
4e14 n _{eq}	400	600

voltage, are beneficial regarding hit efficiency (and leakage current). The recommended bias voltage, based on the results from this thesis, is given by the depletion voltage plus 100 V to 150 V. Table 9.2 gives a comparison of the optimal bias voltage settings.

Table 9.3: Hit efficiency for different tilt angles and thresholds (Thr). The hit efficiency is 0.5% to 1% worse for the lower threshold. This observation is independent of the tilt angle. Values given in brackets are the associated uncertainties referring to the last given digits of the efficiency.

sample	Thr (Vcal)	efficiency (%) at tilt angle				
		0°	15°	35°	55°	75°
1e14 n _{eq}	30	98.77 (28)	98.84 (23)	99.05 (16)	98.79 (21)	98.33 (60)
	35	99.39 (19)	99.50 (17)	99.52 (11)	99.35 (17)	98.77 (55)
2e14 n _{eq}	30	98.61 (24)	98.88 (18)	98.87 (18)	98.77 (19)	98.57 (51)
	35	99.32 (12)	99.54 (9)	99.49 (10)	99.48 (13)	99.11 (39)

Regarding the comparator threshold it was demonstrated that a lower threshold leads to an almost negligible resolution improvement (see table 9.4). However, there is a negative impact of the lower threshold on the hit efficiency which encourages the usage of the standard comparator threshold of 35 Vcal (see table 9.3). The decisive fact is that a reduced hit efficiency results in completely undetected particles while the positive effect (on physics analyses) of improving the resolution by only 1 μm is small. The application of the lower threshold of 30 Vcal would only be justifiable if the best possible resolution is absolutely mandatory.

The test beam results illustrated the importance of performing the pulse height calibration on a regular basis. Otherwise an avoidable deterioration of the resolution might be the consequence. In addition, the laboratory measurement of chapter 8 demonstrate the necessity for a specific electrical calibration of irradiated samples to recover the optimal detector performance. Therefore, the approach to perform a full electrical calibration of the pixel detector at least once a year should be maintained.

The test beam results prove that the Phase I pixel detector is an excellent foundation for upcoming physics analyses.

Table 9.4: Spatial resolution for different tilt angles and thresholds (Thr). The lower threshold provides a slightly improved resolution of about 1 μm . Comparable to the hit efficiency this observation is independent of the tilt angle. Values given in brackets are the associated uncertainties referring to the last given digits of the resolution.

sample	resolution (μm) at tilt angle					
	15°		35°		55°	
	Thr 30	Thr 35	Thr 30	Thr 35	Thr 30	Thr 35
unirrad	9.69 (17)	10.47 (16)	14.81 (17)	15.59 (17)	31.87 (28)	32.74 (31)
1e14 n _{eq}	12.57 (12)	12.75 (12)	16.19 (13)	16.69 (14)	33.88 (42)	34.49 (49)
2e14 n _{eq}	12.09 (12)	12.23 (12)	16.67 (14)	16.88 (14)	30.62 (46)	32.71 (38)
4e14 n _{eq}	-	16.54 (14)	-	30.84 (55)	-	42.27 (1.35)

Part iv

SUMMARY AND OUTLOOK

Now this is not the end. It is not even the beginning of the end. But it is, perhaps, the end of the beginning.

Winston Churchill

10

SUMMARY

In today's world of particle physics enormous efforts are made to expand the frontiers of knowledge about nature. The tools to accomplish this goal are particle colliders and detectors which are improved in steps by adapting new technologies to fully exploit their potential. This is also true for the Large Hadron Collider (LHC), the most powerful collider in high energy physics. This thesis is dedicated to the Compact Muon Solenoid (CMS) experiment, which is one of the particle detectors at the LHC. Two topics regarding the CMS pixel detector, which is the innermost part of the CMS detector, are discussed in detail. The task of the pixel detector is to reconstruct the trajectories of charged particles emerging from the proton-proton collisions.

The first part of the thesis introduces the module production for the CMS Phase I pixel detector which replaced the original pixel detector in early 2017. The original pixel detector performed well but it would have suffered from intolerable inefficiencies caused by the increasing LHC luminosity. The option to increase the luminosity to twice the design value became possible due to the excellent LHC performance and it is beneficial for physics analyses as it increases the recorded statistics. The construction and installation of the Phase I pixel detector was carried out by several universities and research institutes and lasted two years starting in 2015. The new pixel detector includes multiple improvements like an enhanced readout chip to avoid the mentioned inefficiencies and the reduction of the material budget despite of an increase of channels from 66 million to 124 million. Another important modification is the reduced distance between the new innermost pixel detector layer and the interaction point. This allows to improve the resolution and the identification of secondary vertices, which is beneficial for physics analyses relying on b-tagging.

The KIT pixel detector module production started in May 2015 and was finished in June 2016. Altogether 409 modules were produced for the new CMS Phase I pixel detector. This thesis gives an overview of the entire KIT production chain and the final qualification at RWTH Aachen. Two aspects of the production are discussed in more detail. On the one hand, this is the qualification of the bare modules, an intermediate product consisting of a silicon sensor connected to 16 ReadOut Chips (ROCs) forming the heart of the pixel modules. On the other hand, these are the X-ray measurements used to determine the number of dead channels on the final modules and to cross-check the bare module results.

During the bare module qualification electrical tests are performed in order to qualify the bare modules according to predefined grading criteria. First, the current-voltage characteristic of the sensor is measured to identify potential defects leading to the bare module being rejected. Further it is verified whether the ROCs are working properly and the number of defective channels is determined. If a problematic ROC is identified – either not working correctly or having too many defective channels – it is removed and replaced by a new one. Out of 437 produced bare modules 87 had to be reworked whereof 78 (89.7%) rework attempts were successful. According to the bare module grading criteria 406 bare modules are grade A/A- (the minus sign refers to reworked bare modules), which corresponds to the best quality. Among the remaining bare modules, 14 are grade B/B-, which is still fine, and only 17 are grade C/C-

and had to be rejected. The main reason causing a grade B or grade C bare module is related to the current-voltage characteristic.

Out of 420 good bare modules produced at KIT four were sent to the Swiss production consortium (due to a lack of HDIs at KIT) and 409 of the remaining ones were turned into complete modules. Out of these, 368 modules (corresponding to 24,494,080 pixels) were investigated with X-rays where 3191 defective channels, representing 0.013% of all tested pixels, were identified. The final module yield is based both on the qualification at RWTH Aachen and the reception test at ETH Zürich. According to these results 140 modules are grade A/A- and 203 are grade B/B-. Most grade B/B- modules are caused by an unexpected leakage current scaling between $+17^{\circ}\text{C}$ and -20°C . This results in 343 good modules, corresponding to 83.9% of all KIT modules while the proposed number of good modules was 310. The overproportionally high number of 323 mounted KIT modules (the target quantity was 256 mounted modules) shows the good quality of the KIT production.

The second part of this thesis investigates the performance of pixel modules for barrel layers 2 to 4 of the new pixel detector and how it is expected to evolve in the coming years of operation. Layer 1 (built by the Swiss consortium) uses a different ROC and is therefore not included in this study. To be able to fully exploit the potential of the pixel detector in-depth knowledge of the detector performance is required. This concerns properties like current-voltage characteristics and bias voltage as well as high-level quantities such as spatial resolution and hit efficiency. The samples used in this study are a module from the KIT production and multiple smaller samples called **Single Chip Assemblies (SCAs)**. These SCAs consist of a single ROC (instead of 16 for modules) and a smaller version of the silicon sensor matching one ROC.

Laboratory measurements performed at KIT confirm that the detector can be operated reliably for the radiation damage expected at the end of operation. Only at the final fluence ($4e14 n_{eq}$) for layer 2, which suffers most from radiation damage (apart from layer 1), fine tuning is necessary to recover the optimal performance. The required tuning, which is described in this thesis, addresses the supply voltages and a modification of the pulse height calibration. Further, the laboratory measurements are used to investigate the charge collection efficiency. It is shown that the measured signals (at the end of the suggested operation time) are at least ten times higher than the detection threshold of the ROCs.

Further measurements focusing in detail on the performance cannot be carried out at KIT. Hence, a test beam study was performed at DESY, Hamburg. The most important properties determining the detector performance are the hit efficiency and the spatial resolution. Both properties are investigated depending on several parameters including different fluences. The parameters considered are the tilt angle, the bias voltage, the detection threshold and the pulse height calibration. Different tilt angles account for all possible entrance angles of the charged particles traversing the CMS pixel detector. The investigation of the bias voltage dependency shows that higher voltages are preferable to obtain the best achievable resolution while more moderate voltages are beneficial regarding the hit efficiency. The optimal bias voltage is given by the depletion voltage plus 100 V to 150 V. The test beam study also checks whether a smaller detection threshold might be favorable. The standard threshold corresponds to a value of 35 Vcal (about 1750 electrons) while the smaller threshold is set to 30 Vcal (about 1500 electrons) which is close to the accessible lower comparator limit. A comparison of the results for both thresholds reveals that the resolution improvement for the lower threshold is almost negligible. However, the lower threshold results in a hit efficiency reduction of almost one percent. According to that, this thesis suggests to stay with the standard threshold of 35 Vcal. Finally, the test beam study shows that the pulse height calibration of the ROCs should be repeated on a regular basis. Otherwise, the resolution might deteriorate by up to $5\ \mu\text{m}$. The performance study proves that the CMS Phase I pixel detector modules are well suited for the coming years and that it is an excellent foundation for upcoming physics analyses.

Part v

APPENDIX

POSITION DISTRIBUTION OF REPLACED ROCS

The results from the bare module rework process which are introduced in section 6.2.3 did not reveal any systematic effect causing a rework. In this chapter it is investigated if there is any systematic effect concerning the ROC position on the bare module.

Figure A.1 shows the number of replaced ROCs as a function of the ROC position on the bare module. The corner positions of the ROCs are 0, 7, 8 and 15. An inhomogeneous distribution of replaced ROCs would be a hint for a systematic production or qualification failure. It is visible that each ROC position was affected by at least a few rework attempts with a minimum of only two replaced ROCs at position 5. At two positions more than ten ROCs had to be replaced which are corner positions 0 (eleven ROCs replaced) and 8 (16 ROCs replaced). This is to some extent expected as the corner positions are more susceptible to mechanical damage. However, the number of replaced ROCs at the corner positions 7 and 15 is similar to the remaining ROCs. Except for the two ROC positions 0 and 8 there are no conspicuous features indicating a systematic problem (with respect to the available statistics).

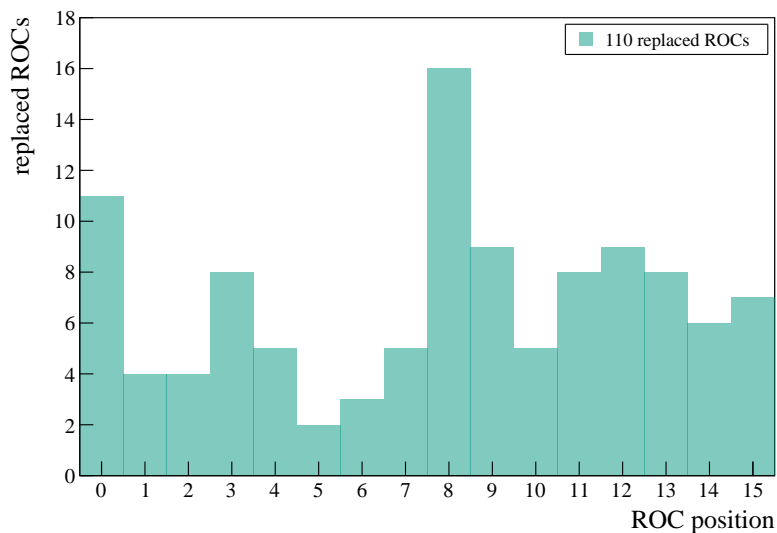


Figure A.1: Number of replaced ROCs as a function of the ROC position on the bare module. The corner positions are 0, 7, 8 and 15. The distribution shows that all ROC positions are affected from rework. The maximum number of replaced ROCs refers to corner positions 0 and 8, most likely since corner positions are more susceptible to mechanical damage.

B

ADDITIONAL RESULTS ON DEFECTIVE PIXELS OF THE KIT MODULES

In section 7.2 the number of defective pixels for complete modules is already discussed in detail which includes a comparison with the results of the bare modules. The plots below serve as additional confirmation for the selection of the standard X-ray cut of five which distinguishes between working and defective pixels.

Figure B.1 presents the number of defective pixels per module for all 368 tested modules at different X-ray cuts. The last bin contains all modules with more than 20 dead pixels. For an X-ray cut of five hits per pixel this corresponds to only 28 modules (8%) but already to about 90 (25%) for the cut at ten. For X-ray cuts from zero to five the major part of the modules has 0 dead pixels and more than 70% of the tested modules have four or less dead pixels. For an X-ray cut of ten the shape of the distribution changes completely and the maximum at zero defective pixels no longer exists. The increasing number of dead pixels caused by the relatively small number of hits for certain pixel positions (below surface mounted HDI components such as capacitors) starts to dominate here.

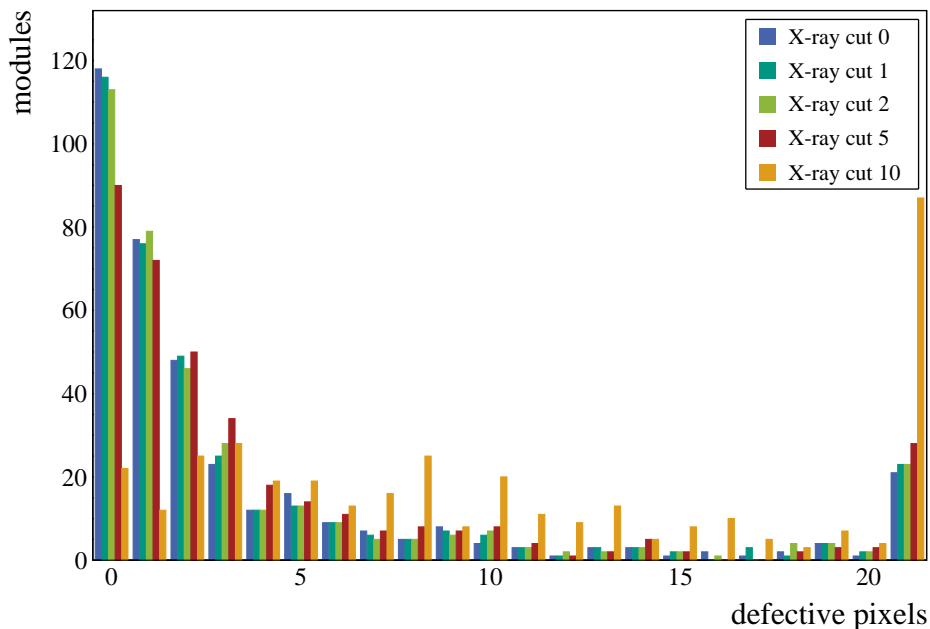


Figure B.1: Dead pixel distribution of the 368 KIT modules tested with X-rays. The last bin represents all modules with more than 20 dead pixels. For X-ray cuts up to five the major part of the tested modules has zero dead pixels. At higher cuts the calculated number of dead channels starts to increase and the maximum at zero dead pixels vanishes.

These results support the selection of an X-ray cut of five hits per pixel, as it is modest and not dominated by low statistics. In addition, the results illustrate the excellent quality of the produced modules in terms of working channels.

Figure B.2 compares the number of dead pixels between bare module and complete modules for different X-ray cuts. The comparison is based on 368 bare module/module pairs which were tested both in the bare module qualification (BBTest) and in the X-ray test. The first entry of the plot represents the 1442 dead channels determined from the bare module qualification. The second entry shows the number of dead channels for X-ray cuts zero (red), five (turquoise) and ten (red). The corresponding numbers of pixels declared as dead are 2371 (X-ray cut zero), 3191 (X-ray cut five) and 10,132 (X-ray cut ten). The third entry presents the number of correlated dead pixels referring to all pixels which were declared dead both in the bare module qualification as well as in the X-ray test. Apparently, the increase of correlated channels for higher X-ray cuts is almost negligible. There are 830 correlated defective pixels at X-ray cut zero and 881 correlated pixels at X-ray cut five while there is barely an increase to 885 correlated dead pixels at X-ray cut ten. This indicates that the increased number of dead channels at higher X-ray cuts is almost exclusively caused by a small number of hits in pixels below surface mounted HDI components. The fourth entry shows the number of uncorrelated defective channels allowing to cross-check the previous results. The uncorrelated defective channels comprise all pixels which are either declared dead in the bare module qualification or in the X-ray test. The distribution of the uncorrelated dead pixels confirms the previous observations that the increase of dead pixels at higher X-ray cuts refers mostly to pixels which were fine in the bare module qualification. This again approves the selection of the standard X-ray cut of five pixels.

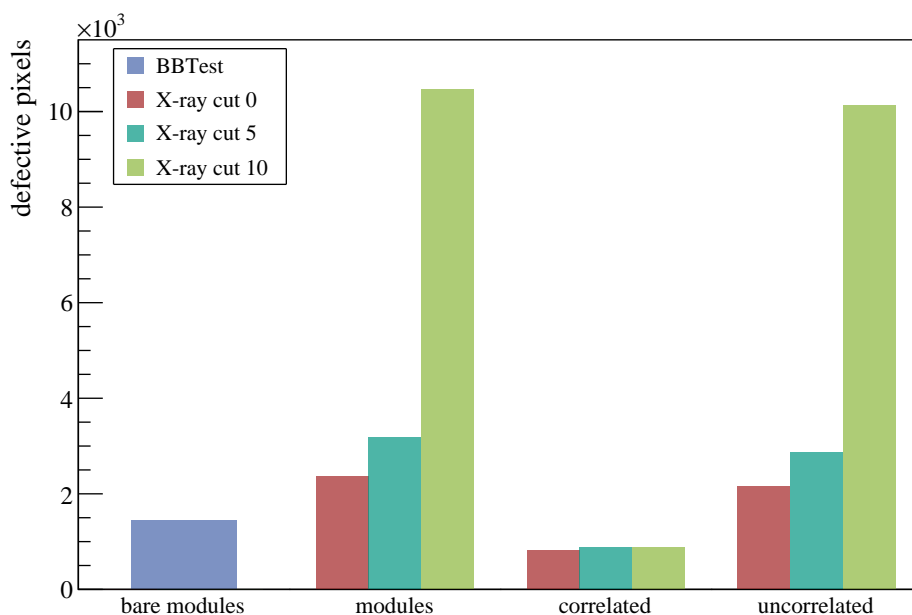


Figure B.2: Comparison of the number of dead pixels between bare modules and complete modules for different X-ray cuts. The number of defective channels clearly increases for higher X-ray cuts. However, the number of correlated dead pixels referring to pixels which were declared dead both in the bare module qualification (BBTest) and the X-ray test remains almost unchanged. In contrast, the number of uncorrelated defective pixels increases significantly with the X-ray cut.

SINGLE CHIP ASSEMBLIES FOR THE PHASE I PERFORMANCE STUDY

In this chapter all single chip assemblies used in the performance study – discussed in chapters 8 and 9 – are introduced. This includes some important parameters and current-voltage characteristics before irradiation.

Table C.1 shows all samples and the most relevant parameters which were produced for the performance study for the Phase I pixel detector. The given values are the irradiation fluences and whether the samples were investigated in the laboratory or in the test beam. Further, the table presents the most important DAC values as well as parameters of the electrical calibration which were determined in a comprehensive study to achieve the best possible detector performance.

Table C.1: Samples produced for the performance study for the Phase I pixel detector. The DAC V_{dig} is used to set the digital supply voltage and I_{ana} is the analog current target applied in the pretest routine. pre. & sha. feedback determine the time constants of the preamplifier and shaper circuits which are tuned via the DACs v_{wllpr} and v_{wllsh} . PH safety margin is the lower saturation limit applied in the PH-Optimization test.

sample	fluence (n_{eq})	investigated in		V_{dig} (DAC)	I_{ana} (mA)	pre. & sha. feedback (DAC)	PH safety margin (DAC)
		lab	test beam				
SD79	1e14	yes	no	7	24	100	40
SD80	unirrad	yes	no	6	24	150	20
SD81	unirrad	yes	no	6	24	150	20
SD84	unirrad	yes	no	6	24	150	20
SD85	unirrad	yes	no	6	24	150	20
SD86	4e14	yes	no	11	28	50	40
SD87	unirrad	yes	yes	6	24	150	20
SD88	2e14	yes	yes	7	24	100	40
SD89	1e14	yes	yes	7	24	100	40
SD90	4e14	yes	yes	11	28	50	40
SD98	2e14	yes	yes	7	24	100	40
SD99	4e14	yes	yes	11	28	50	40
SD100	1e14	yes	no	7	24	100	40
SD101	2e14	yes	no	7	24	100	40
SD102	4e14	yes	no	11	28	50	40

Figure C.1 shows the leakage current of all samples obtained at +17°C before irradiation. The fluences stated in the legend correspond to the irradiation performed afterwards. The graph confirms that most samples have a good current-voltage characteristic (IV-curve). Only SD81 and SD86 have a too strong current increase and a breakdown before 150 V, respectively. The shown IV-curves were also used to decide which SCAs are investigated in the test beam study.

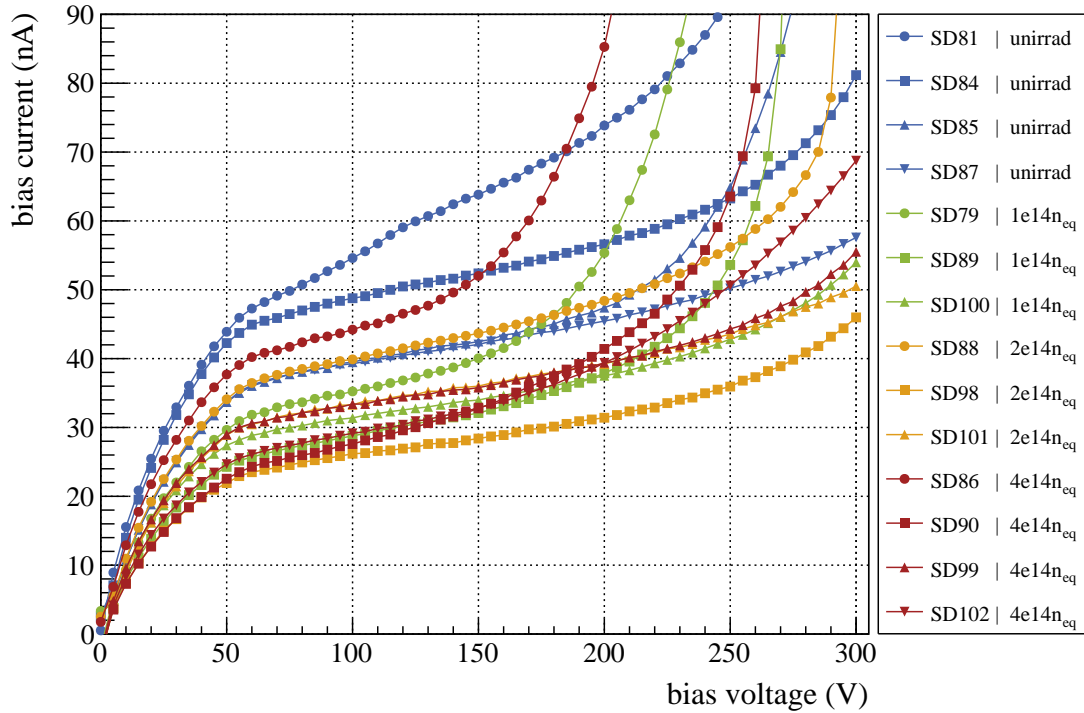


Figure C.1: Current-voltage characteristics of all SCAs produced for the performance study. Aside from SD81 (unirrad) and SD86 ($4e14 n_{eq}$) all IV-curves are fine. SD81 and SD86 have a too strong current increase and a breakdown before 150 V, respectively.

D

ELECTRICAL TEST SETUP

In this chapter the electrical test setup is introduced. It was used for the electrical calibration of the Phase I pixel modules produced at KIT and for the X-ray calibration of the irradiated module which is discussed in section 8.5.3.

The test setup is shown in figure D.1. It allows to test two modules in parallel. They are placed on a cold chuck (identical to the one of the X-ray setup) which is equipped with a Peltier-based cooling system providing temperatures between 30°C and -25°C . The cold chuck is placed inside a light-tight aluminum box. A barrier inside the box reduces the volume which needs to be flushed with dry air in order to prevent condensation. The modules are connected via sacrificial cables and insert cards to custom designed KIT module adapters. The adapters in turn are connected via ribbon cables to the DTBs outside of the box.

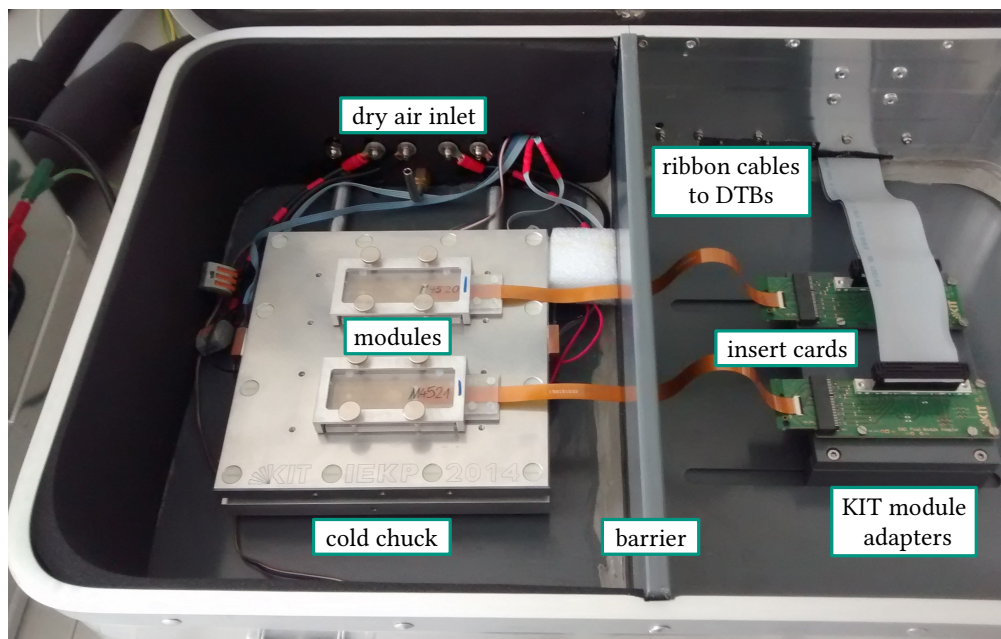
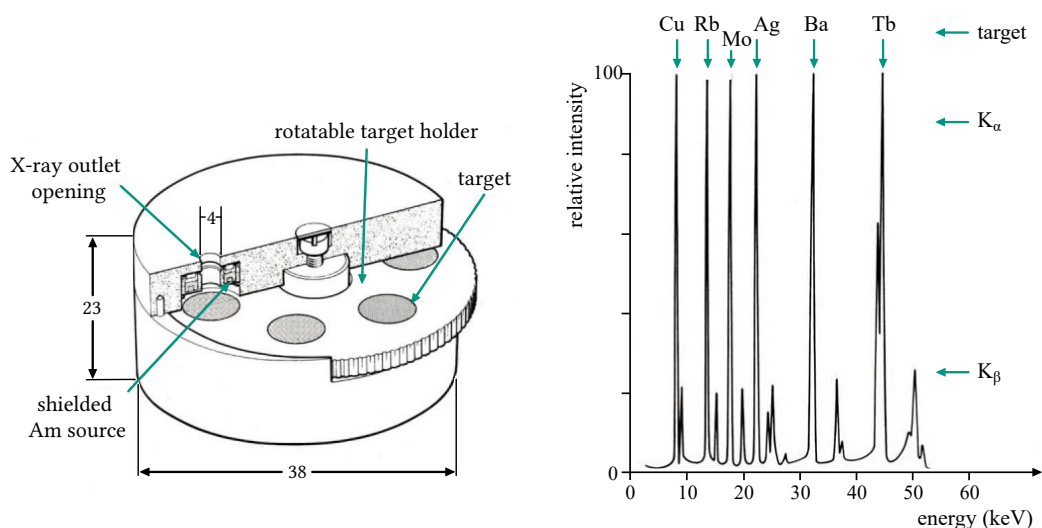


Figure D.1: Electrical test setup for the modules produced at KIT. The setup allows to test two modules in parallel which are placed on the cold chuck (allowing temperatures down to -25°C) inside a light-tight box. A barrier reduces the volume which has to be flushed with dry air to prevent condensation. The modules are connected via sacrificial cables, insert cards, KIT module adapters and ribbon cables to the DTBs located outside of the box. Modified from [Hei16].

X-RAY SOURCE BASED ON AMERICIUM

This chapter describes the X-ray source which was used to perform the X-ray calibration of the irradiated module (see section 8.5.3).

Figure E.1 shows the drawing of the shielded ^{241}Am based X-ray source and the corresponding energy spectrum. The X-ray source, which is shown in figure E.1 (a), relies on ^{241}Am emitting alpha particles (not leaving the closed source) and photons. The photons are used to irradiate one out of six available target materials mounted on a rotatable holder in order to obtain characteristic X-ray photons. The available target materials are copper (Cu), rubidium (Rb), molybdenum (Mo), silver (Ag), barium (Ba) and terbium (Tb). According to latest measurements (13.01.2017) the activity of the ^{241}Am is about 3.43×10^8 Bq. The maximum achievable rate of characteristic X-ray photons is approximately 1.2 kHz/cm^2 . Figure E.1 (b) shows the energy spectrum of the characteristic X-ray photons according to the data sheet. For each target a large K_α contribution and a small K_β contribution are visible. The lowest accessible energy corresponds to Cu (about 8 keV) while the highest is obtained from Tb (about 45 keV).



(a) Drawing of the X-ray source. Photons from the shielded primary α -source irradiate one out of six target materials mounted on a rotatable holder to generate characteristic X-ray photons. These photons leave the X-ray source via the outlet opening.

(b) Energy spectrum of the X-ray source according to the data sheet. Each target has a large K_α contribution and a small K_β contribution. The accessible energy range reaches from 8 keV (Cu) to 45 keV (Tb).

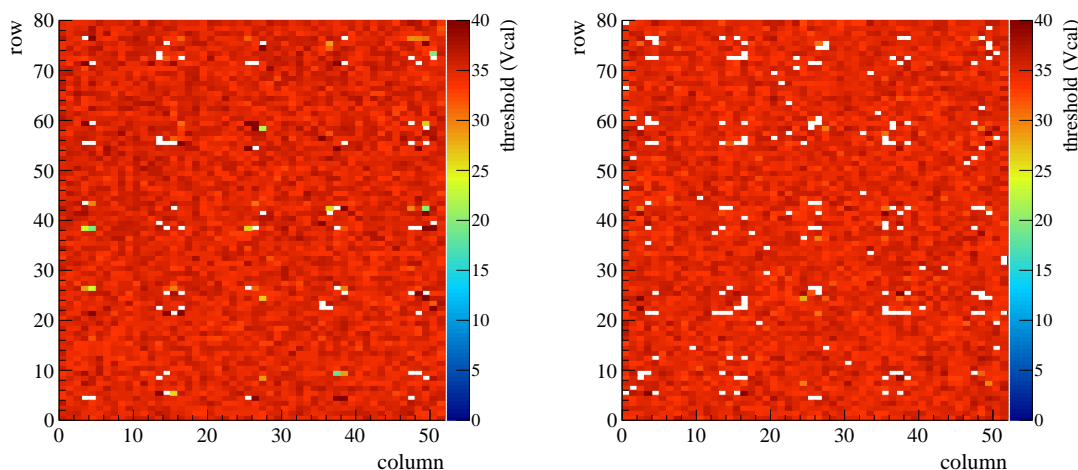
Figure E.1: Drawing of the shielded ^{241}Am based X-ray source and the corresponding energy spectrum. Modified from [Woc17].

 ADDITIONAL LABORATORY RESULTS

In the following chapter threshold maps of irradiated single chips assemblies are discussed. Additionally, X-ray calibrations of the SCAs which were investigated in the test beam are shown.

F.1 THRESHOLD MAPS

The threshold maps allow to investigate the unexpected pattern of pixels with an increased number of hits which was observed for the hit maps shown in figure 8.6.2.



(a) Threshold map of SD90. For most pixels affected by the higher irradiation dose no threshold value could be determined (white spots). The remaining problematic pixels have either thresholds of about 40 Vcal or between 20 Vcal and 30 Vcal.

(b) Threshold map of SD99. For almost all pixels affected by the higher irradiation dose it was not possible to determine the threshold (white spots).

Figure F.1: Threshold maps of the two $4e14 n_{eq}$ SCAs SD90 and SD99 trimmed to a threshold of 35 Vcal. Due to the inhomogeneous irradiation caused by the holes in the carrier PCBs there is a pattern of pixels with different thresholds matching the PCB holes.

Figure F.1 presents the threshold maps of two $4e14 n_{eq}$ SCAs trimmed to a threshold of 35 Vcal. Both threshold maps show an additional feature in form of a regular pattern caused by pixels with different thresholds. The pattern matches the holes in the printed circuit boards carrying the single chip assemblies and it is caused by the inhomogeneous irradiation due to these holes (see section 8.6.2). For the majority of the affected pixels no threshold could be obtained, which corresponds to the white dots of the threshold maps. This is a clear indication that these pixels are not working properly anymore. The remaining affected pixels which have

thresholds either of about 40 Vcal or between 20 Vcal and 30 Vcal are probably also not working optimally.

This behavior might be the reason why these pixels recorded more hits – due to noise or larger clusters – during the laboratory measurements (see figure 8.11). Additionally, it could explain the less efficient spots observed in the test beam (see figure 9.12).

F.2 X-RAY CALIBRATION OF THE SINGLE CHIP ASSEMBLIES

This section shows X-ray calibrations of the single chip assemblies which were investigated in the test beam study. The first out of three plots discusses the X-ray calibrations of all test beam samples obtained at $+17^\circ\text{C}$ and -20°C before irradiation. The second plot is used to check for a potential impact of different thresholds and bias voltages on the X-ray calibration (for an unirradiated SCA). In the third plot X-ray calibrations for three SCAs before and after irradiation are shown. Although a reliable statement is barely possible – due to the neglected trapping – these X-ray calibrations are used to investigate the impact of radiation damage on the detector response behavior.

For each SCA produced for the performance study an X-ray calibration is performed. These X-ray calibrations are one of the selection criteria used to assign the SCAs to the irradiation steps and to decide which SCAs are investigated in the test beam at all.

In figure F.2 the X-ray calibrations of the test beam SCAs are shown. They were performed at $+17^\circ\text{C}$ and -20°C . A comparison of the calibration curves shows that the slopes vary between 38.77 e/Vcal and 49.99 e/Vcal (caused by different response behavior of the ROCs). The X-ray calibration curves for $+17^\circ\text{C}$ and -20°C are very comparable and differ by only 0.7 e/Vcal on average. This was not the case for the analog ROC of the original pixel detector (see e.g [Hos12]) due to the missing temperature compensation of the ROC. In any case, the X-ray calibration curves of the test beam samples do not reveal any conspicuous behavior.

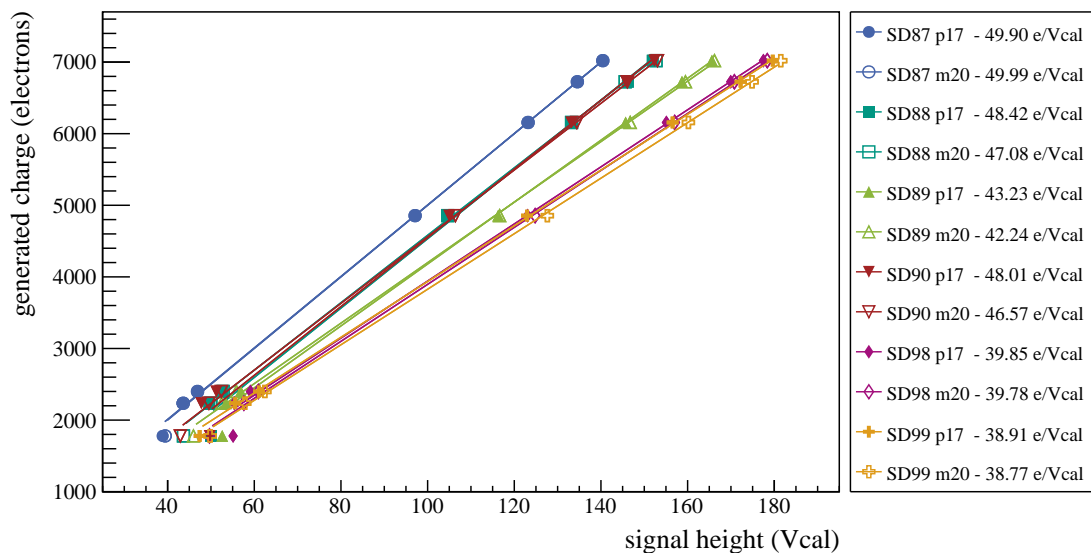


Figure F.2: X-ray calibrations of the test beam samples performed at $+17^\circ\text{C}$ and -20°C before irradiation. The slopes of the calibration curves vary between 38.77 e/Vcal and 49.99 e/Vcal . The average difference between X-ray calibration curves for $+17^\circ\text{C}$ and -20° is only 0.7 e/Vcal .

Figure F.3 shows the X-ray calibrations of the SD88 sample irradiated to a fluence of $2e14 n_{eq}$ which were obtained at different bias voltages and comparator thresholds. There is no recognizable difference between the curves of the two comparator thresholds 30 Vcal and 35 Vcal. For decreasing bias voltages a small shift (about 10 Vcal) of the X-ray calibration curves towards smaller signal heights is visible. This is expected since the signal heights decrease for lower bias voltages (since the sensor is not fully depleted at 100 V and the electric field strength increases with bias voltage) as already presented in figure 8.8.

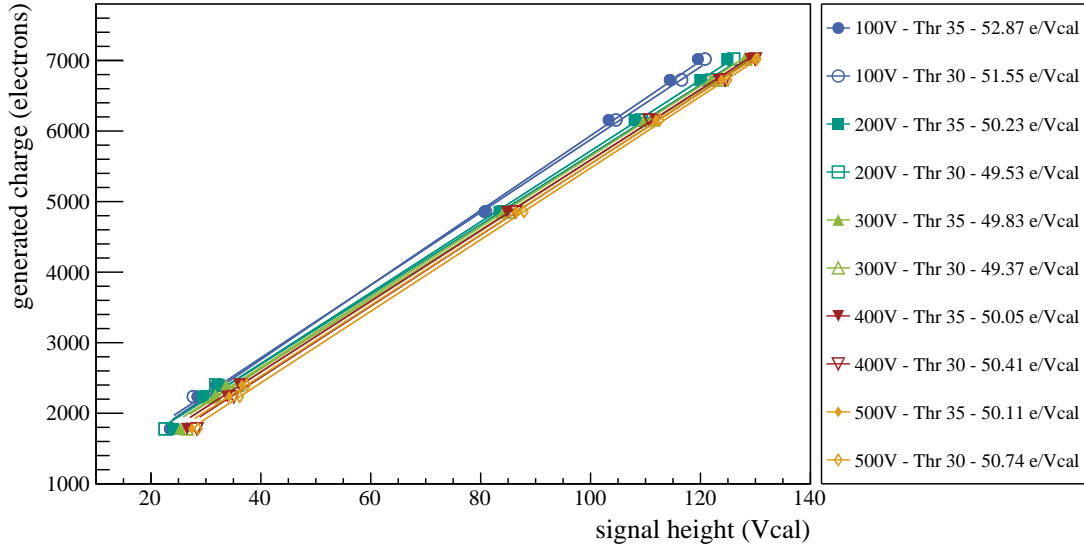


Figure F.3: X-ray calibrations for different bias voltages and thresholds. There is no significant difference between the X-ray calibration curves of the two comparator thresholds. At lower bias voltages the curves are shifted towards lower signal heights.

Figure F.4 shows the X-ray calibration curves of three SCAs corresponding to the three different irradiation steps. As already explained in section 8.5.3 the X-ray calibrations after irradiation are less meaningful since trapping is not taken into account. Hence, the following discussion has to be treated with caution.

The slopes of the X-ray calibration curves obtained after irradiation increase for all SCAs. Further, these curves are shifted towards smaller measured signal heights (given in Vcal). Both observations might be an effect of the increased digital current or the changed band gap reference of the ROC, but probably they are also an effect of charge carrier trapping. First of all, trapping should lead to smaller measured signal heights, which can explain the shift of the curves towards lower signal heights. Second, the more charge carriers are generated, the more of them get trapped. As a consequence high measured signal heights are shifted further due to an increased number of charge carriers being trapped. Especially for the $2e14 n_{eq}$ SCA this is easily recognizable since the shift at lower values is rather small and increases for high signal heights. This explains the increasing slopes of the X-ray calibration curves obtained after irradiation. Nevertheless, for the mentioned reason it is only possible to give a qualitative statement, if any.

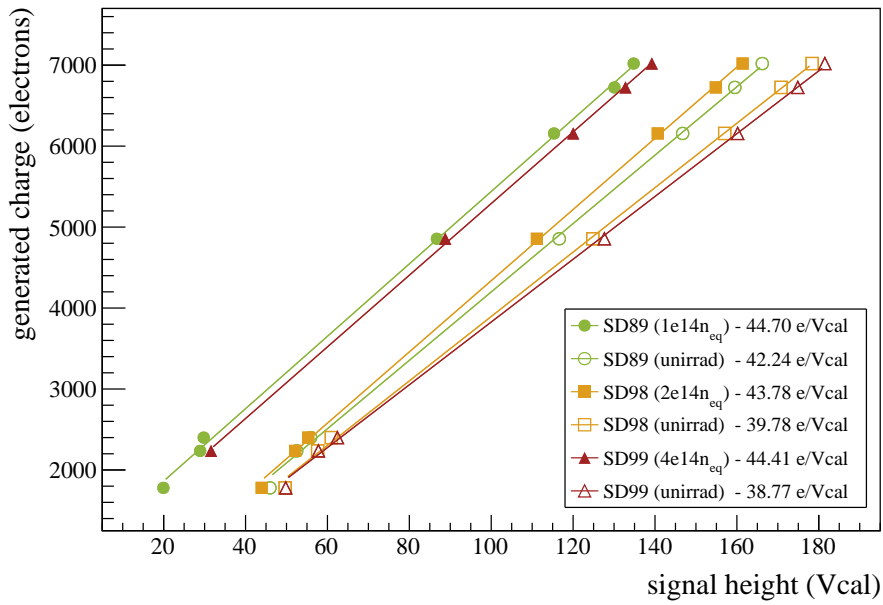


Figure F.4: X-ray calibrations before and after irradiation for three different irradiation steps. X-ray calibrations performed after irradiation have to be treated with caution due to the unconsidered signal height reduction caused by trapping. The X-ray calibration curves obtained after irradiation are shifted towards lower signal heights while the slopes increase. Both observations are probably a symptom of charge carrier trapping.

ADDITIONAL TEST BEAM RESULTS

In the following sections additional test beam results are presented. This concerns the asynchronous data (shifted data streams) and detector properties like cluster size, hit efficiency and spatial resolution.

G.1 ASYNCHRONOUS DATA

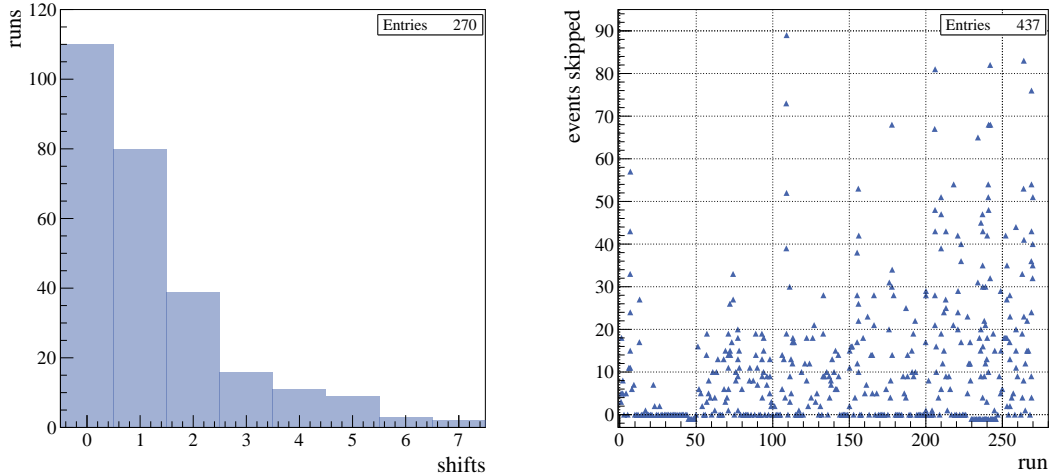
The occurrence of the asynchronous data problem was briefly discussed in section 9.3.1. In this section the problem is investigated in more detail.

An elaborate investigation of the shift problem shows that more than half of all runs is affected. Out of 270 runs 160 contain shifted data which corresponds to about 59.3%. Further, the investigation revealed that runs can suffer from more than one shift. This implies that DUT and REF can lose events at several points during a measurement. Figure G.1 (a) shows the shift distribution for all 270 measurements. The largest fraction corresponds to the 110 runs without any shift, followed by 80 runs containing a single shift. The maximum number of shifts per run is seven, which is the case for only a few runs. Independently of the number of shifts per run, the data of all measurements was successfully re-synchronized.

Additionally, it became apparent that for most shifts more than one event was skipped. In figure G.1 (b) the absolute number of skipped events is shown as a function of the run number. The y-axis indicates how many DUT and REF events are missing. Runs which suffered from several shifts have as many entries in the graph as they have shifts. Measurements without a shift have a single entry at zero events skipped. According to that the 437 entries comprise the 110 runs without shift and 327 shifts distributed over the remaining 160 runs. It is recognizable that for most shifts more than one event is skipped. The maximum number of skipped events in a single run is 89, which occurred in run 109. Further, there are few runs having -1 skipped events. In these runs a single telescope event is missing from the very beginning of the measurement.

Figure G.1 (b) also shows that there were fewer shifts in the beginning of the test beam study, which are the measurements of the unirradiated SCA. All remaining measurements (run numbers > 40) correspond to irradiated samples. Nevertheless, it is not possible to assign the increase of shifts to irradiation for the following reason. The results presented in figure G.1 equally describe the DUT as well as the REF which is the same unirradiated SCA for the complete study. Hence, unirradiated SCAs also experience the increase of shifts for run numbers higher than 40. The fact that DUT and REF equally lose events indicates that the problem is related to a common source. The only component in common is the trigger logic, which implies that the problem might be related to the hardware forming the simple coincidence logic described in figure 9.4.

Figure G.2 shows four plots regarding the shifted data sets of DUT and REF compared to the telescope. Almost in any case DUT and REF events are skipped. In figure G.2 (a) the number of shifts is shown as a function of the step size for all 327 shifts. The step size gives the number



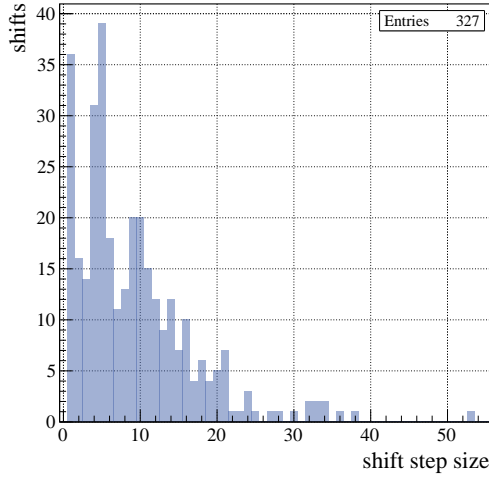
- (a) Shift distribution per run. In total 270 test beam measurements were performed, whereof 160 (about 59.3%) suffer from shifted data. The major part of the affected runs have a single shift, while there are runs with up to seven shifts.
- (b) Absolute number of skipped events as a function of the run number. Measurements containing more than one shift have a corresponding number of entries. All runs without a shift have a single entry at zero events skipped. A value of -1 corresponds to a missing telescope event, which can occur at the start of a measurement.

Figure G.1: Frequency of the shift problem for all 270 runs performed at the test beam.

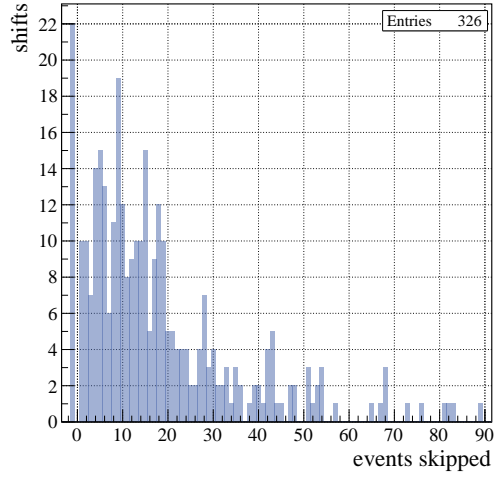
of events skipped per shift. In most cases less than 20 events are skipped while the maximum are 53 skipped events which occurred once. Figure G.2 (b) shows the number of shifts as a function of the absolute number of skipped events per run. The plot refers to 326 out of 327 shifts. The single missing entry corresponds to a shift of -53 skipped events where the minus sign indicates that telescope events were skipped instead of DUT/REF events. This is the only case where telescope events were lost during a measurement. This shift is also visible in the first plot where it is represented by the single entry at the maximum step size of 53. The 22 shifts at -1 events skipped refer to 22 runs where a single telescope event was missing already at the start of the measurement. There are only few runs having more than 50 skipped events while the highest number of skipped events per run is 89. Figure G.2 (c) shows the number of shifts depending on the event number where the shift occurred. For most runs 500,000 events are recorded while there are only a few runs comprising 750,000 events. This is the reason why there are significantly more shifts (per 10,000 events) between 0 and 500,000 events compared to higher event numbers. The plot indicates that shifts occur during the entire measurement and are not limited to certain event numbers. 30 runs had a shift already at the measurement start. Figure G.2 (d) shows the number of shifts as a function of the event step size. The event step sizes states how many events were recorded between two shifts or between measurement start and the first shift. The plot contains only 297 shifts since there are 30 runs which had a shift already at the beginning thus it was not possible to determine the event step size. In many cases the event step size is 50,000 events or less while the highest step size is 650,000 events.

G.2 CLUSTER SIZE

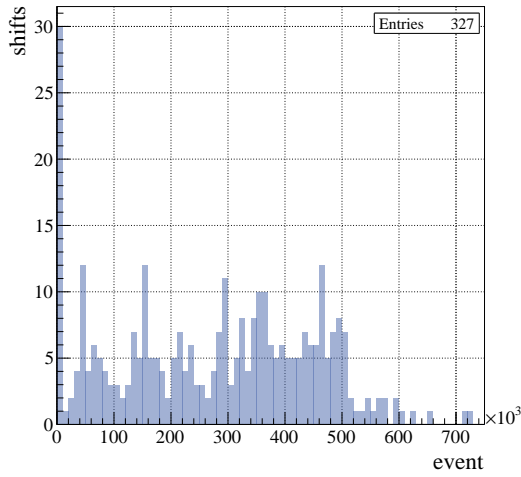
The cluster size is an important detector property as the CMS pixel detector exploits charge sharing to improve the spatial resolution. Therefore, this section presents several additional results regarding the cluster size which complement the results discussed in section 9.3.2. This includes additional intrapixel cluster size maps covering more tilt angles and profile plots through these cluster size maps. Further, intrapixel signal heights maps for seed pixels and



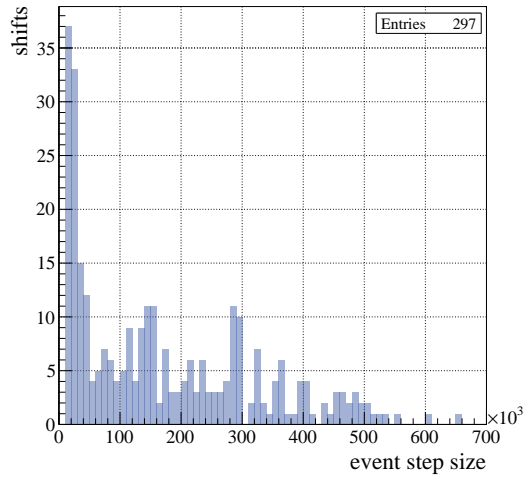
(a) Number of shifts as a function of the shift step size. For most shifts fewer than 20 events were skipped. The maximum number of events skipped in a single shift is 53.



(b) Number of shifts as a function of the absolute number of skipped events per run. The 22 shifts at -1 events skipped refer to 22 runs which had a missing telescope event already at measurement start. The maximum number of events skipped in a single run is 89.



(c) Number of shifts as a function of the event number. The plot shows that shifts occur at any run number. For most runs only 500,000 events were recorded, hence there are only few shifts at higher event numbers. 30 runs had a shift already at the beginning.



(d) Number of shifts as a function of the event step size. In many cases there are less than 50,000 events between two shifts (or between measurement start and the first shift).

Figure G.2: Detailed investigation of the occurrence of shifted events. The number of shifts is given as a function of the shift step size, the absolute number of skipped events, the event number and the event step size.

clusters are shown. Finally, the cluster size is investigated for different bias voltages and thresholds.

G.2.1 INTRAPIXEL CLUSTER SIZE DISTRIBUTION

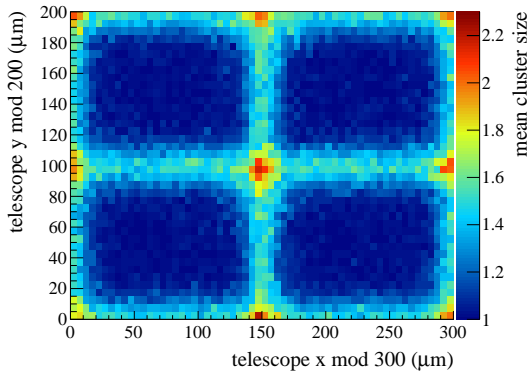
In section 9.3.2.4 the most relevant features of the intrapixel cluster size distribution are discussed referring to two tilt angles (0° and 35°). The results in this section consider also the tilt angle of 15° for completeness.

Figure G.3 shows the intrapixel cluster size maps for an unirradiated sample and a $2e14 n_{eq}$ sample at three different tilt angles¹ (0° , 15° and 35°). Similar results are shown in figure 9.10 but for less tilt angles.

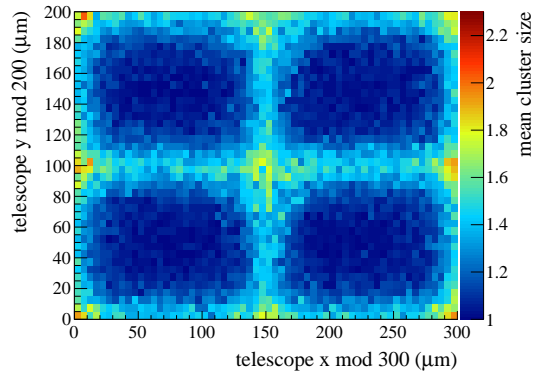
The fiducial hits of each measurement are folded into a 2×2 pixel array showing the cluster size as a function of the track impact position at the sample. The plots on the left-hand side refer to the unirradiated sample and the ones on the right-hand side to the $2e14 n_{eq}$ sample. Apparently, the two samples behave very similar. Only the contours of the cluster size maps of the $2e14 n_{eq}$ sample are less sharp due to radiation damage causing trapping and changing the electric field inside the sensor which affects the determination of the center of charge. At 0° (figure G.3 (a) and (b)) the smaller cluster sizes refer to the inner region of the pixel cells. Because of charge sharing the cluster sizes are larger at the edges and maximum at the corner where four pixels meet. For the 15° measurements (figure G.3 (c) and (d)) the largest clusters are still at the edges and corners, respectively. However, the area corresponding to the smallest cluster sizes (inside the pixels) decreased. This is caused by the electrons traveling $75 \mu\text{m}$ in y -direction inside the sensor at a tilt angle of 15° . As a consequence, the probability for single pixel clusters is limited to track impact positions at the very center of the pixel cells. Additionally, the range of the z -axis indicates that the mean cluster size increased compared to the result at 0° . At 35° (figure G.3 (e) and (f)) the behavior changed significantly. Due to the tilt angle of 35° the electrons travel $200 \mu\text{m}$ in y -direction inside the sensor. This leads to the fact that the smallest cluster sizes (about 2 pixels per cluster) refer to track impact positions at the pixel edges as electrons traverse exactly two pixels. For track impact positions at the center of the pixels the cluster size increases as electrons easily generate charge in three pixels (the electrons traverse the first pixel partially, a second one completely and a third one again partially). The mean cluster size increases further as expected which is indicated by the range of the z -axis. The cluster size maps are examined even further within the next paragraph.

Figure G.4 shows two cluster size profile plots which present the cluster size as a function of the x -coordinate of the track impact position at the sample. In figure G.4 (a) four profiles of an unirradiated sample are given. These profiles represent four cuts through figure G.3 (a) at four different y -coordinates ($25 \mu\text{m}$, $50 \mu\text{m}$, $75 \mu\text{m}$ and $100 \mu\text{m}$). The cluster size in the center of the pixels ($y = 25 \mu\text{m}$, $50 \mu\text{m}$ and $75 \mu\text{m}$) is clearly smaller compared to the cut between two pixels ($y = 100 \mu\text{m}$). Additionally, it is visible that the cluster size increases for x -coordinates of $0 \mu\text{m}$, $150 \mu\text{m}$ and $300 \mu\text{m}$, which corresponds to positions between pixels. Figure G.4 (b) shows four profiles, one for each irradiation step at a tilt angle of 0° . The cluster size profiles of the irradiated samples, especially the one of the $4e14 n_{eq}$ sample, are blurred, which is also indicated by the larger error bars. Further, the cluster size of the $4e14 n_{eq}$ sample is higher in the center of the pixels (between $50 \mu\text{m}$ and $100 \mu\text{m}$ as well as between $200 \mu\text{m}$ and $250 \mu\text{m}$) while it is slightly lower between pixels ($0 \mu\text{m}$, $150 \mu\text{m}$ and $300 \mu\text{m}$) compared to the remaining three profiles. However, the cluster size is still comparable to the unirradiated case and the other two irradiation steps as shown in figure 9.8.

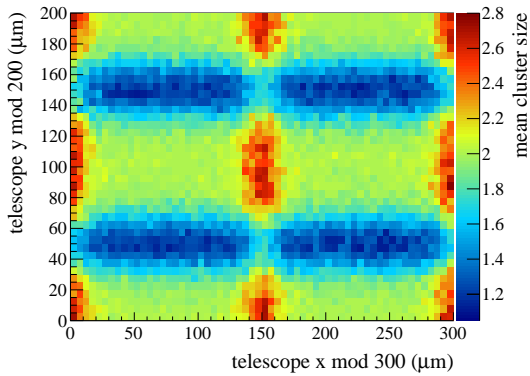
¹ The tilt angle imitates different particle entrance angles and always refers to the y -direction.



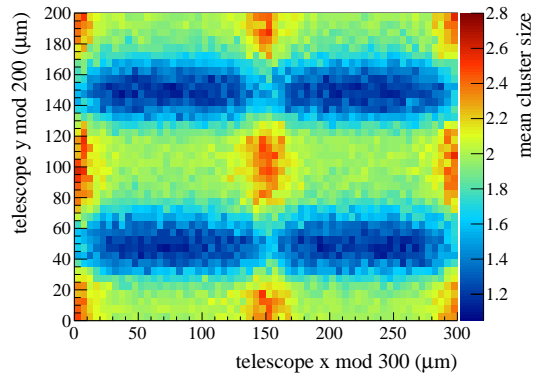
(a) Mean cluster size for an unirradiated sample at 0° . The smallest clusters are located in the inner area of the pixels. Due to charge sharing the cluster sizes are larger at the edges and corners.



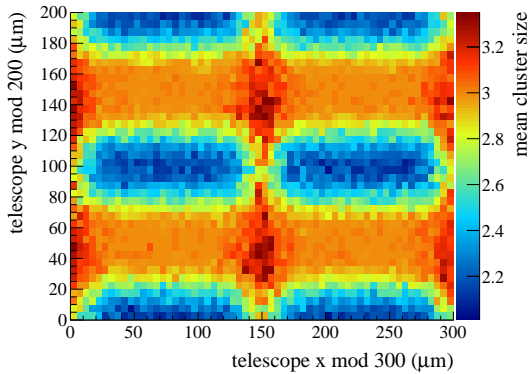
(b) Mean cluster size for a $2e14 n_{eq}$ sample at 0° . Same behavior as figure (a). The contours are less sharp because of radiation damage causing trapping and changing the electric field inside the sensor.



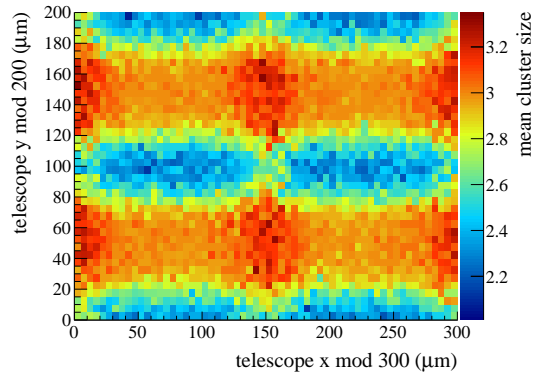
(c) Mean cluster size for the unirradiated sample at 15° . The area corresponding to the smallest cluster sizes decreased because of the tilt angle. Only at the centers of the pixels there is still a considerable probability to generate single pixel clusters as the electrons travel $75 \mu\text{m}$ in y -direction.



(d) Mean cluster size for a $2e14 n_{eq}$ sample at 15° . Same behavior as figure (c). The contours are less sharp because of radiation damage causing trapping and changing the electric field inside the sensor.

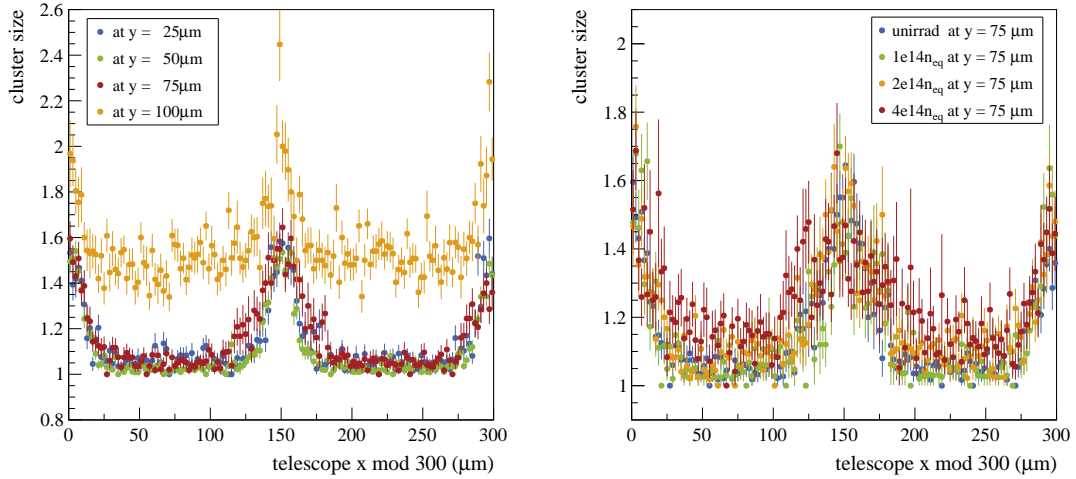


(e) Mean cluster size for the unirradiated sample at 35° . Electrons travel $200 \mu\text{m}$ at this tilt angle which causes mostly two pixel clusters between pixels and larger ones (about 3 pixels) at the center of the pixels.



(f) Mean cluster size for a $2e14 n_{eq}$ sample at 35° . Same behavior as figure (e). The contours are less sharp because of radiation damage causing trapping and changing the electric field inside the sensor.

Figure G.3: Mean cluster size depending on the electron impact position inside the pixels for an unirradiated and a $2e14 n_{eq}$ sample. All fiducial hits are folded into 2×2 pixel arrays to increase the statistics.



(a) Cluster size profiles of an unirradiated sample. The cluster size inside the pixels ($y = 25 \mu\text{m}$, $50 \mu\text{m}$ and $75 \mu\text{m}$) is clearly smaller compared to the region between pixels ($y = 100 \mu\text{m}$). The same is true for the x -coordinate, the cluster size is smaller inside the pixels (between $50 \mu\text{m}$ and $100 \mu\text{m}$ as well as between $200 \mu\text{m}$ and $250 \mu\text{m}$) and larger in between of them ($0 \mu\text{m}$, $150 \mu\text{m}$ and $300 \mu\text{m}$).

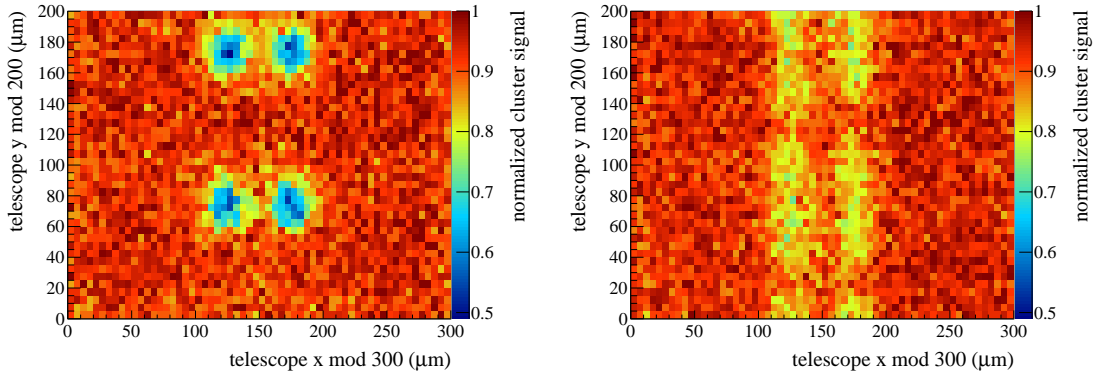
(b) Cluster size profiles for the different irradiation steps. The behavior of the four profiles is relatively comparable. Only the profile of the $4e14 n_{\text{eq}}$ sample is blurred and the cluster size is slightly larger in the pixel centers (between $50 \mu\text{m}$ and $100 \mu\text{m}$ as well as between $200 \mu\text{m}$ and $250 \mu\text{m}$) and smaller between pixels ($0 \mu\text{m}$, $150 \mu\text{m}$ and $300 \mu\text{m}$) compared to the remaining three profiles.

Figure G.4: Cluster size profile plots. The cluster size is given as a function of the x -coordinate of the track impact position. The y -values in the legend correspond to cuts through cluster size maps (see figure G.3) at the corresponding y -coordinates.

G.2.2 INTRAPIXEL CLUSTER SIGNAL HEIGHT

In section 9.3.2.5 the intrapixel signal height of the seed pixel was discussed. Those results confirmed that the bias dots collect charge carriers, which cannot contribute to the measured signal (leading to smaller signal heights). In order to investigate the amount of charge which is actually lost, the intrapixel signal heights of the clusters are investigated.

Figure G.5 shows the cluster signal height as a function of the track impact position for an unirradiated sample at tilt angles of 0° and 15° . The cluster signal heights are normalized to the maximum cluster signal height of the corresponding measurement. At 0° (see figure G.5 (a)) there are four spots – corresponding to the bias dot locations – where the cluster signal height is reduced to about 50% of the maximum value. This is caused by the bias dots collecting the generated charge carriers partially, which in turn cannot contribute to the signal. For all track impact positions outside the bias dot locations, the measured cluster signal heights are very similar, not revealing an additional structure. At 15° (see figure G.5 (b)) the bias dot impact is still visible, but there are two differences. First, the effect of the bias dots is not only limited to the exact bias dot locations. Due to the tilt angle of 15° the electrons travel about $75 \mu\text{m}$ in y -direction affecting more track impact positions. Second, the signal height drop is less strong. Instead of a decrease to 50%, the signal heights are only reduced to about 75% to 80%. Again, this is caused by the tilt angle, as electrons can no longer generate charge exclusively at the bias dot location.



(a) Cluster signal height map at 0° . The cluster signal height is reduced to about 50% at the bias dot locations as the bias dots collect some of the generated charge carriers.

(b) Cluster signal height map at 15° . Due to the tilt angle more track impact positions are affected by the bias dots. At the same time the cluster signal heights are only reduced to about 75% to 80% of the maximum cluster signal height.

Figure G.5: Cluster signal height maps for an unirradiated sample at 0° and 15° . The signal heights are normalized to the maximum cluster signal height. All measurements were obtained at a bias voltage of 200 V.

G.2.3 INTRAPIXEL SIGNAL HEIGHT OF THE SEED PIXEL

The investigation of the intrapixel signal height for the seed pixel discussed in section 9.3.2.5 referred to two tilt angles (0° and 15°). For the sake of completeness additional tilt angles are addresses below.

In figure G.6 the signal heights of the seed pixels are shown as a function of the track impact position for an unirradiated sample. The signal heights are normalized to the maximum seed pixel signal height. As expected, figure G.6 (a) corresponding to a tilt angle of 0° shows that the signal heights of the seed pixels are reduced at the bias dot location due charge carriers collected by the bias dots. The signal heights between the pixels are also reduced which is caused by charge sharing of adjacent pixels. In that case the charge carriers still contribute to the cluster signal height, which is not the case for charge carriers collected by the bias dot. Figure G.6 (b) shows the seed pixel signal height obtained at 15° . The area containing the highest seed pixel signal heights is reduced because of stronger charge sharing between pixels. In addition, the effect of the bias dot is blurred in y-direction due to the tilt angle. In figure G.6 (c) the result corresponding to 35° is shown. At this tilt angle electrons travel about $200\ \mu\text{m}$ in y-direction. This means that electrons traverse at least one pixel completely (in y-direction) independent on the track impact position. As a consequence, the seed pixel signal height always refers to a pixel which was traversed entirely. This is visible in the given seed pixel signal height map which does not show any dependency on the y-coordinate of the track impact position. Only the dependency on the x-coordinate is still present. Between pixels (at $x = 0\ \mu\text{m}$ and $300\ \mu\text{m}$) the measured signal height is slightly reduced due to charge sharing with neighboring pixels. Further, the bias dot still affects the signal height of each seed pixel – as expected – with track impact positions corresponding to the x-coordinates of the bias dots. Figure G.6 (d) presents the seed pixel signal height map at a tilt angle of 55° showing a behavior comparable to the result at 35° . There are no additional effects, aside from less sharp contours due to the smaller amount of data as less tracks traverse the sample at higher tilt angles.

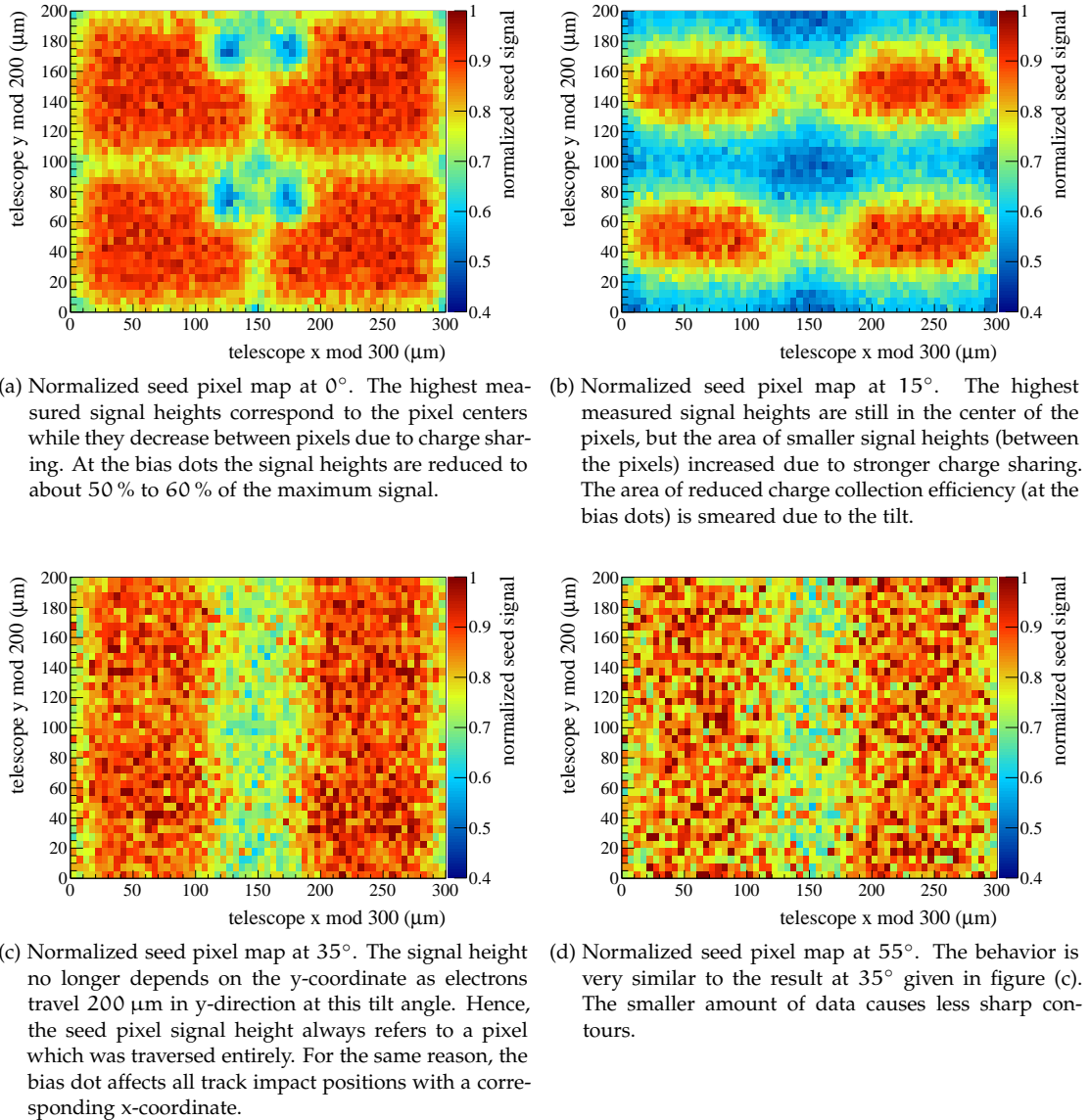
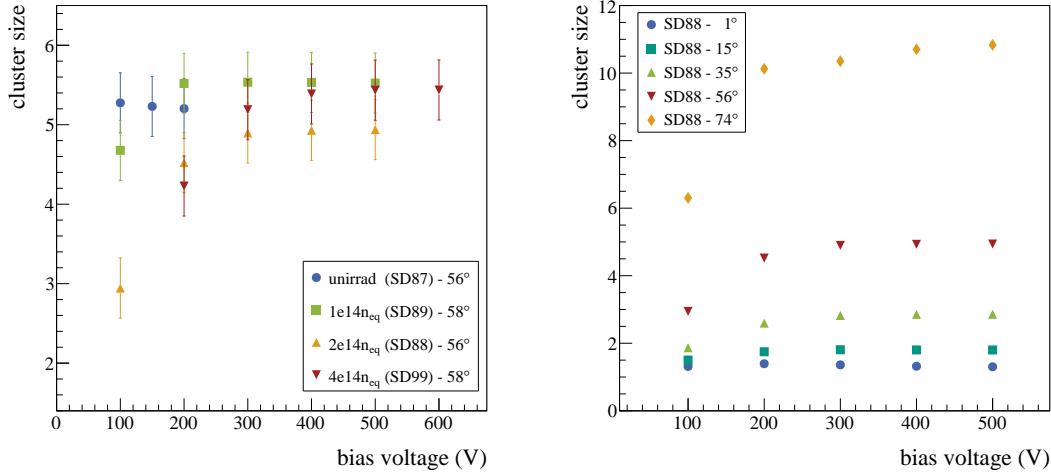


Figure G.6: Normalized seed pixel map of the unirradiated DUT for four tilt angles. The signal heights of the seed pixels are normalized to the highest measured signal. All measurements were obtained at a bias voltage of 200 V.

G.2.4 MEAN CLUSTER SIZE DEPENDING ON THE BIAS VOLTAGE AND THE TILT ANGLE

This section investigates the mean cluster size as a function of the bias voltages and tilt angle including a comparison between different irradiation steps and thresholds.

In figure G.7 the cluster size is shown as a function of the bias voltage. Figure G.7 (a) presents the cluster size for each irradiation step at a tilt angle of about 55° . The three irradiated SCAs show a cluster size increase saturating above the depletion voltage. This effect cannot be observed for the unirradiated SCA since it has to be operated fully depleted as explained in section 4.2.1. Minor deviations between the samples are mostly caused by the small differences of the tilt angles. In any case, the cluster sizes – which vary between 5 and 5.5 pixels per cluster at full depletion – are in good agreement with respect to the shown uncertainties. In



- (a) Cluster size for different irradiation steps. The irradiated samples show a cluster size increase which saturates above the depletion voltage. The corresponding cluster sizes (5 to 5.5 above the depletion voltage) are in good agreement with respect to the given error bars and the slightly different tilt angles.
- (b) Cluster size of the $2e14 n_{eq}$ sample at different tilt angles. The cluster size increases clearly at large tilt angles. The increase at low bias voltages is not visible at tilt angles 0° and 15° because of too small cluster sizes.

Figure G.7: Cluster size as a function of the bias voltage for different irradiation steps and tilt angles.

figure G.7 (b) the cluster size of the $2e14 n_{eq}$ sample SD88 is shown for different tilt angles. The cluster size clearly increases at higher tilt angles as expected. The increase of the cluster size followed by the saturation at higher bias voltages is only visible for the measurements above 15° . This is not visible at 0° and 15° as the cluster sizes are small, even when the sensor is fully depleted.

Figure G.8 shows the cluster size dependency of the tilt angle for the unirradiated sample. The plot also gives a comparison for the two comparator thresholds 30 Vcal and 35 Vcal at three different bias voltages. However, there is no remarkable difference between both the two thresholds and the bias voltages within the given uncertainties. If the difference between the thresholds would have been bigger, larger cluster sizes would have been expected for the lower threshold. The difference between 30 Vcal and 35 Vcal is only about 250 electrons which is apparently too small to see any impact.

G.3 HIT EFFICIENCY PROFILE

Already in section 9.3.3 several results about the hit efficiency are discussed. For the sake of completeness, efficiency profiles through intrapixel efficiency maps as shown in figure 9.15 are discussed here.

Figure G.9 shows three efficiency profiles of a $2e14 n_{eq}$ sample at three different tilt angles (0° , 15° and 35°). Each profile refers to a cut through the efficiency map at $y = 75 \mu\text{m}$ providing a profile through two bias dots (see figure 9.15). For a tilt angle of 0° the impact of the two bias dots is clearly visible decreasing the hit efficiency to about 70%. However, already at 15° there is almost no bias dot effect visible so that the efficiency profiles for 15° and 35° are consistently high through both pixels. Since charged particles inside CMS are bent by the magnetic field they do not traverse the detector perpendicular. Hence, an efficiency drop caused by the bias dot is not expected.

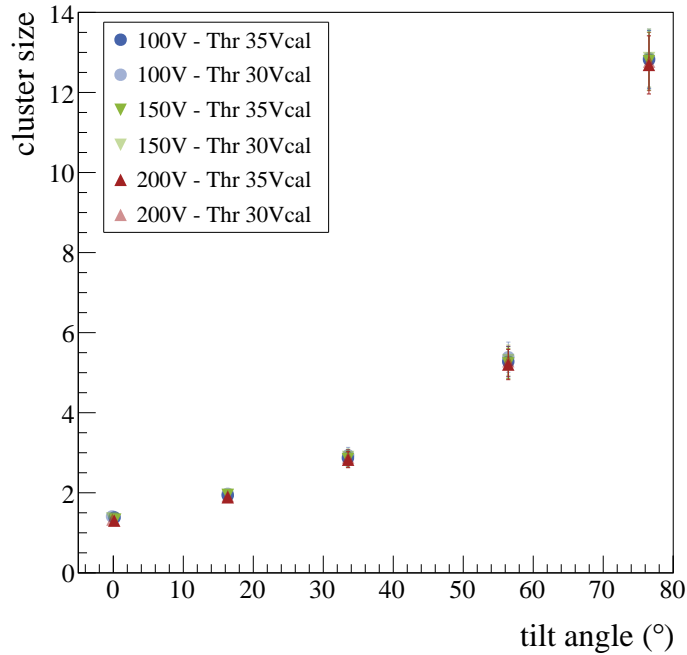


Figure G.8: Cluster size as a function of the tilt angle for different thresholds and bias voltages. There is no considerable difference between both the two thresholds and the bias voltages within the given uncertainties.

G.4 INTRAPIXEL RESOLUTION

In section 9.3.4.1 the most relevant observations concerning the intrapixel resolution are discussed. However, since those results refer to two tilt angles only (0° and 55°), additional tilt angles are addressed in this section.

In figure G.10 eight intrapixel resolution measurements for an unirradiated sample at four different tilt angles (0° , 15° , 35° and 55°) are shown. The given resolutions refer to the **Mean Absolute Difference (MAD)** which is the average distance between DUT hit and track impact position and must not be confused with the intrinsic resolution. Nevertheless, the MAD method allows to investigate the intrapixel behavior qualitatively. The plots on the left-hand side present the resolution in y and the plots on the right-hand side the resolution in xy . Since the tilt goes along the y -direction there is no impact on the resolution in x , thus it is not considered. Figure G.10 (a) shows the resolution in y at 0° . The resolution clearly depends on the y -coordinate of the track impact position. The best resolution (about $5 \mu\text{m}$) is achieved for track impact positions in the pixel center while the worst resolution (above $40 \mu\text{m}$) corresponds to the pixel edges. At 15° the dependency on the y -coordinate decreased distinctly as visible in figure G.10 (c). This is caused by the improved charge sharing also improving the average resolution as indicated by the range of the z -axis. The best resolution (about $5 \mu\text{m}$) is obtained for impact positions very close the pixel center. Apart from this small region, the resolution is relatively homogeneous ($10 \mu\text{m}$ to $15 \mu\text{m}$) across the pixel cells. At a tilt angle of 35° , shown in figure G.10 (e), the dependency on the y -coordinate of the track impact position is even smaller. However, the best resolution (about $8 \mu\text{m}$) no longer corresponds to the pixel center but instead to the region between pixels. This is related to the cluster size. At 35° the mean cluster size for track impact positions between pixels is almost exactly two (see figure G.3 (c)), which is the optimal cluster size to improve the resolution via charge sharing. At all other positions the cluster size is larger, which is the reason for a slightly worse resolution ($10 \mu\text{m}$ to $14 \mu\text{m}$).

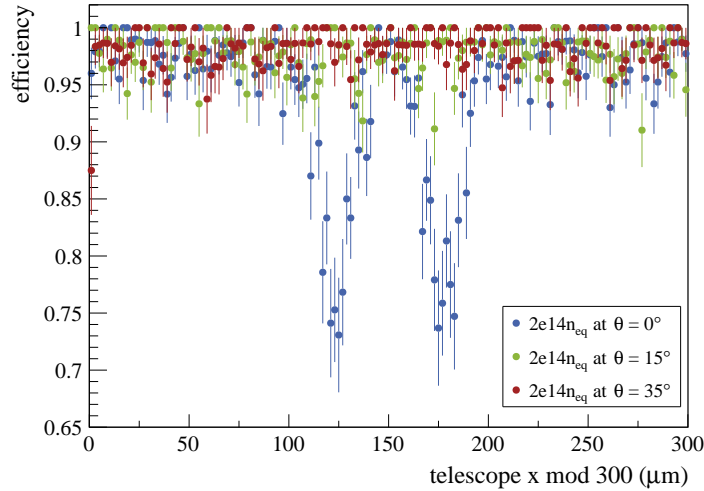


Figure G.9: Hit efficiency profiles through the bias dot for different tilt angles. The error bars are determined by the standard deviation. The impact of the two bias dots is clearly visible at 0° decreasing the hit efficiency to about 70%. At 15° and 35° there is no more efficiency deterioration.

Figure G.10 (g) shows the resolution in y for a tilt angle of 55° . At this tilt angle there is no more dependency on the y -coordinate.

Figure G.10 (b) presents the resolution in xy at 0° . The dependency of the resolution on the track impact position is clearly visible. The best resolution (less than $10 \mu\text{m}$) is obtained for track impact positions exactly at the pixel center. The xy resolution at 15° is shown in figure G.10 (d). As already observed in figure G.10 (c) there is barely a dependency on the y -coordinate of the track impact position at this tilt angle. Therefore, the resolution in xy is mostly dominated by the x -coordinate of the impact position. Only at the centers of the four pixel cells a small effect of the resolution in y is recognizable. In figure G.10 (f) (35°) the influence of the y -coordinate is even smaller and figure G.10 (h) depends exclusively on the x -coordinate of the track impact position. Because of the smaller amount of recorded data – due to the tilt angle – the contours are less sharp at 55° .

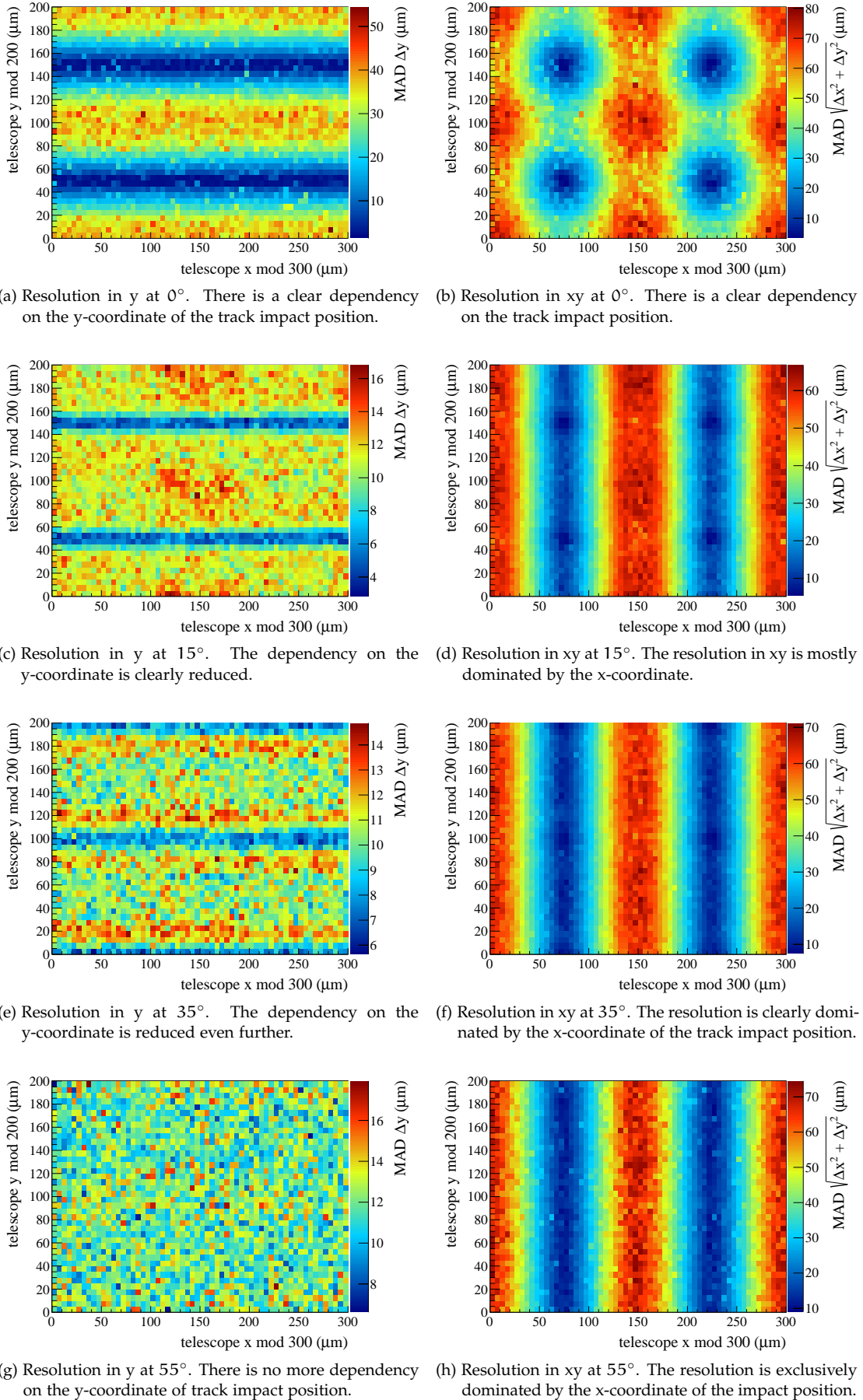


Figure G.10: Intrapixel resolution of an unirradiated SCA at four tilt angles (0° , 15° , 35° and 55°). The resolutions refer to the mean absolute difference (MAD).

LOW TEMPERATURE BUMP BONDING FOR PIXEL SENSOR STUDIES

Although the new CMS Phase I pixel detector was only recently installed and started operating in early 2017, it is already clear that it needs to be replaced in 2023/2024 as a consequence of the LHC schedule. In order to achieve the best possible results regarding the precision of the physics analyses and the potential discovery of rare physics processes, it is necessary to maximize the statistics recorded by the experiments. For this reason, the LHC luminosity will be increased to at least five times the design luminosity when the HL-LHC goes into operation (see figure 2.4). As a result of the increased luminosity, the pile up will increase on average from about 60 to 140 simultaneous proton-proton collisions, which leads to more particles emerging from the collisions and to a higher track density. This will cause a higher detector occupancy deteriorating the tracking efficiency due to ambiguities in the assignment of hits to tracks. To address this issue a new pixel detector will be built with increased granularity (smaller pixels) allowing efficient tracking at higher track densities.

In order to increase the granularity for the new CMS Phase II pixel detector a new sensor with smaller pixels (compared to the Phase I pixel sensor) needs to be developed. However, at the time when the present thesis was written, no appropriate sensors and readout chips with such small pixels were available. Nevertheless, there is still a possibility to investigate smaller pixel pitches. Therefore, a special sensor design (called mixed pitch sensor, introduced in figure H.1) was developed, which can be tested with the PSI46dig ROCs used for the Phase I Upgrade. First results on the performance of these sensors are given in [VBR⁺16]. However, the investigation at a radiation damage corresponding to fluences higher than $1e16 n_{eq}$ [CMS15] (as expected for the HL-LHC) is difficult.

Since the PSI46dig ROCs are developed for the Phase I pixel detector of CMS, they do not provide the required radiation tolerance to be operated at the fluences expected for Phase II. A reliable sensor study (investigating the charge collection, hit efficiency and spatial resolution) is thus only feasible if the bare sensor is irradiated before it is bump bonded to the ROC. The problem of this approach is the high bonding temperature of about 140 °C (see figure 5.6). As mentioned earlier in this thesis (see section 3.3) irradiated sensors have to be cooled to avoid undesired annealing. The high temperatures of the standard bonding process would cause too much annealing making reliable measurements impossible. For this purpose, ETP and IPE jointly developed and investigated different low temperature bump bonding processes. The challenge is to establish a sufficiently strong bump bond connection (for sensor studies) with a low bonding temperature (e.g. 50 °C) applied for a short period of time (about a minute).

The successful development of such a process provides a valuable tool for sensor studies in general. First R&D steps were already performed in 2014 and published in [Kud14]. Based on these low temperature bump bonding results, a test beam study of potential Phase II sensor material was carried out (see [Sch15]). However, the low temperature bump bonding process was still in an early stage, which was indicated by the poor bonding quality.

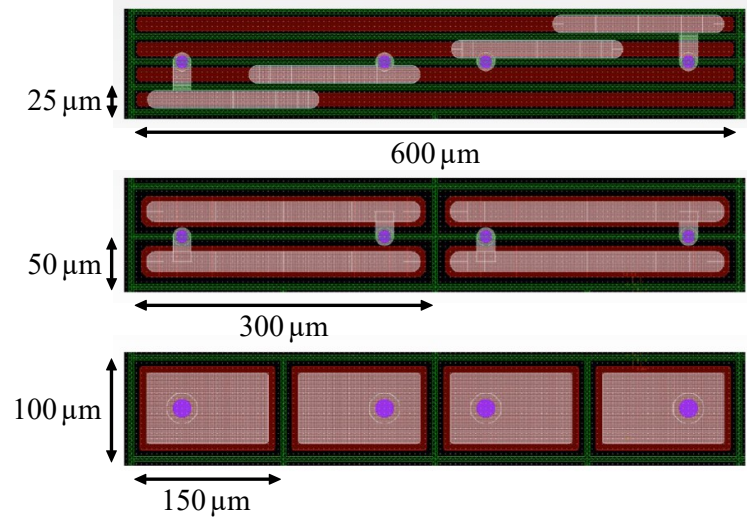


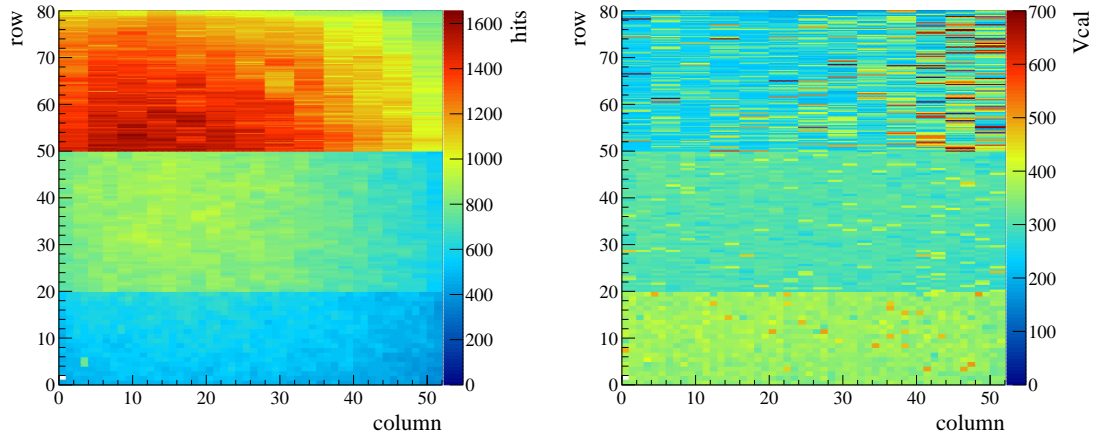
Figure H.1: Pixel geometries of the mixed pitch sensor. The bottom part shows four pixels with a size of $100\ \mu\text{m} \times 150\ \mu\text{m}$ (the standard Phase I pixel geometry). The central region shows $50\ \mu\text{m} \times 300\ \mu\text{m}$ pixels providing a smaller pitch in row direction. The pixels in the top part have a size of $25\ \mu\text{m} \times 600\ \mu\text{m}$. To match the bump bond pattern of the PSI46dig ROC (purple dots) aluminum routing lines (pale regions) are necessary for both non standard pixel geometries. The red areas indicate the pixel implants.

This chapter first introduces a Phase II pixel sensor study that is a major motivation for the development of a working low temperature bump bonding process. Afterwards the general low temperature bump bonding process is described. Finally, the measurements and results for the bonding of the mixed pitch samples (SCAs consisting of a PSI46dig ROC and a mixed pitch sensor) are discussed.

H.1 SENSOR STUDIES FOR THE PHASE II UPGRADE

The motivation to develop a low temperature bump bonding process – aside from providing this option to sensor studies in general – is a Phase II pixel sensor study based on the sensor prototype mentioned before. The ROCs which were used in the development of the low temperature bump bonding process stem from the Phase I module production. The pixel sensor prototypes use a special design which allows to investigate smaller pitches while still matching the bump bond pattern of PSI46dig ROCs. Its pixel matrix is divided into three regions, each formed by pixels with a different geometry.

Figure H.1 shows the pixel geometries of the three sensor regions. The lower region consists of pixels with a size of $100\ \mu\text{m} \times 150\ \mu\text{m}$ which is the standard Phase I pixel geometry used also in the test beam study presented in chapter 9. These pixels extend from row 1 to row 20 of the mixed pitch sensor. The pixels in the middle of the figure have a size of $50\ \mu\text{m} \times 300\ \mu\text{m}$ (row 21 to row 50). Reducing the pitch in one direction and increasing it in the other one allows to keep the pixel area of $15,000\ \mu\text{m}^2$ unchanged. This is required, as the sensor pixels and the pixel unit cells of the ROC have to be of equal size to avoid insensitive sensor areas. Nevertheless, the pitch of $50\ \mu\text{m}$ in the direction of the rows allows to investigate the detector performance for a smaller pitch. In order to match the bump bond pattern of the ROC (purple dots in the figure) aluminum routing lines are necessary. The pixels in the top part have a size of $25\ \mu\text{m} \times 600\ \mu\text{m}$ (row 51 to row 80) which allows to study the detector performance for an even smaller pitch. However, even longer aluminum routing lines are required in this case,



(a) Hit map for unclustered electron hits. It is clearly visible that the number of hits increases for narrower pixels. This is related to larger cluster sizes caused by the small pitch in row direction. Hence, electrons easily generate charge in at least two rows.

(b) Signal height map for unclustered electron hits. Due to the larger cluster sizes the average signal height is lower for narrower pixels. Some pixels, especially in the top part, measure higher signal heights which are probably caused by cross talk due to the aluminum routing lines on top.

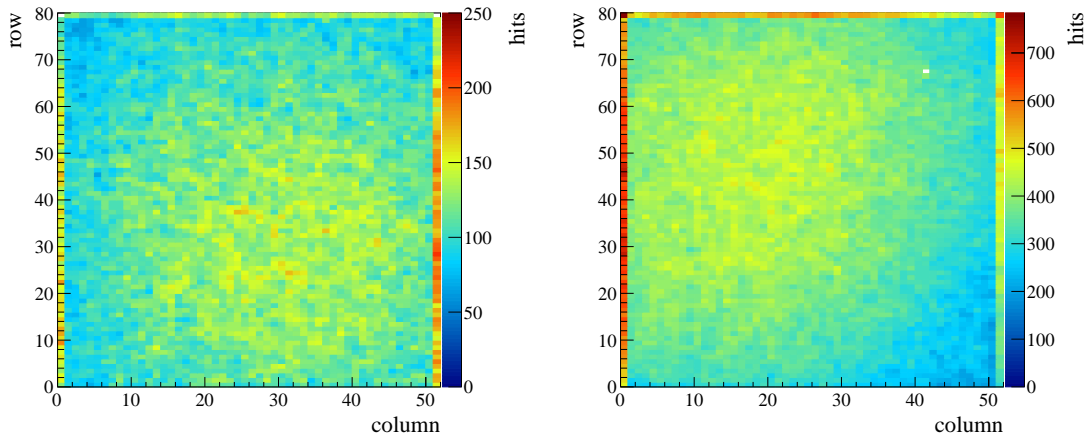
Figure H.2: Hit map and signal height map for a standard bonded mixed pitch sample. The given results were obtained with a ^{90}Sr source.

which makes the detector susceptible to crosstalk [VBR⁺16]. Due to the three regions with different pitches the sensors are referred to as "mixed pitch sensor".

To develop a low temperature bump bonding process for the mixed pitch sensor, a baseline reference is required to qualify the results. For this purpose, some mixed pitch samples were produced with the standard bonding process used during the Phase I module production. The corresponding reference results refer to measurements which are performed with a ^{90}Sr source.

Figure H.2 shows the hit map and the signal height map of a mixed pitch reference sample. The hit map in figure H.2 (a) gives the distribution of unclustered hits obtained from a ^{90}Sr source measurement. The $25\ \mu\text{m} \times 600\ \mu\text{m}$ pixels are in the top part, the $50\ \mu\text{m} \times 300\ \mu\text{m}$ in the middle region and the pixels with the standard size of $100\ \mu\text{m} \times 150\ \mu\text{m}$ are in the bottom region. Obviously, the number of hits increases for the narrower pixels. This is caused by an increase of the cluster size, which in turn is a result of the small pitch in row direction as incoming electrons easily deposit charge in adjacent pixels of different rows. Figure H.2 (b) shows a signal height map of unclustered hits. Again there is a difference between the three regions. Because of the larger clusters in the top region the signal height per pixel is lower (on average) while the highest signals are located in the $100\ \mu\text{m} \times 150\ \mu\text{m}$ pixel region in the bottom part. There are some pixels which do not follow the trend and measure higher signal heights. This is especially true for the $25\ \mu\text{m} \times 600\ \mu\text{m}$ pixels in the top part and probably related to cross talk due to the aluminum routing lines on top of the pixels.

The results introduced above define the benchmark for the low temperature bump bonding process of mixed pitch samples. Before the bonding attempts of the mixed pitch samples are discussed, the general approach is introduced.



(a) Hit map for a sample produced with the standard bump bonding process of the Phase I pixel production. Each pixel is connected as confirmed by the hit map and the spot of the ^{90}Sr source is clearly visible.

(b) Hit map for a low temperature bonded sample relying on gold stud to tin lead bonding. Each pixel is connected and the spot of the ^{90}Sr source is visible. There is only a single pixel which is electrically dead. Due to a higher number of recorded hits the contours are softer.

Figure H.3: Hit maps obtained from measurements with a ^{90}Sr source for a standard bonded and a low temperature bonded sample. Both samples are built from Phase I single chip sensors and PSI46dig ROCs.

H.2 LOW TEMPERATURE BUMP BONDING

When the development of the low temperature bonding process started, several options were available. This includes, for instance, the usage of conductive glues or the Precoat by Powder Sheet (PPS) method, which relies on foils already equipped with small bumps [CBC⁺16]. Among all options, the most promising one is a process based on gold stud to tin lead bump bonding. This process, which represents the low temperature bump bonding process, is described in the next section.

H.2.1 GOLD STUD TO TIN LEAD BUMP BONDING

The gold stud to tin lead bump bonding method was developed using ROCs equipped with tin lead bumps (applied by RTI). A Ball-Wire-Bonder using a thin gold wire of $15\ \mu\text{m}$ allows to equip the bare sensors with gold studs in-house. The gold studs are either placed on the Under Bump Metallization (UBM) or directly on the aluminum pads if no UBM is present. The gold stud bump bonding technology was already tuned in previous studies which have been published in [Hei12] and [Kud14]. The basic idea of the gold stud to tin lead bump bonding process is to press the gold studs into the softer tin lead bumps in order to establish a sufficiently reliable connection. Since this process is based on mechanical deformation only it gets along without high bonding temperatures and minimal annealing. Because of their good availability, Phase I single chip sensors (as used in the test beam study presented in chapter 9) were used to develop the general low temperature bump bonding process.

Figure H.3 shows the hit maps for a standard bonded sample based on tin lead bumps and the standard KIT Phase I bump bonding process (see figure 5.6) and a low temperature bonded sample relying on the gold stud to tin lead process are given. The only difference between the two samples are the gold studs on the sensor side of the low temperature bonded sample and the bonding parameters. The standard bonding process is performed at a temperature of $140\ ^\circ\text{C}$ with a force of $100\ \text{N}$ while the low temperature bonding process relies on a temperature

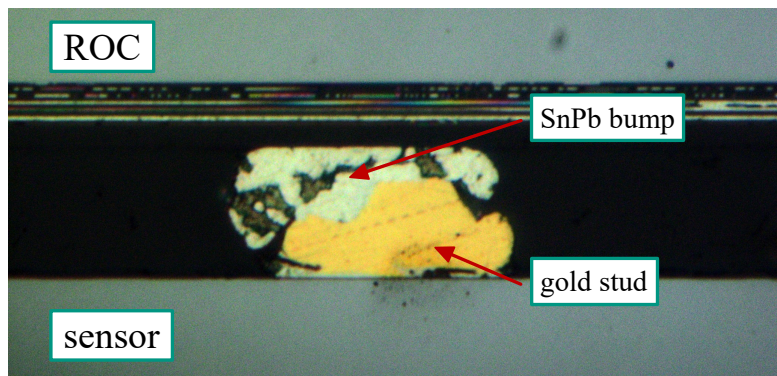


Figure H.4: Cross section of a gold stud to tin lead (SnPb) bump connection. In the top part the ROC and a single tin lead bump are visible. The sensor and a single gold stud are shown in the lower part. The gold stud penetrates into the softer tin lead bump establishing a reliable connection.

of 50 °C (applied for a minute) and a 200 N bond force. These parameters proved¹ to be the most reliable configuration for the gold stud to tin lead process.

Figure H.3 (a) shows the hit map of the standard sample. Each pixel is connected and the spot of the ⁹⁰Sr source is visible (there is only a single electrically dead pixel). In figure H.3 (b) the hit map of the low temperature bonded sample is given. It is clearly visible that this hit map also shows the desired behavior. First of all, all pixels are connected and the spot of the ⁹⁰Sr source is again visible. Due to the higher number of recorded hits for the low temperature bonded sample the contours in the hit map are softer. Apart from that, both samples behave identically which indicates the reliable quality of the low temperature bump bonding process. In addition, cross sections of such a sample were made in order to investigate the quality of the gold to tin lead connection in more detail.

In figure H.4 a cross section of a gold stud to tin lead bump connection is shown. The ROC and one of the tin lead bumps (applied by RTI) are shown in the top part of the picture. In the lower part the Phase I pixel sensor and a single gold stud (applied in-house at IPE) are visible. The cross section shows that the gold stud penetrates into the soft tin lead bump as desired. However, these connections have to provide a certain long term stability required to perform sensor studies.

Figure H.5 shows two hit maps and signal height maps of a sample produced with the gold stud to tin lead bump bonding process. To investigate the long term stability, measurements with a ⁹⁰Sr source are performed before and after ten thermal cycles (between -20 °C and +20 °C). Figure H.5 (a) presents a hit map before thermal cycling. The spot of the ⁹⁰Sr source is clearly visible and all pixels, except for a single electrically defective one, are working properly. Figure H.5 (b) shows a hit map after ten thermal cycles. Apparently, the mechanical stress, caused by the thermal cycling, did not disconnect any gold to tin lead connection as each pixel detected a reasonable number of hits (except for the single electrically defective one). Since the source was located further away the spot is barely visible while the increased number of detected hits per pixel is caused by a longer measurement time. In figure H.5 (c) a signal height map, obtained before thermal cycling, is presented. The majority of the pixels have a comparable response behavior providing signal heights of about 350 Vcal. There are only few pixels with increased signal heights of about 600 Vcal. Figure H.5 (d) shows a signal height map which was obtained after ten thermal cycles. The result is very comparable to the signal height map given in figure H.5 (c). Again most pixels show signal heights of about 350 Vcal and there are only few pixels with higher signal heights of about 500 Vcal. Minor differences regarding the absolute signal heights between the two signal height maps are possible as a new

¹ The range of the investigated bond forces goes from about 100 N to 300 N.

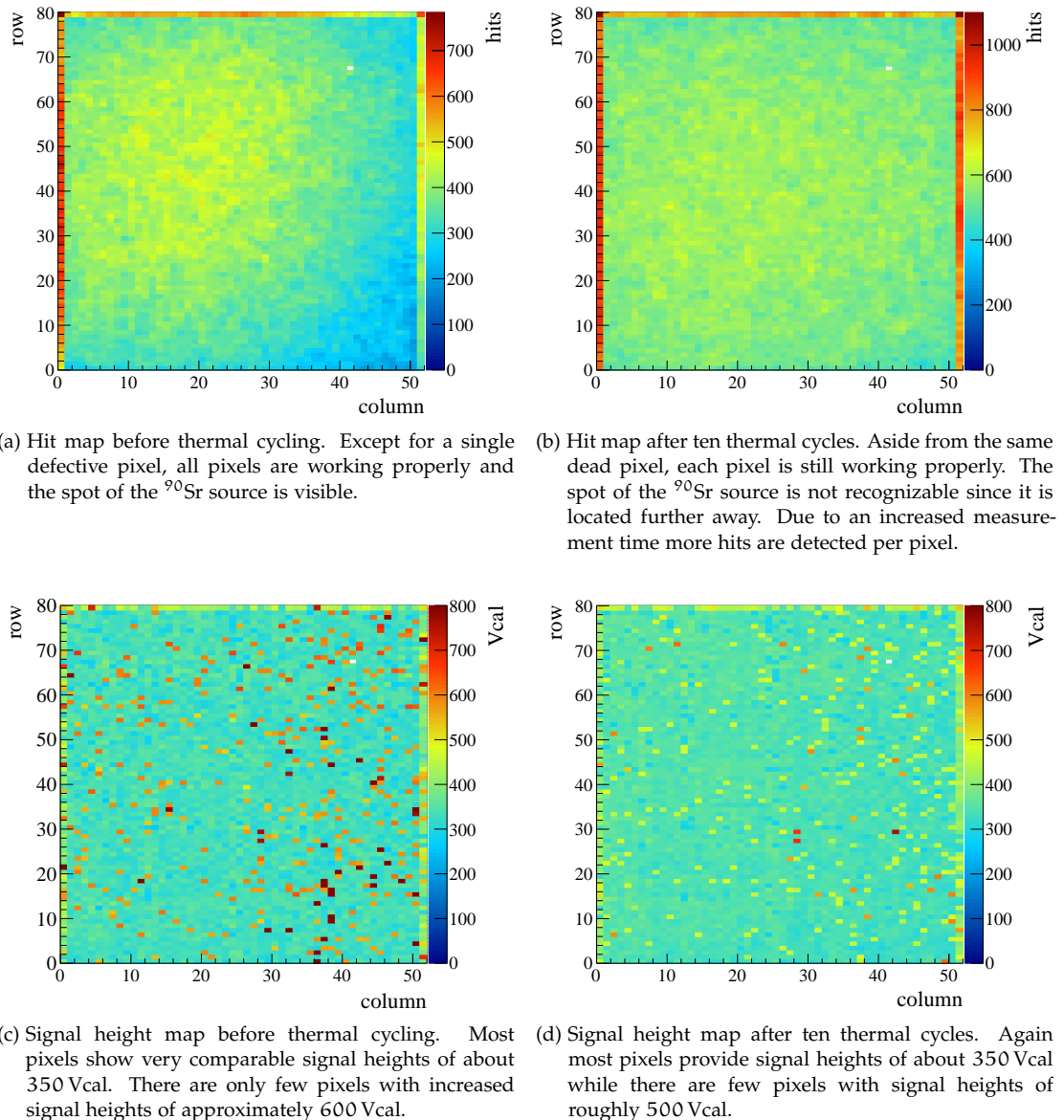


Figure H.5: Hit map and signal height map before and after ten thermal cycles between -20°C and $+20^\circ\text{C}$. The sample was produced with the gold stud to tin lead bump bonding process. Both measurement are obtained with a ^{90}Sr source. After the thermal cycling a new electrical calibration was performed.

electrical calibration was performed after the thermal cycling. The given results confirm that the developed gold stud to tin lead bump bond process is sufficiently long term stable.

While the gold to tin lead bonding process works fine for the Phase I pixel sensors it turned out that this is not the case for the mixed pitch sensors. In principle this process should work for all kind of sensors as long as they can be equipped with gold studs. However, after extensive testing it was concluded that it is not possible to reliably place gold studs on the mixed pitch sensors. The assumption is that the RTI UBM of the mixed pitch sensors is incompatible with gold studs. The PacTech UBM of the Phase I sensor is formed by a palladium layer, a nickel layer and a gold layer while the RTI UBM consists of a titanium tungsten layer, a nickel layer and a gold layer. Additionally, the PacTech UBM is flat while the RTI UBM is U-shaped.

According to that, the incompatibility is either related to the different first UBM layer, the layer thicknesses² or the UBM shape.

As a consequence of the fact that gold studs cannot be applied to the mixed pitch sensors two other options are left. The first and preferred option is using additional mixed pitch sensors without UBM, which would allow to place gold studs directly on the aluminum pads of the sensor. However, it was not possible to receive such sensors within the time frame of this thesis, therefore these tests are postponed to the second half of 2017. The second option is to modify the low temperature bonding process to be able to use the available mixed pitch sensors with RTI UBM. This is addressed in the next sections.

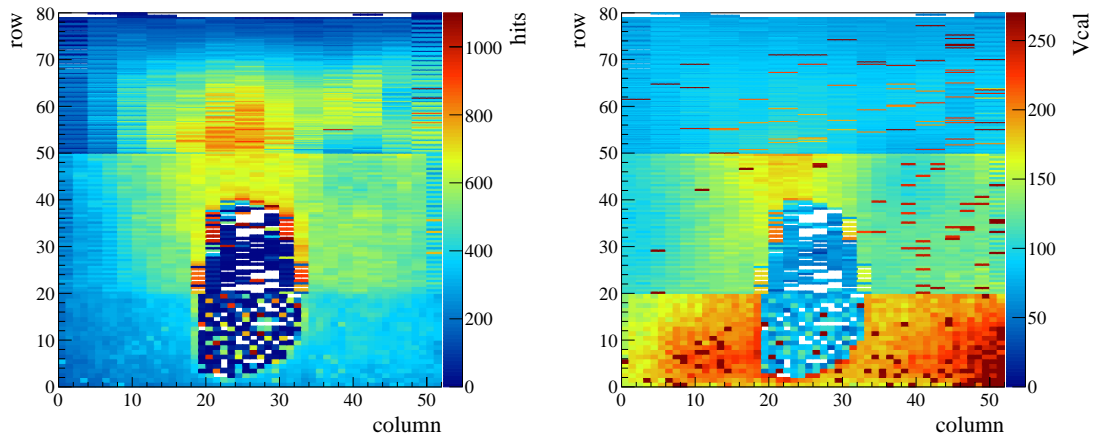
H.2.2 ULTRAVIOLET CURING GLUE

Since gold to tin lead bonding is not an option for the available mixed pitch sensor, other possibilities without gold studs have been evaluated. This means that the connection needs to be established between the tin lead bumps of the ROC and the sensor UBM, but without applying the heat required to establish a reliable intermetallic connection. Therefore, the possibility to support the bump bonds with the help of glue curing under UV light (abbreviated "UV glue" in the following) was investigated. The assumption is that the bonding, although performed at only 50 °C, provides at least a weak connection between the tin lead bumps and the sensor UBM. Immediately after bonding the glue is applied and UV cured to keep the sample exactly in this state and to protect the bump connections. In order to avoid that the glue itself disconnects the bump bonds due to an undesirable volume expansion while curing, the glue was selected carefully. The chosen glue is DELO DUALBOND AD761 [DEL17].

The UV glue is either applied at the corners of the sample or at three edges, excluding the edge where the wire bond pads are located. This approach was tested for bonding forces between 100 N and 250 N. Further, it was investigated whether it is beneficial to apply the glue already before bonding and perform the curing while the bond force is still applied to the assembly.

The best result was achieved for a bond force of 180 N and when the glue was applied after the bonding at the edges of the samples. A measurement with a ⁹⁰Sr source is given in figure H.6. The hit map of the corresponding measurement is shown in figure H.6 (a). The most prominent feature is a large area in the lower central region where almost no hits are detected. This indicates that the tin lead bumps in this region are barely connected to the sensor. Outside of this area and apart from the top row all pixels detected a reasonable number of electrons. However, the spot of the ⁹⁰Sr source, which should be circular, has an irregular shape. This indicates that the bump connections might not be completely flawless even if the pixels detect hits. Figure H.6 (b) shows the corresponding signal height map. Similar to the observation for the hit map the signal heights measured by pixels of the lower central region are suspicious. These signal heights are significantly lower compared to the values of the surrounding pixels which is another indication for barely connected bumps. Aside from this problematic region, the measured signal heights follow the expected trend. The highest signal heights correspond to the lower region while the lowest signal heights are associated to the part having the narrowest pixels and largest clusters. The absolute values of the signal heights are about 50 % smaller compared to the standard bonded mixed pitch sample (see figure H.2 (b)). Instead of an average signal height of about 400 Vcal for the 100 μm × 150 μm pixels in the lower region, the low temperature bonded sample only measures about 150 Vcal to 250 Vcal for the same pixels. With such samples it is barely possible to perform a reliable investigation of the hit efficiency or charge collection, but at least a study of the spatial resolution could be feasible. To investigate the long term stability thermal cycles between -20 °C and +20 °C were carried out. Even after ten cycles no deterioration was visible, which implies that the glue is able to

² The layer thicknesses of the RTI UBM and the exact UBM deposition process are classified information and thus not available.



(a) Hit map of a UV glue supported mixed pitch sample. In the lower central part an area is visible where barely a hit was detected probably due to not connected bumps. Almost all remaining pixels detected a reasonable number of electrons. The visible spot of the ^{90}Sr source does not show the expected circular shape indicating that each connection might not be completely flawless.

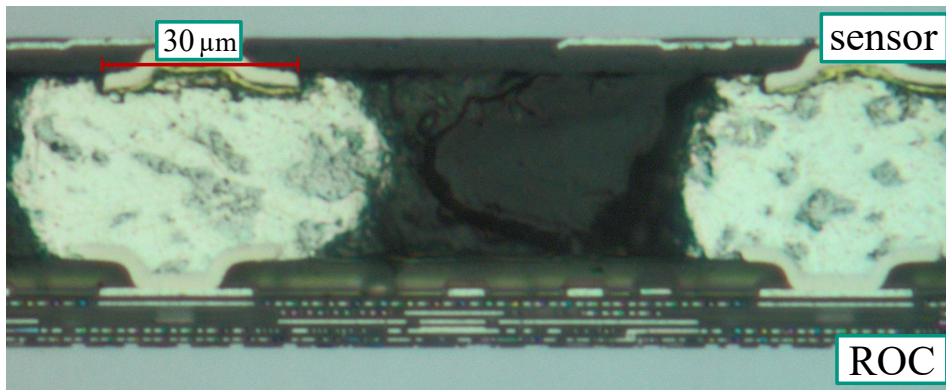
(b) Signal height map of a UV glue supported mixed pitch sample. The signal heights measured by the pixels of the affected lower central region are also suspicious as they are smaller compared to the reference results shown in figure H.2 (b). The expected trend that the lowest signal heights correspond to the narrower pixels in the top part and the highest signal heights to the bottom region is visible.

Figure H.6: Hit map and signal height map for a low temperature bonded mixed pitch sample supported by UV glue. The given results were obtained with a ^{90}Sr source.

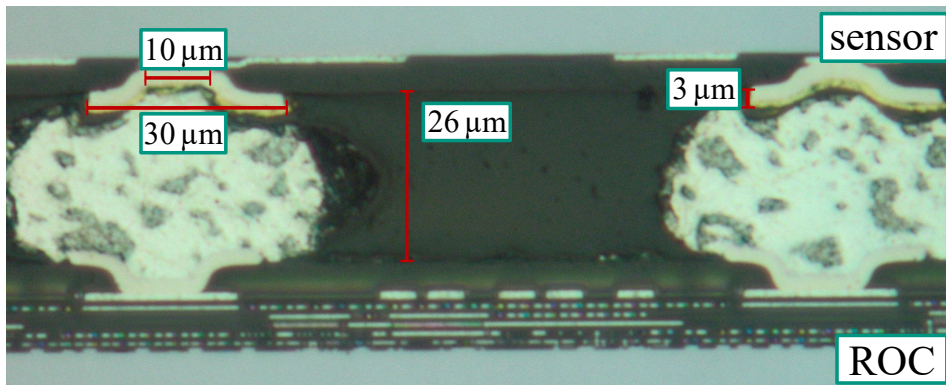
preserve the status of the sample. Again cross sections are used to investigate the bump to UBM connection in more detail.

Figure H.7 shows two cross sections of the sample where UV glue has been applied. In figure H.7 (a) two tin lead bumps located in the properly working region of the hit map shown in figure H.6 (a) are given. When the bumps were pressed down on the sensor UBM they deformed according to the shape of the UBM and established a connection. However, as indicated by some dark areas, the connection between bump and sensor UBM is not as homogeneous as the gold to tin lead connection shown in figure H.4. Still, the connections are good enough to read out charge created inside the sensor. In figure H.7 (b) the cross section through two bumps from the suspicious region in figure H.6 are shown. Again it is recognizable that the bumps have been deformed when they were pressed down to the sensor UBM but they did not establish a permanent connection. Instead, there is a small gap between the tin lead bumps and the sensor UBM. This observation explains the missing hits for the problematic region in figure H.6. It cannot be concluded from the given cross sections whether this gap occurred already during bonding or only after applying and curing the glue. Since the glue is only applied to the ROC edges, unsupported bump connections in the central region might have been intact initially and only have been separated after some time.

The given results confirm that the glue behaves as desired by mechanically stabilizing the sample at least partially. To verify if the connections in the affected central region might be preserved – since they were probably intact after bonding – it is necessary to support the entire volume between ROC and sensor. Therefore, the application of underfill adhesives is investigated in the next section.



(a) Cross section for two tin lead bumps corresponding to the properly working region of the hit map given in figure H.6 (a). When the bumps were pressed down to the sensor UBM they deformed and established a connection. However, the bump to sensor UBM connection is not perfectly homogeneous as indicated by the small dark region in between.



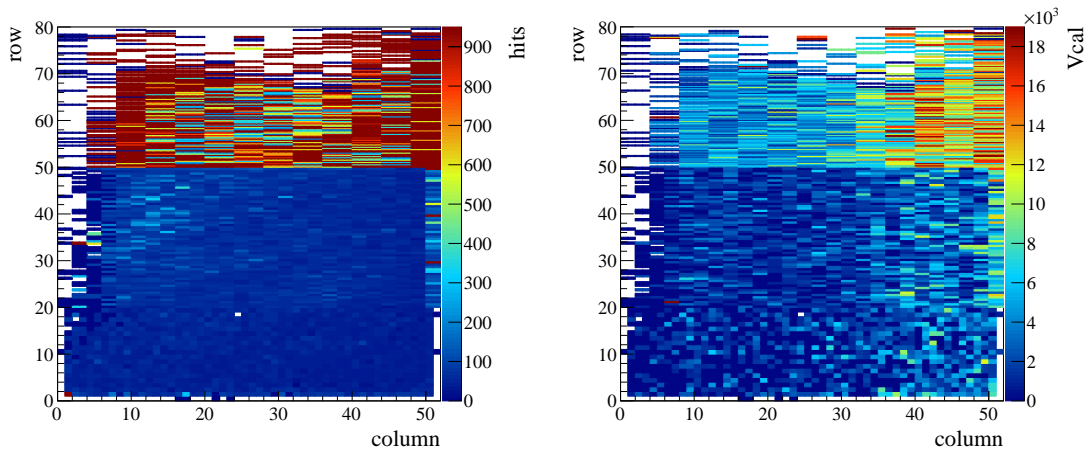
(b) Cross section for two tin lead bumps corresponding to the suspicious area of the hit map given in figure H.6 (a). Although the tin lead bumps were deformed when they were pressed down to the sensor UBM they did not establish a permanent connection as indicated by the gaps.

Figure H.7: Cross sections through two different regions of a low temperature bonded mixed pitch sample supported by UV glue.

H.2.3 UNDERFILL ADHESIVE

In contrast to the glue, no UV light is required to cure the underfill adhesive. Hence, its application is not limited to edges or corners of the sample. In addition, the viscosity of the underfill adhesive allows to fill up the gap between sensor and ROC completely in order to support all bump connections. The lower viscosity is also the reason why the underfill adhesive is exclusively applied after the bonding. Otherwise it could easily spill over onto the bonding table during bonding. The chosen underfill adhesive is EPO-TEK 301-2 [Epo17] due to its ability of curing at room temperature. Similar to the UV glue it was selected carefully to minimize the volume expansion during the curing process to avoid disconnecting tin lead bumps from the sensor UBM.

Figure H.8 shows a hit map and a signal height map of a ^{90}Sr source measurement of a low temperature bonded mixed pitch sample supported by an underfill adhesive (for a bond force of 200 N). The hit map given in figure H.8 (a) contains no problematic region in the lower central region. Instead there are several pixels, especially at the left and top edge, which are apparently not connected as they do not detect any hits. In addition, neither the spot of the ^{90}Sr source nor the typical trend across the three regions, as observed for the standard bonded mixed pitch sample in figure H.2 (a), are visible. Even though most hits were detected



(a) Hit map of an underfill adhesive supported mixed pitch sample. Apart from the left and top edge there are almost no unconnected areas. The number of hits in the top region is overproportionally high compared to the central and bottom regions (cf. figure H.2 (a)).

(b) Signal height map of an underfill adhesive supported mixed pitch sample. The highest measured signal heights correspond to the pixels of the top region (instead of the bottom region) which differs from the expected behavior observed in figure H.2 (b).

Figure H.8: Hit map and signal height map for a low temperature bonded mixed pitch sample supported by an underfill adhesive. The results, obtained with a ^{90}Sr source, differ significantly from the reference measurement (see figure H.2).

in the top region – as expected – the number of hits is overproportionally high compared to the other two regions. At the same time there is no difference (regarding the number of hits) between the middle region formed by the $50\ \mu\text{m} \times 300\ \mu\text{m}$ pixels and the bottom region with the $100\ \mu\text{m} \times 150\ \mu\text{m}$ pixels (see figure H.2 (a)). These observations are a hint for not perfectly connected bumps over the entire sample, although most pixels have detected electrons from the ^{90}Sr source. The situation is similar for the signal height map shown in figure H.8 (b). The highest signal heights are not measured in the bottom part, as expected from figure H.2 (b), but at the top region. Additionally the measured signal heights for the top region are distinctly higher than expected. The sample supported by the underfill adhesive measured signal heights of at least 600 Vcal in the top region while the average signal heights for the standard bonded sample are about 200 Vcal. The too high signal heights are probably related to noise caused by bad electrical conditions due to the aluminum routing lines and the underfill adhesive. Accordingly, the conclusions obtained from the signal height map are an indication for a sub-optimal connection between the tin lead bumps and the sensor UBM.

Similar to the sample supported by UV glue it is not possible to perform a reliable investigation of the hit efficiency or the charge collection efficiency with samples supported by an underfill adhesive. Even the investigation of the spatial resolution might be problematic as indicated by the unexpected signal heights, since they might influence the calculation of the center of charge and thus the determined resolution. The investigation of the underfill adhesive and the UV glue illustrates the difficulties to establish reliable connections with the available mixed pitch sensors at a bonding temperature of around $50\ ^\circ\text{C}$.

H.3 CONCLUSIONS

The results of this chapter confirm the successful development of a reliable low temperature bump bonding process which is based on a reliable connection between tin lead bumps and gold studs. However, this process implicitly demands sensors either without UBM or a suited one allowing to place gold studs. If this is not the case, as observed for the available mixed pitch sensors, the low temperature bonding becomes more difficult or even impossible. Supporting

the bump bonds with UV glue or underfill adhesives does not provide reliable connections. This clearly shows the importance of the UBM selection for sensor studies relying on a low temperature bump bonding process.

BIBLIOGRAPHY

- [3M 17] 3M COMPANY CORP.: *Fluorinert Electronic Liquid FC-72*. <http://multimedia.3m.com/mws/media/648920/fluorinert-electronic-liquid-fc-72.pdf>. Version: April 04, 2017 (cited on page 35.)
- [A⁺12] AGUILAR, J. et al.: Infrastructure for Detector Research and Development towards the International Linear Collider. In: *ArXiv e-prints* (2012), January. <http://adsabs.harvard.edu/abs/2012arXiv1201.4657A> (cited on page 113.)
- [A⁺15] APOLLINARI, Giorgio et al.: *High-Luminosity Large Hadron Collider (HL-LHC): Preliminary Design Report*. Geneva : CERN, 2015 <https://cds.cern.ch/record/2116337> (cited on page 11.)
- [Abb11] ABBANEO, Duccio: Upgrade of the CMS tracker with tracking trigger. In: *J. Instrum.* 6 (2011), C12065. 10 p. <https://cds.cern.ch/record/1452189> (cited on page 13.)
- [ALI17] ALICE COLLABORATION: *ALICE - A Large Ion Collider Experiment*. <http://alice-collaboration.web.cern.ch/>. Version: March 17, 2017 (cited on page 7.)
- [AMS17] AMS-02 COLLABORATION: *AMS 02 - The Alpha Magnetic Spectrometer Experiment at the International Space Station*. <http://www.ams02.org/>. Version: April 04, 2017 (cited on page 35.)
- [ATL12] ATLAS COLLABORATION: Observation of a new particle in the search for the Standard Model Higgs boson with the ATLAS detector at the LHC. In: *Physics Letters B* 716 (2012), No. 1, 1 - 29. <https://doi.org/10.1016/j.physletb.2012.08.020>. – ISSN 0370–2693 (cited on page 3.)
- [ATL17] ATLAS COLLABORATION: *The ATLAS experiment*. <https://atlas.cern/>. Version: March 17, 2017 (cited on page 7.)
- [B⁺05] BAYATYAN, G. L. et al.: *CMS computing: Technical Design Report*. Geneva : CERN, 2005 (Technical Design Report CMS). <http://cds.cern.ch/record/838359> (cited on page 11.)
- [B⁺06] BAYATYAN, G. L. et al.: *CMS Physics: Technical Design Report Volume 1: Detector Performance and Software*. Geneva : CERN, 2006 (Technical Design Report CMS). <https://cds.cern.ch/record/922757> (cited on page 8.)
- [Bar16] BARNEY, David: *CMS Detector Slice*. <https://cds.cern.ch/record/2120661>. Version: January 2016. – CMS-PHO-GEN-2016-001 (cited on page 10.)
- [BBB⁺09] BAUDOT, J. ; BERTOLONE, G. ; BROGNA, A. ; CLAUS, G. ; COLLEDANI, C. ; DEGERLI, Y. ; MASI, R. D. ; DOROKHOV, A. ; DOZIÈRE, G. ; DULINSKI, W. ; GELIN, M. ; GOFFE, M. ; HIMMI, A. ; GUILLOUX, F. ; HU-GUO, C. ; JAASKELAINEN, K. ; KOZIEL, M. ; MOREL, F. ; ORSINI, F. ; SPECHT, M. ; VALIN, I. ; VOUTSINAS, G. ; WINTER, M.: First test results of MIMOSA-26, a fast CMOS sensor with integrated zero suppression and digitized output. In: *2009 IEEE Nuclear Science Symposium Conference Record (NSS/MIC)*, 2009. – ISSN 1082–3654, P. 1169 – 1173 (cited on page 113.)

- [BCC⁺14] BÖHLEN, T. T. ; CERUTTI, F. ; CHIN, M. P. W. ; FASSÒ, A. ; FERRARI, A. ; ORTEGA, P. G. ; MAIRANI, A. ; SALA, P. R. ; SMIRNOV, G. ; VLACHOUDIS, V.: The FLUKA Code: Developments and Challenges for High Energy and Medical Applications. In: *Nuclear Data Sheets* 120 (2014), 211 - 214. <http://www.sciencedirect.com/science/article/pii/S0090375214005018>. – ISSN 0090–3752 (cited on page 91.)
- [BCL⁺04] BRÜNING, Oliver S. ; COLLIER, Paul ; LEBRUN, Philippe ; MYERS, Stephen ; OSTOJIC, Ranko ; POOLE, John ; PROUDLOCK, Paul: *LHC Design Report*. Geneva : CERN, 2004 <https://cds.cern.ch/record/782076> (cited on page 5.)
- [Bet30] BETHE, H.: Zur Theorie des Durchgangs schneller Korpuskularstrahlen durch Materie. In: *Annalen der Physik* 397 (1930), No. 3, 325 - 400. <http://dx.doi.org/10.1002/andp.19303970303>. – DOI 10.1002/andp.19303970303. – ISSN 1521–3889 (cited on page 23.)
- [BGG07] BEHNKE, T. ; GARUTTI, E. ; GREGOR, I.-M.: Test Beams at DESY. In: *EUDET-Memo-2007* EUDET-Memo-2007-11 (2007). <http://www.eudet.org/e26/e28/e182/e283/eudet-memo-2007-11.pdf> (cited on page 112.)
- [BKM11] BLOBEL, Volker ; KLEINWORT, Claus ; MEIER, Frank: Fast alignment of a complex tracking detector using advanced track models. In: *Computer Physics Communications* 182 (2011), No. 9, 1760 - 1763. <http://www.sciencedirect.com/science/article/pii/S0010465511001093>. – ISSN 0010–4655. – Computer Physics Communications Special Edition for Conference on Computational Physics Trondheim, Norway, June 23-26, 2010 (cited on page 117.)
- [BM14] BARTEK, Rachel ; MASCIOVECCHIO, Mario: HDI Testing Procedure for the Digital HDI using LabJack. (2014), August. <https://cds.cern.ch/record/1952337>. – CMS-IN-2014-009 (cited on page 60.)
- [BR97] BRUN, Rene ; RADEMAKERS, Fons: ROOT: An object oriented data analysis framework. In: *Nuclear Instruments and Methods in Physics Research Section A: Accelerators, Spectrometers, Detectors and Associated Equipment* 389 (1997), No. 1, 81 - 86. <http://www.sciencedirect.com/science/article/pii/S016890029700048X>. – ISSN 0168–9002 (cited on page 55.)
- [C⁺08] CHATRCHYAN, S. et al.: The CMS experiment at the CERN LHC. The Compact Muon Solenoid experiment. In: *J. Instrum.* 3 (2008), S08004. 361 p. <https://cds.cern.ch/record/1129810> (cited on page 10.)
- [C⁺14] CHATRCHYAN, Serguei et al.: Description and performance of track and primary-vertex reconstruction with the CMS tracker. In: *J. Instrum.* 9 (2014), May, No. arXiv:1405.6569, P10009. 80 p. <https://cds.cern.ch/record/1704291> (cited on page 10.)
- [C⁺15] CONTARDO, D. et al.: Technical Proposal for the Phase-II Upgrade of the CMS Detector. (2015), June. <https://cds.cern.ch/record/2020886>. – CERN-LHCC-2015-010 (cited on pages 13, 14.)
- [CBC⁺16] CASELLE, M. ; BLANK, T. ; COLOMBO, F. ; DIERLAMM, A. ; HUSEMANN, U. ; KUDELLA, S. ; WEBER, M.: Low-cost bump-bonding processes for high energy physics pixel detectors. In: *Journal of Instrumentation* 11 (2016), No. 1, C01050. <http://stacks.iop.org/1748-0221/11/i=01/a=C01050> (cited on page 184.)
- [CC74] CHELIKOWSKY, J. R. ; COHEN, M. L.: Electronic structure of silicon. In: *Phys. Rev. B* 10 (1974), December, 5095 - 5107. <http://dx.doi.org/10.1103/PhysRevB.10.5095>. – DOI 10.1103/PhysRevB.10.5095 (cited on page 17.)

- [CER06] CERN - EDUCATION, COMMUNICATIONS AND OUTREACH GROUP: *CERN LHC: the guide. faq. frequently asked questions*. Geneva : CERN, 2006 <https://cds.cern.ch/record/999421> (cited on page 6.)
- [Chi13] CHILINGAROV, A.: Generation current temperature scaling. (2013), January. <https://cds.cern.ch/record/1511886>. – PH-EP-Tech-Note-2013-001 (cited on page 22.)
- [CMS97a] CMS COLLABORATION: *The CMS electromagnetic calorimeter project: Technical Design Report*. Geneva : CERN, 1997 (Technical Design Report CMS). <https://cds.cern.ch/record/349375> (cited on page 9.)
- [CMS97b] CMS COLLABORATION: *The CMS hadron calorimeter project: Technical Design Report*. Geneva : CERN, 1997 (Technical Design Report CMS). <https://cds.cern.ch/record/357153> (cited on page 9.)
- [CMS03] CMS COLLABORATION: *CMS has a heart of pixels. Un coeur de pixels pour CMS*. <https://cds.cern.ch/record/1221568>. Version: February 2003. – BUL-PHO-2003-003 (cited on page 50.)
- [CMS11] CMS COLLABORATION: Technical proposal for the upgrade of the CMS detector through 2020. (2011), June. <https://cds.cern.ch/record/1355706>. – CERN-LHCC-2011-006 (cited on pages 12, 13.)
- [CMS12] CMS COLLABORATION: Observation of a new boson at a mass of 125 GeV with the CMS experiment at the LHC. In: *Physics Letters B* 716 (2012), No. 1, 30 - 61. <https://doi.org/10.1016/j.physletb.2012.08.021>. – ISSN 0370-2693 (cited on page 3.)
- [CMS13] CMS COLLABORATION: Identification of b-quark jets with the CMS experiment. In: *Journal of Instrumentation* 8 (2013), No. 4, P04013. <http://stacks.iop.org/1748-0221/8/i=04/a=P04013> (cited on page 34.)
- [CMS15] CMS COLLABORATION: 1-D plot covering CMS tracker, showing FLUKA simulated 1 MeV neutron equivalent in Silicon including contributions from various particle types. (2015), July. <http://cds.cern.ch/record/2039908>. – CMS-DP-2015-022 (cited on page 181.)
- [CMS16] CMS COLLABORATION: A level-1 pixel based track trigger for the CMS HL-LHC upgrade. (2016), July. <https://cds.cern.ch/record/2203806>. – CMS-DP-2016-055 (cited on page 13.)
- [CMS17a] CMS COLLABORATION: *CMS Pixel Production Database*. <http://cmspixelprod.pi.infn.it/cgi-bin/view.cgi?objName=RocWafer>. Version: April 20, 2017 (cited on page 50.)
- [CMS17b] CMS COLLABORATION: *The Compact Muon Solenoid experiment - detector*. <https://cms.cern/detector>. Version: March 30, 2017 (cited on page 9.)
- [CMS17c] CMS COLLABORATION: *The Compact Muon Solenoid experiment - people statistics*. <https://cms.cern/collaboration/people-statistics>. Version: March 17, 2017 (cited on page 7.)
- [Col16] COLOMBO, Fabio: *Packaging and assembly technologies for the pixel detector upgrade and measurement of $\tau\tau$ final states with the CMS experiment at the LHC*, Karlsruhe Institut für Technologie (KIT), PhD Thesis, 2016. <https://ekp-invenio.physik.uni-karlsruhe.de/record/48804>. – IEKP-KA/2016-16 (cited on pages 50, 52, 59 and 74.)

- [Com17a] COMMONS, Wikimedia: *Dotierung im zweidimensionales Siliziumkristallgitter mit Aluminium* [sic]. http://commons.wikimedia.org/wiki/File:Schema_-_p-dotiertes_Silicium.svg. Version: March 17, 2017 (cited on page 19.)
- [Com17b] COMMONS, Wikimedia: *Dotierung im zweidimensionales Siliziumkristallgitter mit Phosphor* [sic]. http://commons.wikimedia.org/wiki/File:Schema_-_n-dotiertes_Silicium.svg. Version: March 17, 2017 (cited on page 19.)
- [CRS02] CITTOLIN, Sergio ; RÁCZ, Attila ; SPHICAS, Paris: *CMS The TriDAS Project: Technical Design Report, Volume 2: Data Acquisition and High-Level Trigger. CMS trigger and data-acquisition project*. Geneva : CERN, 2002 (Technical Design Report CMS). <http://cds.cern.ch/record/578006> (cited on page 11.)
- [CSF⁺08] CHIOCHIA, V. ; SWARTZ, M. ; FEHLING, D. ; GIURGIU, G. ; MAKSIMOVIC, P.: A novel technique for the reconstruction and simulation of hits in the CMS pixel detector. In: *2008 IEEE Nuclear Science Symposium Conference Record*, 2008. – ISSN 1082–3654, 1909 - 1912 (cited on page 120.)
- [Cus09] CUSSANS, David: Description of the JRA1 Trigger Logic Unit (TLU), v0.2c. In: *EUDET-Memo-2009* EUDET-Memo-2009-04 (2009). <https://www.eudet.org/e26/e28/e42441/e57298/EUDET-MEMO-2009-04.pdf> (cited on page 115.)
- [DA⁺12] DOMINGUEZ, A. ; ABBANEO, D. et al.: CMS Technical Design Report for the Pixel Detector Upgrade. (2012), September. <https://cds.cern.ch/record/1481838>. – CERN-LHCC-2012-016 (cited on pages 12, 30, 33, 34, 35, 36, 37, 40, 43 and 47.)
- [DEL17] DELO INDUSTRIE KLEBSTOFFE GMBH & Co. KGAA: *DELO DUALBOND AD761*. https://www.delo.de/fileadmin/datasheet/DELO%20DUALBOND_AD761_%28TIDB-D%29.pdf. Version: June 07, 2017 (cited on page 187.)
- [Dem16] DEMTRÖDER, W.: *Experimentalphysik 3: Atome, Moleküle und Festkörper*. Springer Berlin Heidelberg, 2016 (Springer-Lehrbuch). <https://books.google.de/books?id=tR5kDAAAQBAJ>. – ISBN 9783662490945 (cited on page 15.)
- [Deu17a] DEUTSCHES ELEKTRONEN-SYNCHROTRON DESY: *DESY II Description & Status*. http://particle-physics.desy.de/test_beams_at_desy/desy_ii_description_status/index_ger.html. Version: May 11, 2017 (cited on page 112.)
- [Deu17b] DEUTSCHES ELEKTRONEN-SYNCHROTRON DESY: *EUDET-type beam telescopes*. https://telescopes.desy.de/Main_Page. Version: May 12, 2017 (cited on page 113.)
- [Deu17c] DEUTSCHES ELEKTRONEN-SYNCHROTRON DESY: *Test Beams at DESY*. <http://particle-physics.desy.de/e252106/>. Version: May 25, 2017 (cited on page 142.)
- [Die16] DIERLAMM, Alexander: Private communication. July 2016 (cited on page 107.)
- [Die17] DIERLAMM, Alexander: *Proton Irradiation: The Cyclotron and the Irradiation Setup*. <http://www.ekp.kit.edu/english/264.php>. Version: April 26, 2017 (cited on page 93.)
- [DM16] DE MELIS, Cinzia: The CERN accelerator complex. *Complexe des accélérateurs du CERN*. (2016), July. <https://cds.cern.ch/record/2197559>. – OPEN-PHO-ACCEL-2016-009 (cited on page 6.)
- [Dom07] DOMINGUEZ, Aaron: The CMS pixel detector. In: *Nuclear Instruments and Methods in Physics Research Section A: Accelerators, Spectrometers, Detectors and Associated Equipment* 581 (2007), No. 1 & 2, 343 - 346. <http://www.sciencedirect.com/science/article/pii/S016890020701635X>. – ISSN 0168–9002. – Proceedings of the 11th International Vienna Conference on Instrumentation (cited on page 10.)

- [EB64] ENGLERT, F. ; BROUT, R.: Broken Symmetry and the Mass of Gauge Vector Mesons. In: *Phys. Rev. Lett.* 13 (1964), August, P. 321 – 323 (cited on page 3.)
- [Ebe13] EBER, Robert: *Untersuchung neuartiger Sensorkonzepte und Entwicklung eines effektiven Modells der Strahlenschädigung für die Simulation hochbestrahlter Silizium-Teilchendetektoren*, Karlsruher Institut für Technologie (KIT), PhD Thesis, 2013. <http://digbib.ubka.uni-karlsruhe.de/volltexte/1000038403>. – IEKP-KA/2013-27 (cited on pages 28, 29 and 104.)
- [EBH⁺10] ERDMANN, W. ; BERTEL, W. ; HORISBERGER, R. ; KÄSTLI, H.-C. ; KOTLINSKI, D. ; KÖNIG, S. ; LANGENEGGER, U. ; MEIER, B. ; RADICCI, V. ; ROHE, T. ; STARODUMOV, A. ; STREULI, S.: Upgrade plans for the CMS pixel barrel detector. In: *Nuclear Instruments and Methods in Physics Research Section A: Accelerators, Spectrometers, Detectors and Associated Equipment* 617 (2010), No. 1 - 3, 534 - 537. <http://dx.doi.org/10.1016/j.nima.2009.10.029>. – ISSN 0168–9002 (cited on page 33.)
- [EM13] EL MORABIT, Karim: *Untersuchung von Testverfahren für die Produktion von CMS-Pixel-Modulen*, Karlsruher Institut für Technologie (KIT), Bachelor Thesis, 2013. <https://ekp-invenio.physik.uni-karlsruhe.de/record/48314>. – IEKP-BACHELOR-KA/2013-55 (cited on page 91.)
- [Epo17] EPOXY TECHNOLOGY INC.: *EPO-TEK Products*. <http://www.epotek.com/site/component/products/productdetail.html?cid=19&Itemid=435>. Version: June 07, 2017 (cited on page 189.)
- [Erd10] ERDMANN, Wolfram: The CMS Pixel Detector. In: *International Journal of Modern Physics A* 25 (2010), No. 7, 1315 - 1337. <https://doi.org/10.1142/S0217751X10049098> (cited on page 38.)
- [Erd15a] ERDMANN, Wolfram: *BPIX Module Production Readiness Review: Introduction & Overview*. Version: February 2015. <https://indico.cern.ch/event/373338/contributions/883073/attachments/743488/1019882/2015-02-25-BPix-Module-Production.pdf>. – (not public) (cited on page 39.)
- [Erd15b] ERDMANN, Wolfram: *CMS review of Phase 1 upgrades (LHCC)*. Version: November 2015. <https://indico.cern.ch/event/462092/contributions/1978820/attachments/1190335/1738684/2015-11-30-bpix.pdf>. – (not public) (cited on page 36.)
- [EUT17] *EUTelescope - A Generic Pixel Telescope Data Analysis Framework*. <http://eutelescope.web.cern.ch/>. Version: May 12, 2017 (cited on page 116.)
- [Fel17] FELD, Lutz: *The CMS Silicon Tracker*. https://web.physik.rwth-aachen.de/service/wiki/pub/Feld/FeldVortraege/CMS_Tracker_GSI.pdf. Version: April 27, 2017 (cited on page 10.)
- [Fin16] FINETECH GMBH & Co. KG: *Finetech FINEPLACER® femto Automated sub-micron Die Bonder*. Version: September 2016. <http://www.finetech.de/micro-assembly/products/diebonders1.html> (cited on pages 51, 52.)
- [Fre13] FREUND, Benedikt: *Calibration of the digital readout chip of the CMS Pixel Detector - Phase I Upgrade*, Karlsruher Institut für Technologie (KIT), Diploma Thesis, September 2013. <http://ekp-invenio.physik.uni-karlsruhe.de/record/48305/files/EKP-2013-00046.pdf>. – IEKP-KA/2013-21 (cited on pages 35, 95.)
- [GE07] GAEDE, F. ; ENGELS, J.: Marlin et al. - A Software Framework for ILC detector R&D. In: *EUDET-Report-2007* EUDET-Report-2007-11 (2007). <https://www.eudet.org/e26/e27/e584/eudet-report-2007-11.pdf> (cited on page 115.)

- [GM12] GROSS, R. ; MARX, A.: *Festkörperphysik*. De Gruyter, 2012 (Festkörperphysik). <https://books.google.de/books?id=IaVJAAAAQBAJ>. – ISBN 9783486714869 (cited on page 18.)
- [GM14] GROSS, R. ; MARX, A.: *Festkörperphysik*. De Gruyter, 2014 (De Gruyter Studium). https://books.google.de/books?id=pK_oBQAAQBAJ. – ISBN 9783110358704 (cited on page 16.)
- [Gra53] GRAY, Frank: *Pulse Code Communication*. United States Patent 2632058, March 1953 (cited on page 43.)
- [GT17] GUTHOFF, Moritz ; TADEJA, Slawomir: *Radiation Simulation Plotting tool v.1.5.2*. <https://cms-project-fluka-flux-map.web.cern.ch/cms-project-fluka-flux-map/index.shtml>. Version: April 26, 2017 (cited on page 91.)
- [H⁺95] HOLLEMAN, A. F. et al.: *Lehrbuch der anorganischen Chemie*. de Gruyter, 1995 <https://books.google.de/books?id=eGkvSDAqY9gC>. – ISBN 9783110126419 (cited on page 16.)
- [Har08] HARTMANN, Frank: *Evolution of Silicon Sensor Technology in Particle Physics*. Springer Berlin Heidelberg, 2008 (Springer Tracts in Modern Physics). <https://books.google.de/books?id=JmWoecZA1e4C>. – ISBN 9783540250944 (cited on pages 15, 20.)
- [Hei12] HEITZ, Stefan: *Bump-Bonding-Technologie für das Upgrade des CMS-Pixeldetektors*, Karlsruher Institut für Technologie (KIT), Diploma Thesis, October 2012. <http://ekp-invenio.physik.uni-karlsruhe.de/record/48178/files/iekp-ka2012-16.pdf>. – IEKP-KA/2012-16 (cited on page 184.)
- [Hei16] HEINDL, Stefan M.: *Production and Quality Assurance of Modules and Study of optimized Pixel Sensor Designs for the Upgrade of the CMS Pixel Detector*, Karlsruher Institut für Technologie (KIT), PhD Thesis, 2016. <http://dx.doi.org/10.5445/IR/1000068448>. – IEKP-KA/2016-14 (cited on pages 47, 48, 60, 97, 105 and 161.)
- [Hig64] HIGGS, P. W.: Broken Symmetries and the Masses of Gauge Bosons. In: *Phys. Rev. Lett.* 13 (1964), October, P. 508 – 509 (cited on page 3.)
- [Hil14] HILLERINGMANN, Ulrich: *Silizium-Halbleitertechnologie: Grundlagen mikroelektronischer Integrationstechnik*. Springer Fachmedien Wiesbaden, 2014 <https://books.google.de/books?id=xcx8BAAAQBAJ>. – ISBN 9783834820853 (cited on page 18.)
- [Hit15] HITI, Bojan: *Probe Station for Functionality Tests of Bare Modules for the Phase I Upgrade of the CMS Pixel Detector*, Karlsruher Institut für Technologie (KIT), Diploma Thesis, 2015. <https://ekp-invenio.physik.uni-karlsruhe.de/record/48731>. – IEKP-KA/2015-43 (cited on pages 54, 58.)
- [HK⁺16] HOSS, J. ; KÄSTLI, H.-C. et al.: Radiation tolerance of the readout chip for the Phase I upgrade of the CMS pixel detector. In: *Journal of Instrumentation* 11 (2016), No. 1, C01003. <http://stacks.iop.org/1748-0221/11/i=01/a=C01003> (cited on page 103.)
- [HLBS03] HUFFMAN, A. ; LABENNETT, R. ; BONAFEDE, S. ; STATLER, C.: Fine-pitch wafer bumping and assembly for high density detector systems. In: *2003 IEEE Nuclear Science Symposium. Conference Record (IEEE Cat. No.03CH37515)* Vol. 5, 2003. – ISSN 1082–3654, P. 3522 – 3526 (cited on pages 48, 49.)
- [Hof13] HOFFMANN, Karl-Heinz: *Entwicklung von neuen Sensorkonzepten und Untersuchungen an strahlentoleranten Siliziumstreifensensoren für CMS am Large Hadron Collider in der Hochluminositätsphase*, Karlsruher Institut für Technologie (KIT), PhD Thesis, 2013. <http://digbib.ubka.uni-karlsruhe.de/volltexte/1000034517>. – IEKP-KA/2013-1 (cited on page 16.)

- [Hos12] Hoss, Jan H.: *X-Ray Calibration of Pixel Detector Modules for the Phase I Upgrade of the CMS Experiment*, Karlsruher Institut für Technologie (KIT), Diploma Thesis, September 2012. <http://ekp-invenio.physik.uni-karlsruhe.de/record/48180/>. – IEKP-KA/2012-17 (cited on pages 20, 35 and 166.)
- [Huh02] HUHTINEN, Mika: Simulation of non-ionising energy loss and defect formation in silicon. In: *Nuclear Instruments and Methods in Physics Research Section A: Accelerators, Spectrometers, Detectors and Associated Equipment* 491 (2002), No. 1 & 2, 194 - 215. <http://www.sciencedirect.com/science/article/pii/S0168900202012275>. – ISSN 0168–9002 (cited on page 28.)
- [Int14] INTERGOVERNMENTAL PANEL ON CLIMATE CHANGE: *Climate Change 2013 - The Physical Science Basis: Working Group 1 - Contribution to the Fifth Assessment Report of the Intergovernmental Panel on Climate Change*. Cambridge University Press, 2014. – ISBN 110766182X (cited on page 35.)
- [JSB⁺16] JANSEN, Hendrik ; SPANNAGEL, Simon ; BEHR, Jörg ; BULGHERONI, Antonio ; CLAUS, Gilles ; CORRIN, Emlyn ; CUSSANS, David ; DREYLING-ESCHWEILER, Jan ; ECKSTEIN, Doris ; EICHHORN, Thomas ; GOFFE, Mathieu ; GREGOR, Ingrid M. ; HAAS, Daniel ; MUHL, Carsten ; PERREY, Hanno ; PESCHKE, Richard ; ROLOFF, Philipp ; RUBINSKIY, Igor ; WINTER, Marc: Performance of the EUDET-type beam telescopes. In: *EPJ Techniques and Instrumentation* 3 (2016), No. 1, 7. <http://dx.doi.org/10.1140/epjti/s40485-016-0033-2> (cited on page 113.)
- [Jun11] JUNKES, Alexandra: *Influence of radiation induced defect clusters on silicon particle detectors*, Hamburg U., PhD Thesis, 2011. <http://www-library.desy.de/cgi-bin/showprep.pl?thesis11-031>. – DESY-THESIS-2011-031 (cited on page 29.)
- [Käs13] KÄSTLI, H.-C.: Frontend electronics development for the CMS pixel detector upgrade. In: *Nuclear Instruments and Methods in Physics Research Section A: Accelerators, Spectrometers, Detectors and Associated Equipment* A731 (2013), 88 - 91. <http://dx.doi.org/10.1016/j.nima.2013.05.056>. – ISSN 0168–9002. – Proceedings, 6th International Workshop on Semiconductor Pixel Detectors for Particles and Imaging (PIXEL2012) (cited on pages 33, 43.)
- [KBE⁺06] KÄSTLI, H.-C. ; BARBERO, M. ; ERDMANN, W. ; HÖRMANN, C. ; HORISBERGER, R. ; KOTLINSKI, D. ; MEIER, B.: Design and performance of the CMS pixel detector readout chip. In: *Nuclear Instruments and Methods in Physics Research Section A: Accelerators, Spectrometers, Detectors and Associated Equipment* 565 (2006), No. 1, 188 - 194. <http://www.sciencedirect.com/science/article/pii/S0168900206007674>. – ISSN 0168–9002 (cited on page 40.)
- [Kop15] KOPPENHÖFER, Roland: *Energy Calibration of the Digital Readout Chip PSI46digV2.1-respin for the Phase I Upgrade of the CMS Pixel Detector*, Karlsruher Institut für Technologie (KIT), Bachelor Thesis, 2015. <https://ekp-invenio.physik.uni-karlsruhe.de/record/48724>. – IEKP-BACHELOR-KA/2015-36 (cited on page 91.)
- [Kot16] KOTLINSKI, Danek: Private communication. November 2016 (cited on page 144.)
- [Kud14] KUDELLA, Simon: *Gold-stud bump bonding interconnection technology for the CMS experiment*, Karlsruher Institut für Technologie (KIT), Master Thesis, May 2014. <http://ekp-invenio.physik.uni-karlsruhe.de/record/48571/files/EKP-2014-00082.pdf>. – IEKP-KA/2014-11 (cited on pages 49, 50, 181 and 184.)
- [Lan44] LANDAU, Lev D.: On the energy loss of fast particles by ionization. In: *J. Phys.(USSR)* 8 (1944), P. 201 – 205 (cited on page 24.)

- [LHC17a] LHCb COLLABORATION: *LHCb – The Large Hadron Collider beauty experiment*. <https://lhcb-public.web.cern.ch/lhcb-public/>. Version: March 17, 2017 (cited on pages 7, 35.)
- [LHC17b] LHCf COLLABORATION: *LHCf - Large Hadron Collider forward experiment*. <https://home.cern/about/experiments/lhcf>. Version: March 17, 2017 (cited on page 7.)
- [Lin03] LINDSTRÖM, Gunnar: Radiation damage in silicon detectors. In: *Nuclear Instruments and Methods in Physics Research Section A: Accelerators, Spectrometers, Detectors and Associated Equipment* 512 (2003), No. 1 & 2, 30 - 43. <http://www.sciencedirect.com/science/article/pii/S0168900203018746>. – ISSN 0168–9002. – Proceedings of the 9th European Symposium on Semiconductor Detectors: New Developments on Radiation Detectors (cited on page 27.)
- [Lut07] LUTZ, Gerhard: *Semiconductor Radiation Detectors: Device Physics*. Springer Berlin Heidelberg, 2007 <https://books.google.de/books?id=n56pWTNVqrkC>. – ISBN 9783540716792 (cited on page 30.)
- [M⁺12] MANS, J. et al.: CMS Technical Design Report for the Phase 1 Upgrade of the Hadron Calorimeter. (2012), September. <https://cds.cern.ch/record/1481837>. – CERN-LHCC-2012-015 (cited on page 12.)
- [Mei14] MEIER, Frank: Physics Performance with the CMS Pixel Detector. (2014), December. <https://cds.cern.ch/record/1977837>. – CMS-CR-2014-437 (cited on page 33.)
- [Mes05] MESCHEDE, Dieter: *Gerthsen Physik*. 23. Berlin : Springer, 2005 (cited on page 5.)
- [MoE17] MoEDAL COLLABORATION: *MoEDAL - Monopole and Exotics Detector at the LHC experiment*. <http://moedal.web.cern.ch/>. Version: March 17, 2017 (cited on page 7.)
- [Mol99] MOLL, Michael: *Radiation damage in silicon particle detectors: Microscopic defects and macroscopic properties*, Hamburg U., PhD Thesis, 1999. <http://www-library.desy.de/cgi-bin/showprep.pl?desy-thesis99-040>. – DESY-THESIS-1999-040 (cited on pages 29, 105.)
- [muo97] *The CMS muon project: Technical Design Report*. Geneva : CERN, 1997 (Technical Design Report CMS). <https://cds.cern.ch/record/343814> (cited on page 9.)
- [Nat17a] NATIONAL INSTRUMENTS CORP.: *LabVIEW (Laboratory Virtual Instrument Engineering Workbench) System Design Software*. <http://www.ni.com/labview/>. Version: April 14, 2017 (cited on page 65.)
- [Nat17b] NATIONAL INSTRUMENTS CORP.: *LabWindows/CVI (C for Virtual Instrumentation) Development Environment*. <http://www.ni.com/lwcvl/>. Version: April 10, 2017 (cited on page 54.)
- [Nat17c] NATIONAL INSTRUMENTS CORP.: *Vision Development Module*. <http://www.ni.com/vision/software/>. Version: April 09, 2017 (cited on pages 50, 54.)
- [NIS17] *X-Ray Transition Energies Database*. <https://www.nist.gov/pml/x-ray-transition-energies-database>. Version: April 14 2017. – National Institute of Standards and Technology (cited on pages 65, 100 and 102.)
- [Nür14] NÜRNBERG, Andreas: *Studien an bestrahlten Siliziumsensoren für den CMS Spurdetektor am HL-LHC*, Karlsruher Institut für Technologie (KIT), PhD Thesis, 2014. <http://digbib.ubka.uni-karlsruhe.de/volltexte/1000040990>. – IEKP-KA/2014-87 (cited on page 104.)

- [P⁺16] PATRIGNANI, C. et al.: Review of Particle Physics. In: *Chin. Phys.* C40 (2016), P. No. 10, 100001. <http://dx.doi.org/10.1088/1674-1137/40/10/100001>. – DOI 10.1088/1674-1137/40/10/100001 (cited on pages 18, 23, 24, 25 and 26.)
- [PCH⁺92] PITZL, D. ; CARTIGLIA, N. ; HUBBARD, B. ; HUTCHINSON, D. ; LESLIE, J. ; O'SHAUGHNESSY, K. ; ROWE, W. ; SADROZINSKI, H. F.-W. ; SEIDEN, A. ; SPENCER, E. ; ZIOCK, H. J. ; FERGUSON, P. ; HOLZSCHEITER, K. ; SOMMER, W. F.: Type inversion in silicon detectors. In: *Nuclear Instruments and Methods in Physics Research Section A: Accelerators, Spectrometers, Detectors and Associated Equipment* 311 (1992), No. 1, 98 - 104. <http://www.sciencedirect.com/science/article/pii/016890029290854W>. – ISSN 0168-9002 (cited on page 38.)
- [Pri16] PRINTZ, Martin: *Analysis of n-in-p type silicon detectors for high radiation environment with fast analogue and binary readout systems*, Karlsruher Institut für Technologie (KIT), PhD Thesis, 2016. <http://dx.doi.org/10.5445/IR/1000052766>. – IEKP-KA/2016-09 (cited on page 104.)
- [PRSZ04] POVH, B. ; RITH, K. ; SCHOLZ, C. ; ZETSCHKE, F.: *Povh, B: Teilchen und Kerne.: Eine Einführung in die physikalischen Konzepte*. Springer, 2004 (Physics and astronomy online library). <https://books.google.de/books?id=PIw0leNupOc>. – ISBN 9783540210658 (cited on page 6.)
- [Ram39] RAMO, Simon: Currents Induced by Electron Motion. In: *Proceedings of the IRE* 27 (1939), September, No. 9, 584 - 585. <https://dx.doi.org/10.1109/JRPROC.1939.228757>. – ISSN 0096-8390 (cited on page 30.)
- [RBC⁺05] ROHE, T. ; BORTOLETTO, D. ; CHIOCHIA, V. ; CREMALDI, L. M. ; CUCCIARELLI, S. ; DOROKHOV, A. ; HÖRMANN, C. ; KIM, D. ; KONECKI, M. ; KOTLINSKI, D. ; PROKOFIEV, K. ; REGENFUS, C. ; SANDERS, D. A. ; SON, S. ; SPEER, T. ; SWARTZ, M.: Fluence dependence of charge collection of irradiated pixel sensors. In: *Nuclear Instruments and Methods in Physics Research Section A: Accelerators, Spectrometers, Detectors and Associated Equipment* 552 (2005), No. 1 & 2, 232 - 238. <http://www.sciencedirect.com/science/article/pii/S0168900205012453> (cited on page 105.)
- [RBE⁺10] ROHE, T. ; BEAN, A. ; ERDMANN, W. ; KÄSTLI, H.-C. ; KHALATYAN, S. ; MEIER, B. ; RADICCI, V. ; SIBILLE, J.: Radiation hardness of CMS pixel barrel modules. In: *Nuclear Instruments and Methods in Physics Research Section A: Accelerators, Spectrometers, Detectors and Associated Equipment* 624 (2010), No. 2, 414 - 418. <http://www.sciencedirect.com/science/article/pii/S0168900210007837> (cited on page 105.)
- [Ren15] RENNER, Johanna: *Kalibrationsstudie des neuen Auslesechips des CMS Pixel-Detektors für das Phase-I-Upgrade*, Karlsruher Institut für Technologie (KIT), Bachelor Thesis, 2015. <https://ekp-invenio.physik.uni-karlsruhe.de/record/48617> (cited on page 91.)
- [Ren17] RENNER, Johanna: *Planning and validation of the thermal mock-up for the CMS Pixel Detector*, Karlsruher Institut für Technologie (KIT), Master Thesis, April 2017. <https://ekp-invenio.physik.uni-karlsruhe.de/record/48898/files/EKP-2017-00025.pdf>. – IEKP-KA/2017-13 (cited on page 36.)
- [Ros06] ROSSI, Leonardo: *Pixel Detectors: From Fundamentals to Applications*. Springer, 2006 (Particle Acceleration and Detection). <https://books.google.de/books?id=Jbp73yTz-LYC>. – ISBN 9783540283324 (cited on page 15.)
- [Ros14] Rosso, Antonella D.: HL-LHC updates in Japan. Projet HL-LHC : une réunion fait le point au Japon. (2014), December, 4. <https://cds.cern.ch/record/1975962>. – BUL-NA-2014-272. 51/2014 (cited on page 12.)

- [S⁺17] SIRUNYAN, Albert M. et al.: Particle-flow reconstruction and global event description with the CMS detector. (2017) (cited on page 11.)
- [Sab14] SABES, David: L1 track triggering with associative memory for the CMS HL-LHC tracker. In: *J. Instrum.* 9 (2014), No. 11, C11014. <https://cds.cern.ch/record/2025864> (cited on page 14.)
- [SBD⁺87] SUMMERS, G. P. ; BURKE, E. A. ; DALE, C. J. ; WOLICKI, E. A. ; MARSHALL, P. W. ; GEHLHAUSEN, M. A.: Correlation of Particle-Induced Displacement Damage in Silicon. In: *IEEE Transactions on Nuclear Science* 34 (1987), December, No. 6, 1133 - 1139. <https://dx.doi.org/10.1109/TNS.1987.4337442>. – ISSN 0018–9499 (cited on page 27.)
- [Sch] SCHELL, Daniel: *Working title: Studies for the CMS Phase II tracker (in progress)*, Karlsruher Institut für Technologie (KIT), PhD Thesis (cited on page 69.)
- [Sch05] SCHUBERT, E. F.: *Doping in III-V Semiconductors*. Cambridge University Press, 2005 (Cambridge Studies in Semicondu). https://books.google.de/books?id=_dMiJfCmLFoC. – ISBN 9780521017848 (cited on page 18.)
- [Sch15] SCHELL, Daniel: *Evaluation of Sensor Materials and Technologies for the Innermost Layer of the CMS Pixel Detector at the HL-LHC*, Karlsruher Institut für Technologie (KIT), Master Thesis, August 2015. <https://ekp-invenio.physik.uni-karlsruhe.de/record/48732>. – EKP-2015-00044 (cited on page 181.)
- [Sch17] SCHELL, Daniel: Private communication. March 2017 (cited on page 120.)
- [Sho38] SHOCKLEY, William B.: Currents to Conductors Induced by a Moving Point Charge. In: *Journal of Applied Physics* 9 (1938), No. 10, 635 - 636. <http://dx.doi.org/10.1063/1.1710367> (cited on page 30.)
- [SJ16] SPANNAGEL, Simon ; JANSEN, Hendrik: *GBL Track Resolution Calculator v2.0*. <http://dx.doi.org/10.5281/zenodo.48795>. Version: April 2016 (cited on page 141.)
- [SLS13] SUDAGAR, Jothi ; LIAN, Jianshe ; SHA, Wei: Electroless nickel, alloy, composite and nano coatings – A critical review. In: *Journal of Alloys and Compounds* 571 (2013), 183 - 204. <https://doi.org/10.1016/j.jallcom.2013.03.107>. – ISSN 0925–8388 (cited on page 46.)
- [SM13] SAKUMA, Tai ; McCAULEY, Thomas: Detector and event visualization with SketchUp at the CMS experiment. (2013), October. <http://cds.cern.ch/record/1626816>. – arXiv:1311.4942 (cited on page 8.)
- [SMP15] SPANNAGEL, Simon ; MEIER, Beat ; PERREY, Hanno C.: *The pxarCore Library - Technical Documentation, Reference Manual, and Sample Applications*. (2015), October. <http://cds.cern.ch/record/2137512>. – CMS-NOTE-2016-001 (cited on pages 54, 55.)
- [sol97] *The CMS magnet project: Technical Design Report*. Geneva : CERN, 1997 (Technical Design Report CMS). <https://cds.cern.ch/record/331056> (cited on page 9.)
- [Spa12] SPANNAGEL, Simon: *A High-Rate Beam Test for the CMS Pixel Detector Phase I Upgrade*, Diploma Thesis, November 2012. – IEKP-KA/2012-15 (cited on page 43.)
- [Spa16] SPANNAGEL, Simon: *Test Beam Measurements for the Upgrade of the CMS Pixel Detector and Measurement of the Top Quark Mass from Differential Cross Sections*. Hamburg, U. Hamburg, Dept. Phys., PhD Thesis, 2016. <https://beluga.sub.uni-hamburg.de/vufind/Record/860505286p>. – DESY-THESIS-2016-010 (cited on pages 41, 111 and 112.)

- [Spi05] SPIELER, Helmut: *Semiconductor Detector Systems*. OUP Oxford, 2005 (Series on Semiconductor Science and Technology). <https://books.google.de/books?id=MUMb3y37yqYC>. – ISBN 9780191523656 (cited on page 41.)
- [Sze85] SZE, Simon M.: *Semiconductor devices, physics and technology*. Wiley, 1985 <https://books.google.de/books?id=gb0QAQAAMAAJ> (cited on pages 21, 26.)
- [TA13] TAPPER, Alex ; ACOSTA, Darin: CMS Technical Design Report for the Level-1 Trigger Upgrade. (2013), June. <https://cds.cern.ch/record/1556311>. – CERN-LHCC-2013-011 (cited on page 13.)
- [Tas16] TASKIRDI, Yavuz: *Studien zur Qualität der Modulproduktion am KIT für das Phase I Upgrade des CMS Pixel Detektors*, Karlsruher Institut für Technologie (KIT), Diploma Thesis, October 2016. <https://ekp-invenio.physik.uni-karlsruhe.de/record/48846>. – IEKP-KA/2016-30 (cited on pages 65, 81, 95 and 101.)
- [TOT17] TOTEM COLLABORATION: *TOTEM - Total Elastic and Diffractive cross section Measurement experiment*. <https://home.cern/about/experiments/totem>. Version: March 17, 2017 (cited on page 7.)
- [Tsi09] TSIPENYUK, Yuri M.: *PHYSICAL METHODS, INSTRUMENTS AND MEASUREMENTS – Volume II*. 2009 <https://books.google.de/books?id=2mZ8DAAAQBAJ>. – ISBN 9781905839551 (cited on page 15.)
- [Tur93] TURCHETTA, Renato: Spatial resolution of silicon microstrip detectors. In: *Nuclear Instruments and Methods in Physics Research Section A: Accelerators, Spectrometers, Detectors and Associated Equipment* 335 (1993), No. 1, 44 - 58. <http://www.sciencedirect.com/science/article/pii/016890029390255G>. – ISSN 0168-9002 (cited on page 120.)
- [VBR⁺16] VERNIERI, Caterina ; BOLLA, Gino ; RIVERA, Ryan A. ; UPLEGGER, Lorenzo ; ZOI, Irene: Pixel Sensors with slim edges and small pitches for the CMS upgrades for HL-LHC. (2016), March. <https://cds.cern.ch/record/2142318>. – CMS-CR-2016-043 (cited on pages 181, 183.)
- [VG89] VAN GINNEKEN, Andreas: Nonionizing Energy Deposition in Silicon for Radiation Damage Studies. (1989). – FERMILAB-FN-0522 (cited on page 27.)
- [Woc17] WOCHLE, Jürgen: *4345LV: Am-241 X-ray Quelle variabler Energie*. <https://web.ikp.kit.edu/ssb/>. Version: May 02, 2017 (cited on page 163.)
- [Zim16] ZIMMERMANN, Claudius: *Aufbau eines Praktikumsversuchs zu Siliziumpixeldetektoren*, Karlsruher Institut für Technologie (KIT), Bachelor Thesis, 2016. <https://ekp-invenio.physik.uni-karlsruhe.de/record/48868>. – IEKP-BACHELOR-KA/2016-39 (cited on page 124.)

LIST OF FIGURES

Figure 2.1	Overview of the CERN accelerator complex	6
Figure 2.2	Structure of the CMS detector	8
Figure 2.3	Transverse slice through CMS	10
Figure 2.4	LHC schedule	12
Figure 3.1	Energy band model	16
Figure 3.2	Reduced zone scheme of silicon	17
Figure 3.3	Schematics of doped silicon and the corresponding energy levels	19
Figure 3.4	p-n junction	20
Figure 3.5	Ideal capacitance-voltage characteristics	22
Figure 3.6	Mean energy loss of positive muons in copper	23
Figure 3.7	Energy loss per radiation length of light charged particles in lead	24
Figure 3.8	Energy loss of a 500 MeV pions in silicon	25
Figure 3.9	Cross sections of photon interaction mechanisms in carbon	26
Figure 3.10	Displacement damage functions $D(E)$	27
Figure 3.11	Energy band model of defects	28
Figure 3.12	Working principle of a position sensitive silicon detector	29
Figure 4.1	Comparison of the original and Phase I pixel detector	35
Figure 4.2	Prototypes of the cooling loops and the carbon fiber support structure	36
Figure 4.3	Simulated material budget of the original and Phase I pixel detector	37
Figure 4.4	Exploded view of a Phase I pixel detector module for layers 3 to 4	39
Figure 4.5	Four pixel cells from a CMS barrel pixel sensor	40
Figure 4.6	Simplified block diagram of a pixel unit cell	41
Figure 4.7	Digital encoded data format of the Phase I readout chip	43
Figure 5.1	Workflow of the pixel module production at KIT	46
Figure 5.2	Visualization of the IV grading criteria	47
Figure 5.3	Cross-sectional view of the RTI solder bumping process	49
Figure 5.4	Cross-sectional sketch of a bare module	50
Figure 5.5	Overview of the FINEPLACER [®] femto bonding machine	51
Figure 5.6	Force and temperature profiles of the bump bonding process	52
Figure 5.7	Overview of the bare module probe station	55
Figure 5.8	Internal calibration mechanism of a PUC	56
Figure 5.9	Results from a pixel alive and a KIT bump bond test.	57
Figure 5.10	Pixel detector module for barrel layer 2 to 4 assembled at KIT	61
Figure 5.11	S-Curve test result of a single pixel	62
Figure 5.12	X-ray setup used during production and in further studies	64
Figure 6.1	Sensor wafer position of the bad pretest modules	68
Figure 6.2	Leakage current distribution of the bare modules produced at KIT	69
Figure 6.3	Defective pixel distribution of the bare modules produced at KIT	70
Figure 6.4	Number of replaced ROCs per reworked bare module	71
Figure 6.5	Number of replaced ROCs depending on the rework reason	73
Figure 6.6	Accumulated number of tested KIT bare modules and weekly testing rate	74
Figure 6.7	Yield of the KIT bare module production	75
Figure 7.1	Module leakage current distribution obtained during the X-ray test	78
Figure 7.2	Leakage current correlation between X-ray and bare module tests	79
Figure 7.3	X-ray module hit map and defective pixel maps for X-ray cuts 5 and 20	80

Figure 7.4	Total number of defective pixels of all KIT modules for different X-ray cuts	81
Figure 7.5	Overlay map of all defective pixels determined from the X-ray tests	83
Figure 7.6	Total number of correlated defective pixels depending on the X-ray cuts	84
Figure 7.7	Defective pixel correlation between bare modules and modules	85
Figure 7.8	Comparison between bare module and module grades	86
Figure 7.9	Final grades of the modules produced at KIT	87
Figure 8.1	Carrier PCBs for the single chip assemblies	92
Figure 8.2	ETP irradiation setup at the Zyklotron AG	93
Figure 8.3	Signal height distributions for characteristic X-ray photons and electrons	94
Figure 8.4	Measurement uncertainties for characteristic X-ray photons and electrons	96
Figure 8.5	Current-voltage characteristics of the irradiated module	97
Figure 8.6	Module hit maps for the unirradiated, $1e14 n_{eq}$ and $2e14 n_{eq}$ case	99
Figure 8.7	Module X-ray calibration before irradiation	102
Figure 8.8	Module signal heights in Vcal over bias voltage	103
Figure 8.9	Module signal heights in electrons over bias voltage	104
Figure 8.10	Current-voltage characteristics of the investigated single chip assemblies	106
Figure 8.11	Hit maps of ^{90}Sr measurements before and after irradiation	107
Figure 8.12	Signal heights in Vcal over bias voltage for the single chip assemblies	108
Figure 9.1	Test beam generation at DESY II	112
Figure 9.2	The DATURA beam telescope setup.	113
Figure 9.3	DUT cooling chuck for the test beam setup	114
Figure 9.4	Triggering scheme of the DESY test beam setup	115
Figure 9.5	Workflow of the EU Telescope analysis framework	116
Figure 9.6	Correlation plots before and after event shifting.	119
Figure 9.7	Hit maps of an unirradiated SCA obtained from the test beam study	121
Figure 9.8	Normalized cluster size distributions	123
Figure 9.9	Cluster size as a function of the tilt angle	124
Figure 9.10	Mean cluster size depending on the intrapixel impact position	125
Figure 9.11	Normalized seed pixel map	127
Figure 9.12	Efficiency maps for different samples	129
Figure 9.13	DUT efficiency depending on the x-coordinate of the track	130
Figure 9.14	Hit efficiency depending on the residual cut	131
Figure 9.15	Intrapixel hit efficiency	132
Figure 9.16	Hit efficiency depending on the bias voltage	133
Figure 9.17	Hit efficiency depending on tilt angle and threshold	134
Figure 9.18	Hit efficiency depending on the irradiation uniformity	135
Figure 9.19	Intrapixel resolution for a tilt angle of 0° and 55°	137
Figure 9.20	Profile plots of the intrapixel resolution	139
Figure 9.21	Residual distribution of the y-coordinates	140
Figure 9.22	Pointing resolution of the upstream tracks	141
Figure 9.23	Intrinsic resolution depending on the bias voltage	142
Figure 9.24	Intrinsic resolution depending on the tilt angle	143
Figure 9.25	Impact of the pulse height calibration on the intrinsic resolution	144
Figure 9.26	Intrinsic resolution depending on the irradiation fluence	145
Figure A.1	Number of replaced ROCs as a function of the ROC position	155
Figure B.1	Dead pixel distribution of the KIT modules for different X-ray cuts	157
Figure B.2	Dead pixel comparison between bare modules and modules	158
Figure C.1	Current-voltage characteristics of all SCAs for the performance study	160
Figure D.1	Electrical test setup for the KIT module production	161
Figure E.1	^{241}Am based X-ray source and the corresponding energy spectrum	163
Figure F.1	Threshold maps of two $4e14 n_{eq}$ single chip assemblies	165
Figure F.2	X-ray calibrations of the test beam samples performed before irradiation	166
Figure F.3	X-ray calibrations for different bias voltages and thresholds	167

Figure F.4	X-ray calibrations before and after irradiation	168
Figure G.1	Shift distributions of all test beam measurements.	170
Figure G.2	Number of shifts depending on different parameters	171
Figure G.3	Cluster size maps for three different tilt angles	173
Figure G.4	Cluster size profile plots	174
Figure G.5	Normalized cluster signal height maps	175
Figure G.6	Normalized seed pixel maps for four tilt angles	176
Figure G.7	Cluster size as a function of the bias voltage	177
Figure G.8	Cluster size depending on the tilt angle for different thresholds	178
Figure G.9	Hit efficiency profiles through the bias dot	179
Figure G.10	Intrapixel resolution for different tilt angles	180
Figure H.1	Pixel geometries of the mixed pitch sensor	182
Figure H.2	Hit map and signal height map for a standard bonded mixed pitch sample	183
Figure H.3	Hit map of a standard bonded and a low temperature bonded sample . . .	184
Figure H.4	Cross section of a gold stud to tin lead bump connection	185
Figure H.5	Hit map and signal height map before and after thermal cycling	186
Figure H.6	Hit map and signal height map of a glue supported mixed pitch sample .	188
Figure H.7	Cross sections through the glue supported mixed pitch sample	189
Figure H.8	Hit map and signal height map of a underfill supported sample	190

LIST OF TABLES

Table 4.1	Simulated data loss for the original and Phase I pixel detector	34
Table 4.2	Comparison of the PSI46V2 with PSI46digV2.1-respin	43
Table 6.1	Leakage current classification of the pretest modules	68
Table 6.2	Yield of the KIT bare module rework process	72
Table 8.1	K_{α} transition energies of the available target materials	100
Table 9.1	Test beam measurement program	118
Table 9.2	Optimal bias voltage	146
Table 9.3	Hit efficiency for different tilt angels and thresholds	146
Table 9.4	Spatial resolution for different tilt angles and thresholds	147
Table C.1	Samples for the performance study	159

ACKNOWLEDGMENTS – DANKSAGUNG

The present thesis would not have been possible without the support of many people, to whom I express my greatest thanks!

Die vorliegende Arbeit wäre ohne die Unterstützung zahlreicher Mitmenschen nicht gelungen. Euch möchte ich an dieser Stelle meinen aufrichtigen Dank aussprechen.

Zuallererst gilt mein Dank Herrn Prof. Dr. Ulrich Husemann, für die Möglichkeit meine Promotion am Institut für Experimentelle Teilchenphysik im faszinierenden Gebiet der Detektorentwicklung und -konstruktion durchzuführen.

Prof. Dr. Thomas Müller möchte ich für die Unterstützung während der letzten dreieinhalb Jahre und der Übernahme des Korreferats danken.

Dr. Thomas Weiler danke ich für die ausgiebige Unterstützung, vor allem für die hilfreichen Diskussionen zur Fragestellung und der Messergebnisse.

Mein Dank gilt im Besonderen auch

- Dr. Alexander Dierlamm für die Hilfe bei jeglichen Fragen zu Sensorfeinheiten und die Korrektur dieser Arbeit
- Dr. Hans Jürgen Simonis für die Administration des Netzwerks und der Hardware sowie für viele kurzweilige Diskussionen
- Dr. Stefan Heindl für seinen unermesslichen Einsatz für das Institut, aber auch für zahlreiche und erheiternde Anekdoten zum aktuellen Tagesgeschehen sowie der Korrektur dieser Arbeit
- Daniel Schell für seine Unterstützung im Test Beam und für die Korrektur dieser Arbeit
- Tobias Barvich für seine fortwährende Hilfsbereitschaft bei allerlei technischen Herausforderungen und für zahlreiche amüsante Einfälle
- Anita Weddigen, Pia Steck und Felix Bögelspacher für viele gebondete Samples, Bestrahlungen, die Unterstützung im Test Beam und ein hightech Looping Louie
- Dr. Fabio Colombo für die Korrektur dieser Arbeit
- meinen Mitstreitern Robert Eber, Andreas Nürnberg, Martin Printz, Florian Kassel, Simon Kudella, Marius Metzler und Stefan Maier
- Brigitte Gering und Diana Fellner für alle organisatorischen und bürokratischen Arbeiten
- Dr. Dominik Haitz und Yavuz Taşkirdi für ihre Unterstützung schon während des Studiums
- Julia Onnen für ihre klugen Ratschläge zu Stil und Form dieser Arbeit
- meinen Eltern Andrea und Bernhard Freund, sowie meinen Brüdern Sebastian und Moritz, die mich auch während der letzten Jahre unterstützten

- Stefanie Krickl für die besondere Unterstützung und ihre Geduld in den letzten Jahren auch wenn sie selbst dafür verzichten musste, sowie für die Korrektur dieser Arbeit
- allen Freunden, Verwandten (im Besonderen meinem Onkel Jürgen Decker) und Bekannten für ihre Unterstützung und willkommene Zerstreuung in den letzten Jahren!

Der Landesgraduiertenförderung des Landes Baden-Württemberg und der Karlsruhe School of Elementary Particle and Astroparticle Physics: Science and Technology (KSETA) möchte ich für die Unterstützung während der Promotion danken.

The measurements leading to these results have been performed at the Test Beam Facility at DESY Hamburg (Germany), a member of the Helmholtz Association (HGF).

This work is supported by the Initiative and Networking Fund of the Helmholtz Association, contract HA-101 ('Physics at the Terascale').

DECLARATION

I declare that the work in this dissertation was carried out in accordance with the requirements of the University's Regulations and that it has not been submitted for any other academic award. Except where indicated by specific reference in the text, the work is the candidate's own work. Work done in collaboration with, or with the assistance of, others is indicated as such.

Karlsruhe, July 2017

Benedikt Freund

